Technische Universität München
TUM School of Engineering and Design

Combined analysis on creep and aging of granular materials

Belinda Anna-Maria Jessen

Vollständiger Abdruck der von der TUM School of Engineering and Design der Technischen Universität München zur Erlangung einer

Doktorin der Ingenieurwissenschaften (Dr.-Ing.)

genehmigten Dissertation.

Vorsitz: Prof. Dr.-Ing. Christian Große

Prüfende der Dissertation:

1. Prof. Dr.-Ing. Roberto Cudmani
2. Prof. Juan Carlos Santamarina
3. Prof. Dr.-Ing. habil. Torsten Wichtmann

Die Dissertation wurde am 19.12.2023 bei der Technischen Universität München eingereicht und durch die TUM School of Engineering and Design am 01.07.2024 angenommen.

Preface

In geotechnical engineering, deformations in granular soils are typically assumed to occur almost instantaneously upon applying external loads. While this assumption holds for natural coarse-grained soil deposits, it is not necessarily valid for freshly deposited granular soils or natural soils disturbed by construction processes, such as pile driving or dynamic compaction. These disturbed soils often exhibit delayed grain rearrangements under constant external loads - a phenomenon commonly referred to as creep. Creep is frequently accompanied by changes in soil stiffness and strength over time, a process generally known as aging. Although these phenomena are interrelated at the micromechanical level, a comprehensive investigation of their interplay was absent in the literature prior to Belinda's research. This knowledge gap has left modern soil mechanics unable to fully explain several field observations critical to geotechnical practice, such as the delayed increase in penetration resistance of freshly compacted granular soils or the time-dependent shaft resistance of driven piles. To address this gap, Belinda has employed various experimental techniques and contributed significantly to advancing experimental methodologies. Her work has included the development of two innovative triaxial testing devices and the implementation of a volume measurement system based on the "cell-in-cell" principle, designed to capture the minute volumetric creep deformations of dry soil samples. Additionally, Belinda successfully measured acoustic emissions (AE) and determined seismic wave propagation velocities using advanced sensor technologies to track micromechanical processes during soil deformation. These pioneering techniques are now applied across multiple fundamental and applied research projects at Zentrum Geotechnik.

The experimental findings from Belinda's research are exceptional, as are her contributions to the design of triaxial devices and the development of experimental tools to quantify creep and detect aging in granular soils. A key outcome of her research is the correlation between acoustic emissions and creep strains, which reveals that time-dependent behaviors in granular soils are associated with stick-slip processes at grain contacts. Her analysis shows that these stick-slip events, which resemble micro-earthquakes following the Gutenberg-Richter relationship, are the primary source of creep and aging phenomena. Belinda has demonstrated that a temporary weakening of the granular skeleton may occur after a specific creep time in freshly deposited samples. This weakening is linked to the formation of a few dominant force chains, which initially increase the soil's small-strain stiffness. However, static fatigue at grain contacts eventually causes these force chains to collapse, temporarily increasing the creep rate and reducing stiffness. Over time, the granular structure reorganizes, evolving toward a more stable state with a more uniform distribution of contact forces. This results in a gradual increase in small-strain shear stiffness, a hallmark of the aging process. Furthermore, Belinda has established that the relationship between the creep rate and time, as well as the aging rate with time, can be approximated by linear trends on a double logarithmic scale. Remarkably, the slopes of these trends are close to unity, underscoring the consistency of the underlying micromechanical processes.

Belinda's thesis has profoundly advanced our understanding of creep and aging in granular soils. It provides a robust experimental database for developing, validating, and calibrating advanced numerical models necessary for simulating these time-dependent phenomena in granular materials.

Roberto Cudmani

Abstract

Combined analysis on creep and aging of granular materials

The time- and rate-dependent behavior of granular materials, as well as the associated micromechanical processes, are fundamentally investigated in relation to various state variables. In particular, the focus is on the relationship between creep and aging, analyzed through the evolution of strain and stiffness at very small strains under constant stress. The extensive experimental study includes oedometer and triaxial tests on cylindrical samples, taking into account multidimensional deformation and stress states, as well as varying loading histories. Based on the experimental findings and supported by hypotheses from the literature, a conceptual micromechanical model was developed to describe the relationship between creep and aging. A challenge involved reliably measuring creep deformation, aging, and the underlying micromechanical processes simultaneously in samples with different initial densities and at stresses up to 6000 kPa over test durations of up to three weeks.

The results demonstrate that acoustic emissions can be used to qualitatively determine micromechanical processes. A rate dependence of shear strength is negligible in the granular materials studied. Creep and aging can be attributed to time-dependent changes in the distribution of contact forces within the grain skeleton, induced by particle rearrangements and corresponding changes in particle contacts. The experimental study shows that initially increased contact sliding and particle movement lead to a reduction in structure, thereby decreasing the extent of aging. In samples with initially stable particle structures, a proportional relationship between the normalized rates of creep strain and the relative change in shear modulus at small strains was observed. This relationship is independent of mean stress, deviatoric stress, and initial density.

The proposed conceptual model adequately describes the processes occurring at the micro- and mesoscale. The experimentally determined relationship between creep and aging provide a unique basis for the development, validation, and calibration of advanced contact models.

Keywords: Silica sand, Creep, Aging, Granular materials, Triaxial testing

Kurzfassung

Kombinierte Untersuchung von Kriechen und Alterung granularer Materialien

Das zeit- und ratenabhängige Materialverhalten granularer Materialien sowie die damit verbundenen mikromechanischen Prozesse werden in Abhängigkeit von verschiedenen Zustandsgrößen grundlegend untersucht. Insbesondere steht der Zusammenhang zwischen Kriechen und Alterung im Fokus, welcher anhand der Entwicklung von Dehnung und Steifigkeit bei sehr kleinen Dehnungen unter konstanter Spannung analysiert wurde. Die umfangreiche experimentelle Untersuchung umfasst Ödometer- und Triaxialversuche an zylindrischen Proben, die multidimensionale Verformungs- und Spannungszustände sowie unterschiedliche Belastungsgeschichten berücksichtigt. Basierend auf der experimentellen Untersuchung und gestützt durch Hypothesen aus der Fachliteratur, wurde ein konzeptionelles mikromechanisches Modell zur Beschreibung des Zusammenhangs zwischen Kriechen und Alterung entwickelt. Eine zentrale Herausforderung bestand darin, Kriechverformung, Alterung und die zugrundeliegenden mikromechanischen Prozesse zeitgleich an Proben mit unterschiedlichen Anfangsdichten und bei Spannungen von bis zu 6000 kPa über Versuchszeiträume von bis zu drei Wochen zuverlässig zu messen.

Die Ergebnisse zeigen, dass akustische Emissionen zur qualitativen Bestimmung der mikromechanischen Prozesse genutzt werden können. Eine Ratenabhängigkeit der Scherfestigkeit ist bei den untersuchten granularen Materialien vernachlässigbar. Kriechen und Alterung lassen sich auf zeitabhängige Veränderungen der Kontaktkraftverteilung im Korngerüst zurückführen, welche durch Kornumlagerung und die damit verbundenen Änderungen von Partikelkontakten induziert werden. Die experimentelle Untersuchung zeigt, dass anfänglich zunehmendes Kontaktgleiten und zunehmende Partikelbewegung zu einer abnehmenden Strukturierung und damit Verringerung des Ausmaßes der Alterung führen. In Proben mit anfänglich stabilen Kornstrukturen wurde eine proportionale Beziehung zwischen den normalisierten Raten der Kriechdehnung und der relativen Änderung des Schubmoduls bei kleinen Dehnungen beobachtet. Die Beziehung ist unabhängig vom mittleren Druck, der deviatorischen Spannung und der initialen Lagerungsdichte.

Das vorgeschlagene konzeptionelle Modell kann die auf der Mikro- und Mesoebene ablaufenden Prozesse hinreichend beschreiben. Die experimentell ermittelten Zusammenhänge zwischen Kriechen und Alterung bieten eine einzigartige Grundlage für die Entwicklung, Validierung und Kalibrierung höherwertiger Kontaktmodelle.

Schlagwörter: Quarzsand, Kriechen, Alterung, Granulare Materialien, Triaxialversuch.

Table of contents

Symbols

Latin symbols (A – Z)

Symbol	Name	Unit
A (section 4.1)	observation area for roughness determination	mm²
A (section 4.4)	fractual area	mm²
C	oedometric creep-coefficient with reference to ε and $\ln()$	
C_{AE}	oedometric acoustic emission coefficient with reference to N_{AE} and $\ln()$	
C_α	oedometric creep-coefficient with reference to e and $\log_{10}$	
C_c	oedometric compression index with reference to e and $\log_{10}$	
$C_c{}^*$	curvature coefficient	
C_u	uniformity coefficient	
$CC_{xy}(\tau)$	cross correlation of function X and Y	
D (section 3)	sample diameter	mm
D (section 4)	fractal dimension	
d	burst signal duration of an acoustic emission event	s
d_p	diameter of the loading piston (triaxial cell)	mm
dV_p	volume change of inner cell measured by a volume control device	ml
d_{50}	diameters where 50% of the soil is finer	mm
e	void ratio	
e_0	initial void ratio	
e_{max}	maximum void ratio	
e_{min}	minimum void ratio	
E	signal burst energy of an acoustic emission event	10^{-18} J
f	frequency	Hz
F_n	Normal contact forces	
F_t	Tangential contact forces	
G	shear modulus	Pa
G_0	shear modulus at small strain, i.e. $\gamma = 10^{-5}$	Pa
$\dot{G}_0$	rate of change of small-strain shear modulus	Pa/s
$G_{0,t=0}$	shear modulus at small strain at the onset of creep	Pa
G_{xy}	shear modulus determined with shear waves propagating in x-direction and polarized in y-direction	Pa

Symbol	Name	Unit
G_{yz}	shear modulus determined with shear waves propagating in y-direction and polarized in z-direction	Pa
G_{zx}	shear modulus determined with shear waves propagating in z-direction and polarized in x-direction	Pa
h	sample height	mm
h_0	initial sample height	mm
I_D	relative density according to e_{min} and e_{max}	
l	shear wave travel path	mm
m	inclination describing a power law in a double logarithmic presentation	
N (section 3)	number of wave lengths	
N (section 4)	number of earthquakes	
N_{AE}	number of acoustic emissions events	
$\dot{N}_{AE}$	rate of number of acoustic emission events	
$N_{AE,0}$	number of acoustic emissions events at the onset of a creep phase	
N_G	normalized aging coefficient	
p'	mean effective stress	Pa
p_A	atmospheric pressure, i.e. used as a reference pressure	Pa
p'_0	confining pressure	Pa
q	deviatoric stress	Pa
q_{max}	maximum deviatoric pressure	Pa
R	roundness according to Krumbein and Sloss (1963)	
S	sphericity according to Krumbein and Sloss (1963)	
S_q	mean squared particle roughness	µm
T	temperature	K
t	time	s
t_0	starting time	s
t_c	shear wave travel time determined with the cross-correlation method	s
t_p	shear wave travel time determined with the peak-to-peak method	s
t_{ph}	travel time corresponding to phase velocity	s
t_{pc}	time after primary consolidation or initialization phase	s
t_{ref}	reference time	s

Symbol	Name	Unit
t_s	shear wave travel time determined with the start-to-start method	s
t_{sys}	system time delay	s
U	signal voltage of an acoustic emission event	V
V_0	initial sample volume	ml
v_{ph}	phase velocity	m/s
v_s	shear wave velocity	m/s
v_{s1}	pressure compensated shear wave velocity	m/s
V_T	volume change due to temperature variation	ml
z	depth coordinate for roughness determination	mm

Greek symbols (α – ω)

Symbol	Name	Unit
α_T	volume expansion coefficient	1/°C
$\dot{\gamma}$	shear strain rate	1/s
γ	shear strain	
$\dot{\varepsilon}$	strain rate	1/s
$\dot{\varepsilon}_a$	axial strain rate	1/s
ε_a	axial strain	
ε^e	elastic strain	
ε^{ir}	irreversible (plastic) strain	
ε_q	deviatoric strain	
ε^{pl}	plastic strain	
$\dot{\varepsilon}_r$	radial strain rate	1/s
ε_r	radial strain	
$\dot{\varepsilon}_{vol}$	volumetric strain rate	1/s
ε_{vol}	volumetric strain	
$\dot{\varepsilon}_0$	initial strain rate	1/s
ε_0	initial strain	
$\dot{\varepsilon}_1$	major principal strain rate	1/s
ε_1	major principal strain	
ε_2	intermediate principal strain	
$\dot{\varepsilon}_3$	minor principal strain rate	1/s
ε_3	minor principal strain	
η	stress ratio between deviatoric stress and mean effective stress	
λ	wavelength	mm
ρ	density	g/cm^3
σ'	effective stress	Pa
$\dot{\sigma'}_a$	axial effective stress rate	Pa/s
σ'_a	axial effective stress	Pa
σ'_c	effective confining pressure	Pa
σ_f	time independent stress	Pa
$\dot{\sigma'}_r$	radial effective stress rate	Pa/s
σ'_r	radial effective stress	Pa
σ_v	time dependent, viscous stress	Pa

Symbol	Name	Unit
σ'_0	initial effective stress	Pa
σ'_1	major principal stress	Pa
σ'_3	minor principal stress	Pa
φ'	friction angle	°
φ_{max}	maximum friction angle	°
ϕ_{corr}	corrected phase shift	°
ϕ_{exp}	experimentally determined phase shift	°
ϕ_f	unwrapped phase angle	°
ϕ_{ph}	phase shift	°
ω	angular frequency	°/s

Acronyms (A – Z)

Acronym	Name
AE	acoustic emission
BE	bender element
CPT	cone penetration test
CRS	constant rate of strain
CRS-C	constant rate of strain - creep
DEM	discrete element method
DDT	duration discrimination time
DIC	digital image correlation
EOP	end of primary consolidation
FFT	fast fourier transformation
ICL-C	isotropic constant loading – creep
IIL-C	incrementally isotropic loading - creep
LVDT	linear variable differential transformer
NBR	Nitrile butadiene rubber
OCR	overconsolidation ratio
P&N	positive – negative
P-RAT	piezo-electric ring actuator technique
PTFE	Polytetrafluorethylen
P-wave	primary (or compression) wave
RAT	rearm time
PZT	Lead zirconate titanate
S-wave	secondary (or shear) wave
TESRA	temporary effect of strain rate and acceleration
VPC	volume pressure control

1. Introduction

1.1 Motivation

Granular soils freshly deposited by natural or anthropogenic processes and granular soils that lost their natural structure, by i.e. construction processes such as pile driving or soil compaction by vibration, change their mechanical properties within well-observable scales of time. This time-dependent process is also called aging (Mitchell, 2005). Examples for aging of granular soils regarding mechanical properties such as strength and stiffness are the increasing resistance registered by cone penetration tests (CPT) in fills (Mitchell & Solymar, 1984; Schmertmann, 1991), the increasing shear modulus at small strains (Afifi & Woods, 1971; Anderson & Stokoe, 1978) as well as the increasing bearing capacity of piles posterior to installation (Carroll et al., 2020; Chow et al., 1997; Skov & Denver, 1988). The latter is termed as pile setup effect. A quantitative estimation of this aging effect could lead to a more efficient pile design and hence, to save resources and costs of extensive foundations as those for, e.g. wind power plants on- and offshore (Figure 1.1 (a)).

(a) **(b)**

Figure 1.1: Examples of geotechnical challenges where the consideration of time dependency of granular soils is of significance: (a) Wind power plants on the Baltic Sea off the Danish coast, printed with permission of BWE and (b) Open cast mine in the west of Germany, printed with permission of RWE Power AG

In addition, simultaneously volume changes occur by time at constant effective pressure; this process is called creep. In contrast to fine-grained soils creep in granular materials is less pronounced (Augustesen et al., 2004), however, for certain geotechnical problems time-dependent deformation has to be taken into account.

In very thick fills of granular materials (see Figure 1.1 (b)), deformations due to creep can reach high values which may be in conflict with the requirements of the serviceability limit state. An example of this is the up to 300 m thick deposits, which are formed as a result of the mining of lignite or other natural resources. Such deposits settle by several decimeters over decades (Charles-Cruz et al.,

2008; Kothen & Knufinke, 1990; Levin et al., 2022; Vogt et al., 2013). In particular cases at mining deposits in the West of Germany, the time-dependent behavior of granular soils was investigated using laboratory tests and the evaluation of data collected by measurements in the field (e.g. geodetic surface settlement measurements and monitoring of trial embankments as well as buildings such as bridges). Similar observations were made for large, wet, hydraulic deposits of mining tailings (Charles-Cruz et al., 2008). Long-term monitoring of deformations of a container terminal and quay wall in Sydney (Port of Botany), which were founded on a backfilled layer of sand compacted by vibro-pressure methods to a thickness of about 20 m, show a persistent increase in surface settlement or wall displacement over a period of 40 years (Cudmani et al., 2011). Experience has shown that load-independent time-delayed settlements occur typically in the range of about 0.1 % to 0.5 % considering the height of road and railroad embankments, even when high relative densities were achieved by dynamic compaction. At the same time, an improvement of the mechanical properties (e.g. stiffness by plate loading tests) compared to the end of compaction is often observed. CPT and shear wave measurements, which are carried out after deep compaction and blasting compaction of loose saturated sands for the purpose to check the success of compaction, show a reduction (deterioration) and later a gradual increase in cone penetration resistance or shear wave velocity (improvement) after the pore water pressure caused by compaction was dissipated, which can last for many months following the special ground works (Schmertmann, 1991).

Thus, the time-dependent phenomena of creep and aging occur simultaneously, whereas a relationship between the corresponding measurable quantities, i.e. the strain rate during creep and stiffness changes, is hypothesized. Various researchers have investigated the creep and/or aging behavior of different sands by experiments (Baxter & Mitchell, 2004; Bowman & Soga, 2003; Gao et al., 2013; Murayama et al., 1984; Ye et al., 2022), but without presenting a comparative analysis and an explanation considering the interaction between the two phenomena, which is the objective of the present work.

The German Research Foundation (DFG) funded this research under the project number CU 363/1-1. The support was highly appreciated.

1.2 Research question and aim of this work

Following the research of Levin (2021), who investigated the time-dependent compression behavior of sands under oedometric compression, the present work aims to investigate the time-dependent behavior of granular materials under **triaxial conditions** through laboratory experiments. Additionally, the investigation of creep and rate dependency is extended by aging. The main questions to be answered are: **What is the relationship between creep and aging in granular materials? How can the underlying micromechanical processes explain the investigated behavior?** Furthermore, the overall aim of the work is to provide the experimental basis for simulating the time-dependent behavior of granular materials.

The influences of granular properties such as particle shape, particle size distribution, or particle hardness and of state variables defining, e.g., the stress states, density, and loading history, on the

creep behavior have already been investigated in detail and are summarized, for example, in Levin (2021). In contrast, the effects of state and material on aging are not finally clarified. Therefore, the experimental work aims to answer the question of **how the state variables influence the aging of granular materials under triaxial conditions**. And additionally, **how the granulometric properties of the two investigated materials influence the time-dependent behavior.**

To answer the questions, the first objective was to develop and put into operation two **triaxial test setups** that were specially designed for the requirements of the research question. State-of-the-art and **novel sensor technology** was required to measure creep deformation, assess aging, and capture the micromechanical processes involved, which first had to be planned and introduced in the laboratory since the expertise was not yet available at the institute. The challenge was selecting appropriate sensors, choosing suitable parameters for recording the measurement data, developing, and applying the evaluation methods, as well as interpreting the data.

1.3 Structure of the work and methodology

First, Chapter 2 gives an overview of the micromechanical processes involved in creep and aging known from the literature. In addition, as part of the literature review, special attention is paid to the creep behavior of granular materials under deviatoric loading. The experimental methods presented by the literature to study aging are summarized in Section 2.3.2, and the available studies on the influences on macroscopically measurable aging effects are presented in Section 2.3.3.

In Chapter 3 the experimental setups developed and used for this research and the methodology employed for the analysis are summarized. One central challenge was to assess aging and creep in granular materials simultaneously. Acoustic emissions during the creep phases were detected to capture the micromechanical processes. The methods and evaluation techniques used to measure creep (Section 3.2), aging (Section 3.3), and acoustic emission (Section 3.4) are discussed in detail, and the limitations of the used experimental setups are given.

Chapter 4 contains the description of the experimental program, sample preparation methods, and the presentation of the results from the experimental study. Two materials were considered in the experimental study, each covering certain specific aspects of material properties. The so-called Cuxhaven sand, a moderately uniform graded silica sand, was investigated as a naturally deposited granular material. The second material studied was corundum (alumina) with a compared to Cuxhaven sand similar maximum grain size but owning a very uniform grain size distribution. Corundum served as a comparative material with an in contrast to natural sands significantly higher particle strength. The materials are described in Section 4.1. Oedometric creep tests first validated the acoustic emission method. The results are presented in section 4.4.1. The combined experimental investigation of creep and aging through triaxial testing, including an investigation of the influence of state variables, e.g., stress states and density, followed. The results are presented in Sections 4.4.2 through 4.4.4.

A conceptual model describing the changes in the particle assembly in granular materials, which originates from processes at the microscale defined by the interaction of grains at their contact, is

presented in Chapter 5. This conceptual model builds on the experimental findings and knowledge found in the literature. Furthermore, a relationship between the evolving strain during creep and the small-strain stiffness during aging is proposed in Section 5.3.

A summary, discussion, and outlook conclude the work.

2. Literature review on time-dependent behavior of granular materials

Effects of time-dependency were summarized as creep, stress relaxation and the rate-dependency of the stress-strain response (e.g. Augustesen et al., 2004; Krieg, 2000; Mitchell, 2005). Creep describes the time-dependent evolution of strain under constant effective stress (zero stress rate), whereas relaxation refers to the change in stress by time for zero strain rate. This research adds the aging phenomenon as an effect of time-dependency in granular materials. It is defined as the change of mechanical properties over time at constant effective stress. The considered time scale belongs to periods to be considered by engineers for predicting deformation and bearing capacity of, e.g., foundations or earthwork structures. Aging mainly occurs in freshly deposited or by geotechnical installation processes such as pile driving or soil compaction by vibration disturbed granular materials but is also present in naturally deposited soils. Nevertheless, because of the large period of deposition and diagenesis, considering thousands or even millions of years, the rate of change of mechanical properties is small in natural deposits. It cannot be captured experimentally.

Since the current work builds on the findings of Friedrich Levin (Levin, 2021), who studied the time-dependent compression behavior of sands under oedometric conditions, this thesis serves as the basis for the following presentation of the state of the art regarding the time-dependent behavior of granular materials. Complementary, current research activities related to creep and aging of granular materials are reviewed. A focus is given to the findings on creep and aging under deviatoric loading which were not in the focus of Levin's research. The phenomenon of aging in granular material is highlighted, considering the mechanics at the contact of individual particles (microscale) and particle assembly (mesoscale). Recent studies investigating the influence of state and material on aging are reviewed. Finally, the methods from the literature to identify and evaluate aging in the laboratory are discussed.

2.1 Creep

The magnitude of creep strains is a function of the state variables, the loading path and the granulometric properties of the soil. According to experimental evidence, the magnitude of creep strains increases with increasing effective stress, decreasing relative density, decreasing grain hardness, and increasing angularity as well as surface roughness (Colliat-Dangus et al., 1988; Karimpour & Lade, 2010; Mejia et al., 1988). The initial creep strain rate depends on the strain rate during the previous loading. A larger loading strain rate leads to a larger initial creep strain rate. Furthermore, the creep strain rate decreases with time. The creep deformation generally follows an exponential decrease, see Figure 2.1 (a). Subsequently, the curve of creep strain for a given stress converges for granular materials approximately to a linear decrease with time in log-scale (e.g. Lade & Liu, 1998;

Levin, Vogt, & Cudmani, 2019). Thus, the characteristics of creep strains observable in granular material can be quantified by the coefficient of secondary compression C_α (Taylor & Merchant, 1940),

$$e_0 - \mathrm{e} = C_\alpha \cdot \log \frac{t_{ref} + t}{t_{ref}} \tag{2.1}$$

or equivalently by the coefficient C (Buisman, 1936)

$$\varepsilon - \varepsilon_0 = C \cdot \ln \frac{t_{ref} + t}{t_{ref}} \quad , \tag{2.2}$$

where e_0 is the void ratio and ε_0 the strain at the onset of the creep phase, respectively. The time t_{ref} represents the point of intersection between the linear slope of the curve and time t in log- or ln-scale. Figure 2.1 (b) presents the meaning of Equation (2.2). So far, this relationship is valid for observation times of several days to few weeks.

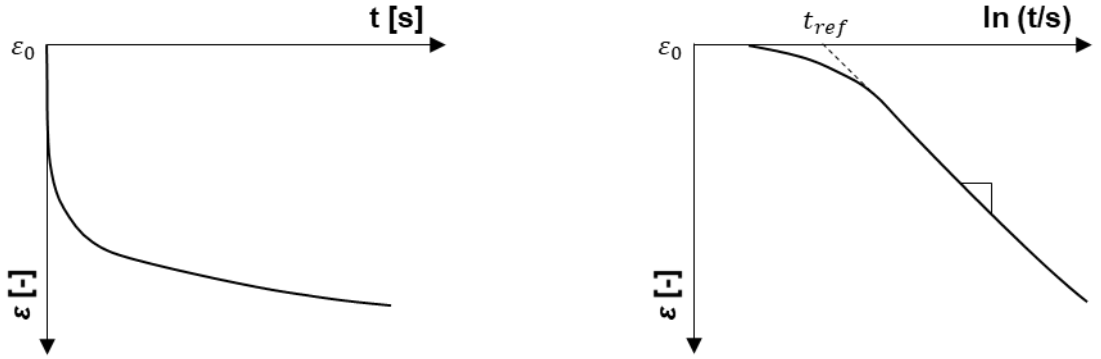

Figure 2.1: (a) Exemplary natural trend of creep strain ε with time t; (b) Definition of coefficient C describing the development of strain ε with time t in ln-scale

2.1.1 Micromechanical processes during creep

Creep in granular materials results from time-dependent micromechanical processes at the level of particle contacts (microscale) and particle assemblies (mesoscale). Different researchers have already investigated some of the relevant micromechanical processes and events on mesoscale during creep. Even under constant load, translation and rotation of sand particles occur with increasing time (Kuhn & Mitchell, 1993; Lade, 2009). Damage of the particle surface and extensive particle breakage can be essential during creep, especially at high stresses (Karimpour & Lade, 2010; Mesri & Vardhanabhuti, 2009). The mechanisms during creep lead to increasing particle contact areas and interlocking effects between particle surfaces (Mesri et al., 1990).

Radjai et al. (1998) describe the load transfer in stressed granular material as bimodal. On the one hand, forces in particle assemblies are transferred by strong force chains (Eber, 2007). On the other hand, weakly loaded clusters provide lateral support to the former. According to Bowman and Soga (2003), deformations during creep start within the weakly loaded clusters: Because of time-dependent slipping and sliding of the lightly loaded particles, the weakly loaded particle clusters rearrange, and the lateral support is withdrawn from the heavily loaded force chains, which consequently buckle to some extent until support is again provided by neighboring particle clusters (see Figure 2.2). There-

fore, the force chains reorient. In addition to the measurable density change (creep strains), the particle assembly is stabilized through the self-supporting structure (Kuwano & Jardine, 2002). The tangential contact forces are reduced, and the contact forces in normal direction predominate. Bowman and Soga (2003) do not explain which mechanisms are responsible for the time-dependent slipping and sliding of the particles.

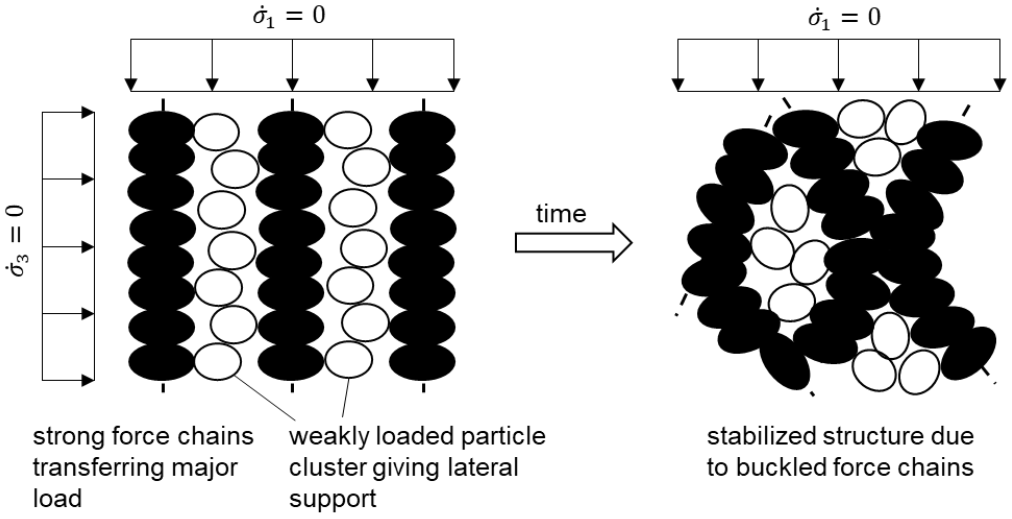

Figure 2.2: Buckling of force chains during creep (modified from Bowman and Soga (2003))

In this regard, some researchers identified contact maturing (also known as static fatigue at contacts) as the primary source of particle rearrangement and time effects under constant pressure in granular materials (Andò et al., 2019; Lade & Karimpour, 2010; Michalowski et al., 2018). This hypothesis is supported by numerical simulations, where contact deformation was considered as the dominant process during creep (Gao et al., 2023). In these simulations a creep model was used to simulate the contact between the particles.

Methods for the identification of time-dependent micromechanical processes

Different experimental and numerical methods have been used in the literature to identify the micromechanical processes involved during creep. The methods can be divided into studies on particle assemblies and individual particles. For example, investigations on individual particles have been performed by Michalowski et al. (2018). The authors measured the time-dependent axial deformation of loaded individual particles and showed the maturing of particle surfaces by comparing microscope images taken before and after creep of particle contacts.

The Discrete Element Method (DEM) as a numerical tool analyzes forces at particle contacts and particle movements for understanding time-dependent micromechanical processes. However, a suitable viscous contact model has to be chosen for the simulations. Suarez (2012), for example, implemented a Hertz-Mindlin contact model incorporating the Rate Process Theory (RPT) to simulate the viscosity at the particle contact. On the other hand, Zhang and Wang (2016) used a simplified Hertz-Mindlin contact model to describe the force-displacement relationships in the normal and tangential directions as well as a rolling resistance contact model that accounts for the moments transferred

through a contact (interlocking effects) between particles. A reduction of the mobilized friction resistance to model static fatigue effects with time at the particle contacts was done by a reduction factor. More recently, Gao et al. (2023) developed the latter contact model with a nonlinear Hertz-Mindlin model and added a creep model (i.e. Burger's model) to describe the viscous effects in tangential direction.

Experimentally, time-dependent changes of the grain size in element tests have been demonstrated by comparing grain size distributions determined before and after creep (Karimpour & Lade, 2013; Lade & Karimpour, 2010). Bowman and Soga (2003) detected rotations of particles on samples after different creep times by optical microscopy of the afterwards resin-injected samples. In addition, X-ray tomography is a modern method for detecting time-dependent motion and fraction of particles. The method has already been used to observe changes in particle orientation and crack propagation (Andò et al., 2019). However, changes of the particle surface during creep, such as contact maturing, cannot be visualized yet. The measurement by X-ray tomography is in regard with the required spatial resolution limited to comparably tiny sections of a sample.
The measurement of acoustic emissions can also provide insight into the micromechanical processes within a soil sample (Michlmayr & Or, 2014). In contrast to the analysis of structural changes through X-ray tomography, measuring acoustic emissions is relatively cost-effective and offers the possibility of describing qualitatively processes within a sample. Because of the use of this method by this thesis, a detailed review is given in Section 3.4.

2.1.2 Creep during deviatoric loading

2.1.2.1 Volumetric creep strain[1]

The evolving volumetric strain during creep can be dilative, contractive or almost zero depending on the corresponding volumetric behavior of the material at equivalent state during monotonic shearing (Kuwano & Jardine, 2002; Suarez, 2012). If the ratio $\eta = q/p'$ is small contractive creep is usually observed whereas dilative creep becomes more likely to occur as η approaches to the shear strength. If creep starts at the reversal point of volumetric change during monotonic shearing, i.e., the point of maximum contraction, volumetric creep is measured to be close to zero (Mejia et al., 1988). A schematic summary of the expected volumetric creep behavior of granular material is shown in Figure 2.3.

[1] The content has been published in Jessen et al. (2024)

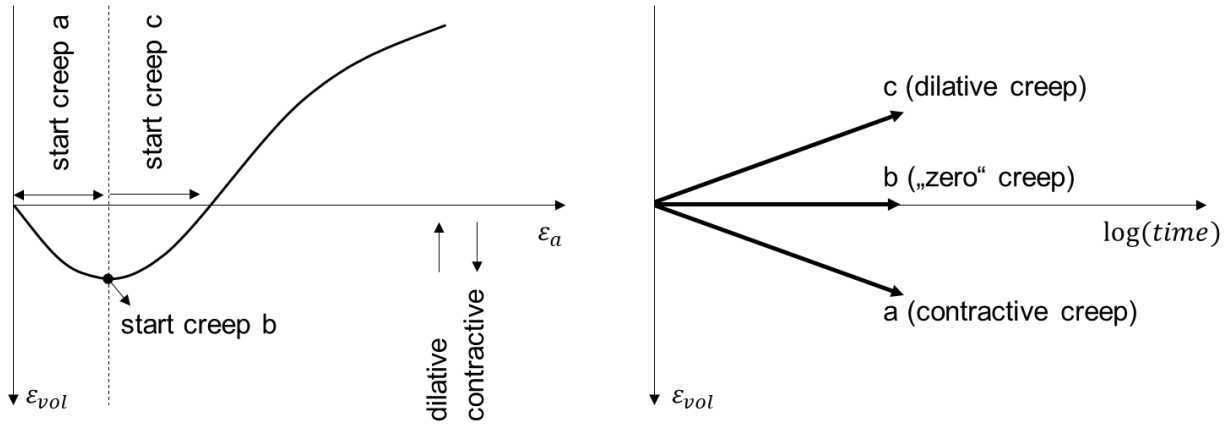

(a) **(b)**

Figure 2.3: Schematic summary of expected volumetric creep behavior depending on the starting point of the creep phase; (a) ε_{vol} - ε_a diagram from monotonic loading and (b) expected volumetric creep behavior with t in log-scale (Jessen et al. (2024))

A change of the direction of the time-dependent volumetric creep strain ε_{vol} with evolving time during creep was observed by Bowman and Soga (2003). The authors linked this change to soil compressibility. The trend of contractive creep is more likely for comparably highly compressible material whereas dilative creep was observed for materials of low compressibility.

In a recent study on creep in calcareous sands under deviatoric loading, as well Ye et al. (2022) observed a change from contractive to dilative behavior during individual phases of creep. The researchers investigated the origin of this effect in detail by comparing the creep behavior of calcareous sand with silica sand. The silica sand did not change from contractive to dilative creep with time. The authors remark that changes of the creep behavior for calcareous sands may result from imperfect saturation of the voids with water during the triaxial test since the particles show complex geometry including cavities that hold a significant amount of air. A degree of saturation less than 100 % can negatively influence the volume measurement due to the delayed pressure-dependent volume change of air, and thus falsifying the interpretation of the volume change measurement of the sample. The authors concluded that despite of certain experimental observations, the volumetric creep behavior of the investigated sands is more likely to be throughout a certain creep phase either continuously dilative or contractive.

Micromechanically, the phenomenon of dilatant creep has not been studied comprehensively. Bowman and Soga (2003) hypothesized that dilative creep is likelier for particles with high particle strength, where particle sliding and rolling are the primary causes of creep deformations. In contrast, contractive creep is more pronounced for particles with low strength that show breakage and asperity yielding as the dominant creep effects, see Figure 2.4. Furthermore, dilatant creep deformation results from sliding particles within the strong force chains. Dense samples of particles with high strength can only achieve a more stable assembly due to restructuring by dilatancy.

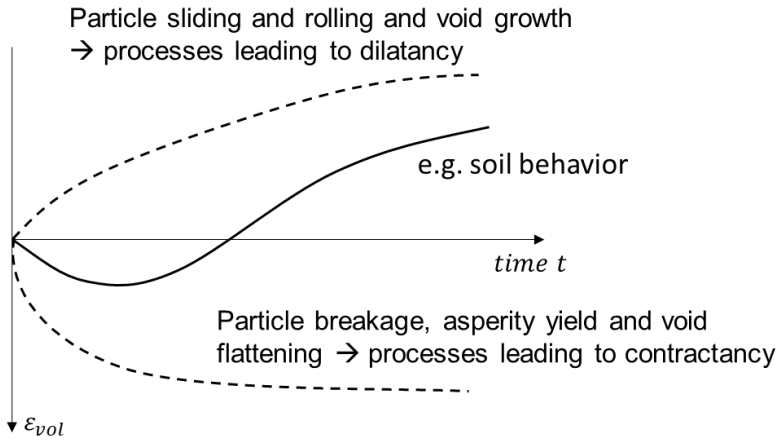

Figure 2.4: Explanation of different volumetric creep behavior depending on granulometric properties (modified from Bowman and Soga (2003))

In contrast, Gao et al. (2023) found by simulation with DEM that normal and tangential contact deformation seems to be the major source for macroscopic creep deformation. Their results show that the contribution of particle rearrangement and contact sliding is very little. Considering exclusively the effect of contact deformation dilatancy during creep for dense sand is associated to normal contact deformation whereas contractancy results from tangential contact deformation.
It is also found that the development of volumetric strain within the weakly loaded particles during creep follows the volumetric creep as observed according to the overall macroscopic deformation. The results of the DEM study by Gao et al. (2023) suggest that the volumetric creep deformation follows the initial trend as a consequence of deviatoric loading prior to the phase of creep, and thus, creep strongly depends on the loading path or hence loading history.

2.1.2.2 Axial creep strain

During triaxial compression, the major principal stress direction coincides with the axis of the sample. For simplicity, the corresponding principal strain is termed axial strain $\varepsilon_a = \varepsilon_1$.. Increasing axial creep strain with increasing deviatoric loading has been measured for granular materials in different studies (Kuhn & Mitchell, 1993; Murayama et al., 1984; Suarez, 2012; Tanaka & Tanimoto, 1988). This dependency can be explained by the increasing ratio of tangential to normal forces at the particle contacts at the beginning of the creep phase with increasing η, followed by a greater tendency for particle sliding. In addition, the likelihood of particle breakage increases with increasing q (Karimpour & Lade, 2013).

Various researchers (Murayama et al., 1984; Singh & Mitchell, 1968; Tanaka & Tanimoto, 1988) found a power law expressing the relationship between the axial creep strain rate $\dot{\varepsilon}_a$ or shear strain rate $\dot{\gamma}$, respectively, and the time t for granular materials at deviatoric loading for the period studied. The slope m is given according to Equation (2.3), which was found to be valid for fine-grained and coarse-grained soils for a deviatoric loading of 30 % to 90 % of the soil strength q_{max} (Singh & Mitchell, 1968).

$$m = -\frac{\Delta log\ (\dot{\varepsilon_a})}{\Delta log\ (t)} \tag{2.3}$$

The value of m was found to be in the range from 0.75 to slightly higher than 1.0. Furthermore, m seems to be independent of the sample density and the extent of the deviatoric loading (Augustesen et al., 2004).

2.1.2.3 Creep failure

Granular soils may show the effect of creep failure like fine-grained soils. At first, creep failure was observed at values of $q/q_{max} \approx 1$ close to the strength of the sample (Mejia et al., 1988; Murayama et al., 1984). Kwok and Bolton (2010) postulated that creep failure occurs when the creep strain in the direction of the major principle stress reaches values similar to the corresponding strain at which q_{max} during monotonic shearing is attained. Moreover, it was found through DEM simulations that creep failure can also occur at deviatoric loading smaller than the maximum applicable deviatoric stress q_{max}, when the strain evolved during creep approaches the value of the strain at the creep stress of the monotonic post peak behavior (Wang et al., 2014). Thus, the time until failure by creep failure decreases with increasing values of q/q_{max}.
Wang and Xia (2021) observed by numerical simulations that as q/q_{max} decreases, the axial strain achieved at the onset of creep failure is slightly larger than the corresponding strain measured from monotonic deviatoric loading. Figure 2.5 shows the results of their numerical simulations. Creep failure was observed for creep phases at q/q_{max} > 0.80 after different times. The authors suggest that the particle assembly at creep failure is not the same as resulting from monotonic deviatoric loading, which might be the reason for the different magnitude of strains observed for the different failure mechanisms.

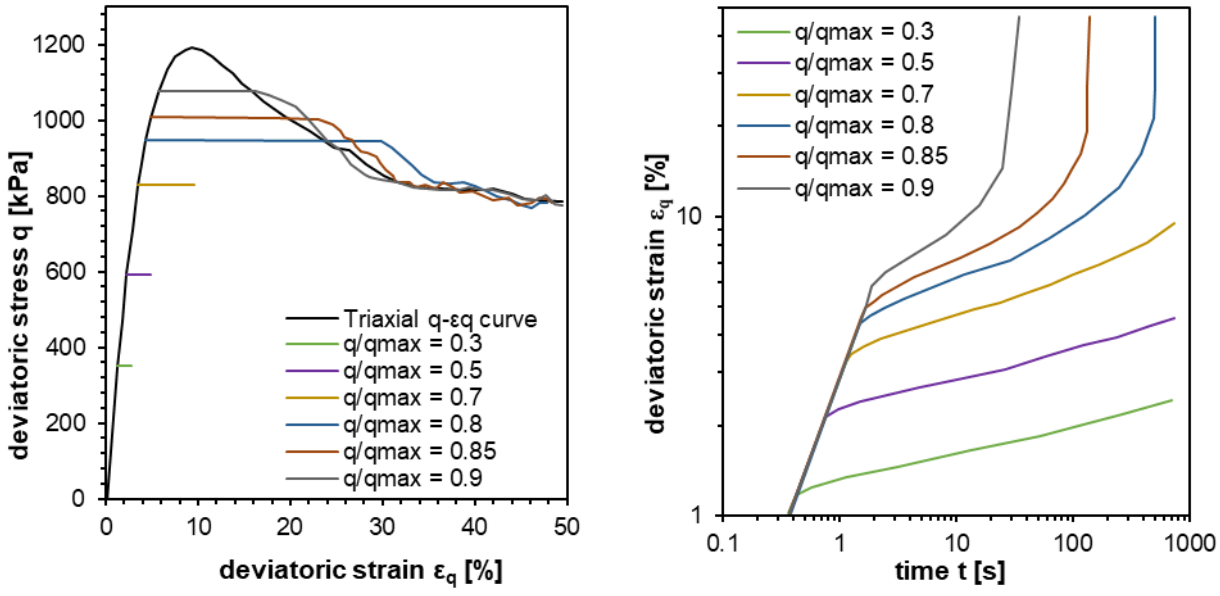

(a) **(b)**

Figure 2.5: (a) Deviatoric stress – deviatoric strain diagram and (b) deviatoric strain – time diagram from numerical simulations of triaxial creep tests on dense sand during creep at varying q/q_{max}-ratios (redrawn after Wang and Xia (2021))

2.2 Strain rate dependence

In this section, the strain rate dependence of the stress-strain behavior of granular material is discussed. In this context, comparably low strain rates, in contrast to high strain rates that may occur, for example, during impact or explosions, are considered.

Tatsuoka et al. (2008) presented four characteristic patterns to describe the behavior of geomaterials following a sudden change in strain rate, including the isotach behavior, the so-called TESRA ("Temporary Effect of Strain Rate and Acceleration") model, a combined isotach and TESRA behavior, and the so-called P&N (Positiv-Negativ) behavior. Figure 2.6 schematically shows these four experimentally observed behavior types.
As first defined by Suklje (1957), isotach behavior implies a unique relationship between strain rate $\dot{\varepsilon}$ and the state of the soil, defined by the stress and void ratio. This relationship applies to fine-grained sediments but has been shown to be invalid for granular materials. In contrast, experimental findings from various researchers (Di Benedetto et al., 2002; Levin, 2021) indicate that the change in stress-strain behavior of clean granular materials due to a sudden strain rate change is only temporary, which corresponds to the TESRA model shown in Figure 2.6.

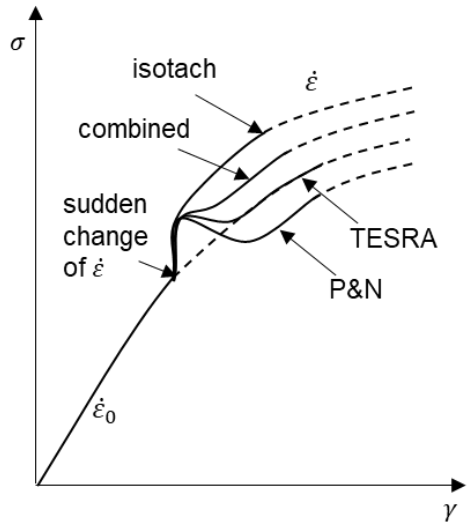

Figure 2.6: Different types of rate-dependency (redrawn after Tatsuoka et al. (2008))

A temporary so-called overshooting was identified for an abrupt strain rate increase, and a temporary so-called undershooting was seen for an abrupt strain rate decrease, as shown in Figure 2.7 (a). The strain, described by the TESRA model, can be decomposed into an elastic ε^e and inelastic (time-dependent and irreversible) ε^{ir} part. The stress may also be decomposed into two components $\sigma = \sigma_f + \sigma_v$, where $\sigma_f = f(\varepsilon^e,\ldots)$ is independent and $\sigma_v = f(\varepsilon^{ir}, \dot{\varepsilon}^{ir},\ldots)$ is dependent on time, which corresponds to the viscous behavior (Di Benedetto, H. Tatusoka, F. & Ishihara, 2002).

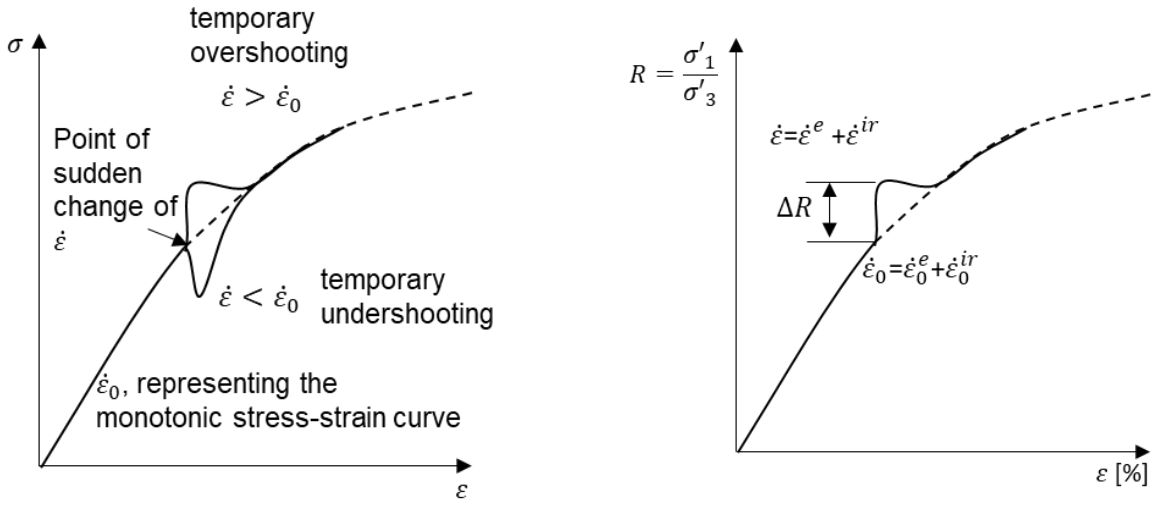

(a) **(b)**

Figure 2.7: (a) TESRA-behavior dependent on the direction of sudden strain change and (b) definition of the stress ratio change ΔR (modified after Di Benedetto et al. (2002))

The change of stress upon a sudden strain rate change can be expressed by the ratio $\Delta R = \Delta\sigma'_1/\Delta\sigma'_3$. In relation to $R = \sigma'_1/\sigma'_3$, the ratio of ΔR can be calculated using the following formula.

$$\frac{\Delta R}{R} = \beta \cdot log_{10}\left(\frac{\dot{\varepsilon}^{ir}}{\dot{\varepsilon}_0^{ir}}\right) \tag{2.4}$$

$\dot{\varepsilon}_0^{ir}$ and $\dot{\varepsilon}^{ir}$ are the irreversible parts of the strain rates before and after the strain rate jump, respectively. The relation proposes that a single material-dependent factor β can describe the magnitude of the change in stress ratio.

However, since it is not formulated in rate-form and the elastic component of the strain rate is not easily to be determined experimentally, the TESRA-model is not appropriate to model the rate-dependent behavior of granular soils.

2.3 Aging

Aging following the definition in this thesis as the time evolution of mechanical properties such as stiffness or shear strength under constant stress can have mechanical, chemical and biological causes. The occurrence of chemical or microbial processes strongly depends on the soil type (i.e. mineralogy and organic matter), the nature of the pore water and environmental influences. Precipitation and deposition of, e.g. carbonates, formed either by the metabolism of microorganisms or by the chemical environment, can lead to cementation of the particles. The presence of pore water, for example, significantly influences the mechanical, and particularly the time-dependent behavior of granular materials. This research considers aging due to mechanical processes, which was defined by Schmertmann (1991) as "pure" aging. For this purpose, the experimental boundary conditions and the materials were selected to minimalize biological and chemical processes leading to aging.

2.3.1 Time-dependent processes on microscale and mesoscale

Afifi and Woods stated in 1971 that the relatively small change in density of granular materials during creep at constant effective stresses cannot adequately explain the increase in shear modulus G_0 at small strain (i.e. $\gamma < 10^{-5}$) with time observed in experiments and that other mechanisms must be responsible. In the 1970ies, mainly chemical and microbial processes were considered to cause aging (Afifi & Woods, 1971; Lee, 1977), but these causes fail to explain aging effects in dry, inert materials. Schmertmann (1991) suggested that micromechanical processes occurring during creep are a main cause of aging. The surface abrasion of particles, formation of micro cracks, and different degrees of particle breakage as well as the particle translation and rotation, which happen at constant pressure, change the arrangement of the granular assembly and induce an evolution of particle contacts (Kuhn & Mitchell, 1993; Lade, Liggio, & Nam, 2009). The time-dependent micromechanical processes during creep can cause lateral deflection (also referred to as “buckling”) of the heavily loaded force chains (Bowman & Soga, 2003; Kuwano & Jardine, 2002) which form a self-supporting network. Thus, the mechanisms during creep cause a rearrangement of forces and a restructuring of the particle contacts resulting in a more stable structure (Bowman & Soga, 2003; Yusa, 2015).

Furthermore, the particle sliding and rolling resistance increases due to the increasing interlocking effect at the particle contacts (asperities) of the individual particles in contact (Mesri et al., 1990). Michalowski et al. (2018) proposed “contact maturing”, which describes the strengthening of particle contacts due to time-dependent abrasion of the surface texture and fracturing of particle asperities, as a further cause of macroscopically observable aging effects. Figure 2.8 shows an example of a particle-to-particle contact before and after conducting a phase of creep under a constant load of 3 N at which the individual particle was loaded. The change of contact surface is evident.

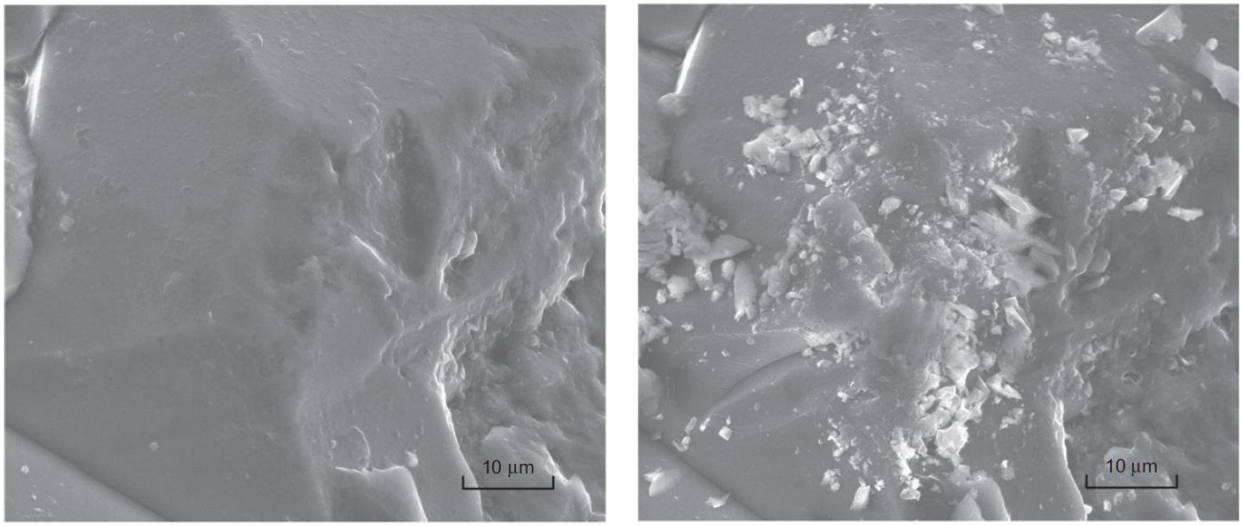

(a) **(b)**

Figure 2.8: Example of a particle-to-particle contact (a) before and (b) after a creep phase of three days while loading the individual particle at 3 N (Michalowski et al., 2018)

Using DEM simulations, Zhang and Wang (2016) predicted a stiffness and dilatancy increase in drained triaxial compression tests and a stiffness and shear strength increase in undrained triaxial

compression tests after creep phases. They used a temporary reduction of the mobilized friction resistance in tangential direction to model micro fracturing of the asperities at the particle contacts. Hence, the particles were forced to rearrange until a new equilibrium state was reached. From the time-dependent rearrangement of particles during creep, the contact normal forces at particle contacts were redistributed and homogenized in terms of direction and magnitude (Gao et al., 2013; Wang et al., 2008). A more uniform distribution of force chains led to a stabilization of the particle assembly and increasingly robust particle contacts, which caused, for examples, an increase in the stiffness at small strains. Following DEM simulations for investigating the influence of varying density on aging, Li et al. (2018) determined the occurrence of so-called “unjamming events” as an interplay with particle contact force homogenization during isotropic consolidation. “Unjamming events” refer to spontaneous particle rearrangements related to a destabilization of force chains in the granular material assembly and, thus, a temporary reduction of the stiffness. Figure 2.9 demonstrates this effect of the occurrence of “unjamming events” on a loose sample of spheres representing Ottawa 20-30 sand loaded isotropically at 100 kPa. The small-strain shear modulus G_0 was determined by carrying out simple shear tests at different aging times with shear strain smaller than 10^{-6}.

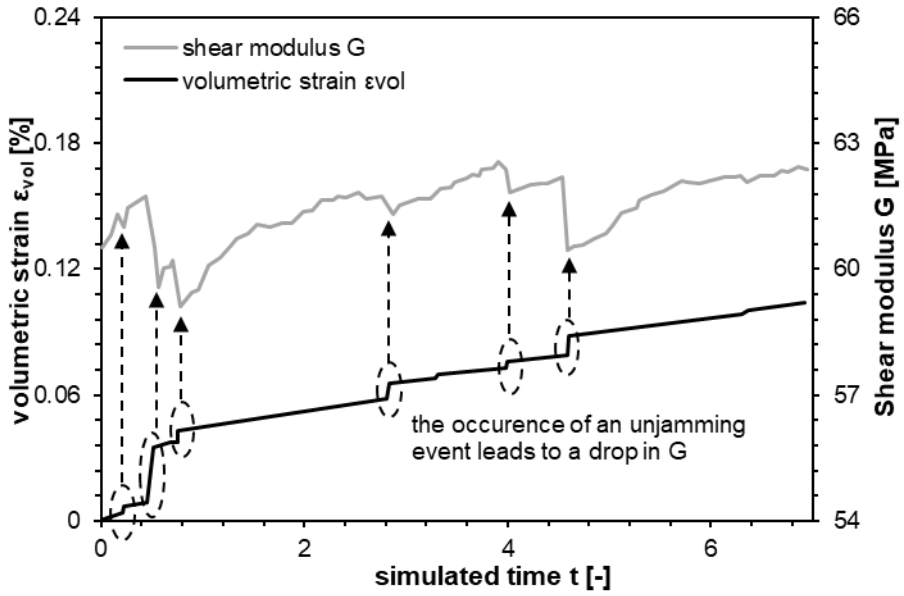

Figure 2.9: Example of the occurrence of “unjamming events” and the subsequent reduction of the shear modulus during aging at isotropic pressure of 100 kPa calculated by DEM simulations of a sample of loose Ottawa sand (redrawn and adapted after Li et al., 2018)

2.3.2 Experimental methods to investigate aging

So far, different methods have been used to assess aging effects in the laboratory. Daramola (1980), Howie et al. (2002) and Suarez (2012) determined the aging of granular soil samples during triaxial compression. For this purpose, the soil samples were consolidated under different pressure. In the publications from 1980 and 2002, the aging of the consolidated samples was determined by the change in stiffness of the sample after different creep times with respect to the value of the beginning of the shear phase. In contrast, Suarez (2012) included creep phases during shearing of the samples,

in which the deviatoric stress at a specific shear strain was kept constant. A temporary increase in stiffness was observed with further shearing for creep phases lasting over varying time periods.

There are also methods to assess aging by following the change in shear modulus G_0 at small shear strains $\gamma < 10^{-5}$ with time. The advantage of these methods is that they can be assumed to be non-destructive. Afifi and Woods (1971) and Wang and Tsui (2009) observed an increase in G_0 with time by performing resonant column tests on dry samples of sand. The samples were consolidated (e.g. step-wise) to different isotropic confining pressures, and the shear modulus G_0 was determined at different times for the smallest device specific reliable shear strain (e.g. $\gamma = 5 \cdot 10^{-6}$). Baxter and Mitchell (2004) and Gao et al. (2013) determined the time-dependent change in small-strain shear modulus G_0 from the measurement of shear wave velocities using Bender Elements. Bender Elements (or other types based on the piezo-electric effect such as ring-shaped actuators) can be easily integrated into conventional test setups for soil characterization, such as oedometer and triaxial test setups, which offers the possibility to evaluate and interpret the measurement of small-strain shear modulus (or equivalently aging) in combination with other soil characteristics such as the shear strength or compressibility.

2.3.3 State and material properties influencing the macroscopic measurable aging effects

The macroscopically observed creep deformation and aging effects depend on state variables, such as the stress and the density as well as granulometric properties such as the particle shape, strength, hardness, and particle surface roughness. The influences on macroscopically measurable creep deformation have already been well studied and are summarized briefly in the scope of this work in Chapter 2.1. Levin (2021) gives a detailed summary of the literature, which is not repeated here. On the contrary, the effects on macroscopically measurable aging have been studied only to a comparably small extent. Experimental studies carried out by different researchers show contradictory results, which can be attributed to the complex processes at the scale of particle rearrangement (mesoscale) and the scale of particle contacts (microscale). In addition, some of the contradictions may result from uncertainties associated with the experimental methodology, such as the performance of the triaxial equipment, and measurement techniques during the tests.

Influence of the confining pressure

Wang and Tsui (2009) observed the change of small-strain shear modulus on dry samples of Ottawa sand and Toyoura sand at different confining pressures (35 kPa and 100 kPa) and initial densities (loose and dense) by so-called multi-stage creep tests in the resonant column device. A multi-stage creep test is an experiment with several creep phases, whereby each creep phase is followed by an increase of confining pressure. They found out that the increase of shear modulus was stronger with decreasing confining pressure. The normalized change of the shear modulus G_0 for the Ottawa sand is given in Figure 2.10 (a). Aging is indicated by the change ΔG_0 with respect to G_0 at the beginning of the creep phase. The loose sample exhibited an increase of 6.0 % after seven days of aging at a confining pressure of 35 kPa, whereas at 100 kPa, an increase of 2.4 % was measured in the same

period. The dense sample showed the same dependency on confining pressure, but less pronounced.

In addition, Gao et al. (2013) also observed an increase of the normalized change of shear modulus with decreasing isotropic pressure in a multi-stage isotropic creep test in a true triaxial test device. The test on Leighton Buzzard sand showed an increase of G_0 of 2.5 % at 200 kPa and 7.4 % at 50 kPa confining pressure after three days of creep (Figure 2.10 (b)). The authors justified the behavior with a decreasing fraction of weak forces transferred by the particle contacts corresponding to a more homogeneous contact force distribution at higher effective pressure and a lower possibility of particle rearrangements under higher loading. Aging was thus directly related to the contact force distribution (e.g. proportion of weak contact forces) and the magnitude of G_0, respectively, at the beginning of creep. The more significant the proportion of strong force chains in the sample, and thus, the more homogeneous the contact force distribution at the beginning of creep, the smaller is the increase in G_0 with time, so the authors.

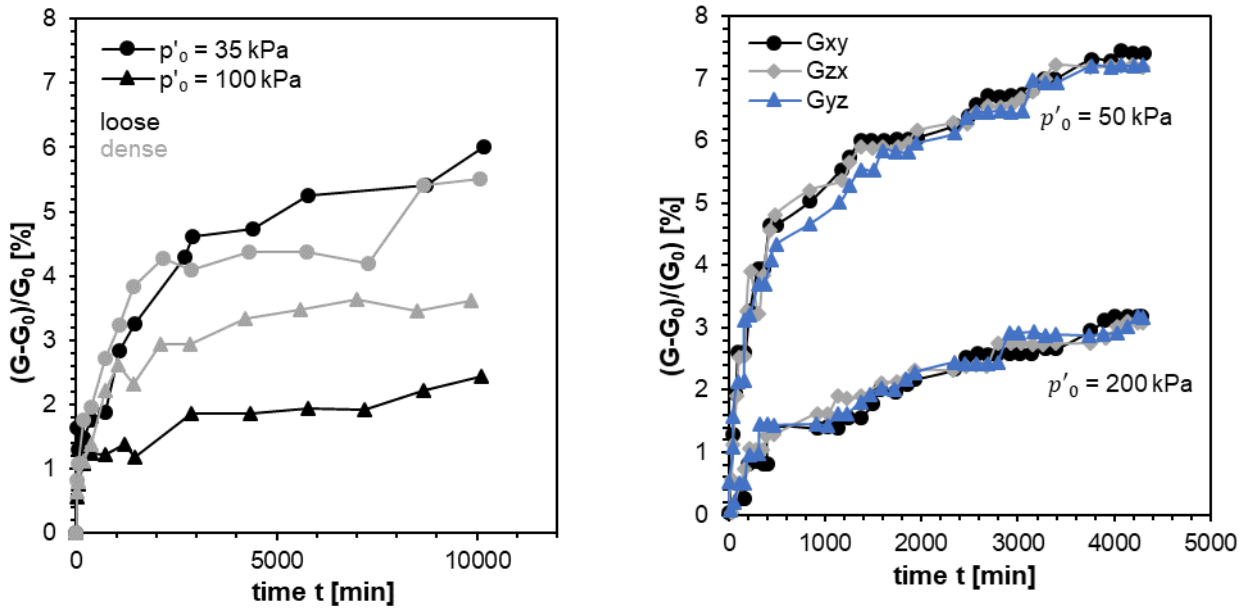

(a) **(b)**

Figure 2.10: Change in small-strain shear modulus G_0 with time under isotropic loading (a) of loose and dense samples of dry Ottawa sand (data taken from Wang & Tsui, 2009) and (b) of a sample of Leighton Buzzard sand (redrawn and adapted after Gao et al., 2013)

Influence of the initial density

Baxter and Mitchell (2004) performed one-dimensional compression tests with aging assessment by small-strain shear modulus observations using Bender Elements at σ_a = 100 kPa in rigid wall cells on Evanston beach sand (sub angular, poorly-graded silica sand with traces of dolomite and d_{50} = 0.30 mm) and Density sand (round, poorly-graded pure silica sand with d_{50} = 0.50 mm) under different densities, temperatures and pore fluids. A more significant increase in G_0 was measured for saturated dense samples of Evanston beach sand than for medium-dense samples during aging up

to 118 days. On the other hand, saturated medium-dense samples of Density sand showed a decrease of G_0 in the first 1000 minutes, whereas dense samples showed a small increase of G_0 over time. Air-dry samples, tested only in the dense state, showed an increase in G_0 with increasing time. An explanation for the decrease in small-strain shear modulus with time was not given. The study of Wang and Tsui (2009), mentioned before, obtained different results for the influence of initial density depending on the effective pressure. At an effective pressure of 100 kPa, dense specimens showed a higher change of G_0 with time compared to specimens in the loose state. The opposite was observed at the confining pressure of 35 kPa, see Figure 2.10 (a).
Li et al. (2018) build on the resonant column tests presented in Wang and Tsui (2008) to perform a DEM analysis in order to clarify the density dependence of the stiffness change. The experimental investigation showed the strongest aging for medium-dense soil samples of Ottawa sand. The authors found in accordance to their numerical simulation a counter play between an increasing homogenization of the contact forces, which favors stiffness increase, and the sudden occurrence of so-called “unjamming events”, which lead to the loss of already interlocked particle contacts and thus to local destabilization (see Figure 2.9). Looser specimens tend to have a greater rate of homogenization regarding the contact forces but are at the same time more susceptible to the occurrence of sudden particle rearrangements at the particle contacts. On the other hand, dense samples have a lower tendency to reach a more uniform contact force distribution but simultaneously are less susceptible to spontaneous loss of particle contacts.

Influence of the loading history

The work of Wang and Tsui (2009) investigates the influence of loading history on the aging of Toyoura sand. It was found that a previous aging phase at lower stress has a negligible effect on the following aging phases at higher stresses during a multi-stage creep test. In contrast, aging after unloading-reloading cycles is lower compared to the aging after virgin loading. The lower aging was explained by the more stable soil structure achieved by the unloading and reloading process, resulting in a more uniform contact force distribution. In addition, Wang and Tsui (2009) found a significantly weaker aging for specimens of granular soil after unloading and explained this by the different processes relevant for the formation of force chains and the corresponding different states of contact force homogenization at the onset of a creep phase. Figure 2.11 (a) plots the aging over time dependent on the loading history.
Gao et al. (2013) observed a weaker aging for samples after unloading compared to samples during virgin loading at the same pressure of 50 kPa at which the creep phase was conducted. As an example, the evolution of the relative change of G_{zx} for the first creep phase (OCR = 1) and for the same Leighton Buzzard sand sample after further loading and creep at 200 kPa and subsequent unloading to 50 kPa is shown in Figure 2.11 (b).

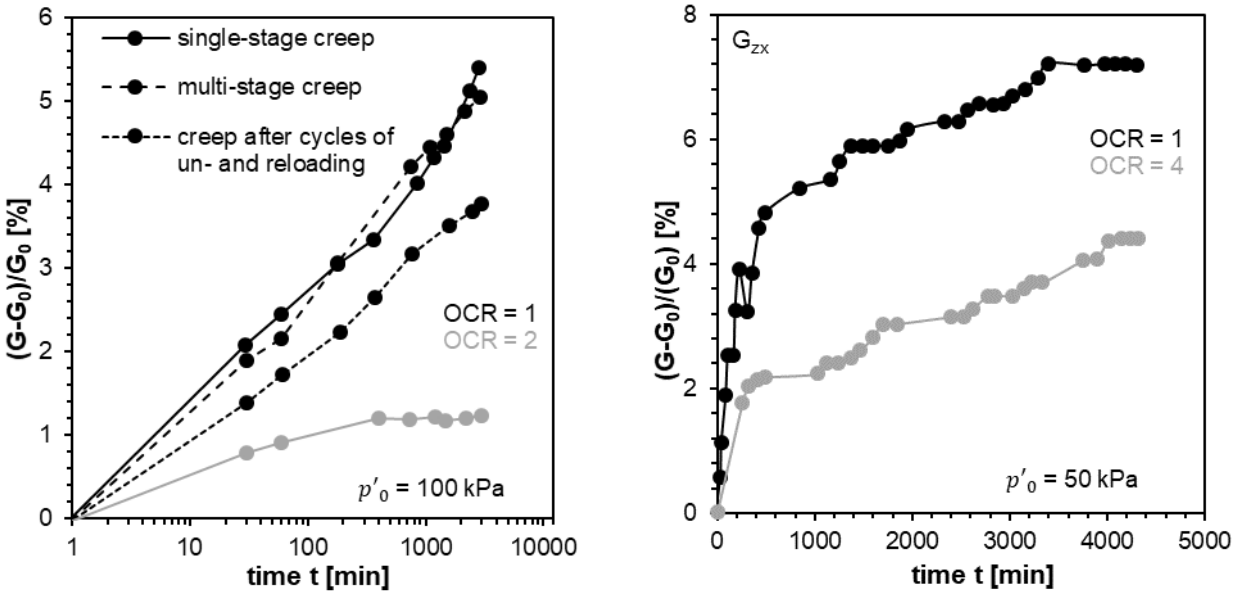

(a) **(b)**

Figure 2.11: Influence of loading history on aging (a) results of Wang and Tsui (2009) and (b) results of Gao et al. (2013); diagrams are redrawn.

Influence of the stress state

Experimental data on the influence of mean stress p' and deviatoric stress q on macroscopic aging are rare. Suarez (2012) studied the effect of creep and aging under triaxial compression at deviatoric stresses of about 0.25 q_{max}, 0.5 q_{max} and 0.75 q_{max} for different granular materials (Two silica sands and Glass beads) at loose and dense relative densities and compared the results with the behavior of corresponding tests comprising monotonic shear. Here, aging was quantified by evaluating the increase in the secant modulus $\Delta q/\Delta\varepsilon_a$ after creep. The increase in stiffness was most significant at the intermediate deviatoric stress at 0.5 q_{max} compared to smaller and higher deviatoric stresses, where for both deviatoric stresses similar aging was measured after 180 minutes.

A comparison of aging at isotropic and anisotropic stress, assessed by the change of the small-strain shear modulus G_0 using Bender Elements, was conducted by Gao et al. (2013) in a true triaxial test device. It was found that the change of G_0 depends on the direction of the shear wave velocity measurement in relation to the loading axis due to the stiffness anisotropy caused by the applied stress. Leighton Buzzard sand at a relative density of about 78 % was used in the investigations. According to the shear wave propagation direction parallel to the loading directions (G_{xy}), a stronger effect of aging was assessed for q = 125 kPa than for q = 175 kPa at a consolidation pressure of 50 kPa during three days of creep. In contrast, the change of G_0 observed perpendicular to the loading direction (G_{zx}, G_{yz}) shows the opposite behavior: stronger increase of G_0 with increasing q. The change of G_0 showed a maximum value at about 3000 minutes, which could also be caused by the lower mean stress p'. The results are summarized in Figure 2.12.

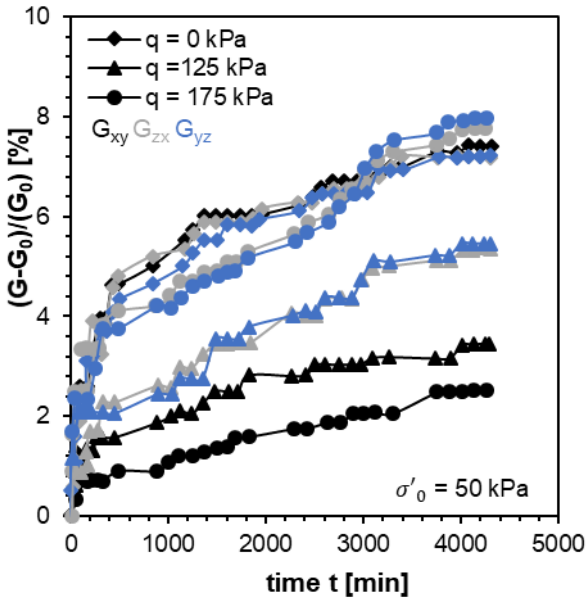

Figure 2.12: Comparison of the change in G_{xy}, G_{zx}, G_{yz} during creep at isotropic and anisotropic pressure (data taken from Gao et al., 2013)

In summary, few researchers have conducted experimental studies on the influences of state and material parameters on the aging effect of granular materials. Although the results differ from each other to some extent, the following conclusions can be drawn:

- The extent of aging increases with decreasing isotropic confining pressure.
- A clear density dependence was not found. Loose samples present a more homogeneous force distribution, but a larger susceptibility to spontaneous particle rearrangements. The opposite is true for dense samples. The extent of aging increases with homogeneity but decreases with the occurrence of particle movements.
- The loading history influences the aging effects since it determines initial soil structure which affects both creep and aging.
- The drawback of using the change of the shear stiffness to judge aging is that ΔG_0 depends on the direction of the measurements for anisotropic state of stiffness.
- The results of investigations on the dependence of aging on deviatoric stress are contradictory. The main problem is that the deviatoric stress and the mean stress are varied simultaneously.

2.3.4 Temporary stiffness change after creep during deviatoric loading

An increase in soil stiffness after phases of constant deviatoric loading in triaxial tests was observed by various researchers (Di Benedetto, H. Tatusoka, F. & Ishihara, 2002; Mejia et al., 1988; Zhang & Wang, 2016). The stiffness increase leads to a temporary change in the stress-strain response, which is gradually diminished with further shearing. The non-permanent soil behavior in accordance to the increased stiffness converges towards the stress-strain curve corresponding to the monotonic loading; the pattern of this convergence varies. Mejia et al. (1988) suggest based on his experimental

study that tests on round particles have a more abrupt and brittle convergence compared to tests on angular particles. Figure 2.13 shows the different patterns for Ottawa sand, a round silica sand, and Tailings sand, which has angular particles and consists mainly of quartz and feldspar.

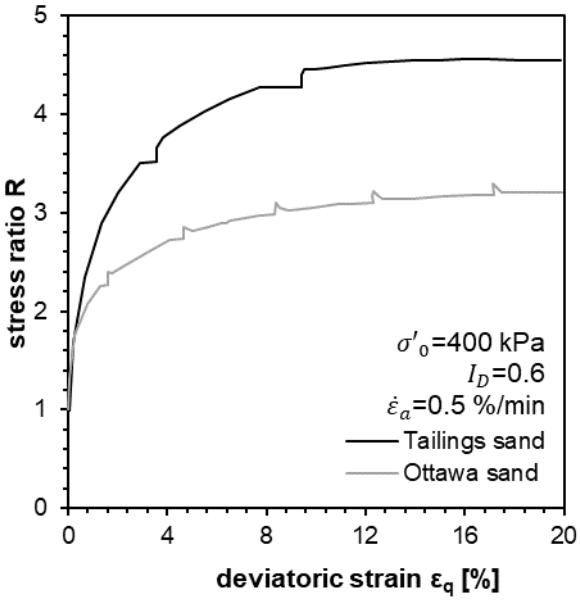

Figure 2.13: Example of temporary stiffness increase after creep phases during triaxial compression test, redrawn after Mejia et al. (1988)

Processes at microscale and mesoscale

Considering the bimodal load transfer in granular materials, the contacts forming the strong force chains primarily carry normal contact forces F_n. The ratio F_n/F_t, considering F_t as tangential contact forces, is relatively large. In contrast, the contacts of the particles in between the strong force chains show a comparably small ratio F_n/F_t. As deviatoric loading increases, the strong force chains align progressively to the direction of the major principal stress. During primary creep under deviatoric loading, it is observed from simulations based on the Discrete Element Method (DEM) that the strongly and weakly loaded particles also align progressively toward the loading direction with time (Kuhn & Mitchell, 1993; Wang et al., 2014; Zhang & Wang, 2016). The particles in the weakly loaded cluster rearrange over time, forming new particle chains carrying strong forces. Thus, load transfer by F_n increases during creep while F_t decrease. Consequently, the possibility of particle sliding reduces, making the soil structure more stable. The effect is more pronounced at small deviatoric stress, because the number of strong force chains and tangential forces within the clusters of weakly loaded particles at the beginning of creep is smaller than at high deviatoric stress(Wang et al., 2014). Moreover, the deviation regarding the F_n/F_t-ratio at the contacts reduces hence the ratio approaches an average value within a certain volume during primary anisotropic creep, leading to homogenization of the contact forces and, thus, more stable contacts. The change in contact force ratio again appears more pronounced for lower deviatoric stress. With increasing deviatoric loading subsequent to a

creep phase, the ratio of tangential to normal forces at the contacts increases again, and the homogenization achieved during creep diminishes (Zhang & Wang, 2016), which can explain the non-permanent increase and decrease in stiffness gained during creep.

2.4 Summary of the review

In summary, the creep behavior of granular materials, particularly under oedometric and isotropic loading, can be well described and quantified by the studies found in the literature. However, creep under deviatoric loading of granular materials has not yet been thoroughly investigated. Few researchers have shown that volumetric strain can increase, decrease, or remain almost the same with time at constant deviatoric stress. The behavior depends on the stress at which creep was investigated and the associated volumetric behavior at that stress during conventional triaxial compression tests. According to the state-of-the-art, the rate-dependent behavior of granular materials can be described by the TESRA behavior, which implies a temporary change in stress-strain response upon a sudden change in strain rate. The current research focuses on the mechanical processes taking place at the level of particle contact and particle assemblies. The basic processes taking place have been identified, but it is not clear how they contribute to creep and aging. Published studies on the influences of state and material parameters on aging are limited and reveal partly contradicting results.

Since the time-dependent phenomena of creep and aging occur simultaneously, a relationship between the corresponding measurable quantities, i.e. the strain rate during creep and stiffness changes is expected. However, studies in which creep and aging of granular materials are simultaneously investigated and interpreted are missing.

This thesis aims to identify the relationship between creep and aging in granular soils through a series of laboratory experiments. The experimental investigation is designed to examine creep and aging simultaneously under isotropic and deviatoric loading, establishing the link between the two effects. Additionally, the study seeks to contribute to the identification of the dependencies of aging on various state variables. The results of this investigation will be interpreted considering the mechanical processes occurring at the micro- and mesoscales, as well as relevant findings from the literature.

3. Experimental methods

Extensive experimental investigations were carried out on cylindrical specimens of granular materials under oedometric and triaxial deformation and loading conditions for the combined investigation of creep and aging effects. For this purpose, two triaxial test setups, which were specially developed for the research question, had to be designed and installed. The main challenge was to reliably record creep deformation, rate-dependent behavior, and aging effects simultaneously on the specimens of different initial densities and at cell pressures of up to 2000 kPa over a duration of up to three weeks. Innovative sensor technology was therefore required, which was initially planned and then implemented to the laboratory. The micromechanical processes were indirectly identified by measuring acoustic emissions during the creep phases. This chapter summarizes the experimental setups and measurement methods for capturing creep deformation, aging, and acoustic emissions. Thereby, the evaluation methods are described, and the limitations of the measurement methods and the experimental setups are discussed.

3.1 Test setups

3.1.1 Oedometer tests[2]

Figure 3.1 provides an overview of the setup for the oedometer tests. Samples with a diameter of 50 mm and an initial height of 15 mm were examined using a conventional oedometer ring of stainless steel (16MnCr5) with a thickness of 25 mm, assuming a lateral restraint of $\dot{\varepsilon}_r \approx 0$. The standard ASTM D2425 (ASTM International, 2020) specifies a minimum diameter of 50 mm and a height of 12 mm, respectively, $H/d_{max} > 10$. In addition, the ratio of D/H should be greater than 2.5. A ratio $D/H > 4$ is recommended to limit the friction force between the inner surface of the oedometer ring and the specimen. The oedometer used in the study had a ratio of $D/H = 3.33$. Thus, the requirements for the minimum oedometer size were met, but the ratio of D/H is less than 4 indicating the friction between the inner of the oedometer ring and the sample will be slightly higher than the value accepted by ASTM. The criterion $H/d_{max} > 10$ was not fulfilled, but the proportion of grains with $d > 1.5$ mm was only 2.4 % (see Section 4.1), hence the influence on the test results may be small or even negligible.

[2] The content has been published in Bock et al. (2022)

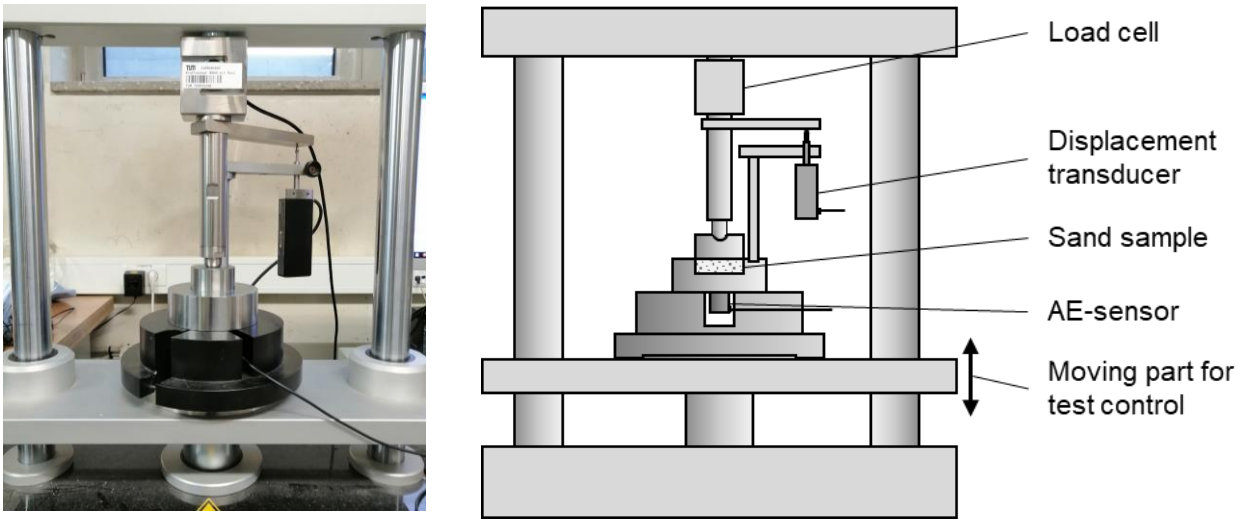

(a) **(b)**

Figure 3.1: (a) Photography and (b) schematic scetch of the oedometer setup (published in Bock et al., 2022)

Instead of porous filters commonly used in oedometer tests, smooth discs of stainless steel transferred the axial load to the sample at the top and the bottom. A load frame with a maximum load capacity of 60 kN controlled the axial strain rate during the phases of loading and the axial stress during the creep phases. The load frame used a ball screw drive powered by a stepper motor. A load cell with a nominal value of 60 kN of the compressive force and a precision expressed by a non-linearity of 0.1 % of full scale measured the axial force. A linear encoder as displacement transducer capable of measuring in a range of +/- 25 mm registered the change in sample height at a resolution of 0.025 µm. The precision of the transducer is given at a value of +/- 1 µm. The accuracy of the sensor is in the range of +/- 5 µm/m. Test control was automatized and along with the data acquisition and visualization controlled by a software.

3.1.1.1 Limitations of the oedometer test

To investigate creep behavior, it is essential to maintain the axial stress σ_a as constant as possible. By using a load frame with an electromechanical spindle drive in contrast to the application of a dead load, minor variations of σ_a are unavoidable. Nevertheless, the use of a spindle drive in combination with a precise regulation mechanism is a relatively cost-effective test setup providing significantly higher precision in load control than actuators driven by hydraulics or pneumatic pistons with rolling membranes. With the proposed test setup, maintaining a constant axial pressure throughout 24 h is more difficult at lower than at higher axial stress σ_a. Special attention had to be paid to the force actuator, load cell and regulation unit to avoid undesired pressure reversals due to load regulation. Owing to the maximum capacity of the load cell of 60 kN, at a stress of, for example, $\sigma_a = 300$ kPa, only 1 % of the load cell capacity is mobilized. At such small loads, the non-linearity of the load cell may significantly affect the measurement accuracy. In addition, the ratio of the stiffness of the load frame, including the load transducer, to the stiffness of the sample also plays a role in the accuracy of the load. For high-loading strain rates $\dot{\varepsilon}_a$ and stiff samples, the axial stress σ_a at the beginning of

the creep phase can be higher than the target value at least for a short period. This so-called overshooting of σ_a compared to the target value can significantly influence the subsequent evolution of creep strains.
Furthermore, other experimental limitations of the oedometric device and associated specimen size can affect the behavior during the loading and creep phases. Friction between the soil sample and the oedometer ring leads to a reduction of stress within the sample and hence strains for a load-controlled test phase. For a strain-controlled test phase the resulting measured stress may be higher compared to the ideal case where no friction rises.
Contact heterogeneity between the loading disk and the sample can result from irregularities in the sample surface. The sample homogeneity and, thus, the test reproducibility increase with increasing specimen size. All mentioned aspects may violate the assumed element test conditions.
However, these influences are equal or at least similar for all tests, so the fundamental trends or qualitative statements should not be affected. Quantitatively, the experimental results are expected to closely correspond to the actual soil behavior.

3.1.2 Triaxial tests[3]

Two almost identical triaxial test setups were used for the experimental investigation. Figure 3.2 shows a photograph of one of the test setups and a schematic sketch of the triaxial cell highlighting the main components.

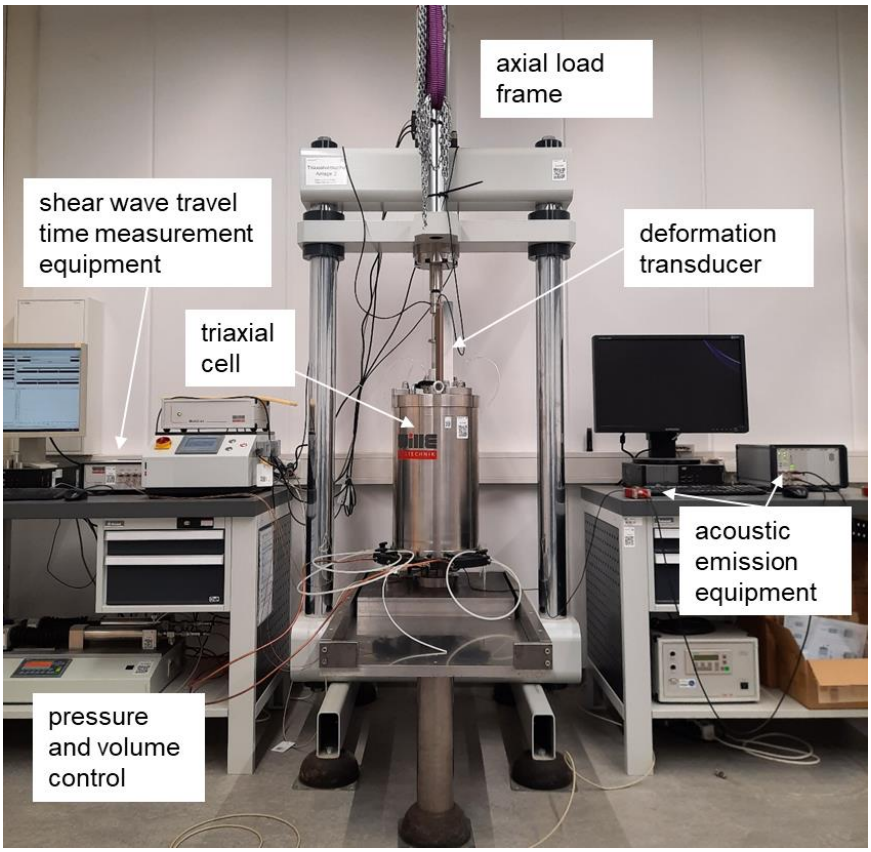

(a)

[3] The content has been published in Jessen et al. (2023)

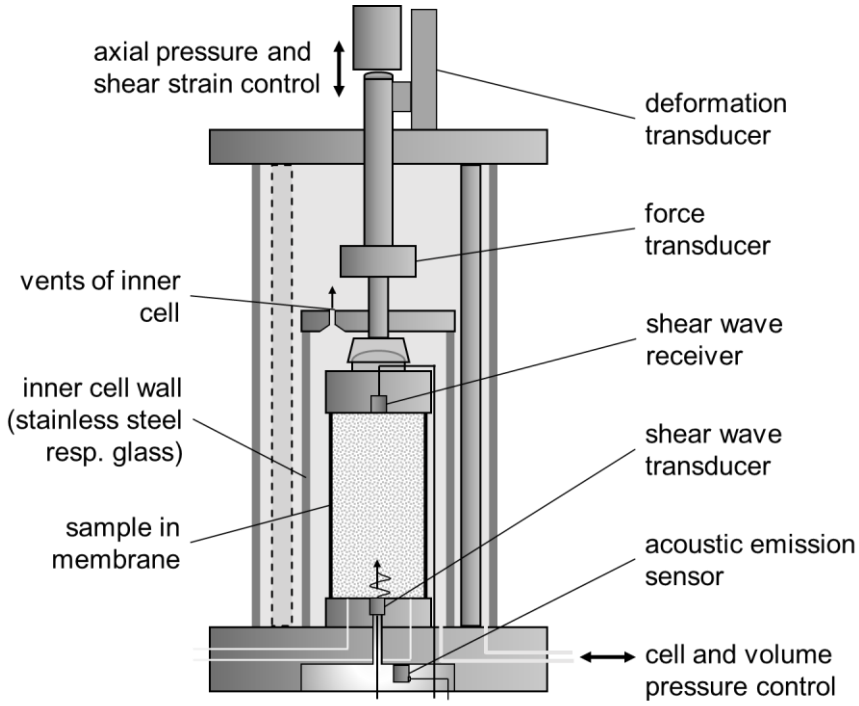

(b)

Figure 3.2: (a) Photography of the triaxial setup and (b) schematic scetch of the triaxial cell including the description of the main components (published in Jessen et al. (2023))

Similar to the oedometer test, the test control was automatized and along with the data acquisition and visualization controlled by a software. Devices with electromechanical ball screw drives for volume and pressure control were used to apply isotropic pressure on the sample. The nominal value of the cell pressure was 4000 kPa, and the resolution of the measured pressure was specified by the manufacturer as 0.1 kPa. During the phases of test initialization, the specimen was continually subjected to a slight additional axial pressure applied by a loading ram penetrating the pressure cell to ensure specimen contact, which is necessary to measure the change of the axial deformation of the specimen. Linear encoders as displacement sensors with a resolution of 0.025 µm placed on the top of the triaxial cell, logging the displacement of the outer piston, measured the axial deformation. The load frames were based on an electromechanical ball screw drive. The capacity was given by a nominal force of 100 kN. The deviatoric loading of the specimens under triaxial compression was accomplished by the strain-controlled movement of the loading ram, which was attached to a movable transverse. The axial force was measured with a cell pressure compensated internal force sensor with a nominal value of 100 kN and an accuracy class of 0.1. These force sensors were placed in the outer cell according to Figure 3.2 (b) to keep the volume in the inner cell as small as possible. The principle of the double cell, which was used for measuring the volume change, is described in Section 3.1.2.2.

3.1.2.1 Limitation of the triaxial test

Concerning the maintenance of the axial pressure σ_a during creep the same limitations apply to the triaxial test as mentioned for the oedometer (Section 3.1.1.1): Due to the use of a load frame with an electromechanical spindle drive, minor variations of σ_a during creep are unavoidable. The deviations

measured during the triaxial creep tests at different deviatoric stresses ranged from 0.05 % to 1.12 %. The cell pressure system is less susceptible to deviations because it is much more inert due to the comparably large cell volume.
Furthermore, friction from the sealing and guidance of the internal loading piston affects the measurement of the axial force in the presented triaxial setup. At the beginning of the tests, stick-slip effects were observed during deviatoric loading well measurable at very low strain rates. A tight seal between the inner and outer cells was mandatory due to the volume measurement described later. Since there is no differential pressure between the fluid of the inner and outer cells, the design of the sealing element is rather challenging when friction is also to be minimized. In consultation with the manufacturer, the design detail of the sealing and loading piston was modified to reduce the negative effects while ensuring a robust seal.
The axial stress on the specimen depends on the mean diameter of the specimen. The exact value, therefore, varies depending on the specimen shape over the specimen height. This effect was neglected in the present experimental investigation, and an average value for the stress was assumed. The influence of the tensile stress carried by the straining membrane during increasing radial strain ε_r was not considered. Additionally, the initial stress, which includes the vertical stress due to the top plate and self-weight of the sample was neglected. Based on the investigation of dry specimens, the self-weight of the cell fluid results in a hydrostatic pressure that varies over the height of the specimen. This variation of the radial stress was not considered. These errors were < 10 kPa for the vertical loading and < 3 kPa for the radial stress acting on the sample by pressurized cell fluid, hence, i.e., less than 2 % of the applied smallest confining pressure during creep.
The vertical deformation was measured using an external deformation transducer on the top plate of the triaxial cell. The deformation of the system, such as the compression of interfaces (e.g. top plate, loading piston), influences the measured axial deformation. However, due to the material behavior of steel in the range of the investigated loading, the components react predominantly elastically and thus do not influence the creep deformation at constant stress, which is of interest in this study.

3.1.2.2 Measurement of volume change

Conventional volume change measurement of the sample in triaxial tests recording the in- and outflowing of pore water was not possible in this study because of the examination of dry specimens. Various methods to measure the volume change of dry (or partially saturated) sand samples can be found in the literature (Lade, 2016; Laloui et al., 2006) and are summarized in the following list:

- Laser optical measurements, such as using a light band micrometer
- Local radial and axial measurements on the sample using LVDTs
- Digital image correlation (DIC) techniques
- X-ray tomography
- Measurement of the in- and outflowing of cell fluid, comprising the so-called cell-in-cell or double-cell principles

All methods show advantages and disadvantages that must be considered when selecting the most appropriate volume change measurement method for the application and budget available.

LVDTs are used to measure the local deformation in axial and radial directions. A positive aspect is that the sensors are connected to the sample, and thus, influences from the test setup can be eliminated. However, the method does not provide any information about the accordingly to the size and geometry of the sample varying or inhomogeneous deformation of the specimen. The definition of the reference length for determining the strain is system-dependent and may have to be selected subjectively. The influence of the disturbance of the sample from mounting as well as the self-weight of the sensors on the deformation behavior cannot be excluded.

Laser optical methods, DIC techniques and X-ray tomography, are expensive options because they require a particular designed triaxial cell, expensive measuring equipment, and specific software. Nevertheless, these methods are interesting because they can determine the actual deformation at a high spatial resolution covering the entire sample. Limitations rises since the observation of considerably large samples result in decreasing resolution and accuracy.

A standard method for partially saturated samples is to measure the in- and outflowing of cell fluid instead of pore fluid. Leong et al. (2004) summarized the influences on volume change measurement methods by using the cell fluid: Accuracy of the volume change measurement device, cell pressure, temperature stability, and creep of the system, conformity of the system in terms of stiffness, hysteresis and water absorption, leakage of the system and membrane penetration. The influence of cell pressure can be eliminated by using the cell-in-cell principle. Since the inner cell is pressure compensated by the outer cell, in which the same pressure prevails, the deformation of the inner cell due to pressure changes is limited. Accordingly, the volume change measurement by measuring in- and outflow of the inner cell fluid is not affected by the cell deformation due to the pressure. The principle of the double cell is similar to the one of the cell-in-cell principle. The difference results from the top plate, which is not pressure compensated. The method used by both principles is limited to measure the volume change of the entire sample; local variations cannot be registered.

For the present research application, the cell-in-cell principle proved to be the most suitable method to measure the volumetric creep deformation of dry granular material since a large sample was planned due to the expected comparably small creep deformations. Methods owing a higher performance are available as listed above but were out of the scope of the given budget. In addition, in relation to most experiments found in the literature comparably high cell pressures were applied in this study; thus, the influence of the change in cell pressure could be minimized by the cell-in-cell principle in contrast to the double cell principle.

The volume change of the samples' during creep was calculated as the change of the inner cell fluid reduced by the volume change in correspondence to the rising penetration of the piston. The volume and pressure control devices with a capacity of 250 ml had a resolution given by the manufacturer of < 0.001 cm^3. The inner cell wall was made of stainless steel or glass, whereas water absorption is not expected in contrast to the use of plastic (Angerer, 2019). Copper tubes were used for setting up the fluid system including high-quality connections and taps that were used to reduce air inclusions. Air inclusions in the inner cell were minimized by locating three vents with conical inlets on the bottom of the top plate of the inner cell, which was slowly filled with deaerated water (see Figure 3.2(b)).

3.1.2.3 Limitations of the volume measurement method

The most significant limitations of the volume change measurements were the time-dependent effects, such as temperature variations, in the cell fluid and the creep deformation of the system. Even temperature changes of less than 1 K can significantly influence the measurement. Therefore, empirical formulas for compensating the temperature influence were used to enhance the accuracy of the measurement. The larger the volume of the cell fluid, the larger the measurement error. Calibration of the used systems was essential and is described in the next section.
For changes in the direction of the movement of the hydraulic pistons situated within the volume pressure control devices, recognizable discontinuities of the measurement were found, probably caused by the inherent deformations of the compressive and comparably flexible piston seal.
Although de-aired water was used and care was taken to avoid air inclusions when filling the inner cell volume, air inclusions could not be completely avoided; these affected the accuracy of the volume measurement. This effect reduces after the pressure increases following the solution of air to water.
In addition, natural rubber membranes used in the first series of tests were replaced by butyl membranes since water diffusion through the rubber membrane can occur in the range of pressure up to 2000 kPa applied in the tests and the test duration of three weeks. The membrane of butyl is known for negligible diffusion. After the tests, a visual inspection of the samples did not reveal any moistening.

3.1.2.4 Calibration and verification of volume change measurement

Calibrating the time-dependent influences on the volume change measurement system was essential. For this, the temperature was continuously recorded by sensors of type PT 100 in the laboratory room and in the water of the outer cell during the experiments. The volume changes due to temperature variations ΔV_T were corrected afterwards using an isotropic expansion approach according to Serway and Jewett (2014) as suggested by Leong et al. (2004).

$$\Delta V_T = V_0 \cdot \alpha_T \cdot \Delta T \cdot (1 + \frac{\alpha_T}{3} \cdot \Delta T + \cdot \frac{{\alpha_T}^2}{27} \cdot \Delta T^2), \tag{3.1}$$

where V_0 is the initial volume of the inner cell fluid system, including tubes and the volume of the pressure and volume control device, α_T is the volume expansion coefficient in 1/°C of the entire system to be determined and ΔT the temperature difference to the initial temperature at the beginning of the test.
The coefficient of volume expansion α_T was determined using a sample dummy with approximately similar dimensions as the investigated soil. In this study, a dummy made of PTFE was isotropically loaded up to 1000 kPa. The pressure was maintained for six days, and the temperature and volume change of the inner cell was recorded. The volume of the inner cells of the two triaxial setups were determined after the test by weighing the cell water after emptying. In addition, the volume of the water inside the copper tubes was calculated using the known cross-section and tube length of each setup. The volume inside the used volume and pressure control device was read at the end of the test and added to the inner cell volumes and volumes of the tubes to obtain V_0. The initial volume of fluid within the volume control device was kept the same when refilling it before each test. This calibration procedure was done individually for each triaxial test setup. V_0 was found to be 6939 cm^3 and

7051 cm^3, respectively. Figure 3.3 shows the results for the triaxial setup No. 1. Considering the temperature expansion of the PTFE dummy, the volume expansion coefficient α_T was found to be 0.0002 1/°C for setup No. 1 and 0.00025 1/°C for setup No. 2, respectively. Thus, the accuracy of the volume measurement was determined to be < 0.03 %.

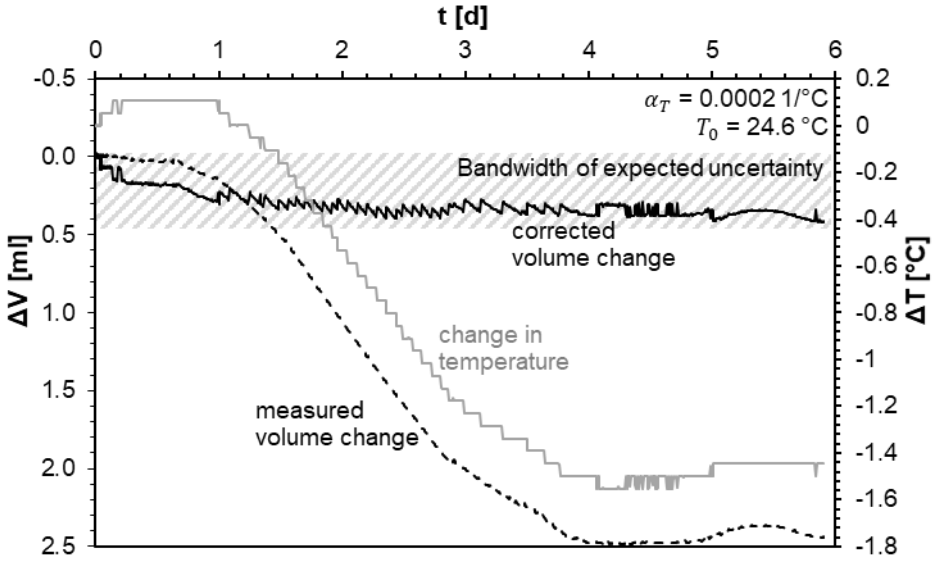

Figure 3.3: Calibration test on triaxial setup No. 1: Measured and corrected volume change and temperature curve over a period of creep of 6 days at 1000 kPa

3.2 Evaluation method of axial and volumetric strain

The axial strain ε_a (or ε_1 according to the direction of the major principal stress, respectively) was calculated by the logarithmic (or natural) formulation according to the initial height of the sample h_0 and the change of current height Δh.

$$\varepsilon_a = -\ln\left(1 - \frac{\Delta h}{h_0}\right) \tag{3.2}$$

The volumetric strain was determined by the volume change of the sample ΔV and the volume of the sample at the onset of shearing or, respectively creep, V_0.

$$\varepsilon_{vol} = -\ln\left(1 - \frac{\Delta V}{V_0}\right) \tag{3.3}$$

The volume change of the sample ΔV was calculated by the volume change of the inner cell dV_p, which was measured by the volume pressure control (VPC) device. The volume change was corrected by the volume displaced by the moving loading piston calculated considering the diameter d_p and the change in sample height Δh. Furthermore, the volume changes due to temperature fluctuation ΔV_T, according to Equation (3.1), were considered. This resulted in the following formula:

$$\Delta V = dV_p + \left(\Delta h \cdot \frac{{d_p}^2 \pi}{4}\right) + \Delta V_T \tag{3.4}$$

The general relationship between the strain components in the principal stress direction and volumetric strains, according to Lade (2016), can be written as

$$\varepsilon_{vol} = \varepsilon_1 + \varepsilon_2 + \varepsilon_3 - \varepsilon_1 \cdot \varepsilon_2 - \varepsilon_2 \cdot \varepsilon_3 - \varepsilon_3 \cdot \varepsilon_1 + \varepsilon_1 \cdot \varepsilon_2 \cdot \varepsilon_3, \quad (3.5)$$

Since overall comparably small strain changes occur during creep of granular materials, the second and third order terms ($\varepsilon_1 \cdot \varepsilon_2$; $\varepsilon_2 \cdot \varepsilon_3$; $\varepsilon_3 \cdot \varepsilon_1$, and $\varepsilon_1 \cdot \varepsilon_2 \cdot \varepsilon_3$) of Equation (3.5) can be neglected. Furthermore, due to the axisymmetric condition $\varepsilon_2 = \varepsilon_3 = \varepsilon_r$. The radial creep strains ε_r can be calculated from

$$\varepsilon_r = \frac{\varepsilon_{vol} - \varepsilon_a}{2} \quad . \quad (3.6)$$

The one-dimensional compression behavior of soils during virgin loading, represented by the change of the void ratio e with respect to the initial void ratio e_0, is widely described by the compression modulus proposed by Terzaghi (1925).

$$e_0 - \mathrm{e} = C_c \cdot \log \frac{\sigma'}{\sigma'_0} \quad , \quad (3.7)$$

where C_C is the compression index and σ'_0 is the initial vertical stress corresponding to e_0.
Creep, i.e. the change in void ratio e with time t, is commonly quantified by the coefficient of secondary compression C_α (Taylor & Merchant, 1940) according to Equation (2.1) or equivalently by the coefficient C (Buisman, 1936) as a function of the change in strain ε according to Equation (2.2).

3.3 Assessment of aging

In the present experimental study, the development of aging and creep had to be assessed simultaneously. For this reason, a non-destructive method was chosen, making it possible to assess aging during creep. Aging was therefore assumed to be proportional to the change of the shear modulus ΔG_0 ($\gamma \leq 10^{-5}$) during creep. Assuming isotropic elastic soil behavior, the value of G_0 can be determined according to Equation (3.8):

$$G_0 = \rho \cdot {v_s}^2 \quad , \quad (3.8)$$

where ρ is the density of the sample and v_s is the propagation velocity of the shear wave in the elastic medium. A non-destructive method to determine the shear wave velocity consists of installing a piezo-electric transmitter and receiver at the bottom and the top of the sample.

In the following, the existing techniques and evaluation methods for assessing the shear wave velocity by piezo-electric sensors are reviewed. The method used in this study, including the evaluation method for the shear modulus at small strains and assessing aging, is presented and finally, the limitations of this measurement technique are pointed out.

3.3.1 Review on the shear wave velocity measurement techniques and evaluation methods

3.3.1.1 Principles of the measurement techniques

Figure 3.4 shows the basic principle of the measurement of shear wave velocity by sensors using the piezo-electric effect.

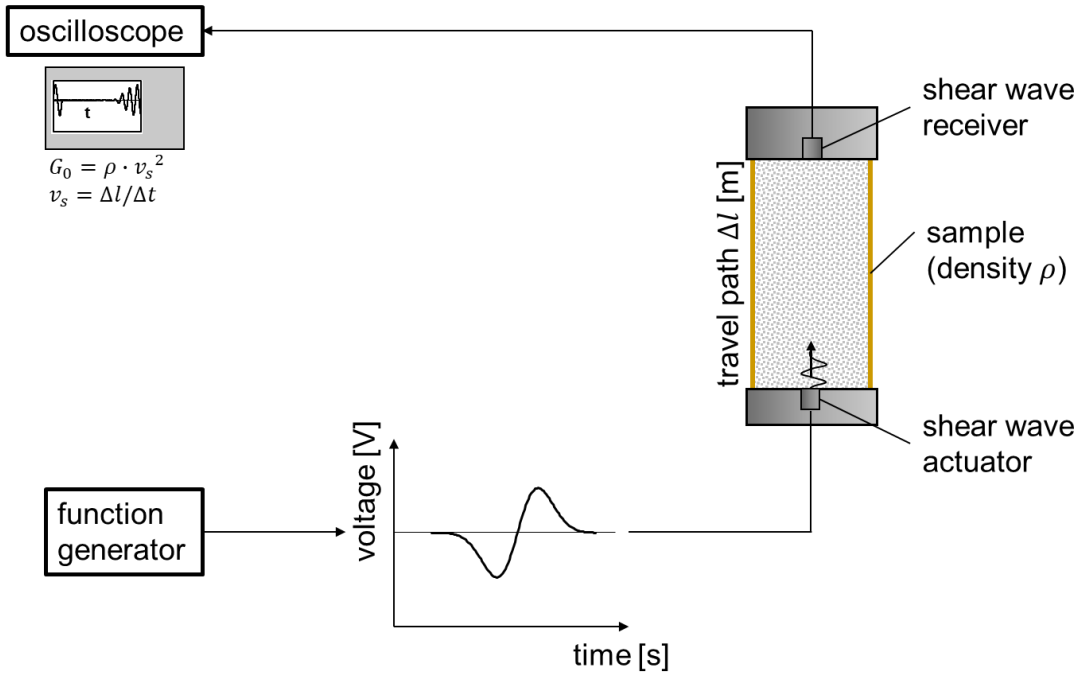

Figure 3.4: Schematic sketch of the shear wave velocity measurement system using the piezo-electric effect

A function generator produces a signal. The waveform and frequency selected depend on the interpretation method subsequently used; a sine or rectangular pulse is usually used for evaluation in the time domain (Yamashita, Kawaguchi et al., 2009). The piezo-electric ceramic of the sensor transforms the electric energy into mechanical energy by deformation and generates a horizontal dynamic excitation that transmits a wave into the soil sample. From the actuator placed at the base of the sample, the shear wave propagates with a certain velocity v_s through the sample and reaches the receiver on the top plate. The piezo-electric ceramic of the sensor converts the mechanical deformation given by the incoming wave back into an electrical excitation that can finally be recorded and visualized by an oscilloscope. The generated signal (before transmitting) or the incoming signal (after receiving) can be amplified to increase the signal amplitude. The travel time Δt of the shear wave can be determined, and the shear wave velocity can be calculated by the knowledge of the travel path Δl, which is influenced by the deformation of the sample.

The piezo-electric ceramics used as shear wave actuators and receivers are commonly made from lead zirconate titanate (PZT) (Leong et al., 2005). Depending on the sensor type, the material is put in different shapes, sizes, and arrangements. Three types of piezo-electric transducers will be presented in the following; moreover Figure 3.5 shows a schematic illustration of their functional principles.

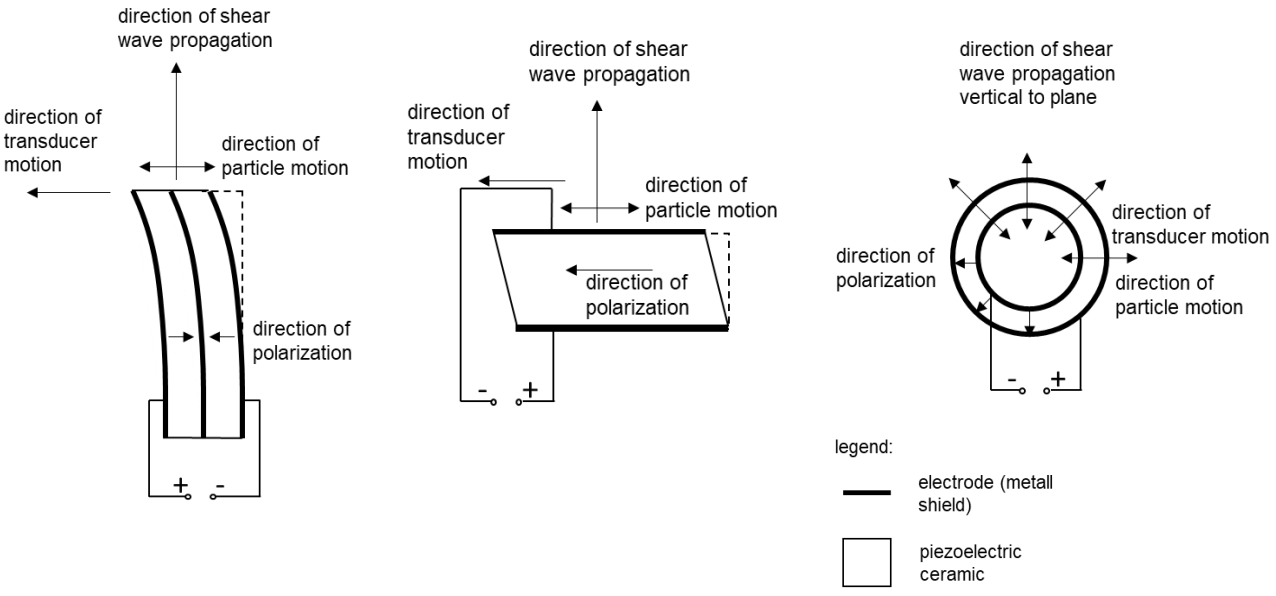

Figure 3.5: Schematic illustration of the operation of (a) a bending actuator in series connection, (b) a disk-shaped ultrasonic device and (c) a ring actuator of type P-RAT (redrawn and supplemented after Brignoli et al. (1996))

The most common type of actuator and sensor in the field of soil mechanics laboratory testing is the so-called Bender Element (BE) (Leong et al., 2005). For BE, two piezo-electric ceramic layers are usually placed on top of each other and separated with a metal shield. The metal shield in the middle and two additional metallic layers on both outer ceramic surfaces work as electrodes. Two different types of electrical connections are commonly used: series and parallel connections, which differ in their resulting polarization direction. An opposite polarization of the two ceramic layers is reached by connecting the outer electrodes of each layer. In contrast, polarization in the same direction is possible by connecting the outer and center electrodes (ASTM International, 2019). If the same voltage is applied to both types of electrical connection, a BE with a parallel connection achieves higher amplitudes. Therefore, this connection is usually used for the actuator. On the other hand, a sensor with a series connection reaches a higher voltage than a sensor with a parallel connection at the same deformation. It is therefore used at best as a sensor, hence receiver (Yamashita, Kawaguchi et al., 2009). A section through the two types of connection is shown in Figure 3.6.

The bending deformation occurs when one of the ceramic layers expands as a result of changing electrical voltage while, depending on the electrical circuit, the other ceramic layer contracts (parallel type) or does not change its shape (series type). The advantage of BEs is that due to the bending element penetrating the sample, the connection to the tested material can be assumed to be very good and thus, the excited signal is usually well transmitted to the specimen. Furthermore, corresponding to a large number of applications given by the literature, there is a wide range of experience. (ASTM International, 2019; Lee & Santamarina, 2005; Sawangsuriya, 2012; Yamashita, Kawaguchi et al., 2009)

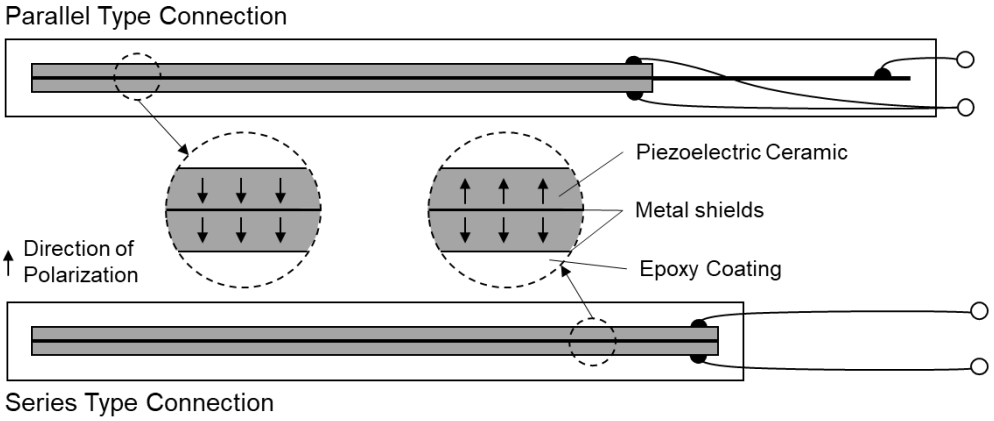

Figure 3.6: Scheme illustrating the different electrical circuits used in piezo-electric Bender Elements: parallel type (top) and series type (bottom) connection (redrawn after Yamashita, Kawaguchi et al., 2009)

Nevertheless, there are limitations of the BE technique, and several issues are discussed controversially in the literature: Due to the penetrating benders, the wave propagation length Δl is not well defined. The tip-to-tip length of the sensor pair is mainly used to calculate v_s (Yamashita, Kawaguchi et al., 2009). Moreover, the excited wave does not form a plane wave front due to the limited dimensions and the one-dimensional bending of the bender elements. In addition to the S-waves, compression waves (P-waves) are induced simultaneously resulting from the movement of the bending plate, as illustrated in Figure 3.7 (Lee & Santamarina, 2005). Since the velocity of the compression waves is higher than that of the shear waves, the waves overlap, and a clear separation of the two wave types by measuring and interpreting the incoming signal can be difficult. The consequences can be uncertain or even incorrect interpretation. Furthermore, the so-called near-field effect occurs at low excitation frequencies or short distances between the BE actuator and sensor compared to the wavelength. The shear wave is accompanied by a rapidly attenuating wave travelling at the speed of the compression wave that as well influences the shear wave response. Thus, the arrival time cannot be determined without a doubt (Sánchez-Salinero et al., 1986). Typical resonance frequencies of BE in soil lie between 3 kHz to 10 kHz and depend on the velocity respectively stiffness of the surrounding soil, as well as the dimensions and the stiffness of the BE itself (Lee & Santamarina, 2005).

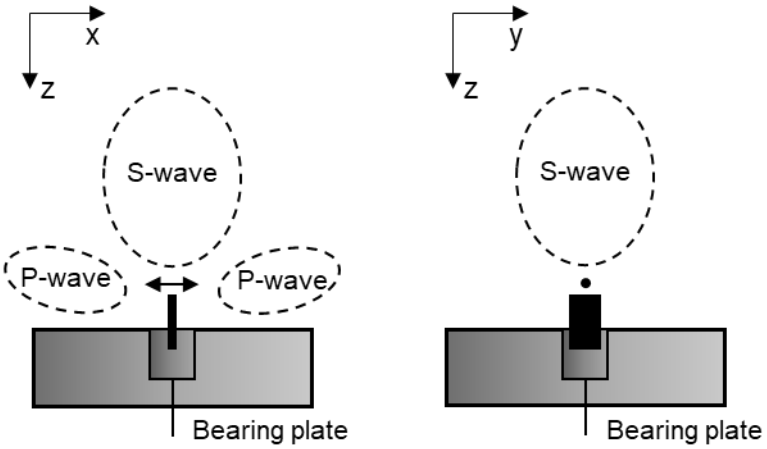

Figure 3.7: Occurence of compression waves (P-waves) due to the movement of Bender Elements (redrawn after Lee & Santamarina, 2005)

So-called ultrasonic sensors have also been used, which allow excitation at a higher frequency of up to 80 kHz (Brignoli et al., 1996). For ultrasonic sensors the electrodes are attached parallel to the direction of polarization, as shown in Figure 3.5 (b). In contrast to the BE, the piezo-electric ceramics do not penetrate the specimen, and the travel length of the wave Δl can be defined with less uncertainties. The system time delay can be rather easily determined by face-to-face tests. However, the signal transmission into the sample is less intense, reducing the amplitudes of the measured signal limiting the possibility of interpretation. Therefore, Brignoli et al. (1996) summarized that this type of sensor is suited for undisturbed, stiff samples or for soils with large grain sizes.

Recently, due to the limitations of the methods of BE and ultrasonic sensors, the idea of creating a new sensor type exciting a plane wave raised at the University of Sherbrooke. Karray et al. (2015) developed the so-called piezo-electric ring actuator method (P-RAT). Instead of piezo-ceramic plate shaped elements, a piezo-electric ring actuator is used. Stones mounted within the ring transfer the radial movements to the specimen without penetrating and disturbing it. Separating the inner stones into four pieces helped to reduce the generation of P-waves to a minimum. Numerical simulations showed that this sensor type creates an almost plane wave front in oedometer tests (Karray et al., 2019). Furthermore, due to the higher resonance frequency of the cylindrical piezo-ceramics compared to BEs in the range of 50 kHz, the excitation frequency can be increased, whereby the unwanted near-field effect gets less significant. Figure 3.8 describes the sensor setup and shows a photo.

(a) **(b)**

Figure 3.8: (a) Description of the setup (adapted after Karray et al., 2019) and (b) photo of a P-RAT mounted in a top plate of an oedometer device

3.3.1.2 Review on evaluation methods

The shear wave velocity measurement using the piezo-electric effect is based on a transient voltage signal visualized and the data saved by an oscilloscope. This signal has to be interpreted properly to determine the travel time of shear wave and thus, to determine the shear wave velocity finally. The literature presents several methods, which can be roughly categorized by those in the time domain and in the frequency domain. The applicability of some of the proposed methods was tested in the scope of this evaluation. Their principles are described in the following.

3.3.1.2.1 Time domain

Figure 3.9 summarizes the most common methods using the transient time-dependent signal for determining the travel time of the shear wave namely, the start-to-start (or first arrival) method, the peak-to-peak method and the approach using cross-correlation.

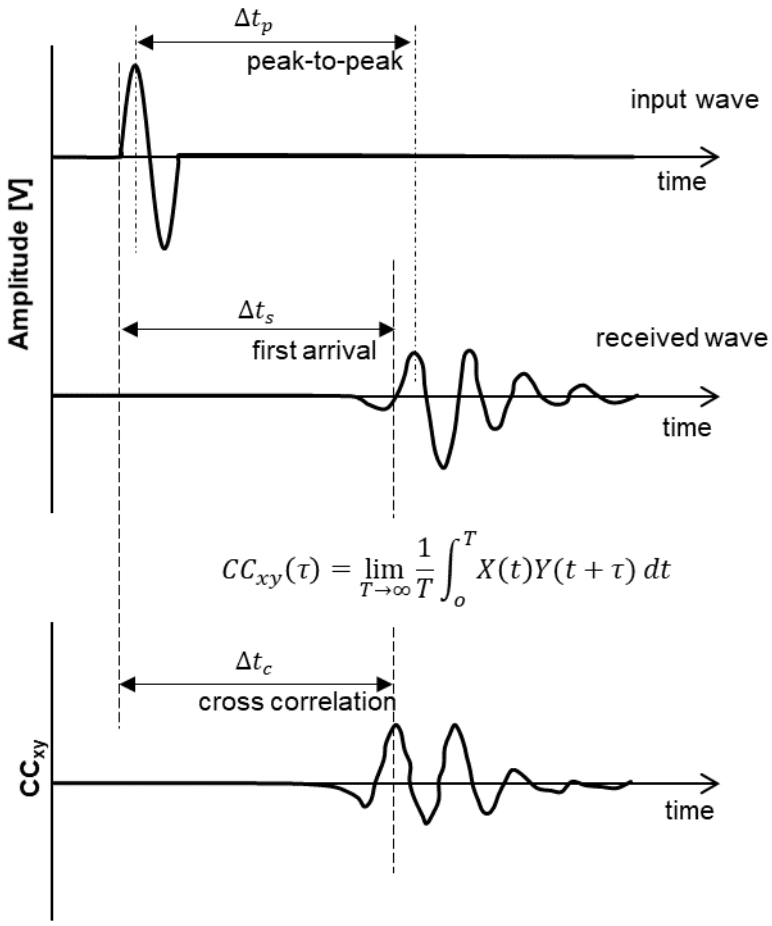

Figure 3.9: Identification methods for shear wave travel time using the time domain (redrawn and adapted after Kawaguchi et al., 2016)

Start-to-start method (or first arrival method)

This method is characterized by its simplicity and is therefore the most widely used. The travel time Δt_s is determined by the time difference between the starting points of the transmitted and recorded wave (Figure 3.9). Various definitions for the first arrival point can be found in the literature and are shown in Figure 3.10.

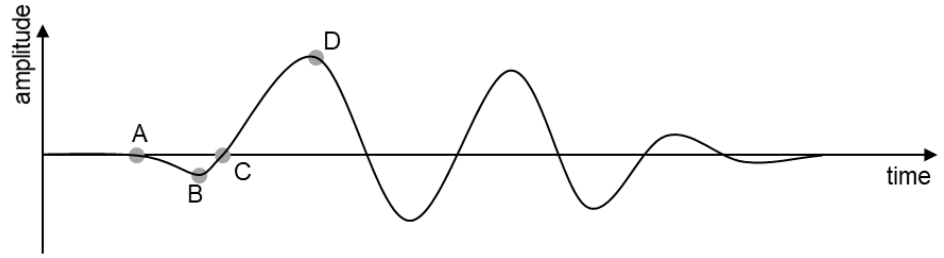

Figure 3.10: Definitions of characteristic points of a transient signal for applying the first arrival method (A, B and C) and of the peak point (D) (redrawn after Yamashita, Kawaguchi et al., 2009)

They can be described by (A) the first deflection, (B) the peak of the first deflection and (C) the first zero crossing. The majority defines the first arrival point as the first zero crossing of the received wave (Yamashita, Kawaguchi et al., 2009). The method is particularly suitable when the arrival of the shear wave may be clearly interpreted by solely visual inspection of an experienced researcher.

Peak-to-peak method

Point D in Figure 3.10 defines the first significant peak of the recorded signal. The peak-to-peak method defines the travel time Δt_P by determining the time difference between the first peak of the applied signal for inducing the shear wave and the first peak of the recorded signal by the sensor (Figure 3.9). This method assumes that the input and output frequencies of the signal are approximately equal (Santamarina & Fam, 1997). However, this assumption should be used with caution, as various factors, such as the sensor type, the shape and frequency of the excitation signal, or sample size, as well as the properties of the material to be investigated, can affect the frequency of the measured signal.

Cross-correlation method

The cross-correlation method compares the outgoing signal $X(t)$ and incoming signal $Y(t+\tau)$ to determine the maximum degree of correlation between the two signals. The propagation time of the shear wave is defined by the time shift Δt_C at which the maximum amplitude of the cross-correlation function $CC_{xy}(\tau)$ occurs (Sánchez-Salinero et al., 1986; Viggiani & Atkinson J.H., 1995). As with the peak-to-peak method, this provides reliable results only when the induced and the recorded signals are similar (e.g. Santamarina & Fratta, 2005).

Coda Wave Analysis

To identify small velocity changes, such as those resulting from minor stress variations or time-dependent effects like aging, the time difference of the first arrivals is often very small. In such cases, analyzing seismic coda waves has proven effective. The coda wave approach compares the two signals in the time domain after they have undergone multiple reflections. In this process, the time shift Δt between the two signals accumulates, making it easier to be identified.

The objective of the evaluation is to determine time differences Δt at various travel times t. This results in a linear relationship between Δt and t, characterized by a slope θ. This slope θ represents also the relative change in velocity Δv of the two signals with respect to the mean velocity $\bar{v}$ and is thus referred to as the stretching factor (Dai et al., 2013). The time shift Δt can be assessed, for instance, by cross-correlating selected time windows. Additional evaluation methods are discussed in Dai et al. (2013).

The methods using the time domain of the recorded signal have in common that they are rather easy to apply and, with good signal quality, also lead to reproducible results that can be assessed by comparably small effort (Yamashita, Kawaguchi et al., 2009). However, the stronger the interfering effects, such as the near-field effect, superposition of S- and P-waves, attenuation, and reflection of waves at sample boundaries in case of interference at large travel distances, the more difficult and subjective becomes the definition of the travel time in the time domain.

3.3.1.2.2 Frequency domain

The methods based on the frequency domain of the recorded signal were developed to overcome the subjectivity of evaluation using the time domain of the signal. The lack of objectivity is associated with, for example, the selection of the point of first arrival. They have in common that the signals inducing the wave by the actuator and the signals measured by the sensor must be decomposed into harmonic waves of known frequencies and amplitudes by, e.g. the Fast Fourier Transformation (FFT). Following this, the problem can be treated as a dynamic system. The velocity of a wave corresponds to the phase shift of the propagating wave between two points in time. By disregarding material dependent attenuation, the velocity v of a plane wave can be determined by

$$v = \frac{\omega}{k}, \tag{3.9}$$

where $\omega = 2\pi f$ represents the angular frequency and $\lambda = 2\pi/k$ is the wavelength. The phase velocity v_{ph} is referred to v. For non-dispersive media, the phase velocity is constant. Granular materials are basically dispersive due to their particulate structure, but the propagation of elastic waves with a wavelength λ significantly larger than the mean diameter of the medium is similar to that in a continuum.

However, a dependence of the phase velocity on frequency for shear waves in soils using a transmitter-receiver system has been found by several researchers (Da Viana Fonseca et al., 2009; Karray et al., 2015). There are different opinions regarding where this dependence results from. Sasche and Pao (1978) summarized the causes of dispersion in a material into geometrical, material, scattering, dissipative and non-linear dispersion. Karray et al. (2015) proposed that the apparent dispersion results from the transmitter-receiver-soil system since the signal generated for inducing the wave is not necessarily the signal transmitted from the sensor to the soil. The measurement of the difference between the electrical signal and the signal that is transferred to the specimen is technically challenging and results in a system error that must be considered in the evaluation. Recent works try to observe the actual vibration of BEs by the means of transparent medias and dynamic high precision laser scanning methods (Liu et al., 2022).

Overall considering the methods based on frequency domain numerous approaches are available, which have been continuously modified, extended, or combined in different ways by researchers. Regarding the scope of the thesis, a brief overview of the basic published methods can be given.

π-point method (e.g. Sasche & Pao, 1978)

Continuous signals with ascending constant frequency f_n over a certain period are sent through the sample. The transmitted and measured signals for a particular frequency f are compared, and the phase shift $\phi(f)$ is determined as a multiplier of π. A frequency that results in a perfectly matching phase is called a π-point. Perfectly in-phase or out-of-phase means that the Lissajous figures show a straight line or the phase shift $\phi(f)$ is an integer multiple of π, respectively. The number of wavelengths $N = k/2 = \phi(f)/2\pi$ can be plotted against the frequency. The slope that may represent the data and that is theoretically a straight line in the case of non-dispersive material behavior corresponds to the travel time of the shear wave. Figure 3.11 (a) shows the relation between number of wavelength and frequency graphically.

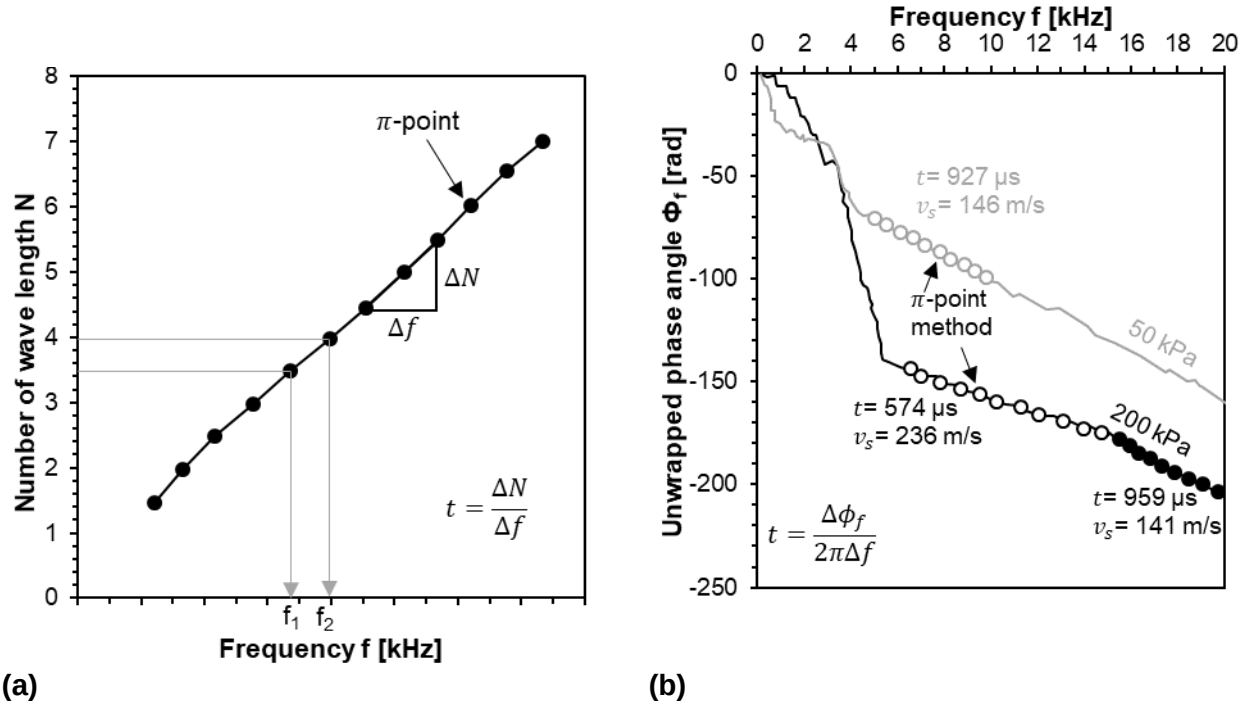

Figure 3.11: Determination of travel time with (a) the π-point method and (b) continuous sweep method (redrawn after Da Viana Fonseca et al., 2009)

Due to the mostly manually controlled gradually frequency change (sweep) of the input frequency, the method is time-consuming and hence only a limited number of π-points can be detected. Furthermore, similar to the cross-correlation the signals driving the wave actuator and the signals measured by the sensor should be similar to perform a reliable comparison and determination of the phase shift (Da Viana Fonseca et al., 2009).

Method of Hussien and Karray (2021)

This interpretation method assumes that the shear wave velocity v_s does not change with frequency (non-dispersive material). Hussien and Karray (2021) stated that the velocity determined in the laboratory by measuring a travel time is the phase velocity v_{ph}, which depends on frequency. Therefore, in contrary to the π-point method $v_{ph}(f)$ is generally not the same as v_s. The difference between the two velocities results from the phase shift of the dynamic transmitter-receiver system. The phase shift between the signal inducing the wave (input) and the signal registered at the sensor (output) determines the experimental phase velocity $\phi_{exp}(f)$. The travel time of the phase velocity $t_{ph}(f)$ is defined as

$$t_{ph}(f) = \frac{\phi_{exp}(f)}{2\pi f} \,. \tag{3.10}$$

Due to the error in phase shift caused by the transmitter-receiver system the experimentally determined phase shift $\phi_{exp}(f)$ needs to be corrected by $\phi_{corr}(f)$ resulting in the phase shift ϕ_{ph} that belongs to the theoretical phase shift of v_s and the travel time t.

$$\phi_{ph} = \phi_{exp}(f) - \phi_{corr}(f) \tag{3.11}$$

From the condition that t is constant at varying frequency f and after transformation follows Equation (3.12).

$$\phi_{corr}(f_i) = \phi_{exp}(f_i) - \left(\frac{f_i}{f_j}\right) \cdot \left(\phi_{exp}(f_j) - \phi_{corr}(f_j)\right) \tag{3.12}$$

Thus, the phase shift correction $\phi_{corr}(f_i)$ of an arbitrary frequency i can be determined if the correction function $\phi_{corr}(f_j)$ of at least one frequency j is known. Through measurements by face-to-face tests of type P-RAT, Hussien and Karray (2021) showed that the emitter and receiver systems can be interpreted as two separate single-degree-of-freedom systems. Thus, the phase shift error of the emitter-receiver system is approximately zero at low frequencies, reaches π at the resonant frequency and equals 2π at high frequencies. The damping ratio of the system controls the shape of the decay of the phase shift error. Assuming that the emitter-receiver system follows the theoretical solution, the phase shift correction value can be easily determined at small frequencies where the phase shift is close to zero. For this purpose, a frequency range should be chosen in which high energy is transferred from the actuator to the specimen to overcome the near-field effect and which is significantly below the resonant frequency of the system. A good approximation for the resonant frequency and the damping ratio of the system can be found by face-to-face or tip-to-tip tests, respectively. Thus, the shear wave velocity can be determined using the corrected phase shift $\phi_{corr}(f)$. The evaluation method is shown exemplary by a test result on Péribonka sand using P-RATs in Figure 3.12.

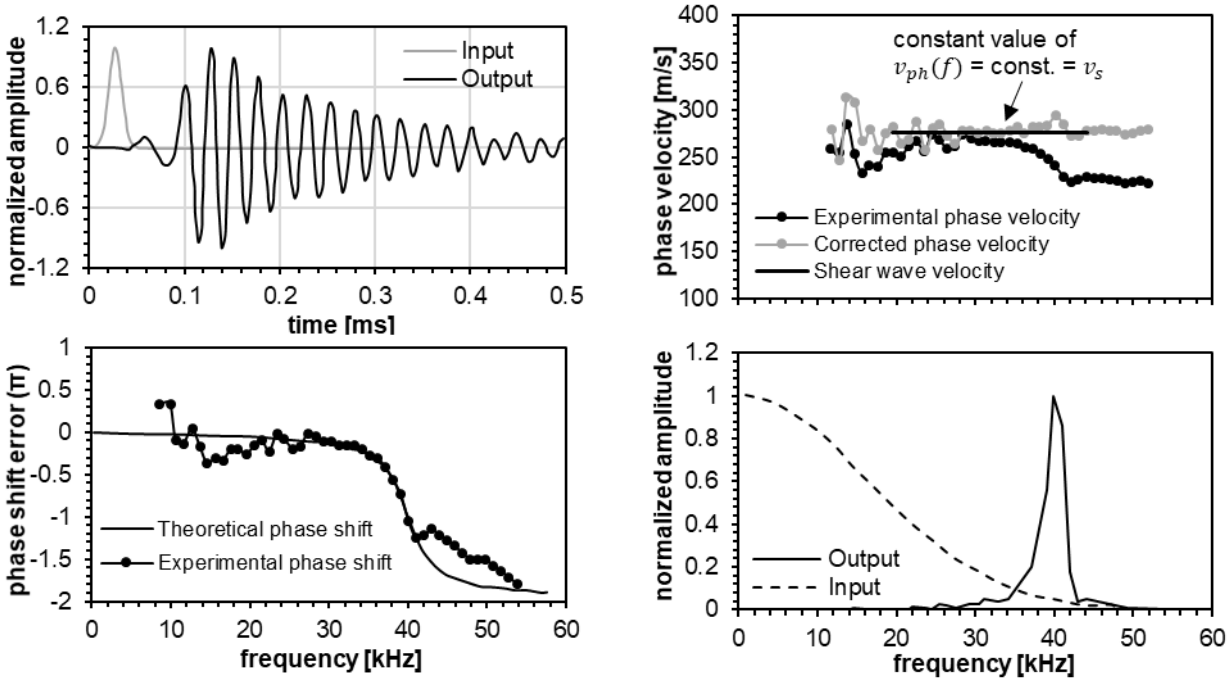

Figure 3.12: Example of interpretation using the method of Hussien and Karray (2021) (redrawn and adapted after Karray et al., 2015)

Sweep method (e.g. Greening and Nash 2004) or Cross-power spectrum technique

This approach uses a sine sweep with automatically increasing frequency as the signal, controlling the movement of the wave actuator. The transmitter and receiver signals are evaluated simultaneously with a spectrum analyzer. The phase angle between the two signals is determined, and the associated coherence function is evaluated. The coherence quantifies the linear relationship between the two transient signals over the frequency. The greater the coherence, the more similar the signals are. At frequency ranges with good coherence, the velocity can be determined from the slope of the best-fit line of the relationship between the unwrapped phase angle ϕ_f and the frequency f. The unwrapped phase angle describes the phase angle that starts at zero and increases continuously; it is also known as the absolute cross-power spectrum phase diagram. In comparison, the wrapped phase shift is given in the range of $-\pi$ and π (or cross-power spectra). Figure 3.11 (b) shows an exemplary result for different isotropic stresses on samples of Toyoura sand. The method is fast and cost-effective but prone to error because an appropriate frequency range must be selected.

The evaluation of the shear wave velocity from the measured signals transferred to the frequency domain is less subjective than the evaluation in the time domain since it is given by the solution considering harmonic waves only. However, some subjectivity is introduced in the methods based on the frequency domain analysis by necessary input of values for variables controlling the evaluation, for example, by the choice of the frequency range considered or the determination of the initial phase shift error. All methods work well in the time and frequency domain if the input signal is similar to the output signal and hence the signal is assumed to be of good quality, i.e. minimal interference effects occur. Therefore, for application it is of special importance to adopt a suitable actuator and

sensor considering the needs and boundary conditions of the experimental setup and the material to be examined.

3.3.2 Methodology used and settings

The research on which the thesis was worked out used piezo-electric actuators and sensors of type (a) BE in parallel connection and (b) ultrasonic devices. Both types of actuators and sensors were obtained by a commercial supplier for geotechnical equipment. Thus, the information about the manufacturing was limited to the datasheets, which are provided in Appendix A.1. In addition to a piezo-electric ceramic inducing shear waves, the ultrasonic actuator additionally consisted of a ceramic that induced compression waves. The ceramic for S-waves was on top of the ceramic of P-waves, and a protective ceramic layer covered the piezo-electric crystal layers. The two different types (a) and (b) of actuator and sensor were mounted into one of the two triaxial test setups. Figure 3.13 shows a photograph of the transmitters attached to the base plate. Fundamental specifications of the two types of piezo-electric actuators and sensors, respectively, are given in Table 3.1.

(a) **(b)**

Figure 3.13: Types of used piezo-electric transmitters mounted in the base plate for the measurement of shear wave velocity (a) Bender Element (b) ultrasonic devices

The same signal processing devices of type DAQ-LS (APS Antriebs-, Prüf- und Steuertechnik GmbH) were used for BE and the ultrasonic devices. Both types of devices worked with the oscilloscope and waveform generator Handyscope HS5 from TiePie. An amplification of 100 was chosen to excite the actuators. The signals were generated with the maximum possible amplitude by the generator of 12 V. As the change of shear modulus with time was expected to be small, a sampling rate of 50 MHz was chosen. A sinusoidal burst signal was generated once per second. For the system using BE, an excitation frequency of 5 kHz, and for the system using ultrasonic devices a frequency of 20 kHz was selected regarding the mechanical resonance of the actuators and sensors, respectively, limited by the unwanted increasing influence of induced P-waves with increasing frequency.

Table 3.1: Summary of settings of shear wave velocity measurement

Setting	Bender Element	Ultrasonic devices
Amplification	100-fold	
Amplitude voltage	12 V	
Sampling rate	50 MHz	
Function generator burst frequency	1 Hz	
Excitation frequency	5 kHz	20 kHz
Mechanical resonance frequency of the sensor pair	6 kHz	47 kHz
System time delay	5.0 µs	1.6 µs

The Multi Channel oscilloscope software (TiePie engineering) was used in order to display the electric voltage signals recorded by the sensors. A low-pass-filter of 50 kHz filtered the recorded signals, which was necessary to reduce noise due to high frequency content overlapping the actual shear wave. To minimize random artefacts and noise, at least 16 subsequent recordings were averaged.

3.3.3 Evaluation method and verification of shear modulus at small strains

The evaluation of the shear wave velocity to determine the small-strain shear modulus G_0 according to Equation (3.8) was performed using the start-to-start method since it was found to have the least uncertainties and lowest scatter compared to the other methods (Yamashita, Kawaguchi et al., 2009). Furthermore, it was the fastest and most intuitive method. The arrival time was chosen according to the first zero crossing (point C in Figure 3.10). A system time delay Δt_{sys} was taken to account to determine the travel time (see Table 3.1). It was determined by tip-to-tip (BE) and face-to-face (ultrasonic devices) measurements, respectively.

For the shear wave travel path l, the current specimen height h is defined when using the ultrasonic emitter and receiver, when using BE the embedding length of the bending plates is subtracted from the specimen height (length considering tip-to-tip).

To validate the evaluation technique of the determination of G_0, experiments on medium-dense and dense Cuxhaven sand were interpreted using the start-to-start method (time domain) and the interpretation method from Hussien and Karray (2021) based on the signals transformed in the frequency domain via FFT. The validation was done for the shear wave velocity v_s since it represents the decisive quantity in the scope of this thesis. The shear wave velocity v_s was determined for different mean effective stresses p' that cover the stress range of the experimental investigation. The experiments were done with the BE and their associated settings according to Table 3.1. The sample preparation and the experimental procedure were performed according to Section 4.2.2 and Section 4.3.2. Figure 3.14 shows the results.

For validation purposes the evaluated shear wave velocity was compared to the results from the literature regarding materials of comparable properties. Various researchers (e.g. Cascante & Santamarina, 1996; Hardin & Drnevich, 1972) proposed a power equation for the shear wave velocity v_s dependent on the mean effective stress p':

$$v_s = v_s \left(\frac{p\prime}{p_a}\right)^{\beta}, \tag{3.13}$$

where v_{s1} is the shear wave velocity at the reference pressure of p_a = 100 kPa and β is an exponent representing the contact behavior and change of particle assembly dependent on the stress (Cha et al., 2014). The reference velocity v_{s1} and the exponent β are directly related to soil compressibility and thus, to fabric changes and to the particle contact behavior. For elastic spherical particles the theoretical solution of Hertzian contacts gives a value of 1/6 for the exponent β. Cascante and Santamarina (1996) showed that processes such as buckling of particle chains, increase in number of contacts, elastoplastic behavior and cone-plane contacts lead to an exponent of β = 0.25, which was measured experimentally for uniform sand. The same exponent was proposed by Lashin (2021) for consolidated, uncemented sands under oedometric conditions. In general, the exponent β increases

with increasing compressibility due to fabric changes and a higher number of particle contacts (Cha et al., 2014).

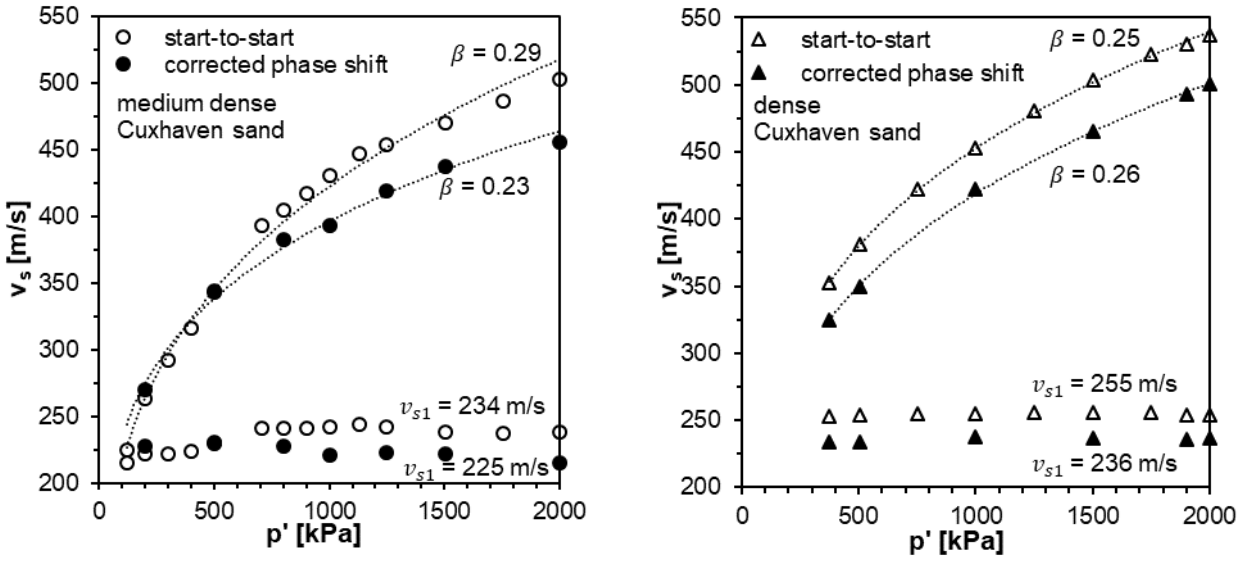

(a) **(b)**

Figure 3.14: Comparison of shear wave velocity evaluated in time domain (first arrival method) and frequency domain (corrected phase shift method) for (a) medium-dense and (b) dense samples of Cuxhaven sand; measurements carried out with BE

According to the experimental data in Figure 3.14, the exponent β ranges for Cuxhaven sand from 0.23 to 0.29 for both methods. Thus, the normalized velocities were determined to be v_{s1} ≈ 225 m/s and 234 m/s, respectively, for the medium-dense sample and v_{s1} ≈ 236 m/s and 255 m/s, respectively, for the dense sample of Cuxhaven sand. These results indicate the level of uncertainty in the absolute value of v_{s1} due to the evaluation method; a per cent deviation below 10 % was found for the samples investigated.

The results presented by this thesis show that for the start-to-start method, the shear wave velocity is higher compared to the values evaluated in the frequency domain, and this trend increases with increasing stress. A similar trend was found by Yamashita, Kawaguchi et al. (2009) when re-evaluating the results using the phase cross-spectrum method compared to the start-to-start method.

Furthermore, the empirical relation of Hardin and Black (1966) was used to describe the dependence of G_0 at t = 0 s on the effective pressure and void ratio and compare the results of this thesis with the results from the literature.

$$G_0 = A \cdot {p_a}^{(1-n)} \cdot (p')^n \cdot f(e) \ , \tag{3.14}$$

where A is a material constant, p_a = 100 kPa is the reference pressure, p' is the mean effective stress, n is a material-specific exponent and related through Equation (3.13) to approximately 2β, and $f(e)$ is a function considering the dependence on void ratio. To describe the influence of the void ratio,

$$f(e) = \frac{(x-e)^2}{1+e} \tag{3.15}$$

was proposed by Hardin and Black (1966). The variable x depends on the shape of the particles, and varies according to Santamarina and Cascante (1996) between 2.17 for round particles and 2.97 for angular particles.
It should be noted that v_{s1} in equation (3.13) already account for the void ratio, offering a physically based approach for determining the shear modulus based on fabric and particle contact behavior (Cha et al., 2014).

In addition, various empirical approaches describing anisotropic states for cylindrical specimens exist. For example, Peiji and Richart (1983) proposed the following formula depending on the stresses σ_1 and σ_3 in the principle directions.

$$G_0 = A \cdot f(e) \cdot p_a \left(\frac{\sigma_1}{p_a}\right)^{n_1} \left(\frac{\sigma_3}{p_a}\right)^{n_2} \tag{3.16}$$

Goudarzy et al. (2018) differentiated between the effects of compression expressed by mean stress $(\sigma_1 \cdot \sigma_3)$ and of shear expressed by (σ_1/σ_3) on the maximum shear modulus G_0 and formulated the following relation.

$$G_0 = B \cdot f(e) \cdot p_a \left(\frac{\sigma_1 \cdot \sigma_3}{{p_a}^2}\right)^{n_c} \left(\frac{\sigma_1}{\sigma_3}\right)^{n_d} \tag{3.17}$$

In summary, the relationships can be reformulated as a function of their bases (stress values). The material-specific exponents n, which depend on the respective stress, can be converted into each other accordingly. Thus, Equation (3.17) was used for validation.

3.3.4 Assessment method of aging[4]

The change of the small-strain shear modulus $\Delta G_{0,t} = G_{0,t} - G_{0,t=0}$ was determined at different times t during the creep phases. By setting t = 0 s at the onset of a creep phase just after achieving the given effective mean stress p', the measurement of shear modulus at small strains $G_{0,t}$ was performed at approximately t = 0 s, 60 s, 120 s, 300 s, and subsequent doubling of the measurement intervals. The change in specimen height due to creep deformation and the corresponding change in density was considered when determining $G_{0,t}$ from v_s.

The evaluation method of aging was based on the start-to-start method. Figure 3.15 illustrates the chosen methodology. For the determination of the change of G_0 with time, instead of evaluating Δt_s from the first zero crossing as to be considered as the first arrival time of the shear wave, the second zero crossing was followed since this point could be more clearly identified in the measurements throughout all tests carried out. The time difference Δt between first and second zero crossing (see Figure 3.15) was determined by the measurement at t = 0 s. It was considered as a constant value for all further individual shear wave velocity measurements within the certain creep phases.

[4] The content has been published in Bock et al. (2021)

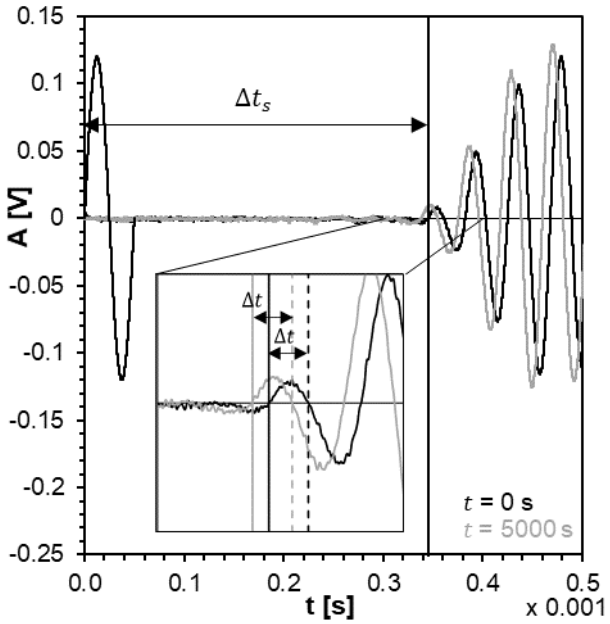

Figure 3.15: Exemplary data illustrating the determination of the shear wave travel time Δt_s with the start-to-start method and illustration of the method for determining $\Delta G_{0,t}$

Anderson and Stokoe (1978) and Schmertmann (1991) assessed the effect of aging on the small-strain stiffness G_0 according to the expression:

$$\frac{G_{0,t}}{G_{0,t=t_{pc}}} = \left[1 + N_G \log\left(\frac{t}{t_{pc}}\right)\right] \quad , \tag{3.18}$$

where N_G is a quantity controlling the intensity of aging and t_{pc} is the end of primary consolidation (EOP) for fine-grained soils or an initialization phase that can be defined independent from consolidation, respectively. The value of t_{pc} is chosen differently in various studies. Equation (3.18) was rearranged for the present study to determine N_G**:**

$$N_G = \frac{G_{0,t=t_2} - G_{0,t=t_1}}{G_{0,t=t_1} \cdot \log\left(\frac{t_2}{t_1}\right)}, \tag{3.19}$$

where t_1 and t_2 represent certain times at which a shear wave velocity measurement was conducted during creep.

3.3.5 Limitations of the assessment of aging based on the shear wave velocity

The limitations of the presented approach to quantify aging can be divided into three main categories: Limitations of the measurement technique based on piezo-electric actuators and sensors, limitations of the evaluation method, and limitations of using the change of the small-strain shear modulus to quantify aging.

3.3.5.1 Limitations of measurement technique based on the piezo-electric actuators and sensors

The quality of the measured signal is crucial for interpreting and evaluating shear wave velocity from the measurements: The more precise and unambiguous the recorded signal, the more straightforward and doubtless the evaluation. Several influences affect the quality of the signal. Table 3.2 gives a summary of influencing factors and exemplary causes.

Table 3.2: Influencing factors on the quality of shear wave velocity measurement

Influencing factor	Examples
Sensor	• Type of sensor and quality of manufacture, including wiring and connections • Contact between sensor and sample • Alignment of the sensor pair to each other
Generated signal	• Frequency of the signal • Amplitude/signal strength • Shape of the input wave
Soil sample	• State variables such as sample density or pressure state • Sample material (e.g., stiffness, particle characteristics, pore fluid) • Sample dimensions (height, diameter, h/D-ratio)

The limitations given by the different types of piezo-electric actuators and sensors, respectively, such as the simultaneous excitation of P-waves or the spatial propagation, are explained in detail in Chapter 3.3.1.1. Based on the use of BE and ultrasonic devices, the BE were more suitable for the investigated granular materials with grain sizes < 4 mm. One challenge linked to the usage of the ultrasonic sensors was the simultaneous and unavoidable excitation of a P-wave due to the design of the wave actuator. The P-wave could not be clearly separated and hence may have influenced the interpretation of the S-wave. Furthermore, the measured signal amplitude was significantly higher when using BE. One reason for this could be the more intense deformation of the BE compared to the ultrasonic device while running both wave actuators at the same maximum amplitude of the exciting voltage signal due to the sensor design, which is associated to a better transmission of the shear wave into the specimen. The contact between the sensor surface and the sample depends on the individual particles arranged directly on the contact surface. Thus, the grain size, grain size distribution, and sample density determine the number of particles in contact. The sensor size should be selected to allow as many grains as possible to transmit the shear wave into the medium, which, for example, contradicts for an increasing sensor size of the BE the aim of as less as possible sample disturbance. The sensor sizes used in this study were specified by the manufacturer and appeared to be appropriate for the investigated material. However, the contact quality differed for each sample, leading to measurement uncertainties. Since the receiver and the transmitter worked with the piezo-electric effect concept, the alignment of the wave actuator and the sensor was crucial to obtain good measurements. In general, the sensors should be aligned in that way that the direction of motion of the piezo-electric crystals is the same. Within the triaxial cell the orientation of the sensor integrated into the base plate determines the orientation of the sensor in the top plate. The orientation was marked at the base plate as well as the top plate so that the actuator and sensor were aligned as precise as possible when the top plate was put on after preparing the sample. Small rotation and eccentricity could not be excluded, which resulted in varying signal quality for the tests on different samples.

Moreover, as well the choice of the type of the signal as given by the amplitude and frequency exciting the wave actuator had a decisive influence on the quality of the measured signal. Concerning the frequency, the influence of the excited P-wave increases with increasing excitation frequency. A phase shift error might be crucial if evaluating using a method based on the time domain. The phase shift and hence the error plays a significant role when choosing a frequency close to or higher than

the resonance frequency of the emitter-receiver-soil system. Therefore, it is advisable to use frequencies that overcome the near-field effect but are lower than the resonance frequency of the system. The exciting frequencies used by this study were selected based on pre-tests and showed in agreement to the literature comparably good results.

The signal amplitude controls the intensity of the deformation of the piezo-electric ceramic, i.e., the higher the maximum value of the generated signal, the greater the deformation of the element and the better the signal quality. However, the shear strain should remain in a range < 10^{-5} to measure the maximum shear modulus. As already mentioned, the setup provided an amplitude limited to a voltage of 12 V by the signal generator. This limited the magnitude of movement at the actuator but on the other hand ensured the measurement of the shear modulus at small strains. Following the literature (e.g. Yamashita, Fujiwara et al., 2009), amplitudes up to 50 V are used for soils enhancing the amplitude of the recorded waves and improving the procedure of evaluating but may disturb the sample close to the sensor, e.g. introducing a rearrangement of the particles.

In addition, the sinusoidal burst and its jerk acceleration at the beginning and end is associated with inducing waves of considerably high frequencies that affected the signal by superposition. Instead, at the current state of knowledge, it seems to be better to use other characteristics of exciting input functions. The so-called chap-function and ond-function avoid jerk acceleration and are shown as examples in Figure 3.16.

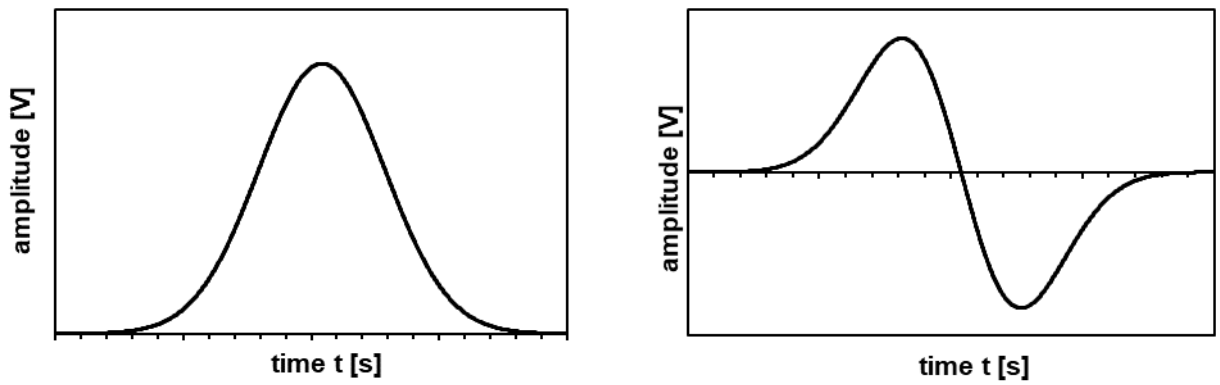

Figure 3.16: Examples for input functions reducing negative impact of high frequencies (a) chap-function and (b) ond-function

Regarding the purpose to measure signals that are well evaluable, the performance of the signal generator is of great importance. The generator should be able to generate the desired excitation signal in form and frequency with high reproducibility. The study used the Arbitrary Waveform Generator from TiePie. The manufacturer gives an accuracy of 0.4 % and a resolution of 12-bit. For comparing the target signal to be used for exciting the wave as given by a mathematical function, the electrical signal of the wave form generator was measured by the oscilloscope. In principle, a good match could be found here. However, a deformation measurement of the transmitter, e.g., through laser Doppler anemometry or interferometers such as done by Liu et al. (2022), was not carried out.

Large sample sizes were advantageous to be able to measure creep deformation in granular samples as precisely as possible because the expected strain is minimal compared to creep in fine-grained soils. The opposite holds for the shear wave velocity measurement: A significant sample height reduces the signal quality due to the superposition of S- and P-waves and reflected and refracted waves at the boundaries casing the effect of a so-called guided wave. Therefore, a small h/D-ratio would have provided a signal strength, that may have been easier to be evaluated, but this conflicted with the requirement for large samples to ensure the measurement of creep strain using conventional displacement transducers.

The state variables and material properties of the specimen influence the characteristics of the signal transmission. With increasing density, increasing effective pressure, and increasing particle stiffness and accordingly, stiffness at the particle contact, better signal transmission and lower attenuation of the signal can be expected due to the increasing number of grain contacts, higher contact forces and stiffness. However, the variation of pressure and density was one of the major subjects in the scope of this thesis.

Furthermore, the pore fluid influences the signal quality. Yamashita, Kawaguchi et al. (2009) identified considerable noise in dry sand samples before the arrival of the shear wave, which was not visible in saturated samples. Additionally, the reverberation time is higher in dry sands.

3.3.5.2 Limitations of the evaluation method to quantify aging

As described in Section 3.3.1.2, evaluating shear wave velocity from the measurements is challenging. Due to the more or less independently from the chosen evaluation methods subjective selection of the time the shear wave arrives at the receiver, the method does not provide doubtless results. In the scope of this research, the concept identifying aging relies on the relative change in the small-strain shear modulus during creep in respect to a reference value defined by the initial shear modulus at the onset of creep. Nevertheless, the measurement of the absolute small-strain shear modulus was verified. By comparing the evaluation using the start-to-start method and the phase-shift-error method in the frequency domain (Section 3.3.3), an uncertainty of G_0 of about 10 % was found. This uncertainty remains for the results of absolute small-strain shear modulus presented in this study.

Furthermore, the relative change of G_0 with time, which corresponds to aging, was determined by following the time-dependent change of the second zero-crossing of the recorded signal. This method was proven to work well as long as the voltage-time signal has not changed its shape during one creep phase. It is assumed that a change in the signal shape corresponds to a change in the travel path of the shear wave through the grain skeleton. Therefore, determining the change in time when the second zero-crossing happens, matching the time of the second-zero crossing for which the initial shear modulus was determined, was no longer possible. Tests where this case occurred, similar to the determination of the initial shear modulus, the first arrival time as well as the time difference Δt to the second zero-crossing was newly defined, and the second zero-crossing was then tracked over time. The use of coda wave analysis might reduce the error caused by the evaluation method. This would need to be verified further.

3.3.5.3 Limitations of the singular emitter-receiver principle for the assessment of aging

The concept that aging can be quantified by the change in shear modulus at small strains based on shear wave velocity measurement using a singular emitter-receiver principle is an assumption whose limitations are explained below. By the term singular, an actuator and a sensor mounted in the axis of the cylindrical specimen allow only an approach where a uniaxial path of the waves needs to be assumed. By doing so, the approach is moreover limited to a certain volume of the specimen and the interpreted stiffness may not be representative to the overall sample. Changes within the sample that may occur along different paths, i.e. in between other boundaries of the specimen particularly regarding the horizontal direction were not considered. Following this and in addition, the governing travel paths corresponding to the "fastest propagation" of the shear wave may change due to restructuring processes during the creep phases, which cannot be assessed by the measuring method applied in the scope of this thesis. In addition, variation of density and particle assembly, hence inhomogeneity of grain contact forces may affect the initial value of $G_{0,t=0}$. Due to the homogenization of particle contact forces with time, the contact force on individual particles forming the propagation path of the shear wave may decrease. In this case, for example, the shear modulus at small strains may get smaller with time compared to the beginning of a creep phase which may be interpreted wrongly as a loss of stiffness.
In summary, the limitations correspond to the assumptions of an element test: The sample of granular particles is assumed to behave like a continuum.

3.4 Quantification of micromechanical processes by acoustic emissions[5]

Acoustic emissions (AE) are mechanical waves generated by the sudden conversion of potential energy to kinetic energy. The AE sensors (or velocity sensors) in contact with the material detect the dynamic motions induced by the waves and convert them into electrical signals. It is widely used for non-destructive material testing (Grosse, 2008). Michlmayr et al. (2012) summarized sources of acoustic emissions in granular materials as follows: friction between grains resulting from rotation and translation, crack propagation within individual particles, buckling of force chains, particle breakage of different intensities at considerably high effective stress and contact maturing at particle surfaces as well as pore water flow. An illustration of the sources of AE in granular materials is given in Figure 3.17.

[5] The content has been published in Bock et al. (2022)

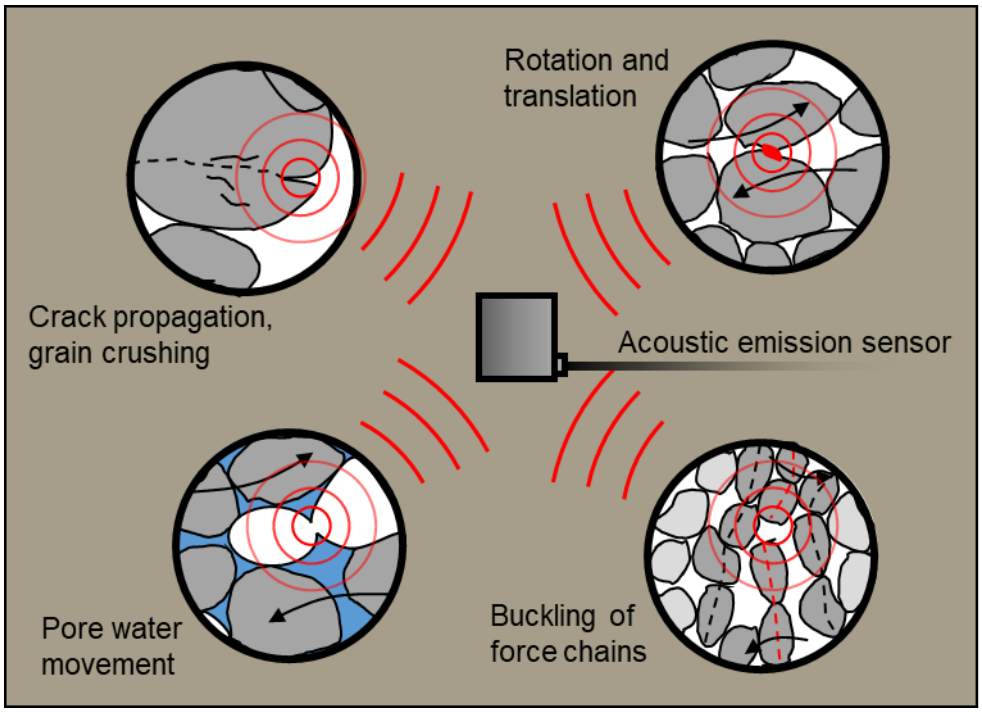

Figure 3.17: Sources of acoustic emissions in granular materials (redrawn and adapted from Michlmayr et al., 2012)

Some of the mechanisms indicated as sources of AE correspond to the time-dependent micromechanical processes during creep listed in Chapter 2. Thus, triggering AEs was seen as a method to provide insight into the micromechanical processes during creep within the sample of granular material. Therefore, in the following, a summary of the general applications of the method in geotechnical engineering and in soil mechanics is given. Furthermore, the measurement technique and settings used in the research are presented, and the limitations of the methods are pointed out. Finally, the basics of the evaluation method are explained.

Review on acoustic emission measurement technique

One application of AE analysis in geotechnical engineering is the continuous monitoring of the stability of slopes of granular material (Koerner et al., 1981; Shiotani & Ohtsu, 1999; Smith et al., 2014). For this purpose, acoustic emissions of a slope are detected using a waveguide that helps to transport the acoustic emissions from the point of generation, in this case, the shear plane within the slope, to the sensor without significant attenuation losses. A waveguide is usually made from a material with low attenuation properties, such as steel (Hardy, 2003). As the acoustic emission rate is directly proportional to the velocity of the slope deformations, continuous control of the slope movement and, thus, a proof of stability of the slope is possible (Smith et al., 2014).

In soil mechanics, AE analysis has already been used to capture the behavior of granular material, i.e. sand, in boundary value problems such as pile penetration (Mao et al., 2015). In addition, element tests such as one-dimensional compression tests (oedometer) and triaxial tests were conducted while measuring the AE of the sample (Koerner et al., 1976; Naderi-Boldaji et al., 2017; Smith & Dixon, 2019). The technology of monitoring AE during shearing and compression tests on granular

material was applied by several researchers. In contrast, the time-dependent micromechanical processes during creep have rarely been monitored by AE analysis so far. Tanaka and Tanimoto (1988) measured acoustic emissions during isotropic and anisotropic consolidation of saturated sand samples from decomposed granite deposits. The authors verified grain movements under constant effective stress due the detection of acoustic emissions. The cumulated number of AE showed a linear trend concerning the time in $\log$ -scale, similar to the time-dependent evolution of strains during creep. Moreover, a linear relationship was observed between the work done by externally applied and measured forces and the cumulated number of AE.

Creep tests under oedometric loading, including the measurement of AE were performed by Brzesowsky et al. (2014). For loading and creep phases at vertical stresses between 14.5 MPa and 30 MPa, the micromechanical processes, in particular grain breakage, were investigated on dry and wet samples of sand with a quartz content > 99 %. The authors found an almost linear relationship between the cumulative number of acoustic emissions and the axial strain, providing evidence of the importance of contact damage and particle breakage to creep. The number of AEs per unit strain was suggested to increase proportionally to the axial stress increase and to decrease with increasing particle diameter by the factor $1/d_{50}$.

In summary, using AE measurement to detect micromechanical mechanisms during creep in granular material is a rather novel methodology. However, some evidence from the literature supported the idea that time-dependent strain change during creep correlates with the cumulated number of AE events (Brzesowsky et al., 2014; Tanaka & Tanimoto, 1988). In contrast to the analysis of structural changes by, e.g., means of X-ray tomography, the measurement of AE is relatively cost-effective. Furthermore, AE analysis offers the possibility of describing qualitatively processes within the whole or at least a large portion of the sample. In contrast, the measurement with X-ray tomography in the required spatial resolution is limited to sample sections.

3.4.1 Experimental setup and evaluation of acoustic emissions

The measurement system for registering the AEs as part of the experiments in the scope of this thesis is mainly made up of the sensor, pre-amplifier, signal processor, software and the settings specifically adjusted. Because of the novel technique in the field of soil mechanics and lack of documentation, an iterative adaption of the components and settings to the material to be examined was required to obtain representative and reproducible results. The sensors for triggering AEs are microphones based on the piezo-electric effects. A sensor of type VS45-H from the company of Vallen Systeme GmbH detected the elastic waves with high sensitivity between 20 kHz and 450 kHz. The peak frequency lies at 280 kHz. The data sheet is provided in Appendix A.1.3. The sensors were mounted at the bottom of the oedometer or triaxial cells to ensure a minimum distance for the AE from the origin within the sample to the sensor. Figure 3.1 (b) and Figure 3.2 (b) illustrate the location of the AE sensors. The sensor had a diameter of 20.3 mm and a height of 22.0 mm. Hot-melt adhesives were used as coupling agents to provide a suitable contact between setup and sensor.

The device of type AEP5 (Vallen Systeme GmbH) pre-amplified the recorded signal. The pre-amplification was processed using a value of 34 dB. An AMSY-6 system of Vallen Systeme GmbH with an

integrated dual-channel signal processor board of type ASIP-2 processed the signal utilizing a sampling rate of 10 MHz for parametric AE-data and 3.333 MHz for full-waveform recording (transient data).

Depending on the objective of the AE measurement, it is sufficient to evaluate and store only specific properties of each AE event that is defined by exceeding a certain amplitude threshold. These properties are, for example, the maximum amplitude, signal duration, or the number of threshold crossings (counts). The method is called a parametric-based evaluation. It was a standard method in the last decades because the power of computers was not yet sufficient to record complete waveforms. In addition, evaluating the records as reduced data is faster and more efficient. With advances in computer technology, it is now possible to record and store continuous waveforms. This method, called transient data recording, can be used for further analysis in the time and frequency domain (Shiotani, 2008). The bias due to the sensor's sensitivity should be considered in this case.
Here, the sampling rate of the parametric AE data was set constant by the used measuring instrument to 10 MHz. This rate also defines the resolution of the arrival time to 100 ns. The sampling rate of the transient signals should be at least two times the maximum frequency of the signals to reconstruct the waveform. This minimum frequency for the sampling rate is based on the Nyquist theorem (Hardy, 2003).

According to

- the expected bandwidth of frequencies resulting from AEs in granular materials (Hardy, 2003; Michlmayr & Or, 2014),
- the sensor sensitivity adjusted to the expected AE-signals and
- the possible settings of the used software for controlling the measuring instruments and data recording,

a digital band-pass filter from 25 kHz to 300 kHz was applied to eliminate the recording of external interfering sources of AE (e.g., ambient vibrations and acoustics, noise of the machine drives).

Prior to the preparation of each sample, pre-tests were performed. In the oedometer, a piece of rubber-type NBR with hardness of shore 70 and in the triaxial cell, a solid dummy made from PTFE were subjected to the test procedure. In addition to background noise, AEs originating from the electromechanically driven loading frame for the oedometer and triaxial setups, and volume and pressure control systems in the case of triaxial tests were measured at similar stress than the actual test series. A value of 3 dB was added to the measured maximum amplitude, as proposed by Vallen (2003).

For oedometer tests, the value was found to be 50 dB. For the triaxial tests, the threshold was determined to be 45 dB. A definite difference of the threshold between minimum and maximum load was not visible. Thus, the amplitude threshold was set constant for measuring AE during all phases of creep during the experiments using the oedometer and triaxial setup. Besides eliminating the background noise, the threshold was necessary to reduce the so-called hit density. If the hit density is too high, so-called hit chains are created that no longer allow the digital time stream to be divided into single hits, because the threshold is no longer undershot. Accordingly, when conducting tests on samples of granular materials, AE events with maximum amplitudes lower than the threshold will not be considered. In contrary, continuous signals of high amplitude may be interpreted and registered

as one AE event. A compromise must be found between the maximum number of hits originating from micromechanical processes in the soil sample and the minimum number of deceptive hits from background noise. The choice of a constant threshold for all creep stresses made it possible to evaluate the influence of applied stresses on the number of AE events.
A so-called rearm time (RAT) and a duration discrimination time (DDT) had to be chosen for the data assessment. The RAT defines when an event ends after it drops below the threshold amplitude. In the case of an echo, a signal can consist of several hits. The DDT defines the minimal time between two hits of a so-called hit cascade. A representation of the defined terms can be found in Figure 3.18.

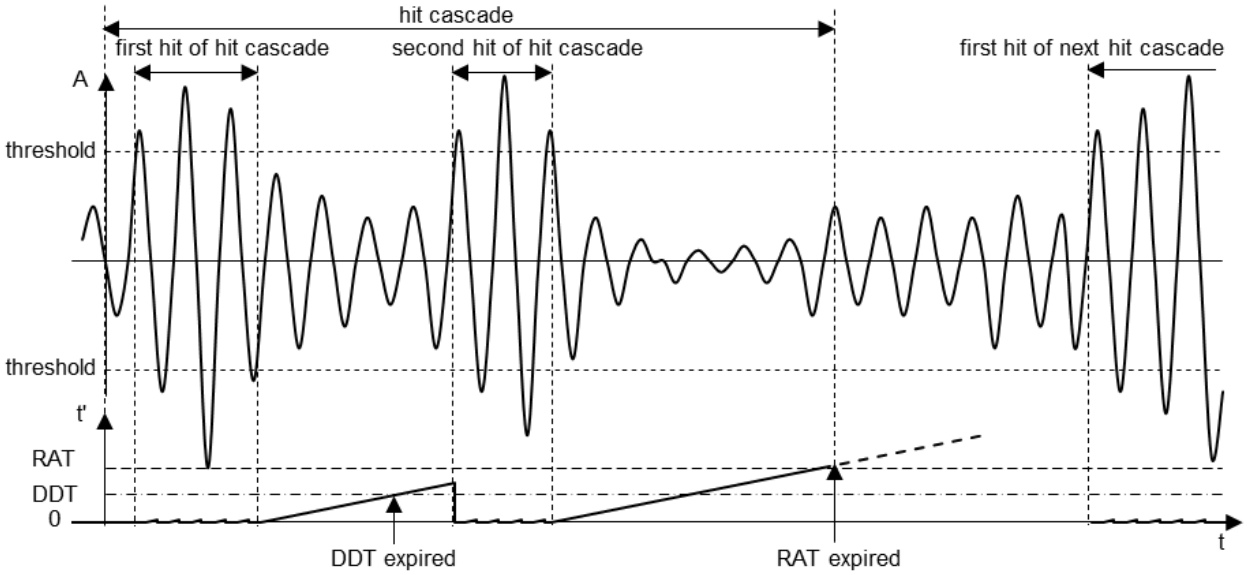

Figure 3.18: Definition of duration discrimination time (DDT), rearm time (RAT) and hit cascade (schematic illustration), modified and redrawn from Vallen Systeme GmbH (2017)

The horizontal axis describes the absolute testing time t. The time t' of the vertical axis describes the time from which the signal falls below the amplitude threshold again. Each hit was interpreted as a separate AE event independent of the signal source by choosing the condition RAT = DDT. Thus, no information was lost by an empirically determined definition. In the case of echoes, two single hits would be measured in a very short time interval and could be filtered out in post-processing. The attenuation of elastic waves in samples of sand was assumed, for example, following the work of Koerner et al. (1976), to be in the range of 1 dB/m to 10 dB/m for frequencies f > 1 kHz. Attenuation is dependent on frequency and applied stresses. Due to the advantage of undistorted data recording, the DDT was chosen to equal the RAT. For materials with high damping, a value between 200 µs and 500 µs should be taken. This range is based on experiences. A general rule is that the greater the damping, the smaller the value. This study's rearm time and duration discrimination time were set to 204.8 µs throughout the research in scope of this thesis. Parametric and transient signals were stored and finally illustrated by the software. The evaluation did not consider signals with durations of less than 30 µs since the number of AE events is of primary interest in this study. Such short signals usually consist of a small number of insignificant threshold crossings or exhibit a singular character of deflection that does not fit the waveform associated with AE events. Therefore, these

signals were not assigned to a separate hit. A summary of the used settings of the measurement systems for oedometer and triaxial tests is given in Table 3.3.

Table 3.3: Summary of settings of AE measurement

Setting	Oedometer tests	Triaxial tests
Pre-amplification	34 dB	
Sampling rate	10 MHz	
Digital band-pass filter	25 kHz to 300 kHz	
Threshold	50 dB	45 dB
RAT = DDT	204.8 µs	

3.4.2 Evaluation method of acoustic emissions

The number of AE events N_{AE} was counted to evaluate the AEs. An AE event was defined as a signal that exceeds the threshold value. In addition, the so-called burst signal energy E was also evaluated, defined by the software producer (Vallen Systeme GmbH, 2017) as the "integral over time of the squared electrical signal within the duration of the burst signal".

$$E = \int_d U^2(t)\ dt, \tag{3.20}$$

where d is the burst signal duration defined as the time between the first and the last threshold crossing, and $U(t)$ is the time-dependent signal voltage of the burst signal. The burst signal energy E has a unit of 1 eu that corresponds to 10^{-14} Vs^2. Using a defined reference resistance of 10 kOhm, 1 eu can be scaled to 10^{-18} J. The burst signal energy E is a measure of the released kinetic energy due to the motion of the grains. E vanishes when internal and external forces are in static equilibrium, i.e., the particles are at rest.

Analogously to the creep coefficient C according to Equation (2.2), a coefficient C_{AE} characterizing the change of AE events with time was defined by

$$N_{AE} - N_{AE,0} = C_{AE} \cdot \ln\frac{t_{ref} + t}{t_{ref}} \quad , \tag{3.21}$$

where N_{AE} represents the cumulative number of detected AE events at time t and $N_{AE,0}$ the cumulative number of AE events at the beginning of the creep phase, respectively. Equation (3.21) is presented schematically in Figure 3.19 with respect to (a) time t and (b) time t in ln-scale.

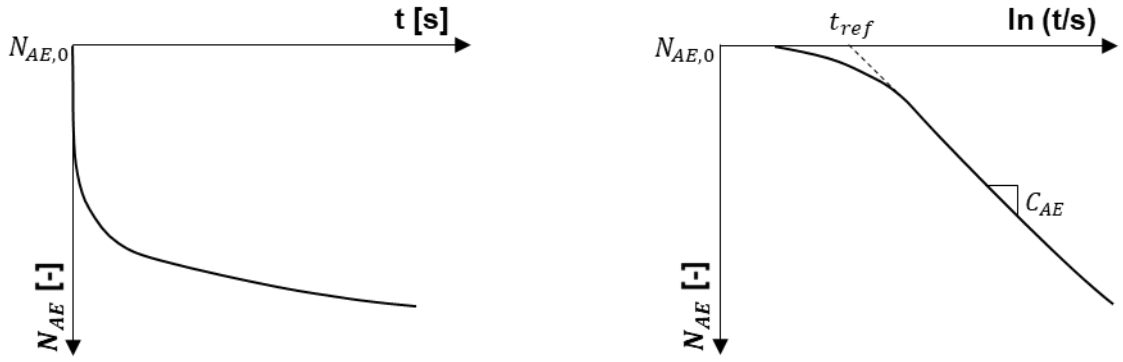

(a) **(b)**

Figure 3.19: (a) Natural trend of number of AE-events N_{AE} with time t; (b) Definition of the coefficient C_{AE} describing the development of the number of AE events N_{AE} with time t in ln-scale during creep

3.4.3 Limitations of the acoustic emission method

The analysis of AEs is strongly influenced by the principles and capabilities of the applied measuring instruments (i.e., type of sensor, amplification, and possibilities of signal filtering), the sample size, and the user-defined control parameters.

For example, the threshold must be carefully chosen by pre-tests to reduce the influence of noise from the loading actuator and environment. Choosing a constant amplitude threshold value independent of the axial stress influences the registered cumulative number of AE events N_{AE}. Furthermore, the detected number of AE events and the signal burst energy strongly depend on the distance between the sensor and the AE source and the material damping. Therefore, depending on the sample size and effective pressure, the AE-sensors capture probably only a fraction of the AE events occurring in the whole sample. For the relatively small samples examined by oedometer tests, it is assumed that the acoustic emissions could be recorded entirely. This assumption is more uncertain for the triaxial tests where large samples were examined. For this reason, only a qualitative comparison of mechanical quantities ε_a and $\Delta G_{0,t}/G_{0,t=0}$ with the AE-quantities N_{AE} and E was possible.

Finally, in the presented experiments, the used sensor was characterized by a relatively wide sensitivity range between 20 kHz and 450 kHz. Despite this, the measured frequency content of each signal rising from an AE was still limited because of the intrinsic bias of the sensor (sensitivity curve, see Appendix A.1.3). Particularly transient signals should, therefore, always be evaluated with great care.

4. Experimental investigation of creep and aging

An extensive experimental study was carried out on samples of Cuxhaven sand and corundum to determine the relationship between aging and creep. The experimental program included oedometer tests and triaxial tests. The specimens were prepared using the dry funnel method and air pluviation. A sand pluviating device was designed exclusively for this purpose. Oedometer tests were used to investigate the one-dimensional compression behavior and to validate the AE method. The consolidated, drained, isotropic compression tests with isotropic constant loading and tests with incremental loading, including creep phases, investigated the aging behavior and creep behavior at different confining stresses and different initial densities of the samples. The comparison of the two test series allowed the evaluation of the dependence on the loading history. Drained triaxial shear tests were used to investigate the strain rate dependence of two granular materials. Furthermore, drained triaxial compression tests with creep phases served to investigate creep and aging under varying deviatoric loading.

4.1 Investigated materials

The experimental investigation includes two materials: Silica sand, taken from a sand quarry near Midlum located on a so-called geest formed by glacial loadings near the city of Cuxhaven, Germany, close to the North Sea and is termed in brief Cuxhaven sand. A second material, corundum, was chosen because of its uniform properties in terms of hardness and its high roundness and sphericity compared to the natural sand.

Table 4.1: Granular properties of Cuxhaven sand and corundum

	Cuxhaven sand	**Corundum**
Particle density and particle strength		
ρ_s [g/m^3]	2.62	3.32
Mohs hardness	6.0 to 7.0	n.d. (specified with > 8.0)
Limit void ratio		
e_{max}	0.75	0.80
e_{min}	0.48	0.59
Grain size distribution		
d_{50} [mm]	0.29	0.89
C_u	2.62	1.32
$C_c{}^*$	1.14	1.00
Particle shape		
Roundness R	0.54	0.87
Sphericity S	0.77	0.80
Roughness S_q [µm]	0.32	0.86

The Cuxhaven sand is of predominately quartz SiO_2 (95 wt. %), which contains traces of albite (3 wt. %) and K-feldspar (2 wt. %). Corundum is an artificial material made of aluminium oxide Al_2O_3 (> 92 wt. %) with proportions of magnesium oxide (< 2.6 wt. %) and calcium oxide (< 2.5 wt. %).

The properties of the granular materials are given in Table 4.1. The grain shape parameters, as well as the particle size distribution, were determined by dynamic image analysis taken by a laser-scanning optical device and compared with the results of the standard sieving method according to DIN EN ISO 17892-4:2017 including additional sieve sizes in the relevant grain size range. The particle size distributions of the uniform and well-graded materials are shown in Figure 4.1 (a).

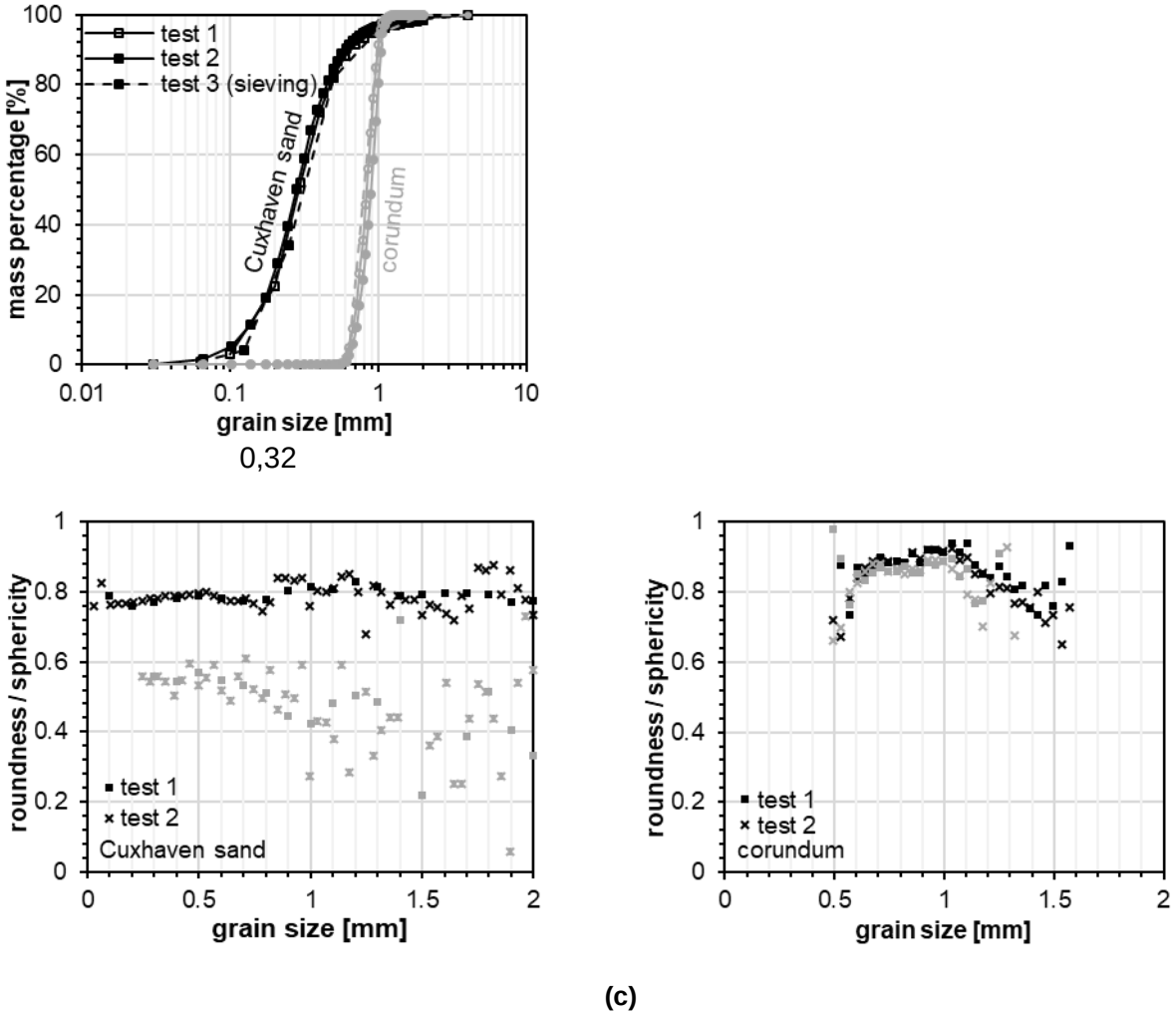

Figure 4.1: (a) Particle size distribution, roudness (gray) and sphericity (black) dependent on the particle size of (b) Cuxhaven sand (c) corundum

Figure 4.1 (b) and (c) present the dependency of roundness and sphericity according to Krumbein and Sloss (1963) on the particle size for the used materials. The roundness and the sphericity were averaged considering the particle size distribution. The values are given representatively in Table 4.1. The surface roughness, measured by a laser-scanning confocal microscope, is described by the two-dimensional parameter S_q. (DIN EN ISO 25178-2:2012)

$$S_q = \sqrt{\frac{1}{A}\iint_A z^2(x,y)dxdy}, \tag{4.1}$$

where A describes the observation area, and z is the height of the surface at positions x and y according to a reference coordinate system. The area of contact between two silica sand grains (Ottawa sand, grain size between 0.6 and 0.84 mm) was illustrated to be in a range of 10 µm by Michalowski et al. (2018). By calculating the theoretical contact area of two spheres (G = 1 GPa, $\nu = 0.2$) with a mean diameter of the Cuxhaven sand, a contact radius of 0.6 µm for 500 kPa and 2.1 µm for 2000 kPa can be estimated. Hence, a Gaussian cut-off filter of 10 µm was used to evaluate the roughness in the scale of the relevant observation of a particle contact which was selected to A = 500 µm^2.

Figure 4.2 illustrates images of the particle shapes taken by a digital microscope, and particle surfaces taken by the microscope for roughness evaluation.

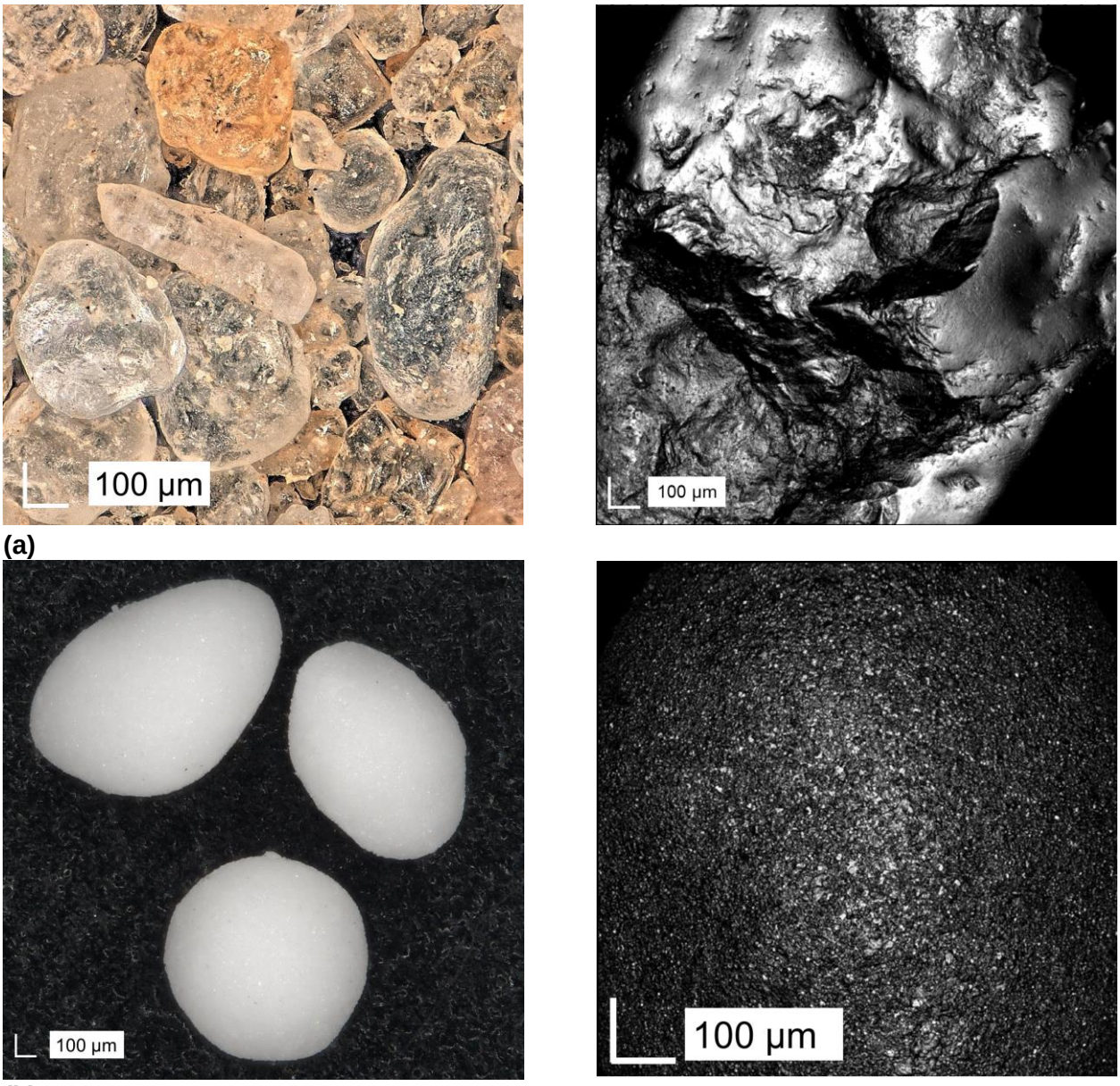

Figure 4.2: Images indicating the particle shape (left side) and surface roughness (right side) of (a) Cuxhaven sand and (b) corundum

4.2 Experimental program

An extensive experimental program has been carried out on cylindrical specimens under multidimensional deformation and stress conditions to determine creep deformations and aging in the two granular materials. Element tests were used to determine the influences of granular properties and state variables on creep, aging, and rate-dependency. A particular challenge was to measure simultaneously creep deformation, rate-dependent behavior, and assess aging effects on comparatively small specimens. Therefore, as described in Section 3.4, the AE measurement method was additionally implemented in the oedometer and triaxial setup. The purpose was, on the one hand, to provide additional information about the micromechanical processes during creep and aging within the specimen and, on the other hand, to be able to detect creep strain beyond the accuracy of conventional deformation transducers.
As the use of AE measurement to detect micromechanical mechanisms during creep in granular materials is rather novel in the field of soil mechanics, an oedometer test series was firstly performed to verify and evaluate the correlation between creep strain and AE.

4.2.1 Oedometer tests[6]

Granular samples were loaded under oedometric conditions at a constant strain rate up to a specific axial stress. This test phase is called loading phase. After a loading phase, the corresponding axial stress was maintained during the so-called creep phase. After a creep time of 24 h, the next test phase was started, and the axial stress was increased at a constant strain rate to the subsequent predefined axial stress that was kept constant over another 24 h. In this way, a so-called multi-stage creep test was carried out, in which the creep phases were performed at axial stresses of 300 kPa, 1000 kPa, 3000 kPa, and 6000 kPa. For the selected stresses, damage at the particle contacts and fracture of asperities occurred, while comprehensive particle breakage was assumed to happen only occasionally. AE were measured continuously throughout the whole test – nevertheless, only the AEs during the creep phases were analyzed for this study. Table 4.2 shows the prescribed and resulting stress and strain rates during the loading and creep phases. With the available experimental setup, radial stress and radial stress rate measurements were not possible.

Table 4.2: Prescribed and resulting stress and strain rates for the loading and creep phase in oedometer testing

Phase of test	Variable	Prescribed conditions	Resulting stress and strain rates	
			Measured	Not measured
Loading phase	Axial stress rate $\dot{\sigma}_a$		$\dot{\sigma}_a \neq 0$	
	Radial stress rate $\dot{\sigma}_r$			$\dot{\sigma}_r \neq 0$
	Axial strain rate $\dot{\varepsilon}_a$	$\dot{\varepsilon}_a \neq 0$		
	Radial strain rate $\dot{\varepsilon}_r$	$\dot{\varepsilon}_r \approx 0$		
Creep phase	Axial stress rate $\dot{\sigma}_a$	$\dot{\sigma}_a = 0$		
	Radial stress rate $\dot{\sigma}_r$			$\dot{\sigma}_r \neq 0$
	Axial strain rate $\dot{\varepsilon}_a$		$\dot{\varepsilon}_a \neq 0$	
	Radial strain rate $\dot{\varepsilon}_r$	$\dot{\varepsilon}_r \approx 0$		

[6] The content has been published in Bock et al. (2022)

Different axial strain rates of $\dot{\varepsilon}_a$ = 0.01 %/min, 0.05 %/min, and 0.5 %/min during the loading phases were investigated. This variation allowed determining the influence of loading strain rate on the strain rate and the rate of AE events during creep.

4.2.2 Triaxial tests

The triaxial tests performed in this study are summarized in Table 4.3. The test procedures are described in detail in the following.

Table 4.3: Summary of performed triaxial tests

Type	Aim	Abbr.	Description
Consolidated drained isotropic compression tests	Stress and density dependent creep and aging behavior at isotropic compression	ICL-C	„Isotropic Constant Loading – Creep“, constant isotropic loading and subsequent creep phases over a period of at least 5 days
		IIL-C	„Isotropic Incremental Loading – Creep“, incrementally isotropic loading with subsequent creep phases over a period of at least 5 days
Drained triaxial compression tests	Rate dependent deformation behavior; dependence of q_{max} of the strain rate	CRS	„Constant Rate of Strain“, specimens were loaded by a constant axial strain rate at constant cell pressure
	Stress-dependent creep behavior and aging at different deviatoric loading	CRS-C	„Constant Rate of Strain – Creep”, specimens were loaded by a constant anisotropic strain rate with subsequent creep phases of at least 5 days at different deviatoric stresses of 0.2 q_{max} and 0.9 q_{max} at constant cell pressure

4.2.2.1 Consolidated drained isotropic compression tests ICL-C and IIL-C[7]

Isotropic compression tests on dry granular specimens were performed to investigate the stress and density-dependent creep and aging behavior under isotropic loading. Furthermore, to investigate the influence of previous creep phases on the posterior creep and aging of the samples, the two test procedures illustrated schematically in Figure 4.3 were used. For the isotropic constant loading – creep test (ICL-C), samples were firstly loaded by a constant isotropic loading rate of 100 kPa/min up to an effective mean stress of p' = 1000 kPa and 2000 kPa, respectively, and allowed to creep for at least five days. In the following, the creep phases of ICL-C-tests are also called single-stage creep phases. The incrementally isotropic loading – creep tests (IIL-C) consisted of single- and multi-stage creep phases. In the first stage, the samples were loaded with the same constant isotropic loading rate of 100 kPa/min up to the first stage of creep at p' = 500 kPa, and the pressure was maintained over at least five days (single-stage creep phase). In the second stage, the pressure was increased

[7] The content has been published in Jessen et al. (2023)

to p' = 1000 kPa at the same rate, and a second creep phase for another five days was implemented. Finally, the procedure was repeated for a third stage with a pressure of p' = 2000 kPa.

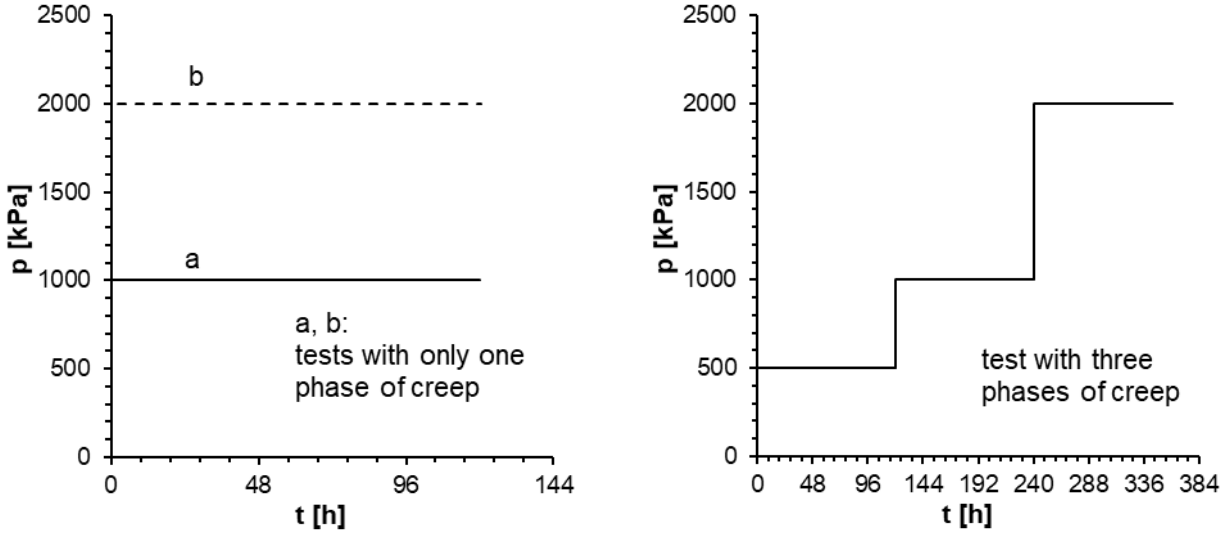

(a) **(b)**

Figure 4.3: Test procedure of (a) ICL-C-tests (single-stage creep phases); (b) IIL-C-tests (multi-stage creep phases and, considering the first phase of creep, single-stage creep phase)

Table 4.4 summarizes the control conditions of the test procedures in the form of pressure and strain rates.

Table 4.4: Prescribed and resulting stress and strain rates for the loading and creep phases of ICL-C and IIL-C-tests

Phase of test	Variable	Prescribed conditions	Measured values
Loading phase	Axial stress rate $\dot{\sigma}_a$	$\dot{\sigma}_a$ = 100 kPa/min	
	Radial stress rate $\dot{\sigma}_r$	$\dot{\sigma}_r$ = 100 kPa/min	
	Axial strain rate $\dot{\varepsilon}_a$		$\dot{\varepsilon}_a \neq 0$
	Radial strain rate $\dot{\varepsilon}_r$		$\dot{\varepsilon}_r \neq 0$
Creep phase	Axial stress rate $\dot{\sigma}_a$	$\dot{\sigma}_a \approx 0$	
	Radial stress rate $\dot{\sigma}_r$	$\dot{\sigma}_r \approx 0$	
	Axial strain rate $\dot{\varepsilon}_a$		$\dot{\varepsilon}_a \neq 0$
	Radial strain rate $\dot{\varepsilon}_r$		$\dot{\varepsilon}_r \neq 0$

During the tests, the AEs were continuously recorded to provide insight into the processes at the microscale, e.g., those resulting from mechanisms at the contact between particles. Furthermore, to determine aging, the change in shear modulus with time was measured at discrete time steps according to Section 3.3.

4.2.2.2 Drained triaxial compression tests CRS

The constant strain rate (CRS) tests aimed to investigate the rate-dependent deformation behavior of granular materials and to identify a possible dependence of shear strength q_{max} on the axial strain rate $\dot{\varepsilon}_a$. The specimens were isotropically loaded at a constant rate of 100 kPa/min to a confining

pressure of 1000 kPa. After 10 minutes of constant isotropic pressure, the samples were sheared with different constant strain rates of up to ε_a = 15 % at constant cell pressure. Three strain rates $\dot{\varepsilon}_a$ = 0.01 %/min, 0.1 %/min, and 1.00 %/min were considered.

An additional test was performed to determine the influence of a sudden change in loading strain rate on the material behavior. The test procedure was similar to the constant strain rate tests. An initial strain rate of 0.1 %/min was chosen, and sudden 10-fold changes in the loading strain rate were implemented.

4.2.2.3 Drained triaxial compression tests with creep phases CRS-C

Constant rate of strain – creep tests were carried out to assess the creep and aging behavior of granular materials under constant deviatoric stress q. Figure 4.4 gives an illustration of the test procedure.

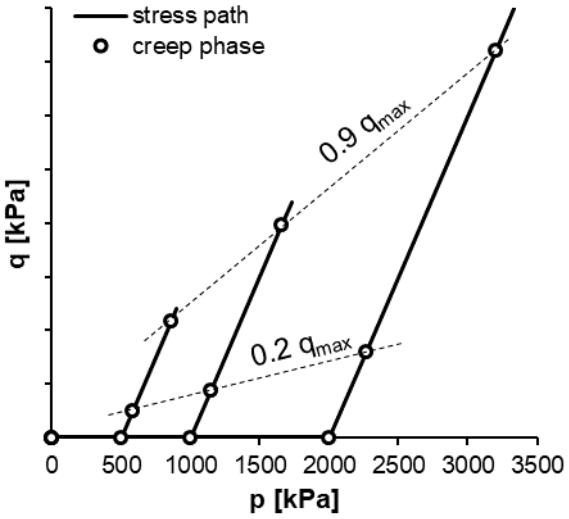

Figure 4.4: Test procedure of CRS-C-tests

In the first phase of the triaxial tests, samples were consolidated at isotropic pressure to p'_0= 500 kPa, 1000 kPa, and 2000 kPa. After 10 minutes of constant isotropic pressure, deviatoric loading was applied by a constant strain rate of $\dot{\varepsilon}_a$ = 0.10 %/min up to a deviatoric stress of 0.2 q_{max}, which was subsequently maintained for at least five days. After this phase of creep, the samples were further loaded with a constant strain rate of $\dot{\varepsilon}_a$ = 0.10 %/min until a deviatoric stress of 0.9 q_{max} was reached. The load was kept constant again for at least five days. Once again, the deviatoric loading was continued until an axial strain of ε_a = 15 % was reached. q_{max} was determined by the conventional drained triaxial compression tests (CRS). During the creep phases, the axial and volumetric creep deformation was measured, and aging was determined by the change of the shear modulus at small strain at certain times t. AEs originating from the granular samples were recorded throughout the test procedure. Table 4.5 summarizes the prescribed and measured stress and strain rates at the described test phases.

Table 4.5: Prescribed and resulting stress and strain rates for the loading and creep phases of CRS-C-tests

Phase of test	Variable	Prescribed conditions	Measured values
Loading phase	Axial stress rate $\dot{\sigma}_a$		$\dot{\sigma}_a \neq 0$
	Radial stress rate $\dot{\sigma}_r$	$\dot{\sigma}_r \approx 0$	
	Axial strain rate $\dot{\varepsilon}_a$	$\dot{\varepsilon}_a$ = 0.10 %/min	
	Radial strain rate $\dot{\varepsilon}_r$		$\dot{\varepsilon}_r \neq 0$
Creep phases at 0.2 q_{max} and 0.9 q_{max}	Axial stress rate $\dot{\sigma}_a$	$\dot{\sigma}_a \approx 0$	
	Radial stress rate $\dot{\sigma}_r$	$\dot{\sigma}_r \approx 0$	
	Axial strain rate $\dot{\varepsilon}_a$		$\dot{\varepsilon}_a \neq 0$
	Radial strain rate $\dot{\varepsilon}_r$		$\dot{\varepsilon}_r \neq 0$

4.3 Sample preparation and repeatability

The presence of water influences the time-dependent behavior of granular materials (Brzesowsky et al., 2014; Ovalle et al., 2015). However, the chemical and biological causes of aging are not the subject of this study. The study of dry granular materials will allow the analyses of predominantly mechanical causes. The samples for the oedometer tests as well as the very loose samples for drained triaxial compression tests were prepared by the dry funnel method. A sand-pluviating device was designed for this purpose to produce the specimens for triaxial testing.

4.3.1 Oedometer tests[8]

As presented in Section 3.1.1, samples with a diameter of 50 mm and an initial height of 15 mm were prepared according to the oedometer dimensions. All specimens were prepared using dry funnel deposition. A steel ruler was used to provide a plane sample surface. The method of dry funnel deposition made it possible to prepare samples of loose relative density of approximately I_D = 0.2. As well samples with a target value of I_D = 0.8 were prepared by dry funnel deposition, including a compaction process by laterally tapping the oedometer ring using a hammer.

To evaluate the reproducibility of the sample preparation, two tests with a loading rate of $\dot{\varepsilon}_a$ = 0.05 %/min and a target value of initial density of I_D = 0.2 were conducted. The loose density for this verification procedure was chosen because a homogeneous and repeatable sample preparation is more challenging for comparably low values of I_D than for dense specimens. Figure 4.5 shows the test results.

[8] The content has been published in Bock et al. (2022)

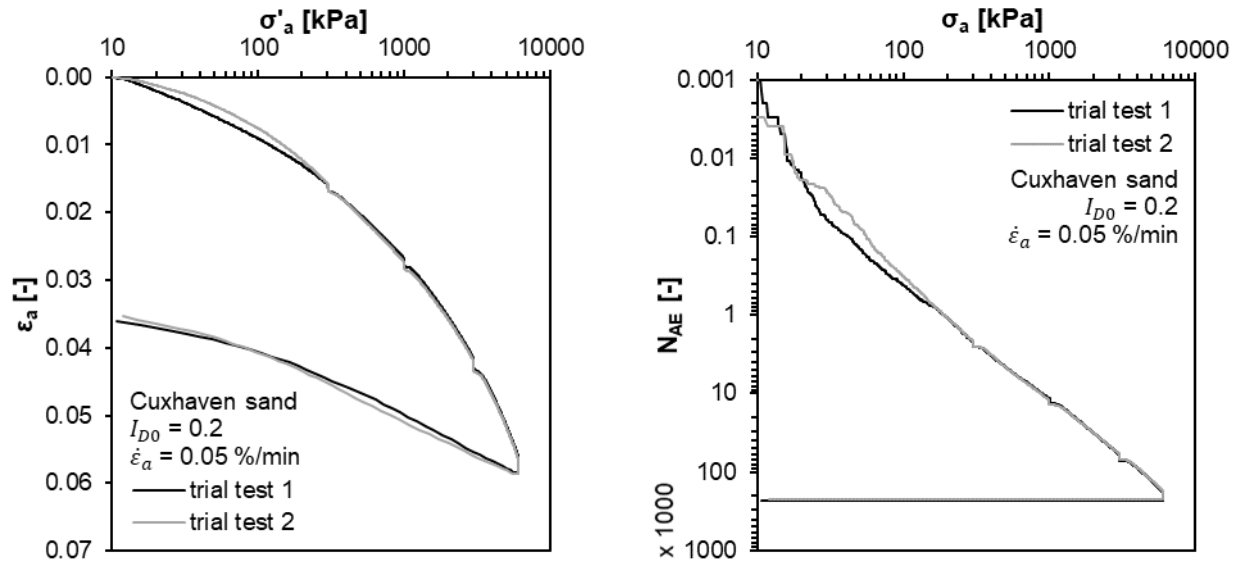

Figure 4.5: Two trial oedometer tests for validating the method of sample preparation comprising loading and creep phases on loose sand of I_D = 0.2 and loading strain rate of $\dot{\varepsilon}_a$ = 0.05 %/min: (a) stress-strain diagram (b) stress-number of AE events diagram

The results of the two trial tests, illustrated by stress-strain curves and stress-number of AE events curves, show minor deviations. Deviations are more pronounced at axial stresses smaller than σ_a = 300 kPa at which the first creep phase was applied. The results demonstrate the reproducibility of the sample preparation method for the oedometer tests.

4.3.2 Triaxial tests

The absolute values of the axial creep strain and correspondingly the strain rates during creep of granular materials are low compared to the strains and strain rates occurring in soft fine-grained and organic soils where the consideration of creep is essential to describe the mechanical behavior comprehensively. Hence, samples with an initial specimen height of 200 mm and diameter of 100 mm were used to improve the measurability of strain changes during creep.

Independent of the sample preparation method, in the scope of this thesis a multi-part specimen mold was developed and built (Figure 4.6 (a)). This mold was used to set up all specimens from granular materials. The dimensions and photos of the specimen mold are given in Appendix A.2.1. After the membrane had been attached to the base of the triaxial cell with O-rings, the specimen mold could be accordingly placed on top of the base plate. The membrane was pulled to the mold using a vacuum, which allowed the initial diameter to be constant over the entire height of the mold, as shown in Figure 4.6 (b). A glued-in grid enabled the homogeneous distribution of the vacuum regarding the complete inner side of the multi-part specimen mold.

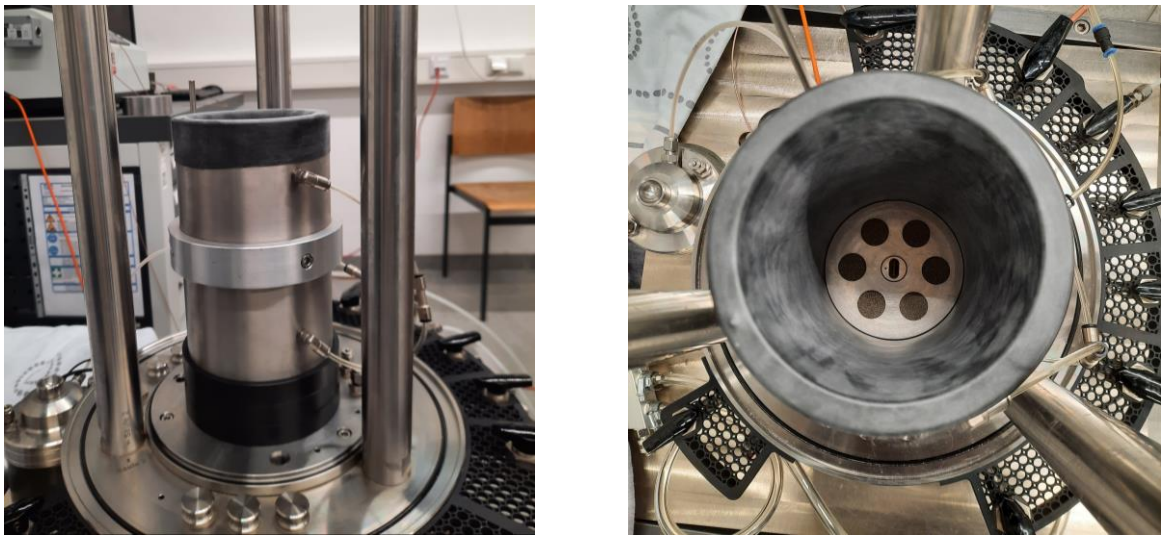

(a) **(b)**

Figure 4.6: (a) Specimen mold for the preparation of samples for the triaxial setup; (b) Pulled butyl membrane along the inner wall of the mold due to vacuum

Different methods are known from the literature to produce axisymmetric samples of granular materials, such as the air pluviation method (Miura & Toki, 1982; Vaid & Negussey, 1984), the slurry deposition method (e.g. Kuerbis & Vaid, 1988), and methods based on tapping compaction by layers (Ladd, 1978; Tatsuoka et al., 1979). In order to prepare homogeneous samples of dry granular materials concerning density, fabric, and grain size distribution that ensure the repeatability of high-quality experiments along with good applicability different sample preparation methods were investigated. Comparing the methods, the air pluviation method using a stationary pluviator, respectively, was chosen to enable a steady material supply. An advantage of the method is that it runs automatically after starting by opening the shutter. Thus, human influence is reduced to a minimum, improving the repeatability.

In the literature, different designs of pluviators were presented (Miura & Toki, 1982; Rad & Tumay, 1987). The basic design consists of a tank, which can be instantaneously opened by a shutter at the base. Depending on the porosity of the opening by, for example, perforated plates, the dry granular material such as sand falls in one or more streams onto the so-called diffuser (usually one or more sieves), which distributes the particles homogeneously over the cross section of the sample. Thus, the sand pluviates into the sample mold. Depending on the design of the pluviator, the drop height, defined by the distance between the last diffusor sieve and the sand surface, varies during the process. If using a fixed diffusor sieve, the falling height reduces because of the rising sample surface within the mold. Height-adjustable devices were used by other researchers but are not well described by the literature and the construction is challenging due to sand trickling out. Within this research, a sand pluviation apparatus was designed to meet the requirements for the sample size of the investigated materials. The apparatus could be directly put on the specimen mold. A labelled plan and a photo of the designed sand pluviator are given in Appendix A.2.2.

The impulse and the kinetic energy of the particles at impact controls the later sample density (Vaid & Negussey, 1984). Thus, two parameters controlling the use of the sand raining device were of

primary interest: drop height and deposition intensity. Firstly, with increasing drop height, the velocity respectively energy of the particles increases, and thus, the specimen density rises. Vaid and Negussey (1984) found that a maximum velocity is reached after a certain drop height depending on the tested material. Preliminary tests were carried out to determine the height at which the achieved density remains almost constant with further increasing falling height. Considering the examined material and boundary conditions, for a drop height exceeding 200 mm, no relevant influence on the density could be determined. Correspondingly, the drop height of the air pluviation device was designed to be at least 307 mm. (Appendix A.2.2). Thus, the influence of drop height on the sample density was not relevant (Vaid & Negussey, 1984). The deposition intensity could vary by using perforated plates with different porosities. Low deposition intensity due to small values of porosity allows the grains to arrange compactly; therefore, dense samples could be achieved. High porosity, which is linked to high deposition intensity, leads in contrast to looser soil samples.

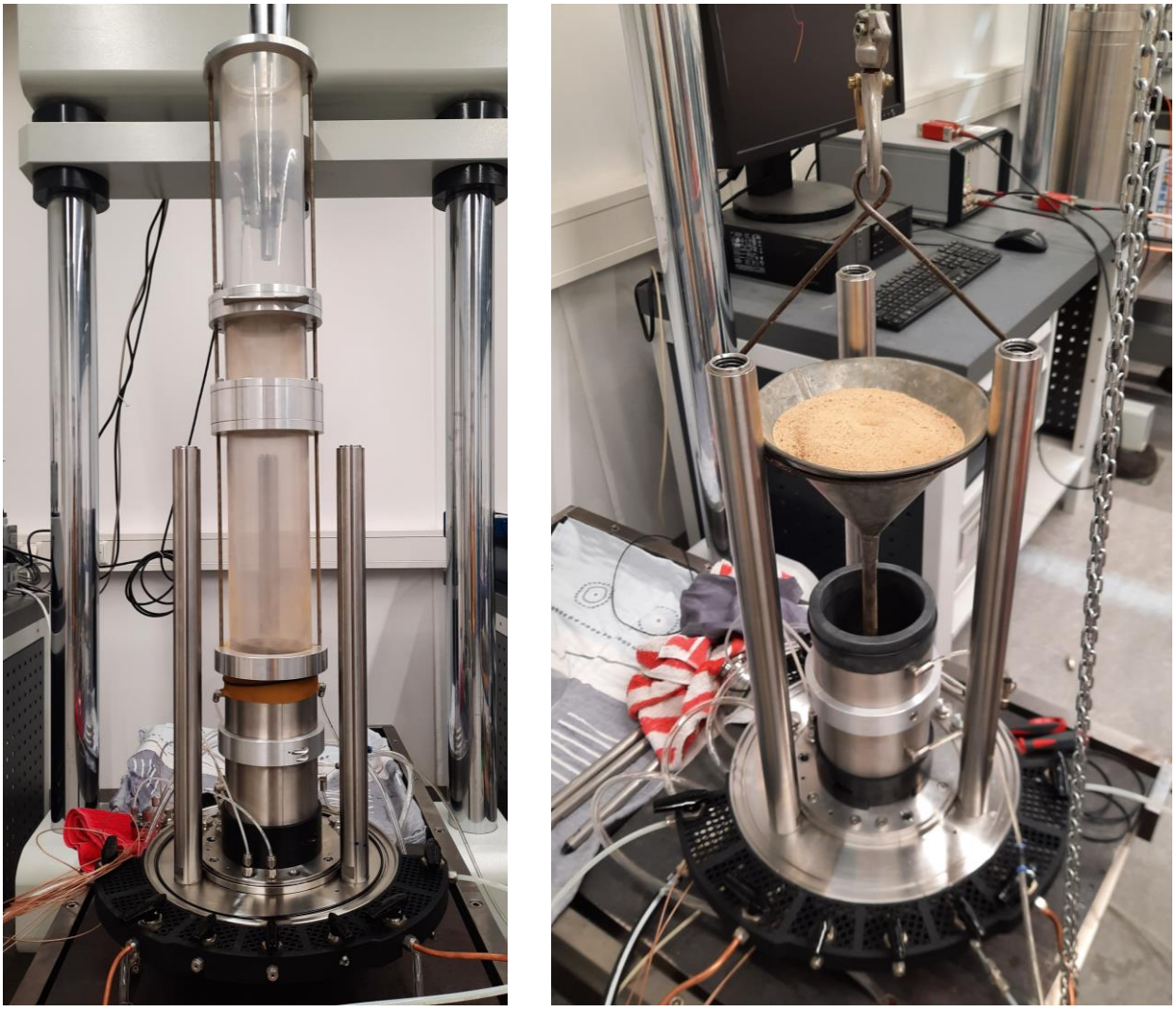

(a) **(b)**

Figure 4.7: Sample preparation by (a) air pluviation and (b) dry funnel deposition method in the triaxial test setup

With the designed air pluviator design, dense to very-dense samples (I_D = 0.75 to 0.91) could be set up using a perforated plate with a porosity of 3 % for Cuxhaven sand and 18 % for corundum. Without a perforated plate (porosity of 100 %), granular samples with a density of I_D = 0.41 to 0.60 were prepared. Figure 4.7 (a) shows a photo of the air pluviation setup placed in the triaxial cell. After the pluviation, the material remaining on the pluviation apparatus was brushed into the specimen mold. The pluviator was removed, and in some cases, additional material had to be added to the mold to fill up the mold until the specimen height of 200 mm was reached. Finally, the surface was smoothed by a metal ruler.

A disadvantage of the used sand pluviator was that only samples with initial densities of medium-dense to very-dense could be prepared. Thus, the dry funnel deposition method had to be used to get samples of loose density. A funnel filled with sand was slowly pulled upwards on a pulley along the surface of the sand, whereby the sand was distributed in the form of a cone in the sample mold until it was filled. A photo of the setup is given in Figure 4.7 (b). The sand surface was finally smoothed with a metal ruler.

After filling the sample mold with the material, the top plate was put on the sample. The vacuum between the sample mold and the membrane was released, and the membrane was pulled over the top plate and fixed with O-rings. Due to the proposed comparably long duration of the test, a minimum number of O-rings of four was necessary to ensure the impermeability considering the flow of cell water at pressures up to 2000 kPa into the sample. The inner diameter of the used O-rings was 70 mm to 80 mm, and the O-ring thickness varied between 3 mm and 4 mm. Before removing the specimen mold, a vacuum in the range of approximately 20 kPa was applied to the sample to guarantee sample stability. The vacuum was removed as an initial cell pressure of p'_0 = 50 kPa was applied. A photo documentation of the steps of the sample preparation method for triaxial tests is shown in Appendix A.2.3.

Lade (2016) defined “the function of the membrane is to transmit a uniform cell pressure onto the soil specimen and to isolate the specimen and its pore fluid and/or pore air from the surrounding pressurized fluid or air in the triaxial cell”. For granular materials and, particularly, at high stresses, problems such as membrane perforation due to grain size and shape, diffusion, and leakage from the cell water into the sample are known. All these effects should be avoided to ensure the membrane function as defined above.

This study used two different membrane materials: In the beginning, widely used natural rubber membranes with a thickness of 1 mm were used. The relatively large thickness was chosen due to the high stresses and long-term experiments. As several problems associated to leakage were noticed, the membrane material was changed and butyl membranes with a thickness of 0.7 mm were used. Butyl rubber membranes ensure low water diffusion, which is especially important for long-term experiments as performed in this research. The butyl membrane is illustrated, for example, in Figure 4.6. Table 4.6 summarizes the characteristics of the used membranes.

Table 4.6: Specification of the used membranes

Material	Diameter	Length	Thickness	Producer	Used for
Natural rubber	100 mm	280 mm	1 mm	PERO GESELLSCHAFT FÜR MESS- UND STEUERTECHNIK mbH	CRS, ICL-C and IIL-C
Butyl rubber	95 mm	280 mm	0.7 mm	REX Gummitechniken GmbH & CO. KG	CRS-C

The sample preparation method for the triaxial tests was validated by drained triaxial compression tests. Three dense samples of Cuxhaven sand (I_D ≈ 0.8) were consolidated at 1000 kPa and sheared with a constant strain rate of $\dot{\varepsilon}_a$ = 0.01 %/min to ε_a = 15 %. Figure 4.8 shows the resulting deviatoric stress-axial strain curves and volumetric strain-axial strain curves.

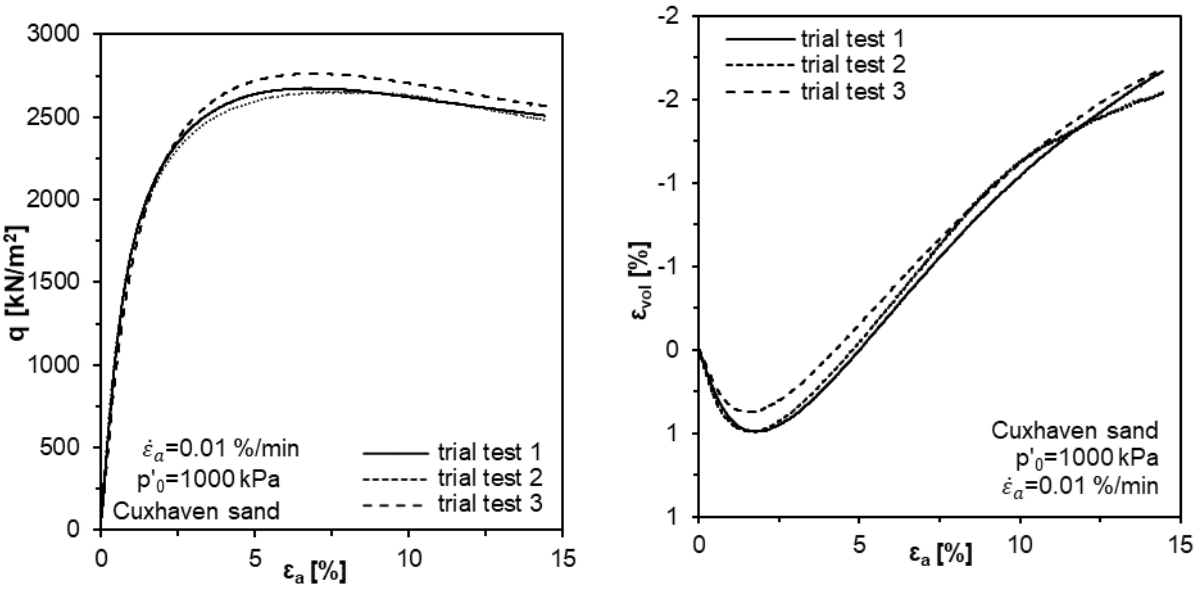

(a) **(b)**

Figure 4.8: Results from trial drained triaxial compression tests for validating the method of sample preparation on Cuxhaven sand with I_D = 0.8 and loading strain rate of $\dot{\varepsilon}_a$ = 0.01 %/min: (a) q-ε_a diagram (b) ε_v-ε_a-diagram

The results of the three trial triaxial tests showed only minor deviations. Therefore, it was concluded that the method is suitable to produce cylindrical specimens from granular materials and that in regard to the sample preparation method reproducible results can be obtained.

4.4 Results and interpretation

The following chapter presents the results of the oedometer and triaxial tests performed. They are first interpreted individually before an overall conclusion is drawn on the combined analysis of creep and aging effect. The investigations considered effective pressures ranging from 300 kPa to 6000 kPa. In this range, which roughly corresponds to common geotechnical boundary-value problems such as CPT and pile foundation, creep is mainly due to the breakage of asperities and abrasion

of the particle surface at the particle contacts. It is assumed that the influence of particle breakage on creep for the investigated materials is negligible in this pressure range.

4.4.1 Oedometer tests[9]

The oedometer test series was carried out on samples of Cuxhaven sand. Figure 4.9 represents the results of the multi-stage creep tests under oedometric conditions using a stress-strain diagram and stress-number of AE events diagram for a loose (I_D = 0.2) and a dense (I_D = 0.8) sample during creep phases lasting for 24 h at σ_a = 300 kPa, 1000 kPa, 3000 kPa, and for the loose sample in addition at σ_a = 6000 kPa.

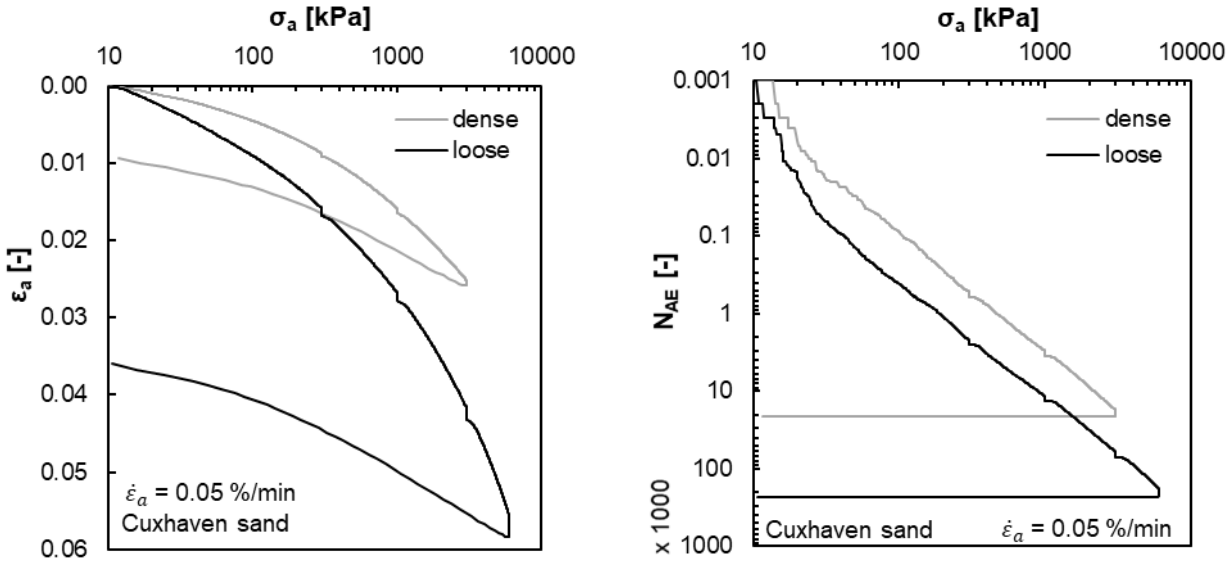

(a) **(b)**

Figure 4.9: Development of (a) axial strain ε_a and (b) number of AE events N_{AE} with axial stress σ_a during oedometer tests comprising loading and creep phases on Cuxhaven sand with a loading strain rate of $\dot{\varepsilon}_a$ = 0.05 %/min and initial relative densities of I_D = 0.2 and 0.8

Figure 4.10 shows the change of axial strain and AEs occurring during the 24 h lasting creep phases for the samples of loose initial density. The results confirm the increase of the strain rate during creep with increasing stress as already reported by e.g., Colliat-Dangus et al. (1988), Mejia et al. (1988), Levin, Vogt, and Cudmani (2019). Likewise, the accumulation of AEs is strongly influenced by axial stress. Micromechanical processes during creep, like particle breakage, particle degradation, and changes at the particle contacts leading to particle rearrangement are highly affected by the energy input, primarily depending on the applied pressure (Lade & Karimpour, 2010).

[9] The content has been published in Bock et al. (2022)

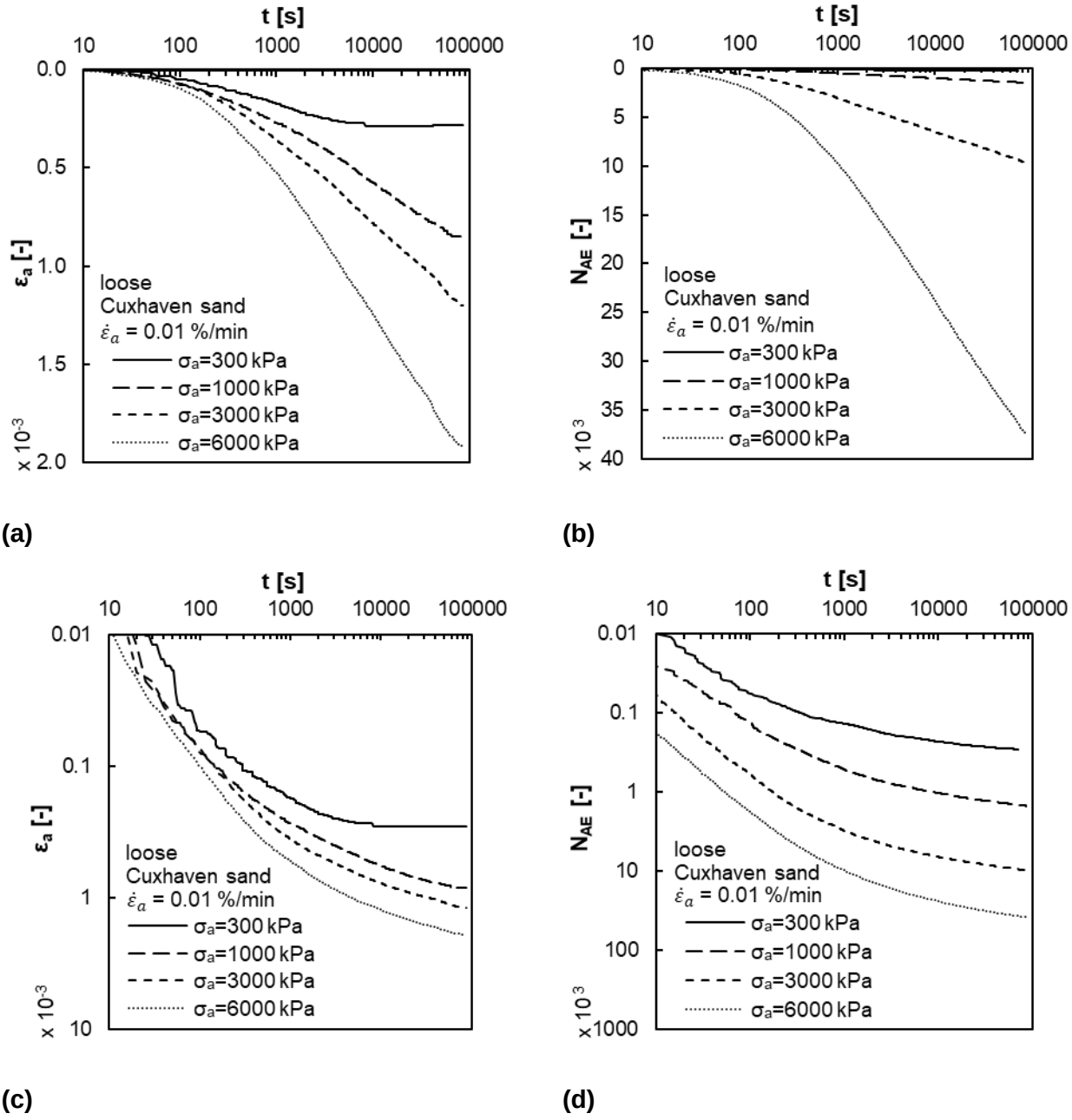

Figure 4.10: Development of axial strain ε_a and number of AE events N_{AE} during creep in a semi-logarithmic (a) and (b) and a double-logarithmic (c) and (d) representation of Cuxhaven sand of loose relative density $I_D = 0.2$ at different axial stress σ_a for a loading strain rate of $\dot{\varepsilon}_a = 0.01$ %/min

After an initialization phase, both the curves showing the axial strain ε_a and the number of AE event N_{AE} approach a linear trend concerning the time in log-scale, hence constant values of C and C_{AE} (Figure 4.10 (a) and (b)).

At an axial stress of σ_a = 300 kPa, creep strains stagnate after approximately t = 10000 s, as shown by Figure 4.10 (a) and (c). However, the cumulative number of AE events still increases beyond t = 10000 s until the end of the 24 h lasting creep phase (Figure 4.10 (d)). The results show that micromechanical processes during creep can be detected using AE measurements even for very

small changes in strain, for which the accuracy of conventional displacement transducers may be insufficient.

In the following, the evaluation for determining a correlation between axial strain and AE events during creep is limited to the analysis of the creep phases at axial stresses of σ_a = 1000 kPa, 3000 kPa, and 6000 kPa. Figure 4.11 shows the evolution of axial strain ε_a and the number of AE events N_{AE} during creep for two different initial relative densities I_D. Lower densities lead to increasing creep strain rates $\dot{\varepsilon}_a$. The same tendency can be observed for the number of AE events: loose samples generate a higher rate of the number of AE events $\dot{N}_{AE}$ during creep than dense samples.

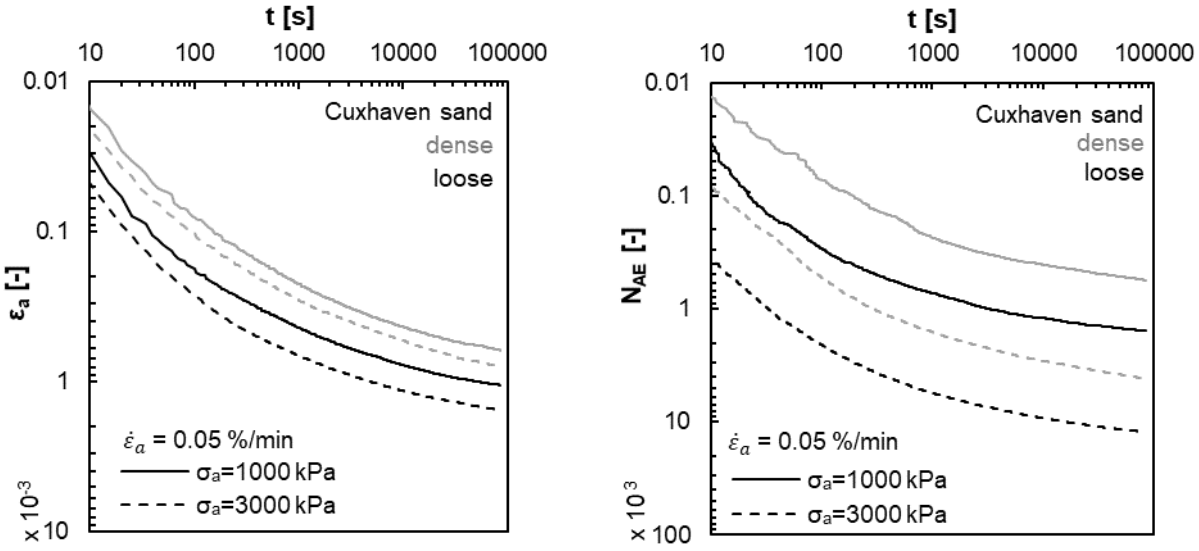

(a) **(b)**

Figure 4.11: Influence of varying initial density; (a) axial strain ε_a and (b) number of AE events N_{AE} during creep at σ_a = 1000 kPa and 3000 kPa for a loading strain rate of $\dot{\varepsilon}_a$ = 0.05 %/min

Karimpour and Lade (2010) and Levin, Cudmani, and Vogt (2019) investigated the influence of loading strain rate on subsequent creep phases. Concluding the results of these publications, the initial strain rate $\dot{\varepsilon}_0$ at the beginning of a creep phase equals the previously applied loading strain rate. The reference time t_{ref} from Equation (2.2) decreases with increasing loading strain rate according to

$$t_{ref} = \frac{C}{\dot{\varepsilon}_0} \quad . \tag{4.2}$$

Therefore, the creep strains after a certain creep time increase with increasing initial loading strain rate. Karimpour and Lade (2010) explained this by the shorter time of the loading phase in which micromechanical events occur at a higher strain rate. Particles within samples comparably slowly loaded rearranged already during the loading phase, leading to a more stable particle assembly at the beginning of the creep phase, resulting in a lower initial strain rate.

The loading strain rate was varied between $\dot{\varepsilon}_a$ = 0.01 %/min, 0.05 %/min, and 0.5 %/min in tests with dense samples of I_D = 0.8 to investigate the influence of the loading strain rate on the number of AE

events. The resulting curves presenting ε_a and N_{AE} measured during creep are shown in Figure 4.12 (a) and (b), respectively.

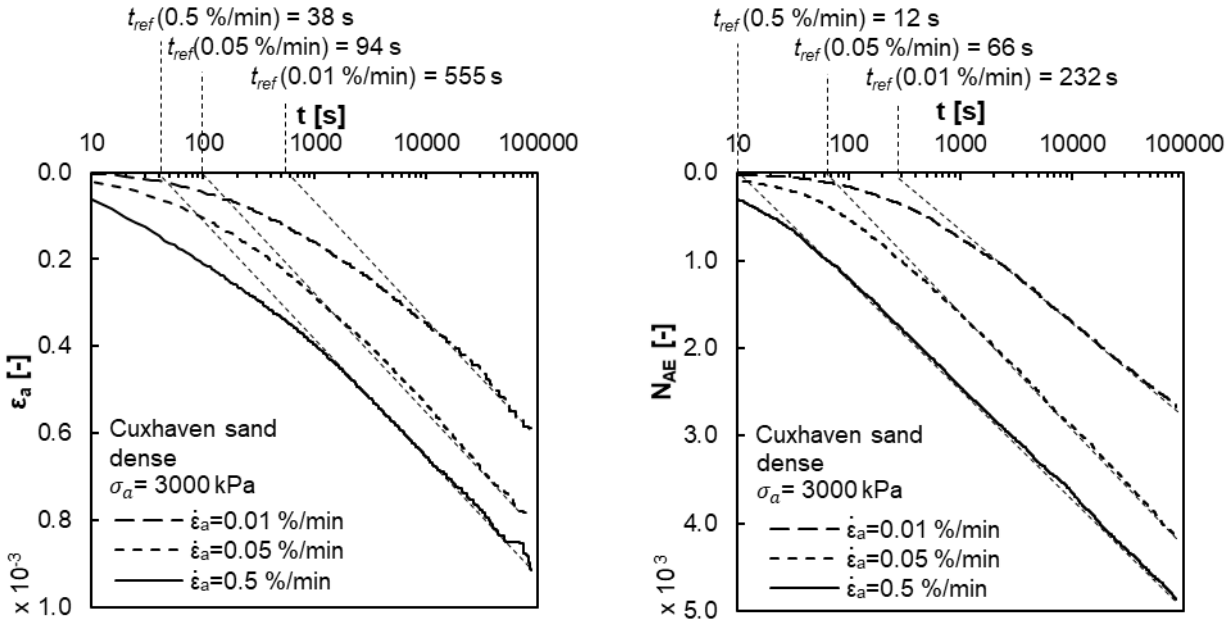

(a) **(b)**

Figure 4.12: Axial strain ε_a (a) and number of AE events N_{AE} (b) during creep at σ_a = 3000 kPa for dense samples at I_D = 0.8 for different loading strain rates $\dot{\varepsilon}_a$

Firstly, the axial strain ε_a during creep follows the same behavior as described by Karimpour and Lade (2010). Moreover, the number of AE events N_{AE} shows higher values at faster loading strain rates $\dot{\varepsilon}_a$. This indicates an increasing number of micromechanical events during the 24 h lasting creep phase with increasing loading rate and confirms the results as given by the literature.

Additionally, like the creep strain, the number of AE events N_{AE} converge towards a linear trend on a logarithmic time scale independent of the loading strain rate. This can also be explained by the decay of micromechanical processes at the particle contacts. At the beginning of the creep phase, AEs occur primarily due to particle rearrangement introduced by particle sliding and rotation as well as buckling of force chains. After major force chains are developed, the particle assembly stabilizes, and static fatigue at the particle contacts becomes the mechanism leading to particle rearrangement (Michalowski et al., 2018), and thus, AE events.

According to Equation (4.2), the reference time t_{ref} depends on the loading strain rate $\dot{\varepsilon}_a$ and the coefficients C and C_{AE}, respectively. At a higher loading rate $\dot{\varepsilon}_a$, the curves of axial strain ε_a and the number of AE events N_{AE} converge comparably fast towards a linear trend concerning the logarithm of time. A constant value of C and C_{AE}, respectively, is reached in a relatively short period.
Using Equations (2.2) and (3.21), the reference times t_{ref} for the creep phases at a stress of σ_a = 3000 kPa and strain rates of $\dot{\varepsilon}_a$ = 0.5 %/min, 0.05 %/min, and 0.01 %/min were calculated. Table 4.7 gives the evaluated values of t_{ref} for both the analysis of the axial strain ε_a and the number of AE events N_{AE} during creep.

Table 4.7: Reference time t_{ref} for creep at $\sigma_a = 3000$ kPa and different loading strain rates $\dot{\varepsilon}_a$ = 0.5 %/min, 0.05 %/min and 0.01 %/min for dense sand samples with an initial relative density of I_D = 0.8

	$\dot{\varepsilon}_a$		
	0.5 %/min	0.05 %/min	0.01 %/min
t_{ref} for ε_a	38 s	94 s	555 s
t_{ref} for N_{AE}	12 s	66 s	232 s

The values of Table 4.7 are in good agreement with the values of t_{ref} that can be determined by drawing a straight line with an inclination of C and C_{AE} respectively according to the recorded data of ε_a and N_{AE} during creep as indicated by Figure 4.12 (a) and (b).

Figure 4.13 (a) shows the development of the coefficient C defined by Equation (2.2) as a function of σ_a. The coefficient C_{AE} defined by Equation (3.21) is presented in Figure 4.13 (b). Figure 4.13 (c) shows the ratio of C/C_{AE}, and Figure 4.13 (d) C versus C_{AE}.

The results show that the influence of the loading strain rate on the coefficients C and C_{AE} at constant initial relative density I_D is negligible. On the contrary, the influence of the initial relative density I_D and the axial stress σ_a on the creep behavior is more significant. Loose samples show higher coefficients C and C_{AE} than dense samples. Both C and C_{AE} increase with increasing axial stress σ_a, but the trends describing this dependency differ for both coefficients. A possible explanation may be the constant value of the amplitude threshold of 50 dB adopted for measuring AE events. Fewer acoustic emissions exceed the amplitude threshold at lower stress σ_a, and fewer AE events N_{AE} are detected than at higher stresses where acoustic emissions reach higher amplitudes. This hypothesis is supported by Fernandes et al. (2010). As already pointed out, the threshold must be set to separate background noise from AE events from the sand samples.

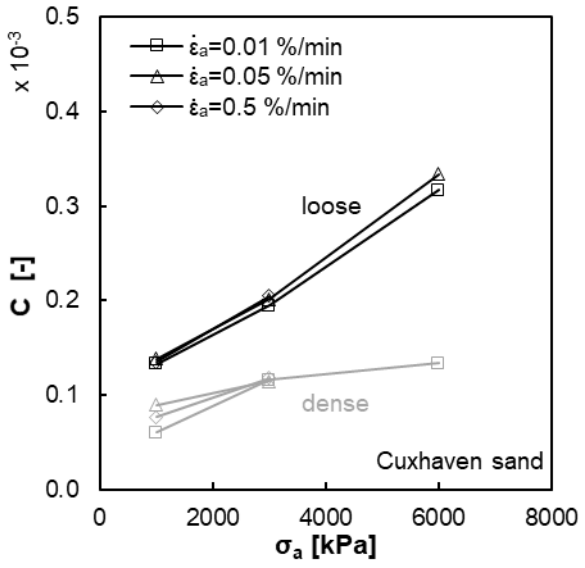

(a)

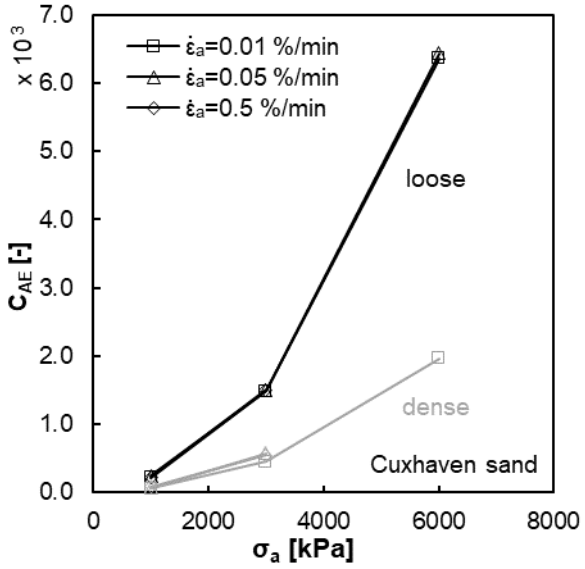

(b)

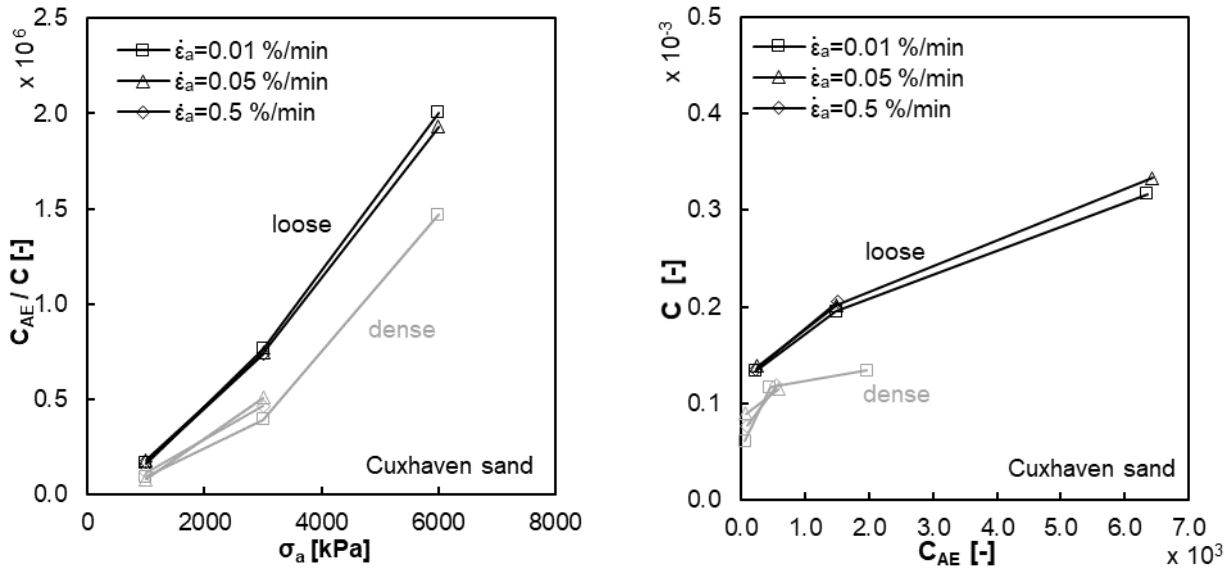

(c) **(d)**

Figure 4.13: (a) Coefficient of the development of axial strain during creep C, (b) coefficient of the development of the number of AE events C_{AE}, (c) ratio C_{AE}/C as a function of the axial stress σ_a, (d) C related to C_{AE} for samples of loose and dense initial relative density I_D = 0.2 and I_D = 0.8 respectively.

The ratio C_{AE}/C increases with rising axial stress σ_a showing the mentioned disproportionality of the two values. The rate of change of the number of AE events, expressed by the coefficient C_{AE}, is increasing faster than the strain rate linked to the coefficient C.

Interestingly, as illustrated by Figure 4.13 (d), at a given coefficient C, the coefficient C_{AE} is much higher for samples of initially high density (I_D = 0.8) than for initially low density (I_D = 0.2). This may indicate that creep strain in samples of low density is driven by particle rearrangement accompanied by AE of low intensity and in contrast, for samples of high density more intense AEs happen to result in the same rate of evolving creep strains.

In Figure 4.14 (a) the axial strain ε_a and the number of AE events N_{AE} during creep are compared at different stress levels. The curves show a stress-dependent proportionality between the strain ε_a and the number of AE events N_{AE}. The relationship is practically unaffected by the initial relative density I_D and strain rate $\dot{\varepsilon}_a$ during the loading phases.
The number of AE events N_{AE} as a function of the work W_S per unit volume according to Equation (4.3) is calculated. For oedometric compression, only the axial stress σ_a and axial strain ε_a have to be considered.

$$W_s = \int \boldsymbol{\sigma} : d\boldsymbol{\varepsilon} = \int \sigma_a \cdot d\varepsilon_a \tag{4.3}$$

Figure 4.14 (b) shows that the comparison between N_{AE} and W_S follows a linear relationship and has a weak dependence on σ_a

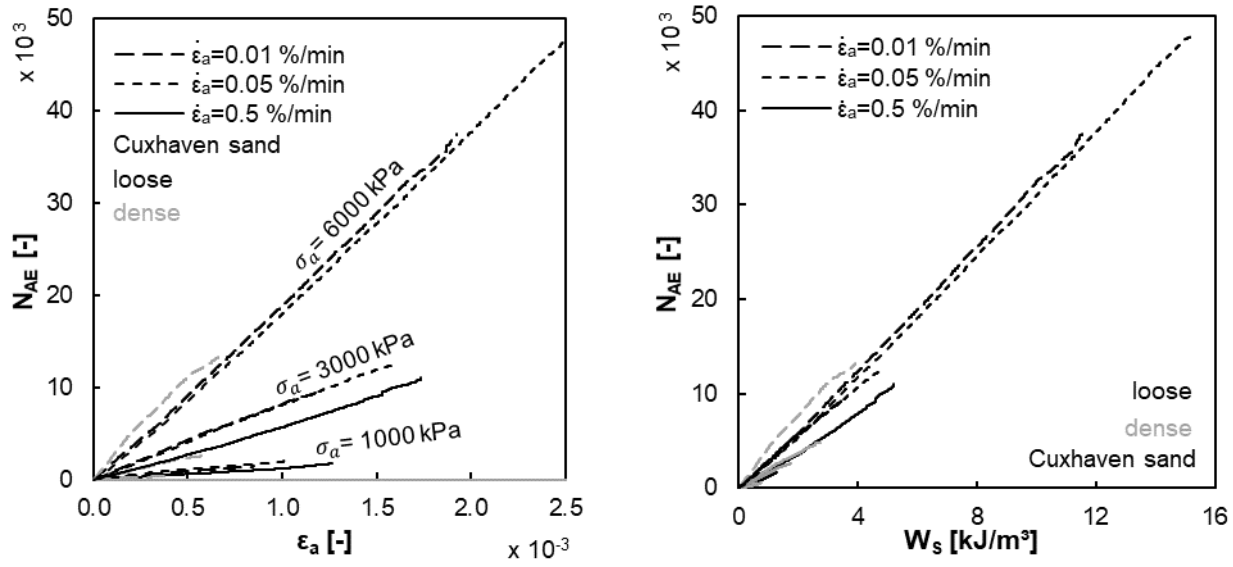

(a) **(b)**

Figure 4.14: (a) Number of AE events N_{AE} depending on the development of axial strain ε_a during creep and (b) AE events N_{AE} with regard to the work W_s; results from tests with varying initial density I_D and strain rate during loading phases $\dot{\varepsilon}_a$

Conclusions

One-dimensional compression tests were carried out on Cuxhaven sand, including strain-controlled loading and creep phases at different axial stresses. Samples with initially loose and dense relative density were tested. During the creep phases, the evolution of the axial strain measured with a displacement transducer and the number of AE events exceeding a certain threshold were evaluated. In agreements with the experimental results of Tanaka and Tanimoto (1988) and Brzesowsky et al. (2014), the number of AE events and the evolution of strain during creep depend on the axial stress and the initial relative density. The axial strain and the number of AE events during creep at different axial stress show a satisfactory correlation between loading strain rates and initial relative densities. Similar to the axial strain, the cumulated number of AE events over the time in log-scale converges to a linear relationship during creep. In analogy to the evolution of strain during creep, governed by a coefficient C, the coefficient C_{AE} characterizes the evolution of the cumulated number of AE events. After a sufficiently long creep time, both C and C_{AE} become independent of the strain rate at the beginning of the creep phase. The density of the samples strongly controls the number of AE events at a given rate of strain. More dense samples emit a much higher rate of AEs at a certain axial strain rate than samples of low initial density. For a certain axial stress, the ratio of axial strains to the cumulated number of AE events during creep can be described as independent from the loading history, hence, the strain rate. The evolution of cumulated number of AE events during creep as a function of the work per unit volume shows a linear relationship almost independent of the initial relative density and the axial stress.

As a general conclusion, the cumulated number of AE events shows a good correlation with the axial strain occurring during creep under oedometric conditions. Moreover, recording micromechanical

events beyond the range of applicability of highly accurate displacement transducers is possible using the measurement of AE. In addition, AE analysis can detect the ongoing micromechanical processes and the resulting particle rearrangements during creep. The oedometer tests confirmed that the methodology of AE measurement can help to understand the fundamental processes involved in creep and aging.

4.4.2 Consolidated drained isotropic compression tests

4.4.2.1 Isotropic Constant Loading – Creep tests ICL-C[10]

In the following, the Isotropic Constant Loading Creep (ICL-C) tests are evaluated concerning creep and aging for Cuxhaven sand and corundum. Different initial densities of the samples and confining pressure, at which creep phases were carried out, were examined. In contrast to the previously described oedometer tests, samples of both, Cuxhaven sand and corundum, were investigated.

Table 4.8 summarizes the initial relative densities I_D and correspondingly the initial void ratios e_0 of the ICL-C-tests. After that, the different initial densities are only referred to as samples of medium-dense and dense or very-dense initial density. The classification refers to the mean values of the tests carried out at varying stresses.

Table 4.8: Initial density of the ICL-C-tests on samples of Cuxhaven sand and corundum

		I_D [-] (e_0 [-])		
Material	**Description**	p' = 500 kPa	p' = 1000 kPa	p' = 2000 kPa
Cuxhaven sand	medium-dense	0.49 (0.62)	0.47 (0.62)	0.51 (0.61)
	dense	0.82 (0.53)	0.89 (0.51)	0.80 (0.53)
Corundum	medium-dense	-	0.51 (0.70)	0.60 (0.68)
	very dense	-	0.90 (0.61)	0.87 (0.62)

Evaluation and validation of the shear modulus $G_{0,t=0}$

As discussed in Chapter 3.3.3, to assess aging, the change of the small-strain shear modulus $\Delta G_{0,t}$ with the time with respect to the initial value $G_{0,t=0}$ was evaluated. Therefore, the initial value $G_{0,t=0}$ determined from the shear wave velocity was first quantitatively validated with the analytical relationship for G_0 of Hardin and Black (1966) (see Equation (3.14)). The calibration parameters of the two investigated materials with respect to Equation (3.14) are summarized in Table 4.9.

Table 4.9: Calibration parameters to describe the dependence of G_0 on the initial pressure and initial void ratio with Equation (3.14) according to Hardin and Black (1966)

Material	x	A	n
Cuxhaven sand	2.17	630	0.46
Corundum	2.17	1240	0.59

Figure 4.15 compares the values of G_0 obtained with Equation (3.16) and the parameters in Table 4.9 and the experimentally determined values of $G_{0,t=0}$.

[10] The results were presented at the 3rd Soil Mechanics Conference of the German Geotechnical Society (Bock et al. (2021))

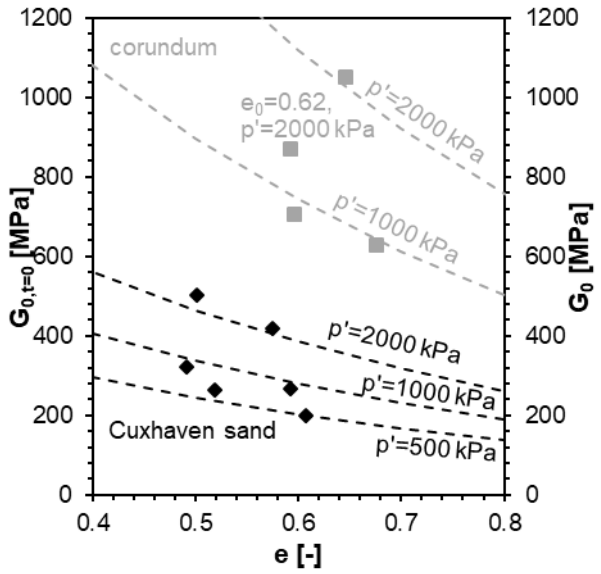

Figure 4.15: Experimentally determined values of $G_{0,t=0}$ from isotropic compression tests on Cuxhaven sand and corundum in comparison to the values of G_0 from Equation (3.16) according to Hardin and Black (1966) with the parameters in Table 4.9

As can be seen, the dependence of the experimental values of $G_{0,t=0}$ on the initial density and the confining pressure can be satisfactory reproduced using Equation (3.14). It is assumed that the experiment on corundum at p' = 2000 kPa and e_0 = 0.62 ($I_{D,0}$ = 0.87) represents an exception, because the measured value of $G_{0,t=0}$ = 872 MPa does not seem plausible. Therefore, the value G_0 = 1136 MPa calculated with Equation (3.14) was used for further evaluation.

Figure 4.16 shows the axial strain ε_a for Cuxhaven sand and corundum for medium-dense, dense, or very-dense specimens and isotropic effective pressures of p' = 500 kPa, 1000 kPa, and 2000 kPa.

Medium-dense samples of Cuxhaven sand show more significant creep strains ε_a after five days than dense soil samples. The creep curves can be approximated with a bilinear function considering a semi-logarithmic scale. The change of the creep coefficient C according to Equation (2.2) occurs after a creep time of approximately t = 1 d. Tendentially the creep strains increase with increasing mean stress p' and decreasing initial density I_D. The creep strains measured from the samples of corundum are significantly lower than those of the samples of Cuxhaven sand. The dependence of the creep strain on the stress and initial density is less pronounced in corundum. After approximately 200 s, the creep coefficient C seems to be constant with increasing time.

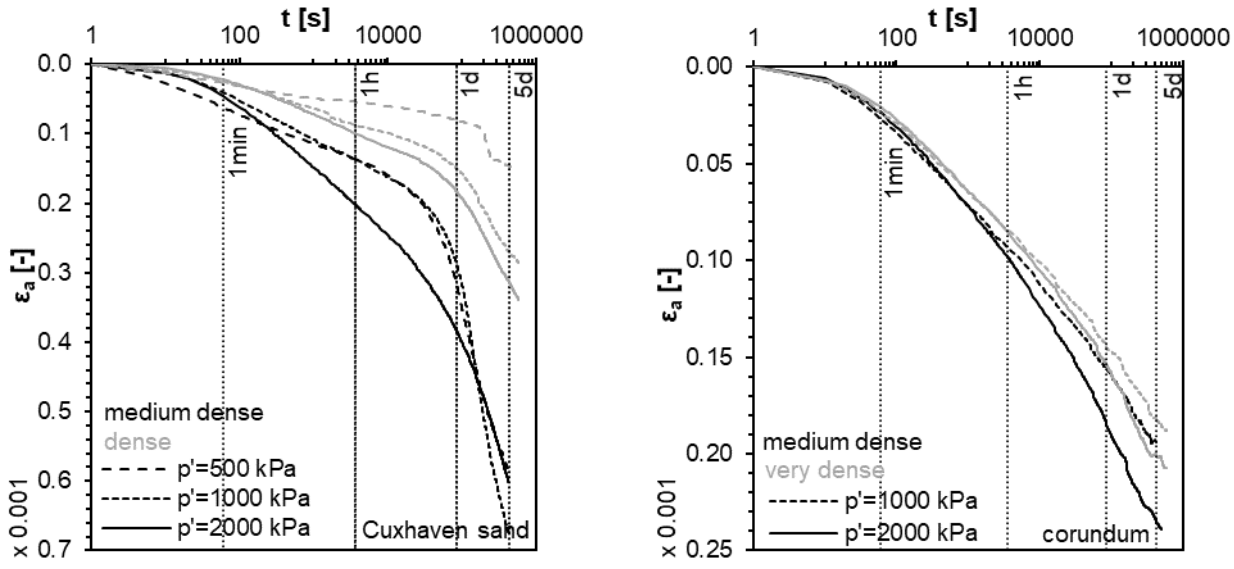

(a) **b)**

Figure 4.16: Axial strain ε_a with t in log scale during single-stage creep phases at isotropic pressures of p' = 500, 1000 and 2000 kPa on medium-dense and dense to very-dense samples of (a) Cuxhaven sand and (b) corundum

The normalized values $\Delta G_0/G_{0,t=0}$ as a function of the time from the onset of creep are shown in Figure 4.17 for Cuxhaven sand and corundum.

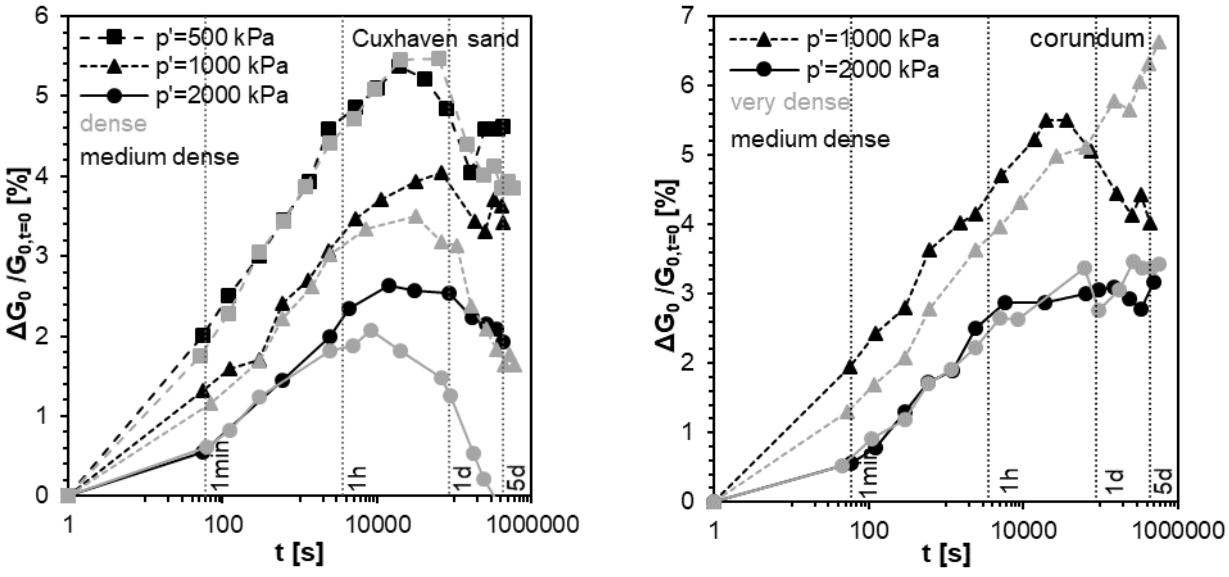

(a) **b)**

Figure 4.17: $\Delta G_{0,t}/G_{0,t=0}$ with t in log-scale during single-stage creep phases at isotropic pressures of p' = 500, 1000 and 2000 kPa on medium-dense and dense to very-dense samples of (a) Cuxhaven sand and (b) corundum

Cuxhaven sand shows, for all tests performed, a linear increase of $\Delta G_0/G_{0,t=0}$ with time in log-scale until a maximum value is reached within the period of one day. After that, the value of $\Delta G_0/G_{0,t=0}$ decreases with increasing time. The decrease is more pronounced for the dense than medium-dense

specimens. With further increasing time, the value of $\Delta G_0/G_{0,t=0}$ for specimens confined to p' = 500 kPa and 1000 kPa remains almost constant at values ranging between $\Delta G_0/G_{0,t=0}$ = 1.7 % (I_D = 0.8 and p' = 1000 kPa) and 4.5 % (I_D = 0.5 and p' = 500 kPa). For the samples of Cuxhaven sand loaded to p' = 2000 kPa, a further decrease of $\Delta G_0/G_{0,t=0}$ is seen even after five days from the onset of creep.

Like Cuxhaven sand, corundum shows a linear increase of $\Delta G_0/G_{0,t=0}$ with t in log-scale. However, for corundum, after an initial increase of $\Delta G_0/G_{0,t=0}$, a reduction of $\Delta G_0/G_{0,t=0}$ is observed only for the mean stress at p' = 1000 kPa and I_D = 0.5. At p' = 2000 kPa, $\Delta G_0/G_{0,t=0}$ seems to stagnate at about 3.0 % to 3.5 % after 1 h. The very-dense sample of corundum, for which the creep phase at a mean stress of p' = 1000 kPa was evaluated, increased almost steadily to a value of $\Delta G_0/G_{0,t=0}$ = 6.5% after five days.

The value of N_G according to Equation (3.19) is shown in Figure 4.18 as a function of the mean stress p'. Here, the rate was evaluated for the linear part of the curve $\Delta G_0/G_{0,t=0}$ versus $\log(t)$ for t_1 = 60 s and t_2 = 10000 s, respectively.

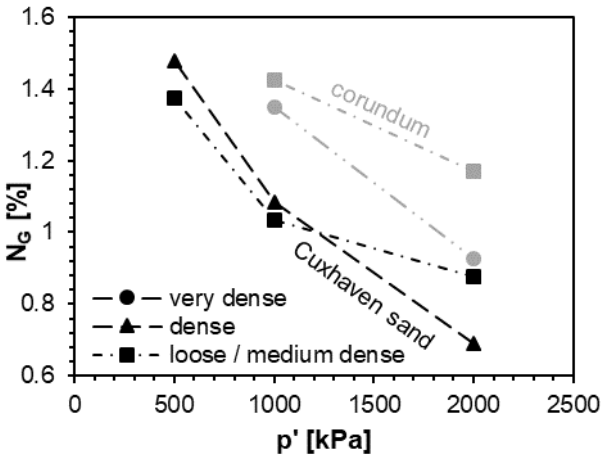

Figure 4.18: N_G versus p' of single-stage creep phases on medium-dense and dense to very-dense samples of Cuxhaven sand and corundum

The initial increase of $\Delta G_0/G_{0,t=0}$ measured in tests on corundum samples is more significant than in tests on Cuxhaven sand samples. N_G or $\Delta G_0/G_{0,t=0}$ show a clear dependence on the mean stress p'. As the mean effective stress p' decreases, N_G increases. No clear dependence of N_G on initial density of the samples was observed in the experiments conducted on samples of medium-dense to dense (for Cuxhaven sand) or very-dense (for corundum) initial densities.

According to the present measurement results, a continuous increase of the shear modulus at small strains $G_{0,t}$ with increasing time during creep cannot be confirmed. The results of the initial increase in $G_{0,t}$ are consistent with the observations of Wang and Tsui (2009) and Gao et al. (2013). So far, a decrease or stagnation of $G_{0,t}$ was only observed by Baxter and Mitchell (2004).

Conclusions

The investigations on aging of Cuxhaven sand and corundum show initially an increase of $\Delta G_0/G_{0,t=0}$ with the time in $\log$-scale during creep under isotopic compression in the range between p' = 500 kPa and 2000 kPa. After a time ranging between 1 h and 1 d from the start of the creep phase, a maximum value of $\Delta G_0/G_{0,t=0}$ is achieved, and then either a continuous decrease of $\Delta G_0/G_{0,t=0}$ or a decrease followed by a stagnation is observed. In addition, some of the tests with corundum show a steady increase of $\Delta G_0/G_{0,t=0}$ during the testing time. The initial changes of $G_{0,t}$ of Cuxhaven sand samples and corundum samples show a dependence on the mean stress p' but practically no dependence on the initial relative density I_D. For sand, the dependence of $\Delta G_0/G_{0,t=0}$ on the density becomes evident only at large confining pressure (p' = 1000 kPa and 2000 kPa) after the maximum value of $\Delta G_0/G_{0,t=0}$. For corundum, the opposite happened, i.e. the dependence of $\Delta G_0/G_{0,t=0}$ on the density was only observed for p' = 1000 kPa.

According to the current state of the art, it is evident that mechanical processes at the level of individual particle contacts strongly influence aging, represented as the change in the small-strain shear modulus G_0. The evolution of creep strain in Cuxhaven sand shows an increase with increasing time, which is caused by delayed particle rearrangement caused by damage at the particle contact surfaces. Even though the mechanisms are very complex, the change of G_0 must be connected to redistributions of contact forces in the granular skeleton. The change of the void ratio in the range of 10^{-4} is negligible and, therefore, cannot be considered as the cause for aging. To better understand the processes happening at the meso- and microscale and the causes of the time-dependent change of the shear modulus at small strains, AEs will be considered for further interpretation.

4.4.2.2 Isotropic Incremental Loading – Creep tests[11]

To investigate the influence of previous creep phases on the development of creep strains, aging and AEs, so-called Isotropic Incremental Loading – Creep (IIL-C) tests were carried out and compared with the results of the isotropic constant loading – creep tests presented in Chapter 4.4.2.1. Consequently, the ICL-C tests and the first stage of the IIL-C test are called single-stage creep tests, and multi-stage creep tests mean the second and third stages of the IIL-C tests. The following results of the single-stage and multi-stage creep tests at mean stresses of p' = 500 kPa, 1000 kPa and 2000 kPa are presented for dense to very-dense samples of Cuxhaven sand. The evaluated quantities are the axial strain, the change in G_0, and the number of AE events during creep phases.

The curves that show the results of the single-stage creep phases are given in black color, and those of the multi-stage creep phases are highlighted in gray color. In addition to the linear representation over time, the logarithmic representation is chosen to visualize the results concisely. Figure 4.19 shows the axial creep strains (a) with time and (b) with time in $\log$-scale.

The experiments on Cuxhaven sand show that the axial strain ε_a during creep increases with isotropic stress, as other researchers already observed, e.g., Kuwano and Jardine (2002) and Lade and Liu (1998). Single-stage creep tests show a higher axial creep strain than creep phases of multi-stage

[11] The content has been published in Jessen et al. (2023).

creep tests characterized by at least one creep phase prior to the evaluated creep phase at similar mean stress p'. Regarding the behavior shown in the $\log(t)$ - ε_a – diagram, the results from the single-stage creep tests show a changing slope with time between 1 h and 1 d following the start of the creep phase, which is not evident for multi-stage creep.

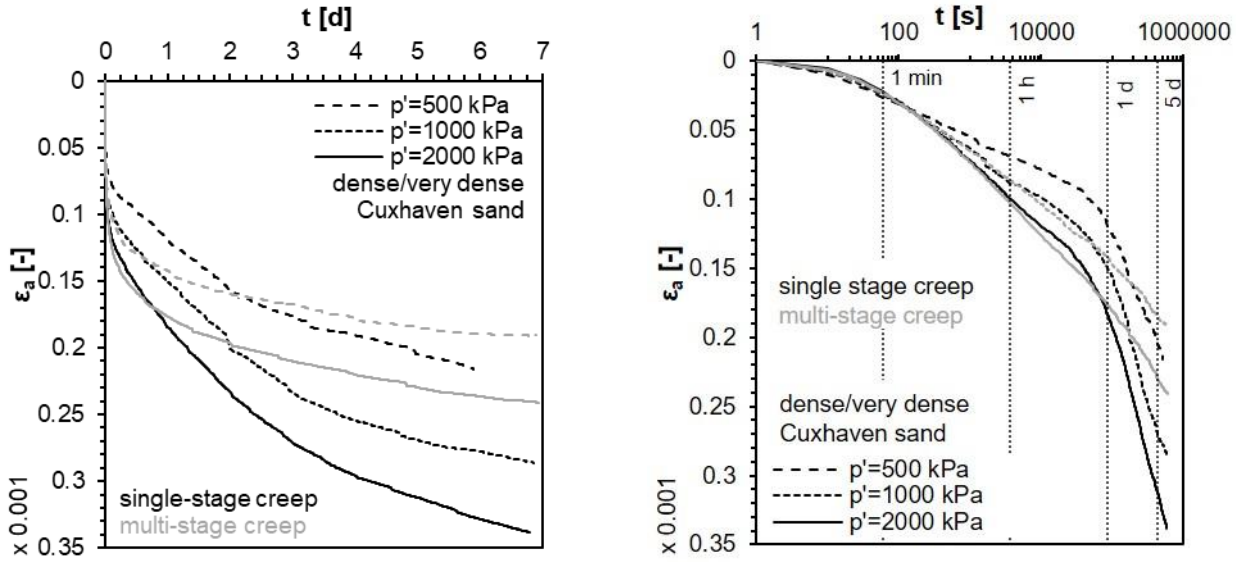

(a) **(b)**

Figure 4.19: Axial strain ε_a of single- and multi-stage creep phases at mean stresses of 500, 1000 and 2000 kPa on dense to very-dense samples of Cuxhaven sand using a (a) linear and (b) logarithmic time scale

The change of the shear modulus $\Delta G_{0,t}$ with time t during creep normalized by the value of $G_{0,t=0}$ as a function of t and $\log(t)$ is shown in Figure 4.20 (a), respectively (b).

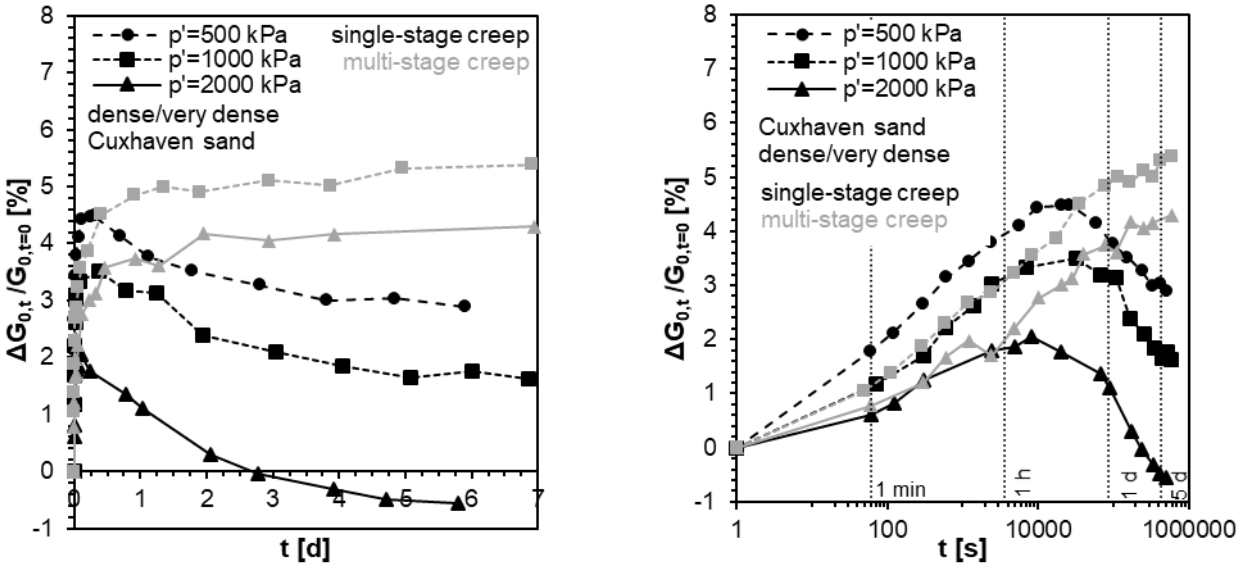

(a) **(b)**

Figure 4.20: $\Delta G_{0,t}/G_{0,t=0}$ of single- and multi-stage creep phases at mean stresses of 500, 1000 and 2000 kPa on dense to very-dense samples of Cuxhaven sand using a (a) linear and (b) logarithmic time scale

Cuxhaven sand showed a nearly linear increase of $\Delta G_{0,t}/G_{0,t=0}$ with $\log(t)$ until a time ranging between 1 h and 1 d. Afterward, $\Delta G_{0,t}/G_{0,t=0}$ reduces with increasing time for the single-stage creep tests. In contrast, G_0 in phases of creep that were conducted after at least one previous creep phase did not show any decrease within five days. As can be seen in Figure 4.20 (b), aging, assessed with $\Delta G_{0,t}/G_{0,t=0}$, increases with decreasing mean stress p', which is mainly due to the initial change of G_0.

Figure 4.21 (a) presents the change of the accumulated number of AE events N_{AE} with time. The number of AE events N_{AE} for samples of Cuxhaven sand increases with mean stress p'; the pressure dependency is significant. Thus, N_{AE} was normalized with the corresponding $N_{AE,max}$ for better comparison of the general behavior and is shown in Figure 4.21 (b) considering the logarithmic time scale. In the $N_{AE}/N_{AE,max}$- $\log(t)$ – diagram, the normalized curves follow a similar trend for all single-stage creep phases but show a different shape for multi-stage creep phases. In general, the evolutions of N_{AE} and ε_a with time for the single- and multi-stage creep phases are qualitatively similar.

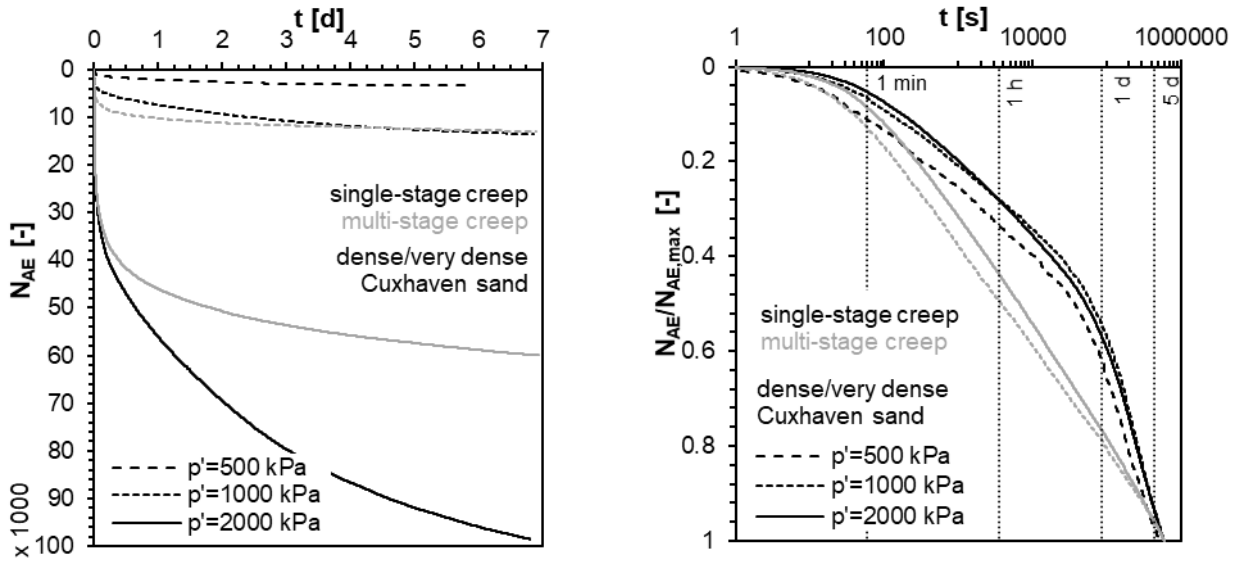

(a) **(b)**

Figure 4.21: Evolution of (a) number of acoustic emissions N_{AE} with time and (b) normalized number of AE events $N_{AE}/N_{AE,max}$ with t in log-scale of single- and multi-stage creep phases at mean stresses of 500, 1000 and 2000 kPa on dense to very-dense samples of Cuxhaven sand

Both, the detected number of AE events and the evaluated signal burst energy, as presented in the following, strongly depend on the distance between the sensor and the source, and on the material damping. Therefore, the AE sensor probably only captured a fraction of the AE events occurring in the sample. For this reason, only a qualitative comparison of the mechanical quantities (ε_a and $\Delta G_{0,t}/G_{0,t=0}$) with the quantities derived from the AE measurement (N_{AE} and E) was possible.

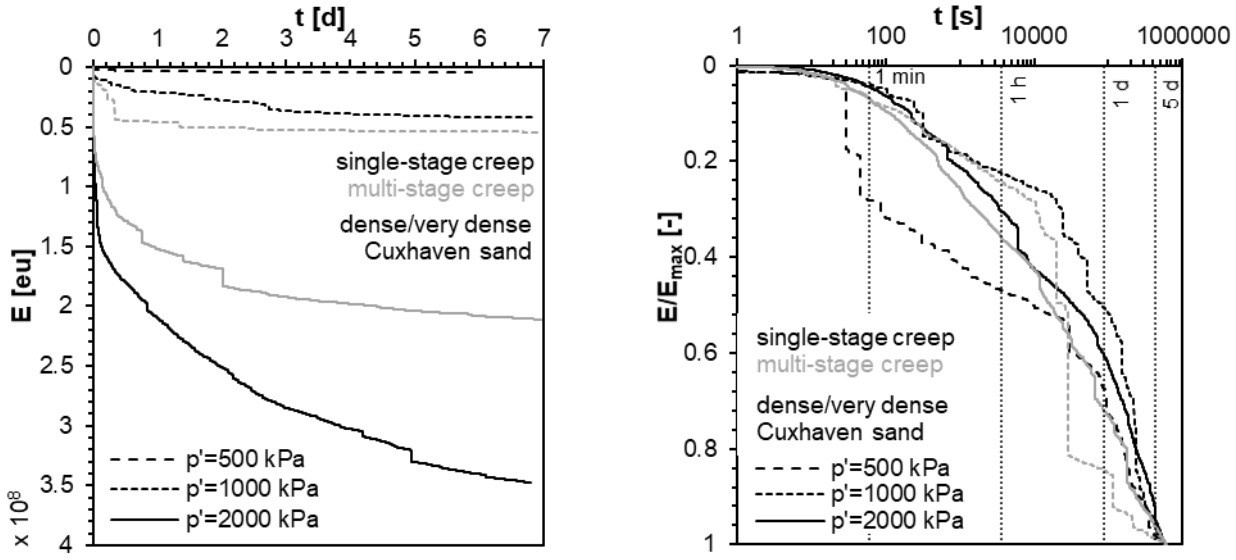

(a) **(b)**

Figure 4.22: Evolution of (a) signal burst energy E with time and (b) normalized signal burst energy E/E_{max} vs. t in log-scale of single- and multi-stage creep phases at mean stresses of 500, 1000 and 2000 kPa on dense to very-dense samples of Cuxhaven sand

Figure 4.22 (a) shows the evolution of the accumulated signal burst energy E with time. Corresponding to the number of AE events N_{AE}, E increases significantly with increasing mean stress p'. The time-dependent change of E normalized to E_{max} considering a logarithmically scaled axis of time is presented in Figure 4.22 (b). The signal burst energy E evolves stepwise with time during creep, and the magnitude of the sudden energy releases varies over time.

In Figure 4.23 the number of AE events (ordinate) exceeding a specific energy value E (abscise) is plotted using a double logarithmic scale, as commonly in the field of seismology. It shows the relationship between the number of seismic events and their magnitude, which is proportional to the logarithm of the energy release during a seismic event. Even if boundary conditions of earthquakes do not match the triaxial testing boundary conditions, events with low energy emissions (low magnitude) are more frequent than events with significant energy emissions (large magnitude). This corresponds to the characteristic of seismic events. For E > 1000 eu, the relationship between N_{AE} and E is approximately described by

$$\log(N_{AE}) = b - a \cdot \log(E), \tag{4.4}$$

which is the empirical Gutenberg-Richter's relationship between the number of seismic events N exceeding a given magnitude and the magnitude of earthquakes M. The intercept b is generally pressure- and history-dependent, while the parameter a controlling the inclination of the curve shows minor dependence on pressure.

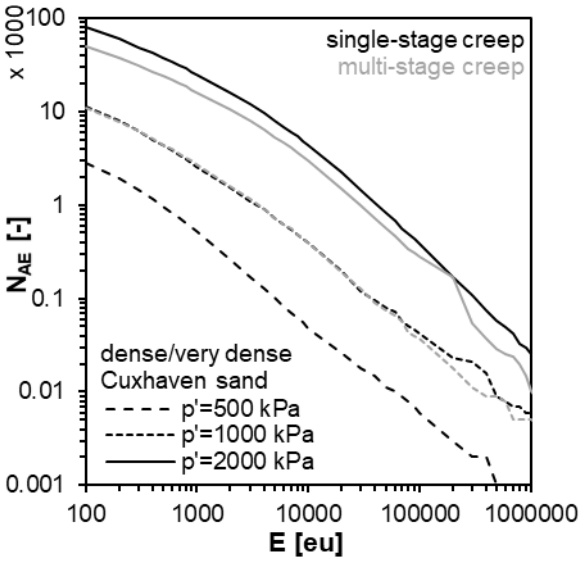

Figure 4.23: Number of AE events N_{AE} exceeding E of single- and multi-stage creep phases at mean stresses of 500, 1000 and 2000 kPa on dense to very-dense samples of Cuxhaven sand

As a result of the evaluation of the multi-stage creep phases, a ranges from 0.96 to 1.16, and in the single-stage creep phases, from 0.91 to 1.05, with the larger value of a at higher mean stress p'. Regarding the history dependence, Figure 4.23 shows that fewer AE events occur in the multi-stage creep phase at p' = 2000 kPa than in the single-stage creep phase. In the multi-stage creep phase with p' = 1000 kPa, the number of AE events are similar to those of the single stage creep tests for E < 40000 eu. For larger energies the behavior is qualitatively similar to the tests with p' = 2000 kPa.

As for real earthquakes, the experimentally determined a-value is around the unity. Effectively, in numerous publications examining the spatial and temporal variations of the a-value for seismic regions, it has been found that the value is a constant, varying only slightly in the range of $0.8 \leq a \leq 1.2$ (Rundle et al., 2003). Moreover, it has been recognized that the Gutenberg-Richter relationship is valid for different natural phenomena that exhibit fractality (Turcotte, 1997). In addition, a relationship between a and the fractal dimensions D has been demonstrated for earthquakes. The following relationship can be established for the number of earthquakes N with fracture areas greater than A occurring in a specific area and time (Varotsos et al., 2004).

$$N(>A) = C \cdot A^{-d}, \tag{4.5}$$

where d is correlated with the exponent a and is directly linked to the dimension D of the fractal structure of earthquakes epicentres in the region (Lei & Kusunose, 1999). C is a constant to be determined.

Li et al. (2022) investigated the relationship between the fractal dimension of particle shape as well as the particle size distribution and the axial stress of a calcareous sand under oedometric compression. They observed that both, the fractal dimension of the particle shape and fractal dimension of the particle size distribution increased confidently with the axial loading. The significant change of the

fractal dimensions was related to the significant change of the particle shape and the particle size distribution caused by extensive grain breakage of the calcareous sand.
Therefore, it can be presumed that the a-value controlling the micro-seismic events in the soil sample is related to the fractal structure (e.g. asperity or particle breakage) of the soil skeleton. The fact that the a-value slightly increases with increasing pressure indicates that the fractal dimensions related to the grain size and to the grain shape is also slightly changing (Li et al., 2022).
The result indicates that the observations of the change of the a-value with the state of the soil could provide valuable information about the intensity of grain damage.

It is assumed that the energy releases (AEs) are associated with the sudden conversion of potential to kinetic energy related to instant sliding at the particle contact and particle motion. The larger the energy release, the larger the number of contacts sliding and the larger the redistribution of contact forces. Large energy jumps can be associated with the collapse of force chains and the rearrangement of particles and thus, the redistribution of forces in the particle skeleton. The change in axial strain rate $\dot{\varepsilon}_a$ and rate of the number of AE events $\dot{N}_{AE}$ with time supports this explanation.

Figure 4.24 (a) shows $\dot{\varepsilon}_a$ for the single and multi-stage creep tests as a function of time in a double logarithmic plot. The trend of the values of $\dot{N}_{AE}$ are plotted in Figure 4.24 (b) and shows, compared to Figure 4.24 (a), a similar evolution with t in log-scale.

The relationship between the axial creep rate $\dot{\varepsilon}_a$, respectively $\dot{N}_{AE}$ and creep time t observed in the experiments can be described by Equation (4.6) and Equation (4.7).

$$\dot{\varepsilon}_a = c_{\dot{\varepsilon}_a} \cdot t^{-m_{\dot{\varepsilon}_a}} \tag{4.6}$$

$$\dot{N}_{AE} = c_{\dot{N}_{AE}} \cdot t^{-m_{\dot{N}_{AE}}} \text{ with } m_{\dot{\varepsilon}_a} \approx m_{\dot{N}_{AE}}. \tag{4.7}$$

This relationship is equivalent to the relation proposed by Singh and Mitchell (1968) as given by Equation (2.3). The exponent m decreases slightly with increasing mean stress, e.g., $m_{\dot{\varepsilon}_a}$ = 0.93 for p' = 1000 kPa and $m_{\dot{\varepsilon}_a}$ = 0.90 for p' = 2000 kPa were determined in the multi-stage creep phases. The lower p' and hence the lower the forces at the grain contacts, the faster the particle assembly stabilizes and the smaller the creep strains. The factor $c_{\dot{\varepsilon}_a}$ or $c_{\dot{N}_{AE}}$, respectively, is defined by the initial strain rate or rate of number of AE events. c is assumed to be material and state dependent. The dependence on p' is more pronounced for the rate of number of AE events than axial strain rate.
For the single-stage creep phases, a temporary quasi-stagnation, or considering the mean stress p' = 500 kPa an increase of $\dot{\varepsilon}_a$, respectively $\dot{N}_{AE}$, is observed between 1 h and 1 d, associated with the rupture of large force chains and significant redistribution of forces towards a more stable structure. Stabilization is indicated by $\dot{\varepsilon}_a$ (or $\dot{N}_{AE}$) approaching a relationship with the initial inclination m again. As shown in Figure 4.24 (b), the stagnation is less abrupt for higher values of p' and occurs at a higher rate.

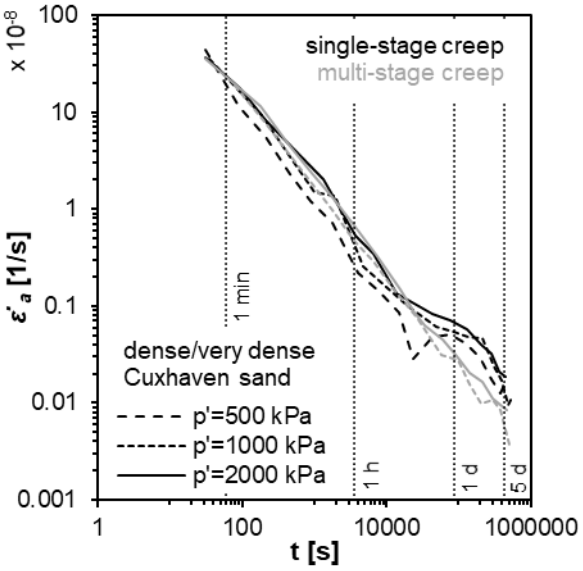

(a)

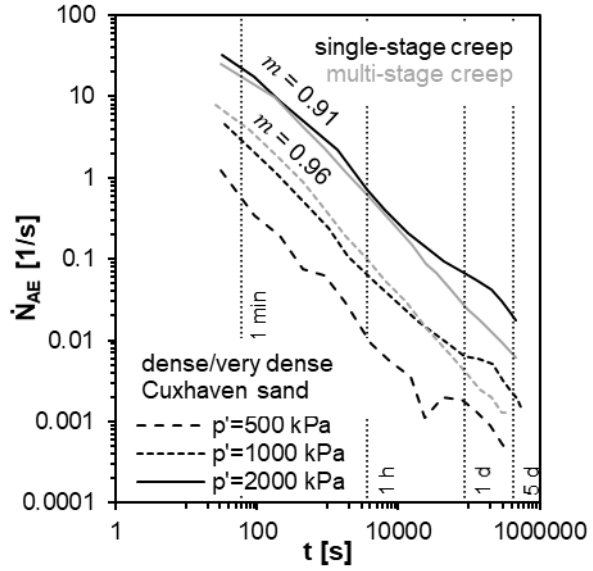

(b)

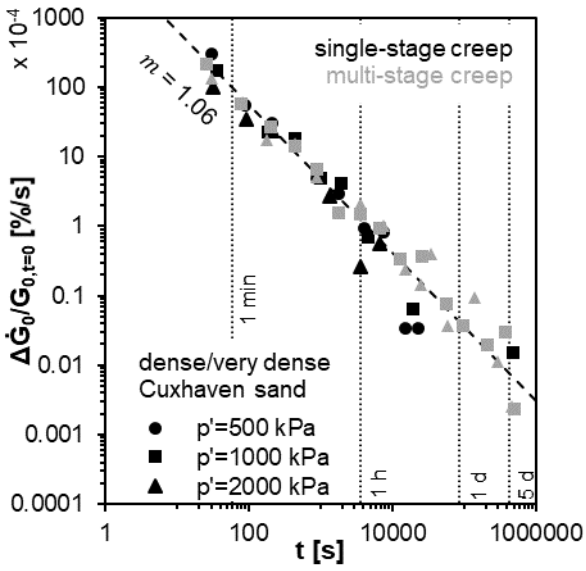

(c)

Figure 4.24: (a) Axial strain rate $\dot{\varepsilon}_a$, (b) rate of number of AE events $\dot{N}_{AE}$ and (c) rate of the normalized change of small-strain shear modulus $\Delta\dot{G}_{0,t}/G_{0,t=0}$ versus t in log-scale of single- and multi-stage creep phases at mean stresses of 500, 1000 and 2000 kPa on dense to very-dense samples of Cuxhaven sand

Figure 4.24 (c) shows the normalized rates of change of the shear modulus $\dot{G}_{0,t}/G_{0,t=0}$ with $\dot{G}_{0,t}$ estimated as $\approx (\Delta G_{0,t=t_2}/G_{0,t=0} - \Delta G_{0,t=t_1}/G_{0,t=0})/(t_2 - t_1)$. $\dot{G}_{0,t}/G_{0,t=0}$ follows the same trend described by Equation (4.6) for $\dot{\varepsilon}_a$ and $\dot{N}_{AE}$. The time at which negative values of $\dot{G}_{0,t}/G_{0,t=0}$ are observed during the single-stage creep phases, which are not plotted in the double logarithmic diagram, coincides with the time at which the stagnation of $\dot{\varepsilon}_a$, respectively $\dot{N}_{AE}$ occurs. The dependence of $\Delta G_{0,t}/G_{0,t=0}$ on the mean stress (see Figure 4.20) is only visible for the initial rate $\dot{G}_{0,t}/G_{0,t=0}$. $\dot{G}_{0,t}/G_{0,t=0}$ then appears to be independent of p'. The exponents m for $\dot{N}_{AE}$ and $\dot{G}_{0,t}/G_{0,t=0}$ are similar to the exponent

corresponding to the trend of $\dot{\varepsilon}_a$. This result strongly indicates that creep and aging result from the same micromechanical processes and a relationship between two phenomena is likely.

Figure 4.25 shows the relationship between the normalized change of small-strain shear modulus $\dot{G}_{0,t}/G_{0,t=0s}$ and the axial creep strain $\dot{\varepsilon}_a$ related to the initial creep strain rate $\dot{\varepsilon}_{a,t=60s}$ calculated between t = 0 s and 60 s. Due to its logarithmic axes, the diagram only covers the experimental data for decreasing creep rates or increasing changes in the shear modulus, respectively.

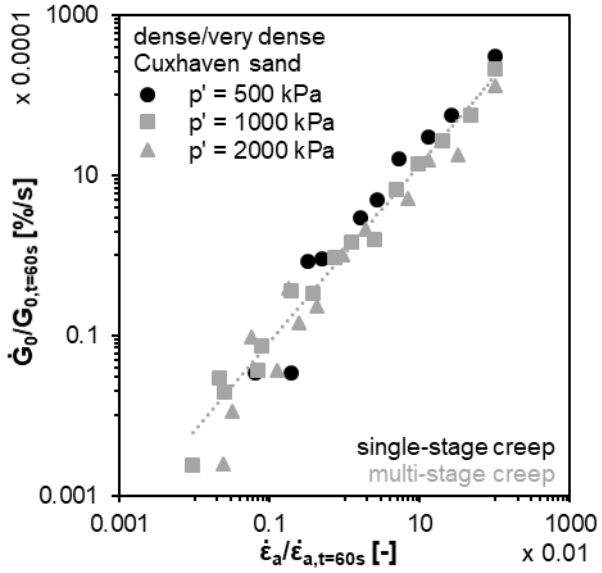

Figure 4.25: $\dot{G}_{0,t}/G_{0,t=0s}$ versus $\dot{\varepsilon}_a/\dot{\varepsilon}_{a,t=60s}$ of single- and multi-stage creep phases at mean stresses of 500, 1000 and 2000 kPa on medium-dense to very-dense samples of Cuxhaven sand

This relationship can also be described by a power law, whose exponent is about the unity. It shows a slight dependence on the mean stress p': higher values of $\dot{G}_{0,t}/G_{0,t=0s}$ with lower p' at the same value of $\dot{\varepsilon}_a/\dot{\varepsilon}_{a,t=60s}$. Nevertheless, this illustration suggests a proportionality between the two phenomena for the case of multi-stage creep tests.

Conclusions

In summary, the following conclusions can be drawn from the experimental investigations:

- Cuxhaven sand shows increasing axial creep strain with increasing isotropic pressure, whereas the extent of aging increases with decreasing pressure.
- The time-dependent evolutions of the number of AE events and axial creep strain follow the same trend.
- Considering the single-stage creep tests, an increase followed by a decrease in the small strain shear modulus quantifying aging is observed. The higher the isotropic stress, the less pronounced is the initial increase of $\Delta G_{0,t}/G_{0,t=0}$ and the more pronounced is the subsequent decrease with time.
- The decrease of $\Delta G_{0,t}/G_{0,t=0}$ is accompanied by a temporary quasi-stagnation of the axial strain rate and the rate of number of AE events $\dot{N}_{AE}$.

- Within the considered period of five days and for the same isotropic pressures the multi-stage creep test shows less creep and therefore, a more pronounced aging than the single-stage creep tests.
- The stepwise evolution of the burst signal energy E indicates the time-dependent occurrence of particular events at the micro- and mesoscale that lead to the rearrangement of particles. The relationship between the number of AE events N_{AE} exceeding a given energy threshold and the corresponding energy E is approximately linear using a double logarithmic scale. Thus, the Gutenberg-Richter relationship applies to micromechanical processes. The a-value can indicate the damage intensity of particles.
- The axial strain rate, the rate of number of AE events and the rate of change of small-strain shear modulus with time follow a power law. This link between aging, creep and micromechanical processes points to a strong underpinning causality.
- The relation of $\log\left(\dot{G}_{0,t}/G_{0,t=0s}\right)$ and $\log\left(\dot{\varepsilon}_a/\dot{\varepsilon}_{a,t=60s}\right)$ seems to be proportional.

The experimental results suggest that a time-dependent restructuring of the particle structure takes place.

4.4.3 Drained triaxial compression tests

The aim of the drained triaxial compression tests at constant rate of strain (CRS-tests) was to investigate the rate-dependent deformation behavior of two granular materials. It should be found whether a dependence of q_{max} on the strain rate exists. Thus, nine CRS-tests on Cuxhaven sand and four tests on corundum were carried out. Three different strain rates were evaluated, namely, 0.01 %/min, 0.1 %/min, and 1.0 %/min. Furthermore, samples of different initial densities (loose, medium-dense, and dense) were prepared and tested. The consolidation pressure for all tests was set to p_0 = 1000 kPa. A summary of the related initial densities and void ratios of each test is given in Table 4.10.

Table 4.10: Initial density of the CRS-C-tests on samples of Cuxhaven sand and corundum

		I_D [-] (e_0 [-])		
material	**description**	$\dot{\varepsilon}_a$ = 0.01 %/min	$\dot{\varepsilon}_a$ = 0.10 %/min	$\dot{\varepsilon}_a$ = 1.00 %/min
Cuxhaven sand	very loose	0.12 (0.72)	0.08 (0.73)	0.09 (0.73)
	medium-dense	0.47 (0.62)	0.48 (0.62)	0.48 (0.62)
	dense	0.81 (0.53)	0.83 (0.53)	0.80 (0.53)
Corundum	medium-dense	-	0.52 (0.69)	0.50 (0.70)
	dense	-	0.84 (0.63)	0.84 (0.63)

Figure 4.26 shows the stress-strain behavior in terms of q-ε_a-diagrams for (a) Cuxhaven sand and (b) corundum. Both materials show the well-known dependence of the stress-strain behavior on density under drained shearing: As the initial density increases, the maximum shear resistance increases. After the peak the shear resistance decreases toward the critical state. Until the maximum axial strain in the test of ε_a = 15 %, the medium-dense sand samples do not develop a peak strength, while the medium-dense corundum samples do.

Only slight deviations in stress-strain behavior were observed at different rates of axial strain $\dot{\varepsilon}_a$ for the Cuxhaven sand. The magnitude of the deviations is within the range of repeatability of the tests.

In particular, the curves do not precisely overlap for samples of loose sand, which can be attributed to the challenging sample preparation creating samples of loose sand and the slight variation in initial density (Table 4.10).

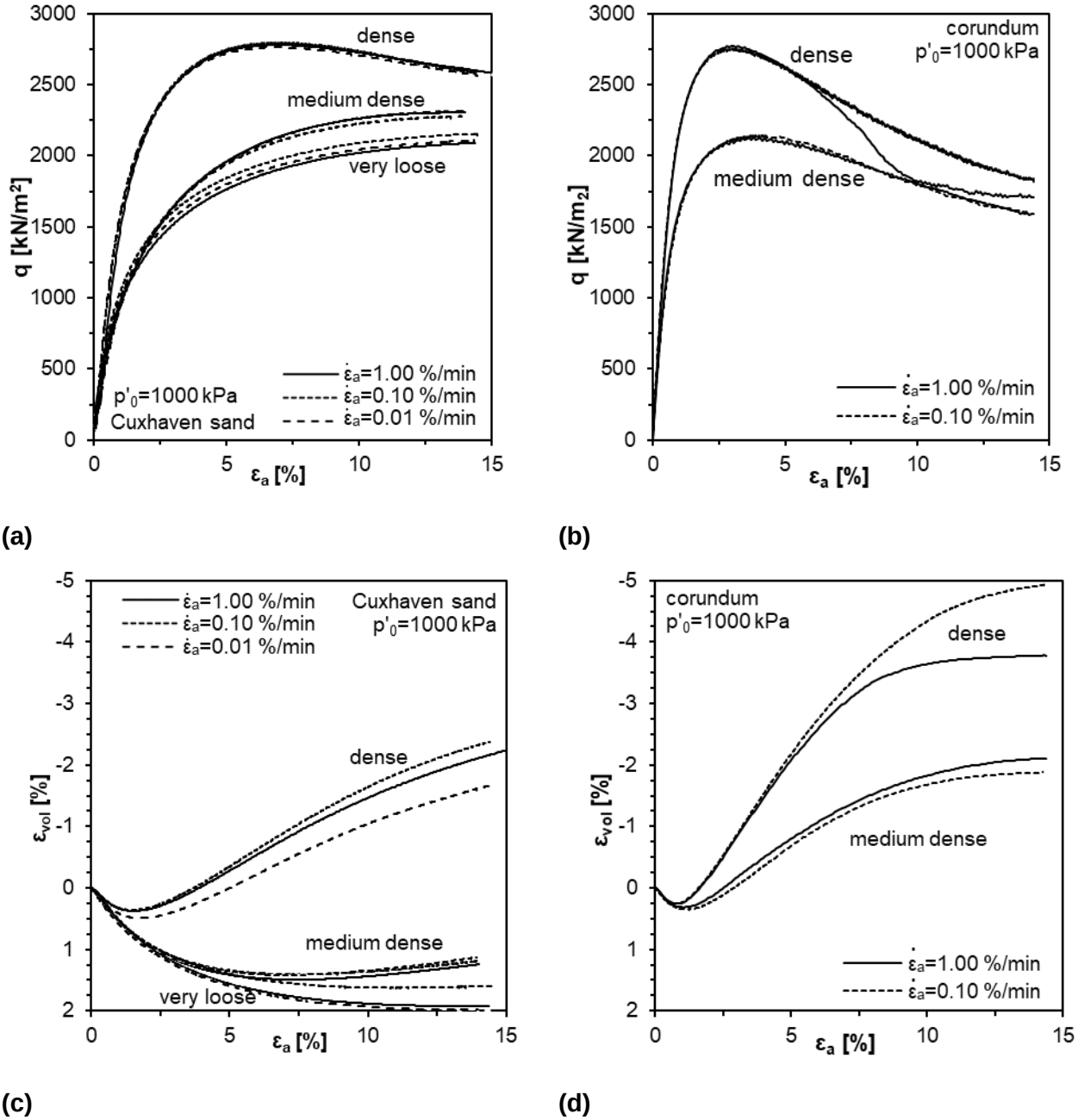

Figure 4.26: Stress-strain behavior and the corresponding axial strain-volumetric srtain behavior from drained triaxial compression tests with constant axial strain rates of 0.01 %min, 0.1 %min and 1.0 %min of very loose to dense samples of (a)/(c) Cuxhaven sand (b)/(d) corundum at p_0 = 1000 kPa

The results of the CRS-tests on corundum show qualitatively similar stress-strain behavior as the tests on Cuxhaven sand. After about ε_a = 5 %, a drop in deviatoric stress q is observed at a strain rate of $\dot{\varepsilon}_a$ = 1 %/min for the dense specimen. In this case, the sheared specimen showed localization of the shear zone (see Figure 4.27 (c)). The other samples, after disassembly of the cell, show the

typical barrel shape (see Figure 4.27 (b)), which indicates plastic failure without localization. Figure 4.27 (a) shows a sample of corundum before loading.

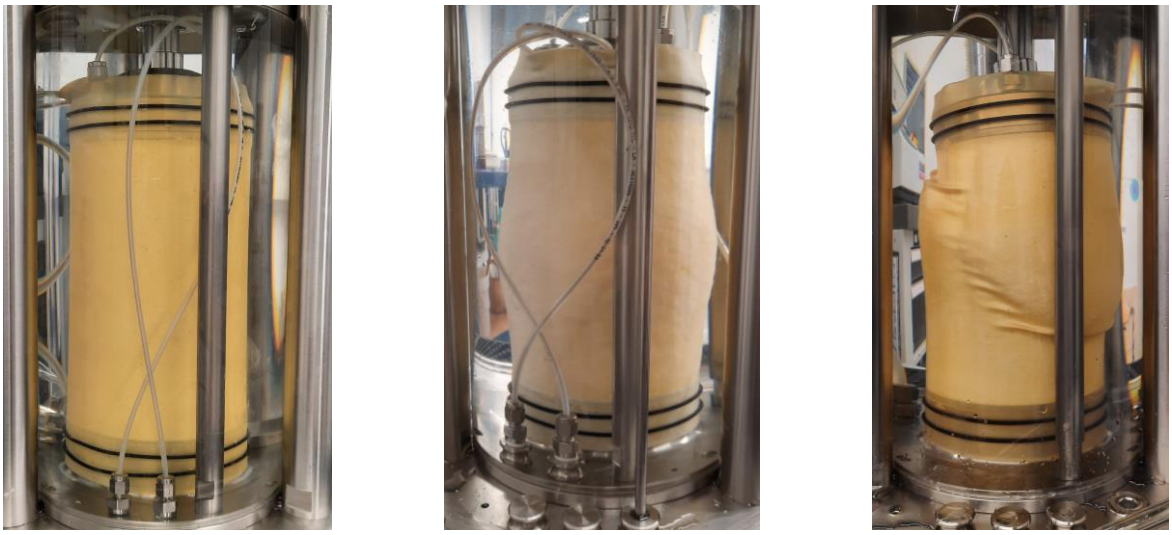

(a) **(b)** **(c)**

Figure 4.27: Photography of samples of corundum (a) after sample preparation and before loading; and after the test at ε_a = 15 % for (b) the medium-dense sample loaded with $\dot{\varepsilon}_a$ = 0.01 %/min and (c) the dense sample loaded with $\dot{\varepsilon}_a$ = 1 %/min

The values of q_{max} and φ_{max} derived from drained triaxial compression tests at constant strain rates are given in Table 4.11. q_{max} was evaluated either at the peak or at the maximum axial strain achieved in the test.

Table 4.11: Comparison of q_{max} and φ_{max} from triaxial compression tests with different constant axial strain rates on samples of Cuxhaven sand and corundum at p_0 = 1000 kPa

		q_{max} [kPa] (φ_{max} [°])		
Material	**Description**	$\dot{\varepsilon}_a$ = 0.01 %/min	$\dot{\varepsilon}_a$ = 0.10 %/min	$\dot{\varepsilon}_a$ = 1.00 %/min
Cuxhaven sand	very loose	2109 (30.9)	2154 (31.2)	2091 (30.7)
	medium-dense	2327 (32.5)	2293 (32.3)	2311 (32.4)
	dense	2765 (35.5)	2813 (35.8)	2789 (35.6)
Corundum	medium-dense	-	2756 (31.1)	2771 (31.0)
	dense	-	2143 (35.4)	2133 (35.4)

The comparison of the tests with different axial strain rates $\dot{\varepsilon}_a$ shows a deviation of q_{max} between 0.23 % for dense samples of corundum to a maximum of 1.70 % for loose samples of Cuxhaven sand relative to the mean value of q_{max}. The most significant deviation is observed in the tests on the very loose specimens, for which the difference in initial density was also the largest. The maximum difference of q_{max} corresponds to a difference in the maximum friction angle φ_{max} of about 0.86 % with respect to the mean value of φ_{max} of the very loose samples of Cuxhaven sand. The results show that a systematic dependence of q_{max} on the strain rate cannot be identified within the examined range of $\dot{\varepsilon}_a$ for the materials studied.

Figure 4.26 (c) and (d) show the volumetric strain ε_{vol} as a function of the axial strain ε_a for the triaxial compression tests. In accordance with the stress-strain behavior, the volumetric strain ε_{vol} does not

show a systematic dependence on the axial strain rate $\dot{\varepsilon}_a$. The deviations of the experiments for a given density in ε_{vol}-ε_a-space can be attributed primarily to the limitations of the cell-in-cell volume measurement method. The influence of temperature is more pronounced for long lasting tests and, therefore, is more significant for tests at low axial strain rates $\dot{\varepsilon}_a$. The sudden localization of the shear zone of the dense corundum specimen at $\dot{\varepsilon}_a$ = 1.0 %/min leads to a flattening of the ε_{vol} curve at considerably smaller values of ε_a compared to the specimen loaded at $\dot{\varepsilon}_a$ = 0.1 %/min.
The dilatancy is more pronounced for corundum than for sand. It is assumed that due to the uniformity of the particle size distribution, the spherical particle shape and the higher particle strength of corundum, the sliding of the particles and, thus, an increase in volume was necessary during shearing. As expected, the volume increase (dilatancy) is more pronounced at higher initial densities. In the case of sands, only the very loose samples show purely contractive behavior.

Drained triaxial compression test with sudden changes in axial strain rate

The results of the constant strain rate tests indicate that the influence of strain rate on the resistance of Cuxhaven sand and corundum against deviatoric loading is negligible. In order to investigate the strain-rate-dependent behavior after a sudden change in axial strain rate $\dot{\varepsilon}_a$, a drained triaxial compression test with several jumps of the axial strain rate was carried out. A medium-dense sample (I_D = 0.48) of Cuxhaven sand was first consolidated at p'_0 = 1000 kPa. Jumps of the axial strain rate slowing down or increasing by a 10-fold to the axial strain rate of the previous loading phase were implemented. The development of the deviatoric stress q with the axial strain ε_a was compared to the results from a drained triaxial compression test including creep phases in which q was kept constant (Section 4.4.4). The tests were carried out at the same initial confining pressure p'_0 and initial relative density I_D. The test results, including the applied axial strain rates of the individual test phases are shown in Figure 4.28.

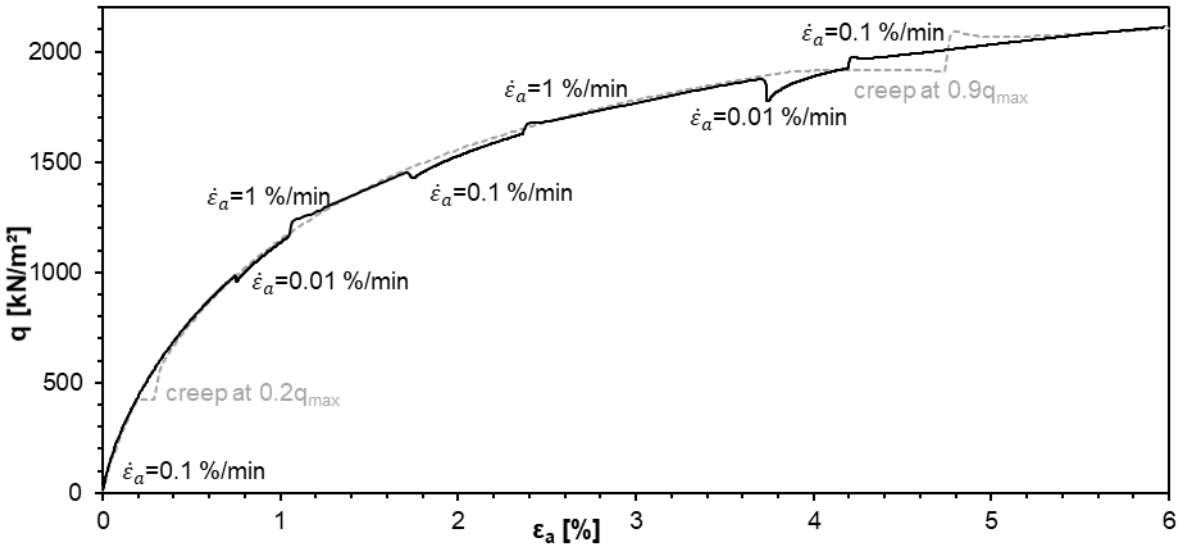

Figure 4.28: Comparison of triaxial compression test including creep phases (gray) and test with jumps of the axial strain rate (black) on samples of Cuxhaven sand at p'_0 = 1000 kPa and I_D = 0.48

The experiment shows that the effect of a sudden change in axial strain rate is temporary. This behavior corresponds to the TESRA behavior according to Tatsuoka et al. (2008), Di Benedetto et al. (2002) and Levin (2021). The axial strain rate jumps were performed at different axial strains ε_a. With increasing axial strain ε_a and thus increasing deviatoric stress q, a more pronounced initial increase or decrease in the initial stress change ΔR was measured corresponding to the experiences of Di Benedetto et al. (2002), see Equation (2.4). Furthermore, the increment of axial strain $\Delta\varepsilon_a$ to converge towards to the q-ε_a curve given by the triaxial compression test carried out at constant $\dot{\varepsilon}_a$ depends obviously on the axial strain rate and the relative change of axial strain rate.

Conclusions

The results of the triaxial compression tests carried out at constant axial strain rate show that for the examined granular materials, the dependence of the stress-strain behavior and the volumetric behavior are not systematically affected by the strain rate when a constant strain rate is applied during the shearing. The observed differences for different strain rates can be associated to unavoidable differences in the initial state due to sample preparation and other effects related to the experimental setup.
A sudden change of the axial strain rate $\dot{\varepsilon}_a$ during shearing of Cuxhaven sand confirmed the TESRA behavior. The convergence of the deviatoric stress q after a sudden change of $\dot{\varepsilon}_a$ towards the corresponding curve of a triaxial compression test with a constant $\dot{\varepsilon}_a$ depends on the magnitude of the change in $\dot{\varepsilon}_a$.

4.4.4 Drained triaxial compression tests with creep[12]

Drained triaxial compression tests including creep phases (CRS-C) were carried out to assess the creep and aging behavior of the investigated materials under constant deviatoric stress q. For this purpose, medium-dense to dense samples of dry Cuxhaven sand were prepared and examined in the triaxial test setup. During the creep phases, axial and volumetric creep strain were measured, and aging was assessed by the change in small-strain shear modulus $G_{0,t}$ at specific times t. Acoustic emissions (AE) generated in the granular specimens were recorded to provide insight into the micromechanical processes during creep. The initial densities I_D and the corresponding void ratios e_0 of the samples examined by the individual experiments of type CRS-C are listed in Table 4.12.

Table 4.12: Initial density of the CRS-C-tests on samples of Cuxhaven sand

		I_D [-] (e_0 [-])		
Material	**Description**	500 kPa	1000 kPa	2000 kPa
Cuxhaven sand	medium-dense	0.41 (0.64)	0.41 (0.64)	0.43 (0.63)
	dense	0.75 (0.55)	0.88 (0.51)	0.82 (0.53)

Verification of the small-strain shear modulus G_0 at the start of the creep phases

The empirical function shown in Equation (3.17) is used to find a surface describing the influence of the deviatoric stress on $G_{0,t=0}$. The constant x can be determined by fitting the function of $k \cdot f(e)$ to the curve G_0 against e depending on the mean stress using regression. By plotting $G_0/f(e)$ against

[12] The content has been published in Jessen et al. (2024)

σ_1/σ_3 and $(\sigma_1 \cdot \sigma_3)/{p_a}^2$, the material-specific coefficients of Equation (3.17) can be determined by curve fitting, as suggested by Goudarzy et al. (2018). The constants for Cuxhaven sand are shown in Table 4.13.

Table 4.13: Coefficients for empirical determination of $G_{0,t=0}$ under anisotropic stress $\sigma_1 \neq \sigma_3$

Equation	x	A	n_c	n_d
(3.17)	2.85	0.32	0.22	-0.16

The surface describing $G_{0,t=0}$ as a function of ${\sigma'}_1/{\sigma'}_3$ and $({\sigma'}_1 \cdot {\sigma'}_3)/{p_a}^2$ as well as the small-strain shear modulus at t = 60 s ($G_{0,t=60s}$) are shown in Figure 4.29. Since immediately after the start of the creep phase at constant q the shear modulus at small strains G_0 temporarily decreased, the small strain shear modulus $G_{0,t=60s}$ at t = 60 s was used as a reference value to assess aging by the change of $\Delta G_0/G_{0,t=60s}$. An explanation of the instant decrease and further increase of G_0 during the creep at constant q was not found yet. It might be that the grain structure needs time for the transition from the loading phase to the creep phase and hence constant stress.

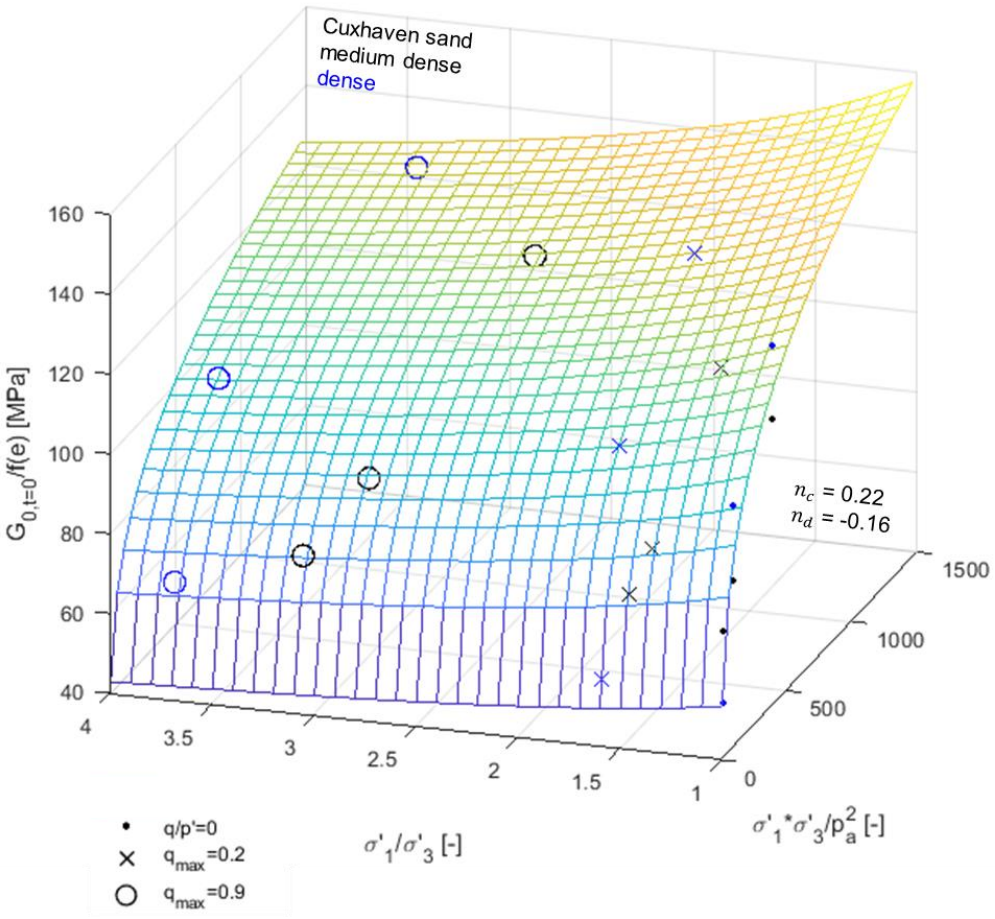

Figure 4.29: Surface describing $G_{0,t=0}/f(e)$ (for isotropic stresses) and $G_{0,t=60s}/f(e)$ (for anisotropic stress) as a function of the stress state using Equation (3.17) for Cuxhaven sand evaluated from CRS-C-tests

Santamarina and Cascante (1996) stated that the shear wave velocity is more affected by the stress in the direction of particle motion (radial direction aligned to $\sigma'_3 = p'_0$)) than by the stress in the direction of wave propagation (vertical direction according to σ'_1). Thus, the sensitivity of G_0 to the axial stress σ'_1 is lower than to the initial confining pressure $\sigma'_3 = p'_0$. Furthermore, G_0 is expected to become larger with increasing p' and comparably only slightly smaller with increasing q, i.e., increasing mean stress stabilizes the grain structure while increasing deviatoric loading destabilizes the structure. The fact that for the parameter n_d a negative value was found (see Figure 4.29) shows the reducing influence of the deviatoric stress q on the small-strain shear modulus G_0.

Results of the drained triaxial compression tests with creep

Figure 4.30 (a) presents the relationship between the deviatoric stress q and the axial strain ε_a and Figure 4.30 (b) shows the development of the volumetric strain ε_{vol} in respect to the axial strain ε_a of the triaxial compression tests on Cuxhaven sand.

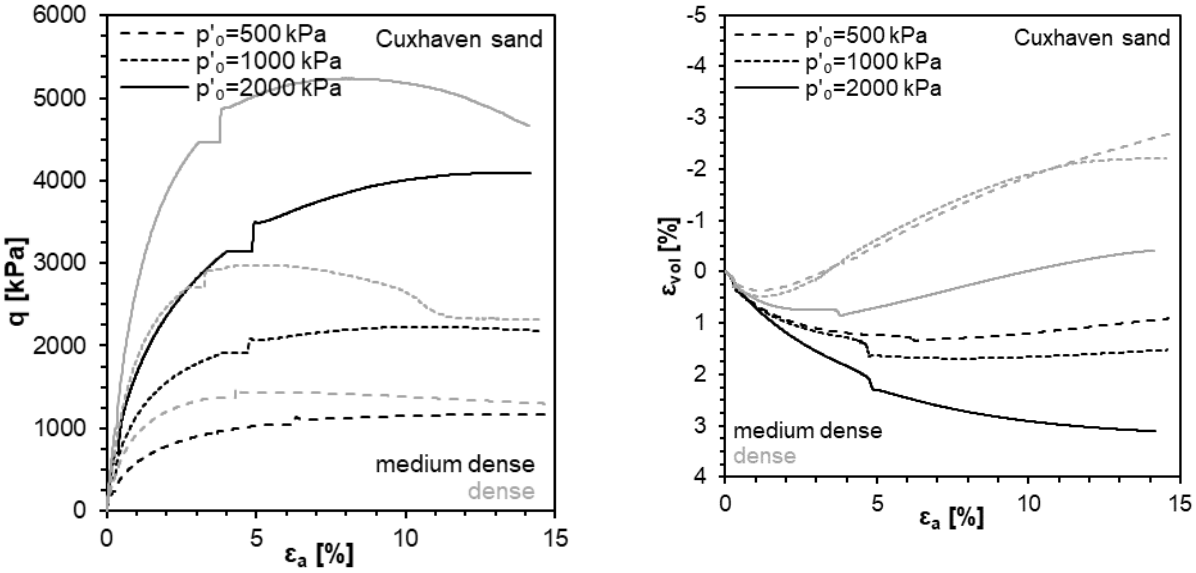

(a) **(b)**

Figure 4.30: (a) Stress-strain behavior and (b) volumetric strain-axial strain curve at varying p'_0 of medium-dense and dense samples from Cuxhaven sand evaluated from CRS-C-tests

The development of q and the change of the volumetric strain ε_{vol} corresponds to the expected behavior for granular materials: With increasing initial density $D_{r,0}$, the resistance against deviatoric loading, as well as the dilatancy increase. As the mean pressure p increases, the maximum measured deviatoric stress q_{max} increases, and the dilatancy decreases. The dense sand sample loaded by q at a confining pressure of p'_0 = 1000 kPa shows a decrease in deviatoric stress at an axial strain of about ε_a = 10 %. Significant shear strain localization was observed after the peak, as shown in Section 4.4.3, was observed. The volumetric behavior of the dense sample with a confining pressure of p_0 = 500 kPa does not fit the pattern of the other test results. The cause is not known yet.

Figure 4.30 (b) shows that the creep phases at 0.2 q_{max} start in the contractive part of the volumetric strain behavior for all tests performed with different p'_0 and I_D. The onset of the creep phases at

0.9 q_{max} is either in the contractive part, dilative part, or close to the inflection point of the volumetric behavior during shear. Figure 4.31 shows the evolution of the volumetric strain ε_{vol} with time measured at constant deviatoric stress of q = 0.2 q_{max} and q = 0.9 q_{max}.

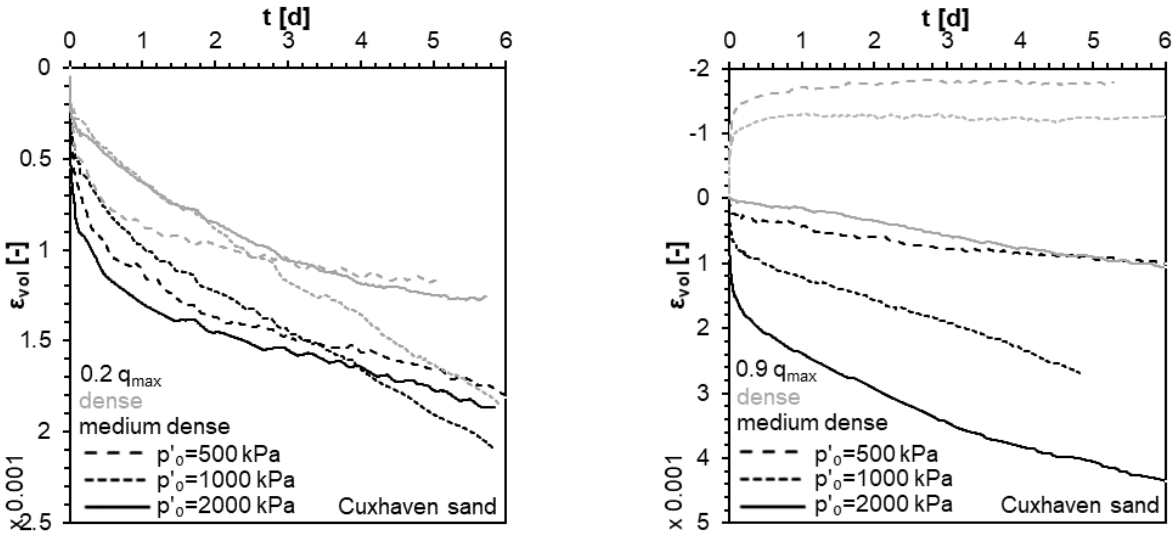

(a) **(b)**

Figure 4.31: Volumetric strain ε_{vol} during creep at (a) q = 0.2 q_{max} and (b) q = 0.9 q_{max} at varying p'_0 of medium-dense and dense samples of Cuxhaven sand

During the creep phases at q = 0.2 q_{max}, a purely contractive creep deformation was measured, which shows a density dependence: As the initial density $D_{r,0}$ increases, the measured volumetric creep strain ε_{vol} decreases. The medium-dense samples of the examined silica sand show contractive creep even at q = 0.9 q_{max}. Dilative creep, on the other hand, is measured for dense samples consolidated at 500 kPa and 1000 kPa. Creep phases starting at the turning point regarding the development of the volumetric strain for deviatoric loading, which is approximately valid for the creep phases of the dense specimen at 2000 kPa, and the medium-dense sample at 500 kPa, show little volumetric strain within the range of the volume measurement accuracy.
An increasing compaction for medium-dense samples or decreasing loosening for dense samples was observed with increasing confining pressure p'_0. After a creep time of about one day, dilative creep of the dense samples ceased.

The results of the acoustic emission measurement of the CRS-C tests were investigated in detail for the medium-dense specimens of Cuxhaven sand and were linked to the results of the isotropic incremental loading – creep tests presented in Section 4.4.2.2.[13] Therefore, the results of the measured axial strain ε_a and the cumulated number of AE events N_{AE} during the creep phases under isotropic loading (q/p' = 0) and anisotropic loading at the stress states of 0.2 q_{max} (q/p' ≈ 0.36) and 0.9 q_{max} (q/p' ≈ 1.15) are given below. Different line types highlight the variation of consolidation pressures (p'_0 = 500 kPa, 1000 kPa and 2000 kPa), while the color variation indicates the differentiation of the q/p'-ratio.

[13] The results were presented at the IS-PORTO 2023: 8th International Symposium on Deformation Characteristics of Geomaterials (Bock et al. (2023))

Figure 4.32 presents the evolutions of ε_a and N_{AE} with time t. It shows that N_{AE} follows qualitatively the same time- and stress-dependent trend as ε_a. ε_a and N_{AE} increase with increasing q/p'-ratio, which is in accordance with the investigations of Tanaka and Tanimoto (1988). Whereas the values of ε_a at the same q/p'-ratio but different pressure p'_0 after five days of creep are approximately in the same range, the influence of the pressure p'_0 on the number of AE events N_{AE} is significant. A reason for this may be the influence of soil structure, pressure, and density on the propagation characteristics of elastic waves, as shown by Lin et al. (2020). With increasing confining pressure or densification process, the travel path of the elastic waves decreases due to the restructuring of the particles (e.g., formation of strong force chains) through the sample to the acoustic emission sensor and, in addition, the attenuation of the waves is also reduced due to stiffening at particle contacts. Thus, more AE events can be detected as the pressure p'_0 increases for the same amplitude threshold.

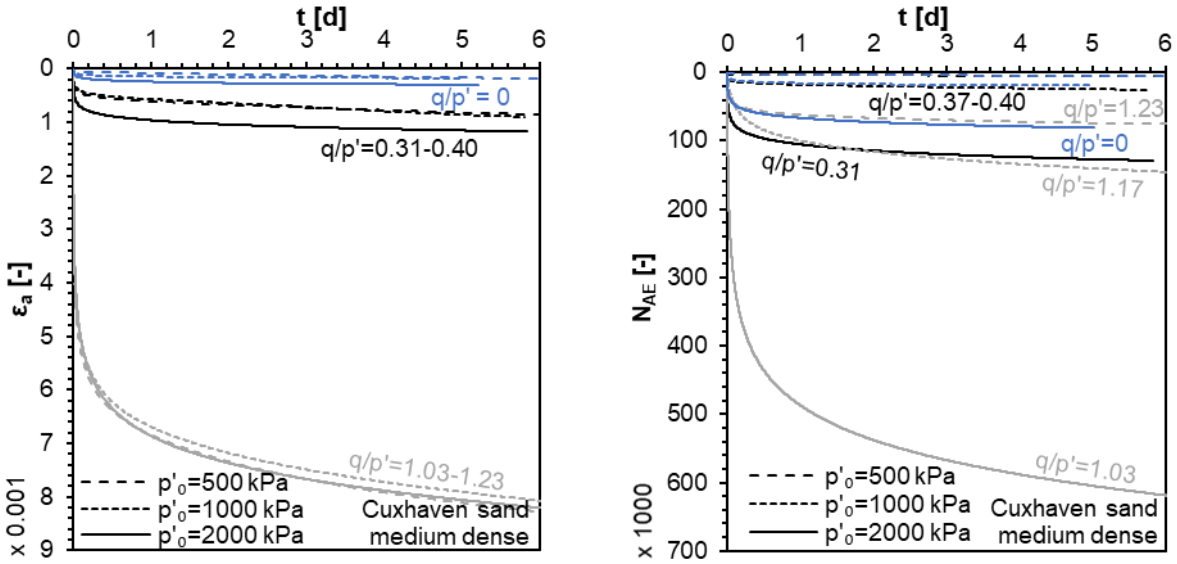

(a) **(b)**

Figure 4.32: (a) Axial strain ε_a and (b) number of AE events N_{AE} with time t for creep phases at varying p'_0 and q/p'-ratios of medium-dense samples of Cuxhaven sand

In Figure 4.33, the curves of ε_a and N_{AE} evolving with time during creep are shown using semi-logarithmically scaled diagrams. An almost linear relationship between ε_a and N_{AE}, respectively, with $\log(t)$ can be observed after a specific period since the beginning of the creep phases. Thus, the axial strain ε_a developing during creep could be described by the well-known creep coefficient C (Buisman, 1936) according to Equation (2.2); the acoustic emission coefficient C_{AE} can be defined analogously (Equation (3.21)). Generally, both, C and C_{AE} depend on p'_0, q/p' and the initial density.

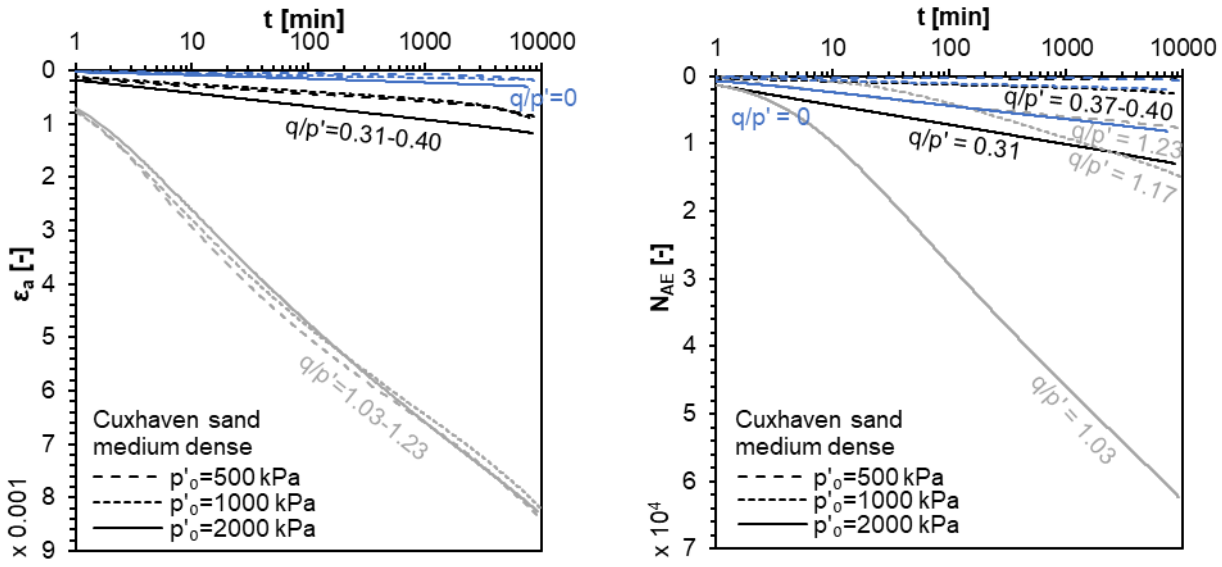

(a) **(b)**

Figure 4.33: (a) Axial strain ε_a and (b) number of AE events N_{AE} with t in log-scale for creep phases at varying p'_0 and q/p'-ratios of medium-dense samples of Cuxhaven sand

Furthermore, the axial creep strain rates $\dot{\varepsilon}_a = d\varepsilon_a/dt$ and rates of the number of AE events $\dot{N}_{AE} = dN_{AE}/dt$ were calculated and are presented in Figure 4.34 versus time t in a double logarithmic diagram. By the findings interpreted from Figure 4.34, the relationship between $\dot{\varepsilon}_a$ and $\dot{N}_{AE}$, respectively, and the time t can be satisfactorily described by Equation (4.6). The exponent m_{ε_a} for Cuxhaven sand increases from 0.93 for q/p' = 0 to 0.98 for higher q/p'-ratios. Similar results are obtained for the rate of the number of AE events $\dot{N}_{AE}$ with $m_{N_{AE}}$ varying between 0.95 and 0.98. The exponents m_{ε_a} and $m_{N_{AE}}$ were determined within the time interval of 10 min and 1000 min after the start of the creep phase, in which the slope of the curves presented by the diagrams of Figure 4.34 is assumed to be linear considering the double logarithmic scale.

Higher values of m_{ε_a} and $m_{N_{AE}}$ indicate a slower decrease of the axial strain rate $\dot{\varepsilon}_a$ and the rate of the number of AE events $\dot{N}_{AE}$, respectively, and thus, a slower stabilization at the particle contacts during creep within the sample.

Thus, the stress-dependent creep behavior (Figure 4.32) appears to correspond to the different initial axial strain rates $\dot{\varepsilon}_a$ or initial rates of the number of AE events $\dot{N}_{AE}$, followed by an almost identical exponential decrease. Higher initial rates of $\dot{\varepsilon}_a$ and $\dot{N}_{AE}$ were observed as the deviatoric stress q increases and, in the case of $\dot{N}_{AE}$, as the mean stress p' increases.

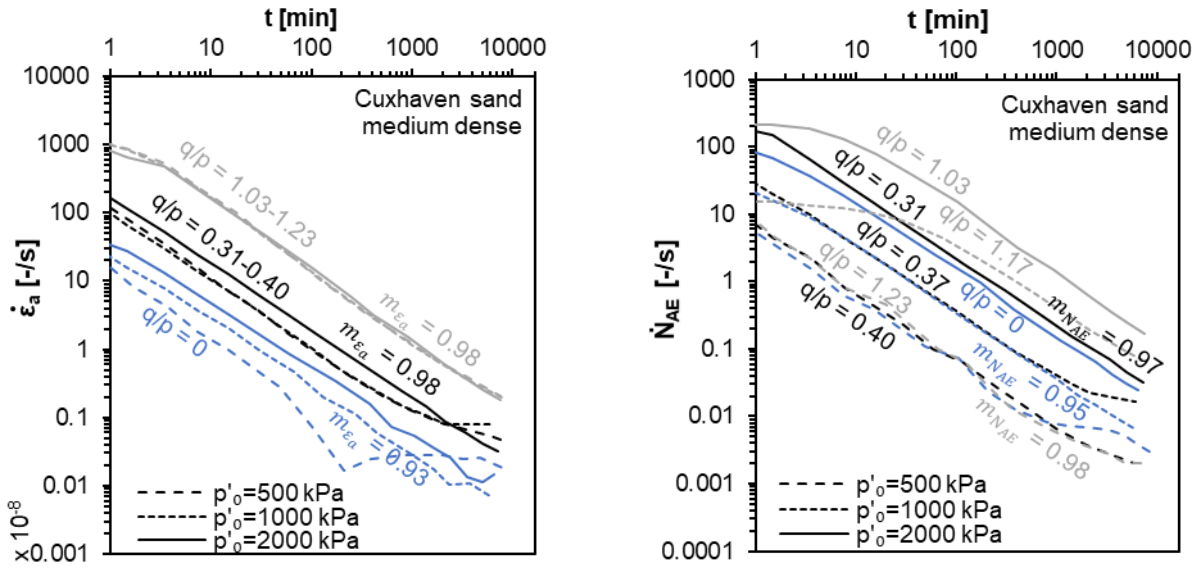

(a) **(b)**

Figure 4.34: (a) Axial strain rate $\dot{\varepsilon}_a$ and (b) rate of number of AE events $\dot{N}_{AE}$ with t for creep phases at varying p'_0 and q/p'-ratios (double logarithmic scale) of medium-dense samples of Cuxhaven sand

The axial creep strain ε_a and the number of AE events N_{AE} during the creep phases are compared in Figure 4.35 (a). The double logarithmic axis used in the diagram indicates approximate linearity between these two measured quantities. The first measured values $\varepsilon_{a,0}$ and $N_{AE,0}$ plotted in the diagram correspond to the time of t = 10 s after reaching the deviatoric stress q during creep. Thereby, the initial axial creep strain $\varepsilon_{a,0}$ is larger for the creep phases with higher q/p'-ratio, while the initial number of AE events $N_{AE,0}$ is not following a clear trend concerning the ratio of q/p'. In contrast, the $N_{AE,0}$ increased with higher stress p_0, whereas ε_a was less affected. An exception is measured for the creep phase at q/p' = 1.17 and p'_0 = 1000 kPa, which has a lower value of $N_{AE,0}$ than the experiment at p'_0 = 500 kPa. A change of the linear relationship between $\log(\varepsilon_a)$ and $\log(N_{AE})$ is noticed for samples at p'_0 = 2000 kPa and q/p' > 0.31 as well as for the test at p'_0 = 1000 kPa and the highest applied stress ratio of q/p' = 1.17. A reason for this behavior might be related to the higher values of t_{ref} according to Equation (2.2) or Equation (3.21), respectively. The varying time at the beginning of the creep phase, where the linear trend has not been established due to the preceding loading phase, is more significant because of the double logarithmic data representation.

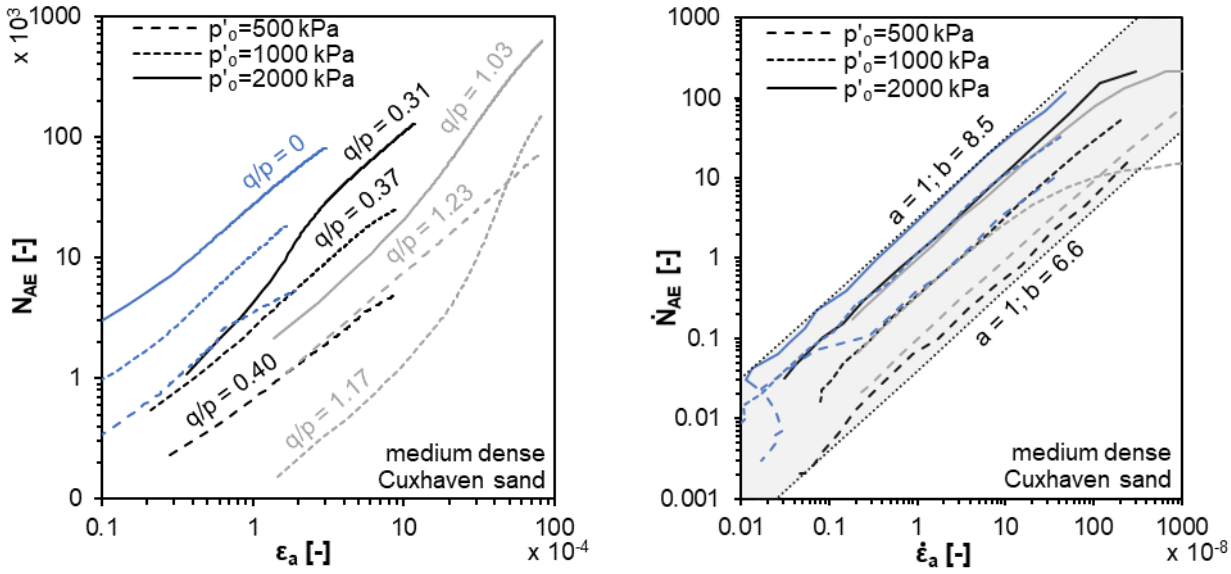

Figure 4.35: (a) Axial strain ε_a versus number of AE events N_{AE} and (b) axial strain rate $\dot{\varepsilon}_a$ versus rate of number of AE events $\dot{N}_{AE}$ of samples of medium-dense Cuxhaven sand

The diagram of Figure 4.35 (b) compares the axial strain rate $\dot{\varepsilon}_a$ in log-scale with the rate of the number of AE events $\dot{N}_{AE}$ in log-scale. Accordingly, a relationship between $\dot{\varepsilon}_a$ and $\dot{N}_{AE}$ is suggested for the investigated material as follows

$$\dot{N}_{AE} = 10^b \cdot {\dot{\varepsilon}_a}^a, \tag{4.8}$$

where a and b are assumed to be material-dependent parameters and as well probably dependent on the initial density. The parameter a is stress state-independent, whereas b has to be determined as a function of p' and q. For the investigated ranges of ${p'}_0$ and q/p', the parameter a can be approximated as a = 1 for all experiments, whereas b varies in the range between 6.6 and 8.5: With increasing consolidation pressure ${p'}_0$, b increases. Furthermore, b is slightly higher for isotropic compared to anisotropic stress conditions. The experiments at anisotropic stress $q/p' > 0$ with constant ${p'}_0$ show similar values of b.

Aging is presented in diagrams showing curves of $\Delta G_{0,t}/G_{0,t=60s}$ against t for creep phases at a deviatoric loading of q = 0.2 q_{max} and 0.9 q_{max} in Figure 4.36.

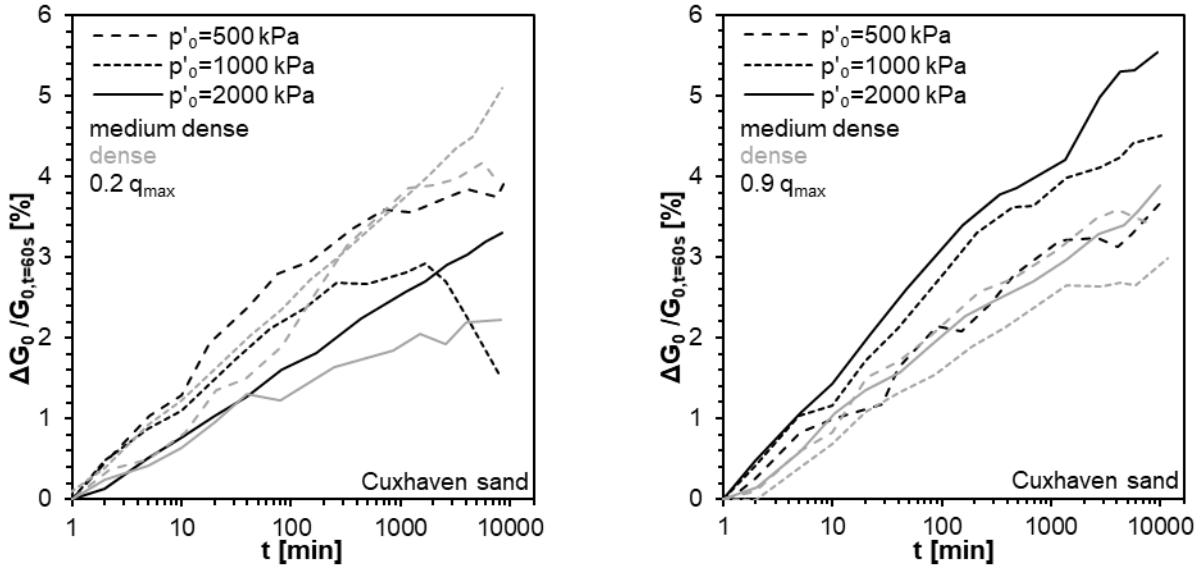

(a) **(b)**

Figure 4.36: $\Delta G_{0,t}/G_{0,t=60s}$ at (a) 0.2 q_{max} and (b) 0.9 q_{max} for varying p'_0 of medium-dense and dense samples of Cuxhaven sand

The evolution of $\Delta G_{0,t}/G_{0,t=60s}$ with time at q = 0.2 q_{max} (Figure 4.36(a)) indicates that the lower the confining pressure p'_0, the stronger the aging. This trend was already observed for aging under isotropic stress, e.g., in Section 4.4.2 or Gao et al. (2013). A systematic dependence on the initial density $D_{r,0}$ is not evident. At p'_0 = 2000 kPa, medium-dense samples showed higher aging rates than dense samples. At p'_0 = 500 kPa and 1000 kPa, respectively, the aging behavior for all samples was similar, or even a more pronounced aging was observed for dense samples. On the contrary, at q = 0.9 q_{max}, a stronger increase of $\Delta G_{0,t}/G_{0,t=60s}$ with increasing p'_0 was mostly observed. Slightly stronger aging was detected for medium-dense samples that observe contractive volumetric creep. Furthermore, at higher deviatoric stress, $\Delta G_{0,t}/G_{0,t=60s}$ appears to increase continuously, at lower deviatoric stress the decrease of the change in shear modulus with time as obtained for the single stage creep tests at isotropic pressure was observed in some cases. After five days of creep, the increase of $\Delta G_{0,t}/G_{0,t=60s}$ for Cuxhaven sand achieved values between 1.5 % and 5.5 %.

It should be noted that a decrease of $\Delta G_{0,t}/G_{0,t=60s}$ with time, as observed for the medium dense sample at a confining pressure of p'_0 = 1000 kPa and during creep at q = 0.2 q_{max} corresponds to a deviation in the time-evolution of the axial strain rate $\dot{\varepsilon}_a$ from the power function defined by Equation (2.3). In fact, as can be seen in Figure 4.34 (a) $\dot{\varepsilon}_a$ decreases with time much slower than indicated by the power function. This correlation between the negative rate of change of the shear modulus and the deviation of $\dot{\varepsilon}_a$ from equation (2.3) has been observed for single-stage creep tests at constant isotropic pressure, see Chapter 4.4.2.2. The observed behavior can be attributed to sudden rearrangement in the grain skeleton due to “unjamming events”.

In the following the time-dependent change of the rate of $\dot{G}_0 = dG_0/dt$ referred to the initial shear modulus at small strain measured 60 seconds after the start of the creep phase $G_{0,t=60s}$ is analyzed. Figure 4.37 shows the relation between $\dot{G}_0/G_{0,t=60s}$ and t. The double logarithmic diagram does not

show negative rates of changes of G_0 that where indeed measured during some tests at comparably high values of t.

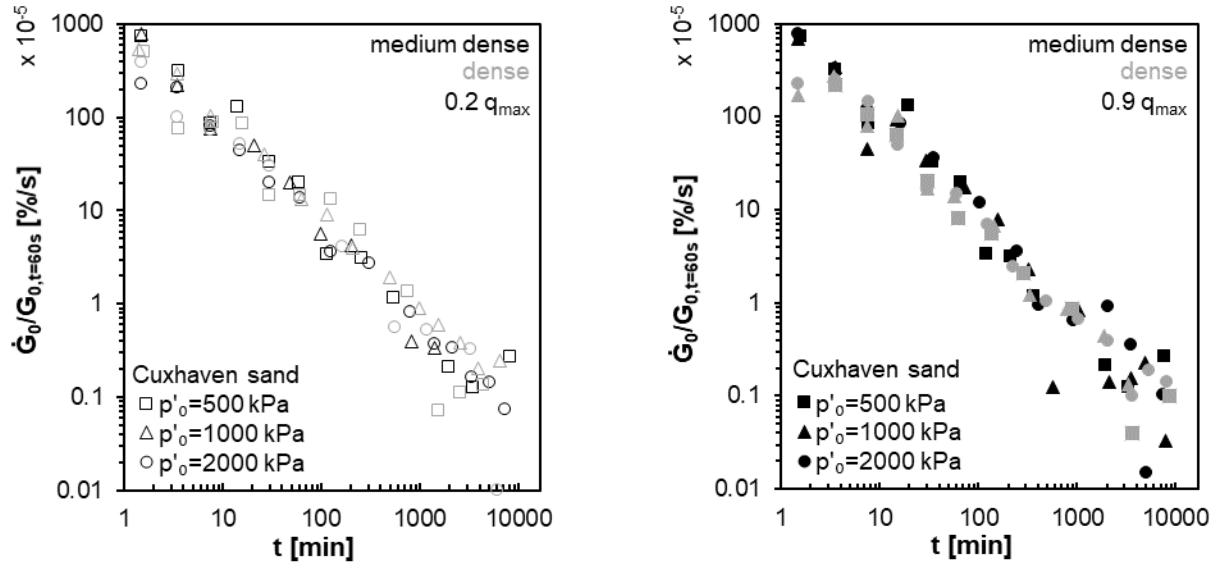

(a) **(b)**

Figure 4.37: $\dot{G}_{0,t}/G_{0,t=60s}$ with time t at (a) 0.2 q_{max} and (b) 0.9 q_{max} for varying p'_0 of medium-dense and dense samples of Cuxhaven sand

The experimental results indicate that the power function in Equation (2.3) for creep also describes the aging behavior at constant deviatoric stress. For the inclination of the individual data from different creep phases a mean value of m = 1.05 was determined. Furthermore, the results as presented by the diagrams of Figure 4.37 show that the normalized rate of change of G_0 is almost independent from p', q and $D_{r,0}$.

For illustrating the relationship between creep and aging, $\dot{G}_{0,t}/G_{0,t=60s}$ is plotted versus $\dot{\varepsilon}_a/\dot{\varepsilon}_{a,t=60s}$ in Figure 4.38 using a logarithmic scale for both axis of the diagram. In addition to the CRS-C-tests, the results from the multi-stage creep tests at different isotropic pressures (see Figure 4.25) indicated as q/p' = 0 are included. Naturally, only positive values of $\dot{G}_{0,t}$ are considered in the plot.

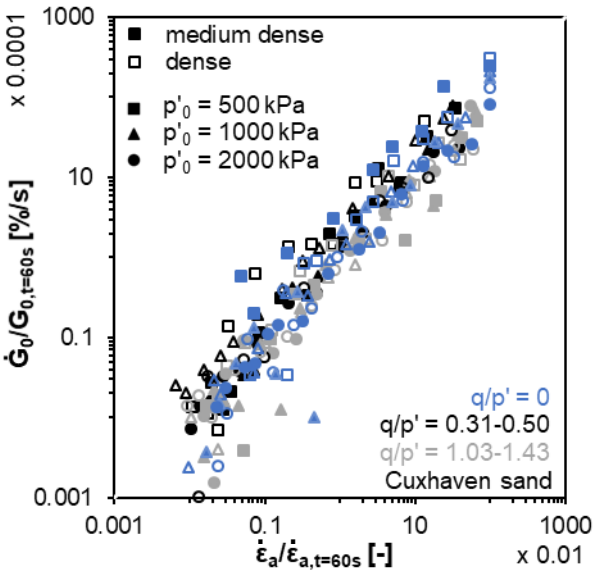

Figure 4.38: $\dot{G}_{0,t}/G_{0,t=60s}$ versus $\dot{\varepsilon}_a/\dot{\varepsilon}_{a,t=60s}$ for varying p'_0 and q/p'-ratios of medium-dense and dense samples of Cuxhaven sand

The experimental results indicate a linear relationship between the logarithm of $\dot{G}_{0,t}/G_{0,t=60s}$ and the logarithm of $\dot{\varepsilon}_a/\dot{\varepsilon}_{a,t=60s}$ since the exponent is approximately $m \approx 1$, $\dot{G}_{0,t}/G_{0,t=60s} \approx \dot{\varepsilon}_a/\dot{\varepsilon}_{a,t=60s}$.

Conclusions

Multi-stage creep tests at different deviatoric stress q during drained triaxial compression were performed on dry, medium-dense, and dense samples of silica sand from Cuxhaven. Creep and aging were investigated at anisotropic stress at about q = 0.2 q_{max} and 0.9 q_{max}. The following conclusions are drawn:

- The results confirm that volumetric creep strain ε_{vol} at deviatoric stress q can be dilative, contractive, or zero depending on the volumetric strain at the beginning of creep. The extent of dilative creep ε_{vol} seems to be limited.
- The number of AE events N_{AE} and the axial strain ε_a show a similar evolution with time during creep. The relationship between ε_a and N_{AE}, respectively, with t in log-scale can be described by the coefficients C and C_{AE}, which are not constant during the creep phase. However, it seems that after a certain time since the start of the creep phase, the coefficients are independent of the elapsed time. C and C_{AE} depend on p', q/p'-ratio and the initial density $D_{r,0}$.
- The rates $\dot{\varepsilon}_a$, $\dot{N}_{AE}$, and $\dot{G}_{0,t}/G_{0,t=60s}$ during creep follow a power function with time, whereby the exponents m_{ε_a}, $m_{N_{AE}}$, and m_{G_0}, respectively, are about the unity for all conducted tests. The rates at the onset of the creep phase $\dot{\varepsilon}_{a,0}$ and $\dot{N}_{AE,0}$ increase with p' and q/p'-ratio, whereas the rate $\dot{G}_{0,t=0}$ seems to be independent of the stress.
- The relationship between $\log(\dot{\varepsilon}_a)$ and $\log(\dot{N}_{AE})$ described by a power law using the parameters a and b suggests that $\dot{\varepsilon}_a$, as well as ε_a, can be evaluated from $\dot{N}_{AE}$. For the conducted experiments, parameter a is stress independent, whereas parameter b depends on the stress. Both parameters are most likely dependent on the material and the density.

- Aging at q = 0.2 q_{max} is similar to the aging behavior at isotropic stress: Stronger aging for lower confining pressures p'_0 and thus the opposite behavior than for the axial creep strain ε_a. On the contrary, the change of G_0 at q = 0.9 q_{max} increases with increasing p'_0.
- Dilatant creep (dense samples) is accompanied by slightly less ageing expressed by $\Delta G_0/G_{0,t=60s}$ than contractive creep (medium-dense samples).
- The relationship between $\log(\dot{G}_{0,t}/G_{0,t=60s})$ and $\log(\dot{\varepsilon}_a/\dot{\varepsilon}_{a,t=60s})$ was found to be linear.

The combined study of aging and creep at different loadings of constant deviatoric stress using triaxial compression tests showed that the influences of the particle distortions during deviatoric loading are important. The deviatoric loading leads to a degradation of the structure of the particle assembly determining the structure at the beginning of a creep phase, which significantly influences creep and aging.

5. Conceptual model and discussion

In the following, a conceptual model assuming a time-dependent behavior of normal and shear forces at particle contacts is presented to explain the experimental observations qualitatively. The conceptual model also attempts to unify our considerations with the descriptions of micromechanical processes given by the literature. The difference between creep and aging under isotropic and deviatoric states is highlighted. A proposal for the relationship between creep and aging concludes the experimental investigations.

5.1 Change of the particle assembly during creep under isotropic pressure[14]

As described by Yusa (2015), the soil fabric, also termed as the structure of particle assembly in the scope of this thesis, at the onset of a creep phase plays a significant role in the evolution of aging. During isotropic compression, the distribution and orientation of the particles become random (Bowman & Soga, 2003; Thornton & Barnes, 1986; Wiebicke et al., 2020). Thus, at the onset of creep (t = 0 s) of single-stage creep tests at isotropic stress, the particle assembly is rather homogeneous in terms of the governing force chains (no clustering). The conceptual model considering isotropic loading is shown in Figure 5.1. The vertical lines represent schematically force chains, which carry the pressure acting on the sample. For the sake of simplicity despite the isotropic loading the illustration shows only force chains in the vertical direction and omits the illustration of horizontally aligned force chains. Certainly, force chains will develop in both vertical and horizontal directions during isotropic compression.
Initially, the force chains are evenly distributed but relatively unstable and may redistribute randomly at a comparably high frequency (State A in Figure 5.1).

Initial instability of force chains results from the varying strength and stiffness at the contacts between particles. Each particle contact shows time-depended behavior as a function of the magnitude of the transferred shear and normal force. Creep rupture of force chains during creep at the mesoscale may occur delayed at loadings close to the breakage of small particle asperities changing the particle morphology and surface texture. Under high loads, extensive particle breakage may happen. The weakest contacts fail or at least change at a faster rate during phases of loading and at the start of a creep phase. A more pronounced initial instability of the force chains and the resulting rearrangement of particles causes the creep rate to show the largest value at the beginning of a creep phase. With increasing time during creep, the particles cluster and interlock (Bowman & Soga, 2003). In comparison to the initial state, contact forces concentrate in fewer but comparably stiffer so-called “strong” force chains (State B in Figure 5.1.). The normal and the tangential contact forces carried by particle clusters within the strong force chain increase, whereas they decrease in the “weak” cluster. The stronger and more localized the force chains, the initially stiffer the assembly of particles is. Following

[14] The content has been published in Jessen et al. (2023).

this, the number of sliding contacts tends towards a minimum, and the creep rate decreases. Nonetheless, the stiffness of strong force chains is not permanent due to delayed processes at the microscale causing softening at the contact and particle breakage of different intensity, ranging from changes of surface texture at the contacts, breakage of particle asperities to more comprehensive particle failure. An abrupt destabilization of the concentrated force chains may occur after some of the strongly loaded contacts within a force chain fail, possibly causing a chain reaction through which the condition of several contacts changes from stick to slip at almost the same time.

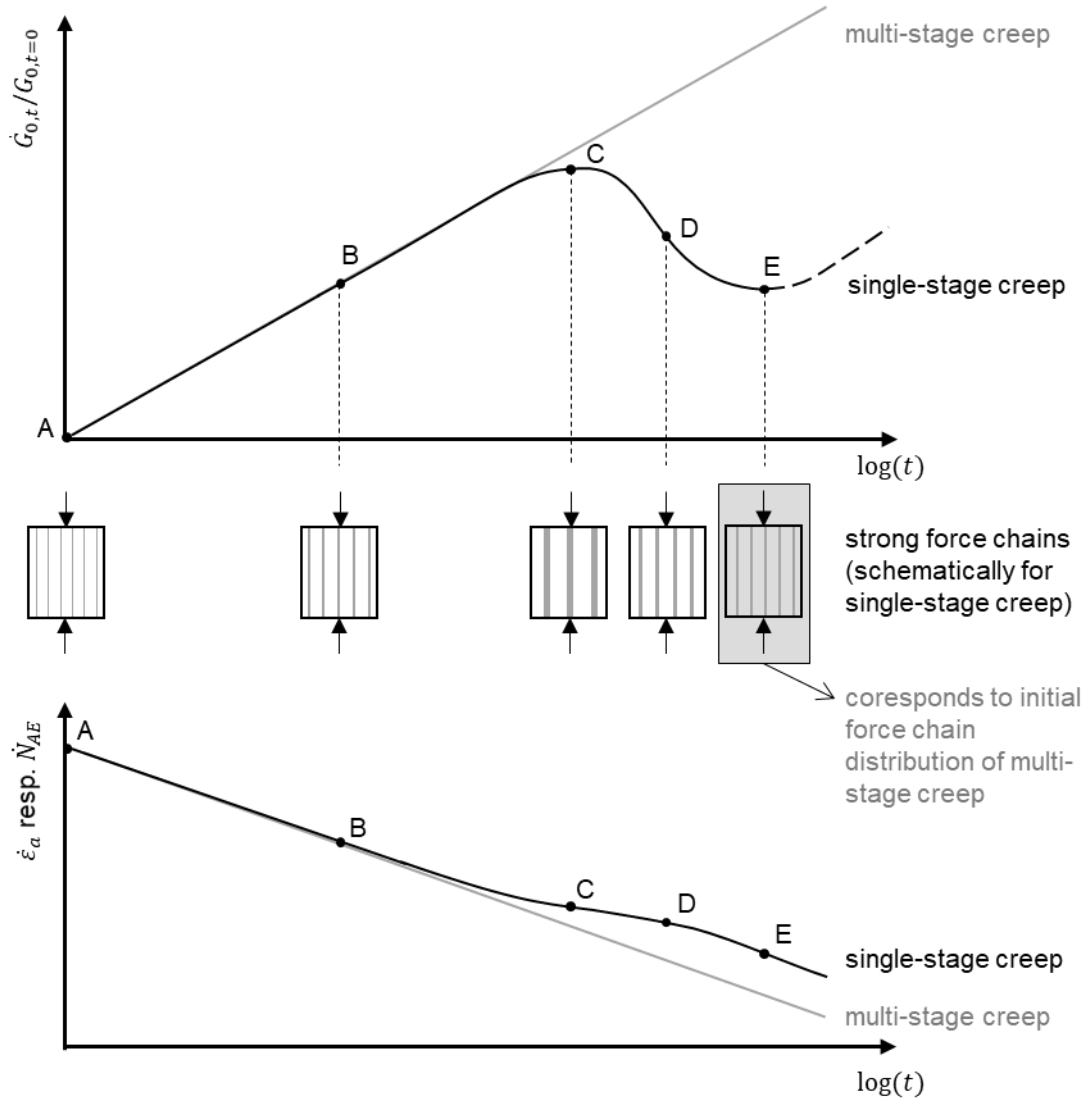

Figure 5.1: Schematic representation of the conceptual model explaining creep and aging behavior under isotropic conditions in granular material (for simplicity only the vertical loading direction is illustrated) (Jessen et al., 2023)

State C is interpreted as the onset of failure of the strong force chains. This state corresponds to the maximum value of $\Delta G_{0,t}/G_{0,t=0}$ within the observation time and the maximum fluctuation of contact forces. Abrupt contact slip and particle rearrangement are associated with a discrete release of elastic energy. The detected sudden changes in the recording of the signal burst energy E (Figure 4.22) indicate that abrupt energy releases happen during creep. However, because of the limitations of the

conducted AE measurements, it is not possible to capture the energy conversion occurring precisely at state C in the experiments.
The collapse of the strong force chains leads to a contact force redistribution from the previously strongly to the previously weakly loaded particle clusters. The temporary destabilization of the particle assembly at state C causes the non-permanent stagnation of the creep rate observed in the experiments. The process of restabilization from C to E takes a comparably long time in contrast to the initial stabilization. These differences regarding the increasing stiffness rate may be associated with secondary collapse effects, which are comparable to aftershocks occurring days and weeks after strong earthquakes. During the restabilization, the structure evolves toward a more homogeneous force distribution in comparison with state C. Eventually, the aging process will continue after point E. Macroscopically, the different rates at which stiffness increases are indicated by the changing exponent m in Equation (4.6) describing the time-dependent evolution of $\dot{\varepsilon}_a$ and $\dot{N}_{AE}$ respectively.
As mentioned, the initial fabric and force chain distribution within the particle assembly is influenced by the loading history. Assuming that the duration of previous creep phases in multi-stage creep tests is long enough to induce destabilization, the initial structure at the start of the subsequent creep phases is more stable than at the start of a creep phase in a single-stage test. Thus, the monotonic increase of the shear modulus at small strain observed in the creep phases of multi-stage creep tests results from the homogenization process of force chains achieved in the previous creep phase.

5.2 Change of the particle assembly during creep under deviatoric stress[15]

Time effects such as the change in creep strain expressed by $\dot{\varepsilon}_a$ and $\dot{\varepsilon}_{vol}$, respectively, as well as ageing quantified by $\dot{G}_{0,t}$ at constant deviatoric stress ($\dot{q}$ = 0) depend on the effective mean pressure p' and the deviatoric stress q. Looking at the particle scale, an increasing mean pressure p leads to a stabilization of the force chains due to increasing normal forces at the particle contacts. In contrast, an increasing deviatoric stress q leads to a destabilization due to rearrangement of the particles, as the tangential forces at the particle contact increase. In drained triaxial compression tests, both p' and q increase, leading to a counterplay of the above effects. According to the presented results, at high values of q, the destabilization process during creep dominates.

The initial fabric of the particle assembly plays an essential role characterizing the time-dependent processes at micro- and mesoscale. During deviatoric loading, the strong force chains initially concentrate in the direction of the principal stresses. A destabilizing state is reached after increasing deviatoric loading, i.e., the particle structure of strong force chains dissolves marking the phase of dilatant behavior.
Thus, the particle assembly of samples that were examined by conducting a creep phase at a deviatoric stress of $q = 0.2q_{max}$ resembles a state of of comparably homogeneously distributed force chains. Weak contacts that are prone to an early time-dependent failure are moreover already matured. Ageing, assessed by an increase in $\Delta G_{0,t}/G_{0,t=60}$, as well as contractive volumetric creep deformation was observed during all phases of creep. This behavior is similar to the so-called isotropic multi-stage creep phases shown in Figure 5.1.

[15] The content has been published in Jessen et al. (2024)

With increasing deviatoric stress q, destabilization due to particle rearrangements becomes more pronounced. The destabilization is expressed by a decreasing shear modulus at small strain G_0 with increasing deviatoric stress q (see Figure 4.29). Thus, creep at a deviatoric stress of q = 0.9q_{max} begins in a destabilized state, and the strong force chains must be rebuilt with time.

As expected, the experimental study indicates that dilatant creep results from an increase in radial strain ε_r, i.e. the sample radius. This results from buckling of force chains formed in the axial direction. Figure 5.2 shows a conceptual model considering the mechanical processes at the scale of force chains and the particle assembly. A dense particle assembly can only achieve stabilization by evasion of the particles in the radial direction.

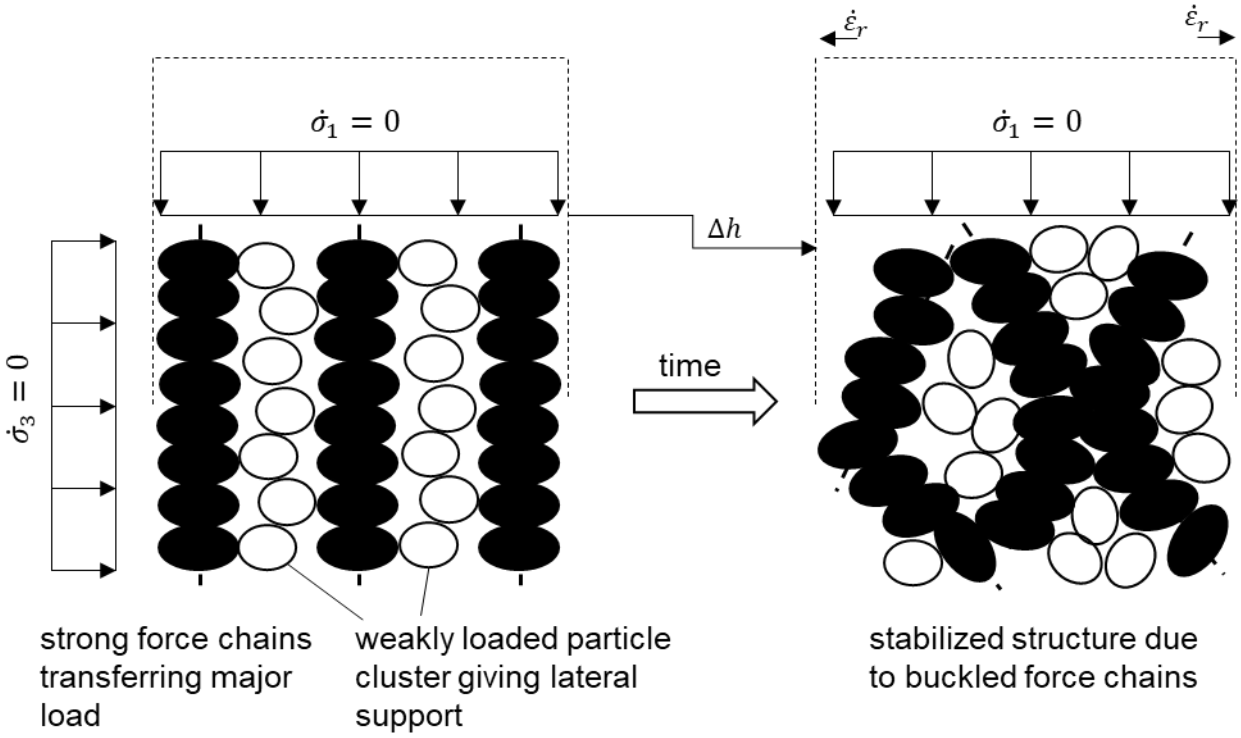

Figure 5.2: Conceptual model on mesoscale explaining dilatant behavior during creep at constant deviatoric stress

5.3 Concluding remarks on the relationship between creep and aging

The experimentally identified correlation between the rate of small-strain stiffness, the rate of the number of acoustic emissions, and the rate of axial strain indicates a strong causality. It can therefore be concluded that both time-dependent phenomena are based on related micromechanical processes:

Changes in contact forces and particle rearrangements that lead to the formation, degradation, and reconstruction of force chains and, thus, to changes in the structure of the particle assembly result in a macroscopically measurable change in density (creep deformation). This process leads, subsequently, to a more stable structure of the particle assembly, as the buckled force chains form a self-

supporting network. At the same time, however, already-aged particle contacts are destroyed, and the aging process begins again at newly formed contacts. Therefore, the sudden loss of particle contacts enhances the development of creep deformation while counteracting the extent of aging achieved by homogenization of force chains, contact forces, and contact maturing.

Once a stable structure is reached, such as in the multi-stage creep phases after an initialization phase, a proportional relationship can be found between the evolution of creep strains and aging, which is determined by the change in small-strain shear modulus. The relation of $\log\left(\dot{G}_{0,t}/G_{0,t=0s}\right)$ and $\log\left(\dot{\varepsilon}_a/\dot{\varepsilon}_{a,t=60s}\right)$ shown in Figure 4.38 appears to be proportional. The exponent of the power law is again approximately equal to one. This means, that if the axial creep strain rate decreases linearly with time in double logarithmic scale, the shear modulus G_0 also increases at a decreasing rate on a double logarithmic scale.

The absolute value of creep and aging is therefore directly related to the initialization phase before the proportional relationship is reached. The stress-dependent creep and aging behavior corresponds to the different initial rates, followed by an almost identical exponential decrease in the rates.

6. Summary, discussion, and outlook

The present work collects, evaluates, and interprets the state-of-the-art of the time-dependent behavior of granular materials, including creep, strain rate dependency, and aging. A comprehensive experimental study was performed to quantify the time- and rate-dependent behavior of granular materials under oedometric and triaxial conditions and to find the relationship between creep and aging.

For this purpose, an oedometer test cell and two experimental setups for triaxial tests were planned and put into operation. The setups and measurement techniques were specifically designed for the combined analysis of creep and aging. In the triaxial tests the volume change during creep was measured using the cell-in-cell principle. Aging during creep was assessed by the change in small-strain shear modulus over time, which was determined by the shear wave velocity. Therefore, Bender Elements and ultrasonic devices were adapted to the triaxial test setups. In addition, acoustic emissions were recorded during the creep phases to detect micromechanical processes considered to happen at the scale of individual particles and their contacts. The experimental methods, limitations, and evaluation methods for the simultaneous analysis of creep and aging were explained in detail, for which no experience was yet available at the laboratory.

Cuxhaven sand, a natural silica sand taken onshore close to the German North Sea, and the artificially produced corundum were investigated. The materials differ in their particle size distribution and in the parameters of particle shape and particle strength. Creep and aging induced by mechanical processes were the focus of this study. Thus, dry samples were examined to minimize, e.g., chemical effects where pore water may play a significant role. The samples were prepared by air pluviation and dry funnel deposition. The air pluviator and the specimen mold used for the triaxial test samples were specially designed for the investigated materials.

So-called multi-stage oedometer tests with creep phases at axial stresses between 300 kPa and 6000 kPa were initially carried out on Cuxhaven sand. The tests confirmed by the correlation of axial strain and the number of acoustic emissions that acoustic emissions during creep are linked to the mechanical processes at micro- and mesoscale. In addition, the study shows that by recording micromechanical events using the acoustic emission analysis, creep deformation is well observable beyond the capabilities of high-accuracy displacement transducers. The one-dimensional compression tests showed that acoustic emissions follow the same trend as the axial creep deformation. Consequently, the relationship between the number of acoustic emission events and the time in logarithmic scale of a creep phase could be described by a coefficient C_{AE} similar to the well-known coefficient C used for representing creep.

Single- and multi-stage creep phases during drained triaxial compression tests were performed on Cuxhaven sand and partly on corundum to investigate the aging and creep behavior at different stresses and varying initial densities. Moreover, the dependence of creep and aging on the loading

history was studied. Creep phases with a duration of at least five days at isotropic stresses of p'_0 = 500 kPa, 1000 kPa, and 2000 kPa as well as at different deviatoric stresses q, in particular q = 0.2q_{max} and q = 0.9q_{max}, where q_{max} is associated to the maximum shear strength of the materials determined from drained triaxial compression tests, were investigated.

The results confirm and complement the dependencies on the state parameters of creep and aging of granular materials found in the literature:

- The extent of aging increases with a decrease in isotropic confining stress, while the axial creep strain shows the opposite behavior.
- The number of acoustic emissions representing the micromechanical processes within the investigated samples follow the evolution of axial strain.
- Axial creep strain decreases with increasing initial density. In contrast, a dependency on the initial density for the extent of aging is not trivial.
- The loading history influences creep and aging, as the initial fabric of the granular material at the beginning of a creep phase is crucial. The initial fabric is related to the homogeneity and pattern of strong force chains as well as the rate at which these strong force chains fluctuate. Single-stage creep tests showed after an initial increase a non-permanent decrease in the small-strain shear modulus with time, which was not investigated during the multi-stage creep phases where the change of the small-strain shear modulus seemed to increase monotonously with time. In addition, during the single-stage creep phases, the samples showed higher creep strains, but less aging compared to samples during multi-stage creep phases.
- Increasing creep strain with increasing q/p'-ratio was observed. The dependency of aging on the deviatoric stress q could not be clarified, as aging at q = 0.2 q_{max} and 0.9 q_{max} showed no clear distinction. A main problem is that the deviatoric stress and the mean stress were varied simultaneously.

An exponential approach to describe the axial strain rate, the rate of the number of AE events, and the rate of change in small-strain shear modulus with time was found, with exponents similar for all tests performed, ranging from 0.9 to 1.17. Furthermore, the results of the acoustic emission measurement of the single- and multi-stage creep phases at isotropic pressure showed that the Gutenberg-Richter relationship applies to micromechanical processes. The a-value can indicate the damage intensity of particles. The evolution of the signal burst energy confirmed the time-dependent occurrence of sudden particle rearrangements based on static fatigue effects at the particle contacts.

The results confirm that for triaxial compression tests on an angular to round silica sand the volumetric strain can increase, decrease, or remain almost the same with time at constant deviatoric stress. At a deviatoric stress, where the sample showed contractant behavior during conventional drained triaxial compression tests, creep resulted in a volume reduction. At a deviatoric stress, where dilative behavior is experienced at the onset of creep, an increase in volume was observed during creep. The extent of dilative creep appeared to be limited.

Furthermore, triaxial compression tests with varying but throughout the individual tests constant axial strain rates were performed on Cuxhaven sand and corundum of different densities to evaluate the rate dependency of granular materials. The results showed a negligible effect of the axial strain rate

on the shear strength of the tested specimen. An additional test including jumps of the axial strain rate was performed on Cuxhaven sand and confirmed that the influence of a sudden change of the axial strain rate is non-permanent and follows the TESRA behavior. While maintaining the constant strain rate after a jump of the axial strain rate, the sample response converges to that of the corresponding conventional triaxial compression test.

It is concluded that creep and aging are based on interacting micromechanical processes that lead to a change in the fabric. The initial soil structure at the beginning of creep is crucial, thus creep and aging are dependent on loading history. A conceptual model describes the reorganization of the particle structure during creep under isotropic pressure and deviatoric stress.
A counterplay between the homogenization of contact forces and the occurrence of spontaneous losses of particle contacts determines the macroscopically measurable behavior. A proportional relationship between $\log\left(\dot{\varepsilon}_a/\dot{\varepsilon}_{a,t=60s}\right)$ and $\log\left(\dot{G}_{0,t}/G_{0,t=60s}\right)$ for samples with an initially stable structure was found. The relationship between creep and aging is almost independent of mean stress, deviatoric stress, and initial density.

The results of the investigations provide a well-documented experimental database comprising the state-of-the-art and novel measurement techniques applied to element tests. The results can be used for the development, validation, and calibration of advanced contact models required for the realistic simulation of time- and rate-dependent behavior in granular material, e.g., using the discrete element method.

Further experimental and numerical investigations considering the individual material properties at different scales of observations will be necessary to elaborate further on the dependencies. In addition, especially in the context of boundary value problems linked to applied challenges as they exist in naturally or anthropogenically formed soils, further effects, such as the behavior at different degrees of water saturation, varying chemistry of the pore water, and temperature influence, can be investigated to better understand, e.g., the increase in pile bearing capacity or resistance measured by penetration tests and plate loading tests. Another field of possible future investigations concerns the extension of scale and time of experimental observation.

References

Afifi, S. S., & Woods, R. D. (1971). Long-Term pressure effects on shear modulus of soils. *Journal of the Soil Mechanics and Foundation Division*, *97*(10), 1445–1460.

Anderson, D. G., & Stokoe, K. H. (1978). Shear Modulus: A Time-Dependent Soil Property. *Dynamic Geotechnical Testing, ASTM STP 654*, 66–90.

Andò, E., Dijkstra, J., Roubin, E., Dano, C., & Boller, E. (2019). A peek into the origin of creep in sand. *Granular Matter*, *21*(11). https://doi.org/10.1007/s10035-018-0863-5

Angerer, L. (2019). *Experimental evaluation of the suction-induced effective stress and the shear strength of as-compacted silty sands* [Dissertation]. Technische Universität München.

ASTM International (2019). *Standard Test Method for Determination of Shear Wave Velocity and Initial Shear Modulus in Soil Specimens using Bender Elements*. ASTM International.

ASTM International (2020). *Standard Test Methods for One-Dimensional Consolidation Properties of Soils Using Incremental Loading.* ASTM International.

Augustesen, A., Liingaard, M., & Lade, P. V. (2004). Evaluation of Time-Dependent Behavior of Soils. *International Journal of Geomechanics*, *4*(3), 137–156. https://doi.org/10.1061/(ASCE)1532-3641(2004)4:3(137)

Baxter, C. D. P., & Mitchell, J. K. (2004). Experimental Study on the Aging of Sands. *Journal of Geotechnical and Geoenvironmental Engineering*, *130*(10), 1051–1062. https://doi.org/10.1061/(ASCE)1090-0241(2004)130:10(1051)

Bock, B., Vogt, S., & Cudmani, R. (2021). Zeitabhängige Änderung des Schubmoduls bei kleinen Scherdehnungen in granularen Materialien. *Proceedings of the 3. Bodenmechanik Tagung, Online*. https://dggt.de/images/PDF-Dokumente/bm-02s.pdf

Bock, B., Vogt, S., & Cudmani, R. (2023). Acoustic Emission During Creep under Triaxial Compression. *Proceedings of the 8th International Symposium on Deformation Characteristics of Geomaterials (IS-Porto)*. https://www.issmge.org/uploads/publications/121/122/isdcg2023-22-1-c.pdf

Bock, B. A.-M., Levin, F., Vogt, S., & Cudmani, R. (2022). Acoustic Emission of Sand during Creep under Oedometric Compression. *Geotechnical Testing Journal*, *45*(2), 20210007. https://doi.org/10.1520/GTJ20210007

Bowman, E. T., & Soga, K. (2003). CREEP, AGEING AND MICROSTRUCTURAL CHANGE IN DENSE GRANULAR MATERIALS. *Soils and Foundations*, *43*(4), 107–117. https://doi.org/10.3208/sandf.43.4_107

Brignoli, E. G. M., Gotti M., & Stokoe, K. H. (1996). Measurement of Shear Waves in Laboratory Specimens by Means of Piezoelectric Transducers. *Geotechnical Testing Journal*, *19*(4), 384–397.

Brzesowsky, R. H., Hangx, S. J. T., Brantut, N., & Spiers, C. J. (2014). Compaction creep of sands due to time-dependent grain failure: Effects of chemical environment, applied stress, and

grain size. *Journal of Geophysical Research: Solid Earth*, *119*(10), 7521–7541. https://doi.org/10.1002/2014JB011277

Buisman, A. S. K. (1936). Results of Long Duration Settlement Tests. *Proceedings of the 1st International Conference on Soil Mechanics and Foundation Engineering*(I), Article F-7, 103–106.

Carroll, R., Carotenuto, P., Dano, C., Salama, I., Silva, M., Rimoy, S., Gavin, K., & Jardine, R. J. (2020). Field experiments at three sites to investigate the effects of age on steel piles driven in sand. *Géotechnique*, *70*(6), 469–489. https://doi.org/10.1680/jgeot.17.P.185

Cascante, G., & Santamarina, J. C. (1996). Interparticle Contact Behavior and Wave Propagation. *Journal of Geotechnical Engineering*, *122*(10), 789–872. https://doi.org/10.1061/(ASCE)0733-9410(1996)122:10(831)

Cha, M., Santamarina, J. C., Kim, H.-S., & Cho, G.-C. (2014). Small-Strain Stiffness, Shear-Wave Velocity, and Soil Compressibility. *Journal of Geotechnical and Geoenvironmental Engineering*, *140*(10), Article 06014011. https://doi.org/10.1061/(ASCE)GT.1943-5606.0001157

Charles-Cruz, C. A., Cousens, T. W., & Stewart, D. I. (2008). *Compressibility and Creep Behaviour of Hydraulically Placed PFA and Mine Tailings Fills*. 12th International Conference of International Association for Computer Methods and Advances in Geomechanics (IACMAG), Goa, India.

Chow, F. C., Jardine, R. J., Nauroy, J. F., & Brucy, F. (1997). Time-related increases in the shaft capacities of driven piles in sand: Technical Note. *Géotechnique*, *47*(2), 353–361.

Colliat-Dangus, J. L., Desrues, J., & Foray, P. (1988). Triaxial Testing of Granular Soil Under Elevated Cell Pressure. In R. Donaghe, R. Chaney, & M. Silver (Eds.), *Advanced Triaxial Testing of Soil and Rock* (290-310). ASTM International. https://doi.org/10.1520/STP29082S

Cudmani, R., Jörger, R., & Wolski, K. (2011). Sydney, Hafenerweiterung Port Botany: Wirtschaftliche Lösungen für höchste geotechnische Anforderungen. In Technische Universität Berlin (Chair), *Proceedings of the 7. Hans-Lorenz-Symposium*.

Da Viana Fonseca, A., Ferreira, C., & Fahey, M. (2009). A Framework Interpreting Bender Element Tests, Combining Time-Domain and Frequency-Domain Methods. *Geotechnical Testing Journal*, *32*(2), 100974. https://doi.org/10.1520/GTJ100974

Dai, S., Wuttke, F., & Santamarina, J. C. (2013). Coda Wave Analysis to Monitor Processes in Soils. *Journal of Geotechnical and Geoenvironmental Engineering*, *139*(9), 1504–1511. https://doi.org/10.1061/(ASCE)GT.1943-5606.0000872

Daramola, O. (1980). Effect of consolidation age on stiffness of sand. *Géotechnique*, *30*(2), 213–216.

Deutsche Institut für Normung e.V. (2017). *Geotechnische Erkundung und Untersuchung - Laborversuche an Bodenproben - Teil 4: Bestimmung der Korngrößenverteilung*. Beuth Verlag GmbH.

Deutsches Institut für Normung e.V. (2012). *Geometrische Produktspezifikation (GPS) - Oberflächenbeschaffenheit: Flächenhaft - Teil 2: Begriffe und Oberflächen-Kenngrößen*. Beuth Verlag GmbH.

Di Benedetto, H., Tatsuoka, F., & Ishihara, M. (2002). Time-Dependent Shear Deformation Characteristics of Sand and their Constitutive Modelling. *Soils and Foundations*, *42*(2), 1–22. https://doi.org/10.3208/sandf.42.2_1

Di Benedetto, H. Tatusoka, F., & Ishihara, M. (2002). Time dependent shear deformation characteristics of sand and their constitutive modelling. *Soils and Foundations*, *42*(2).

Eber, W. (2007). *Measurements on the Structural Contribution to Friction in Granular Media* [Dissertation]. Technische Universität München, München.

Fernandes, F., Syahrial, A. I., & Valdes, J. R. (2010). Monitoring the Oedometric Compression of Sands with Acoustic Emissions. *Geotechnical Testing Journal*, *33*(5), 102501. https://doi.org/10.1520/GTJ102501

Gao, Y., Chen, Q., Yuan, Q., & Wang, Y.-H. (2023). The kinematics and micro mechanism of creep in sand based on DEM simulations. *Computers and Geotechnics*, *153*, 105082. https://doi.org/10.1016/j.compgeo.2022.105082

Gao, Y., Wang, Y.-H., & Su, J. C. P. (2013). Mechanisms of Aging-Induced Modulus Changes in Sand under Isotropic and Anisotropic Loading. *Journal of Geotechnical and Geoenvironmental Engineering*, *139*(3), 470–482. https://doi.org/10.1061/(ASCE)GT.1943-5606.0000772

Goudarzy, M., König, D., & Schanz, T. (2018). Interpretation of small and intermediate strain characteristics of Hostun sand for various stress states. *Soils and Foundations*, *58*(6), 1526–1537. https://doi.org/10.1016/j.sandf.2018.09.002

Grosse, C. (2008). Introduction. In C. Grosse & M. Ohtsu (Eds.), *Acoustic emission testing: Basics for research - applications in civil engineering* (pp. 3–10). Springer.

Hardin, B. O., & Black, W. L. (1966). Sand Stiffness Under Various Triaxial Stresses. *Journal of the Soil Mechanics and Foundations Division*, *92*(SM2), Article 4712, 27–42.

Hardin, B. O., & Drnevich, V. P. (1972). Shear Modulus and Damping in Soils: Measurement and Parameter Effects (Terzaghi Leture). *Journal of the Soil Mechanics and Foundations Division*, *98*(6), 603–624. https://doi.org/10.1061/JSFEAQ.0001756

Hardy, H. R. (2003). *Acoustic Emission/Microseismic Activity: Volume 1: Principles, Techniques and Geotechnical Applications*. Taylor and Francis.

Howie, J. A., Shozen, T., & Vaid, Y. P. (2002). Effect of ageing on stiffness of very loose sand. *Canadian Geotechnical Journal*, *39*(1), 149–156. https://doi.org/10.1139/t01-085

Hussien, M. N., & Karray, M. (2021). Piezoelectric Ring-Actuator Technique: In-Depth Scrutiny of Interpretation Method. *Geotechnical Testing Journal*, *44*(1), 20180205. https://doi.org/10.1520/GTJ20180205

Jessen, B. A.-M., Cudmani, R., & Vogt, S. (2023). Creep and ageing of granular materials under isotropic pressure. *Acta Geotechnica*(19), 1999–2012. https://doi.org/10.1007/s11440-023-02015-y

Jessen, B. A.-M., Vogt, S., & Cudmani, R. (2024). Combined study of creep and ageing under deviatoric loading in granular materials. *Acta Geotechnica.* Advance online publication. https://doi.org/10.1007/s11440-024-02476-9

Karimpour, H., & Lade, P. V. (2010). Time Effects Relate to Crushing in Sand. *Journal of Geotechnical and Geoenvironmental Engineering*, *136*(9), 1209–1219. https://doi.org/10.1061/(ASCE)GT.1943-5606.0000335

Karimpour, H., & Lade, P. V. (2013). Creep behavior in Virginia Beach sand. *Canadian Geotechnical Journal*, *50*(11), 1159–1178. https://doi.org/10.1139/cgj-2012-0467

Karray, M., Lefebvre, G., Khayat, K., Hussien, M. N., Mhenni, A., Romdhane, M. B., Naji, S., Soliman, N., Diab, G. E.-D., Lashin, I., Ghali, M., Anglade, J., Lapierre, J., Tchabacha, H., & Challouf,

W. (2019). The Piezo-electric Ring Actuator technique (P-RAT) – 16 years of progress. *Proceedings of the GEOSt.John's*.

Karray, M., Romdhan, M. B., Hussien, M. N., & Éthier, Y. (2015). Measuring shear wave velocity of granular material using the piezoelectric ring-actuator technique (P-RAT). *Canadian Geotechnical Journal*, *52*(9), 1302–1317. https://doi.org/10.1139/cgj-2014-0306

Kawaguchi, T., Ogino, T., Yamashita, S., & Kawajiri, S. (2016). Identification method for travel time based on the time domain technique in bender element tests on sandy and clayey soils. *Soils and Foundations*, *56*(5), 937–946. https://doi.org/10.1016/j.sandf.2016.08.017

Koerner, R. M., Lord, A. E., McCabe, W. M., & Curran, J. W. (1976). Acoustic Emission Behavior of Granular Soils. *Journal of Geotechnical Engineering Division*, *102*(GT7), 761–774.

Koerner, R. M., McCabe, W. M., & Lord, A. E. (1981). Acoustic Emission Behavior and Monitoring of Soils. In V. P. Drnevich & R. E. Gray (Eds.), *ASTM STP: Vol. 750. Acoustic Emissions in Geotechnical Engineering Practice, ASTM STP 750* (93-141). ASTM. https://doi.org/10.1520/STP28343S

Kothen, H., & Knufinke, H.-U. (1990). Restsetzungen auf Neulandflächen. *Braunkohle*(10), 24–29.

Krieg, S. (2000). *Viskoses Bodenverhalten von Mudden, Seeton und Klei* (Heft Nr. 150) [Dissertation]. Universität Fridericiana, Karlsruhe.

Krumbein, W., & Sloss, L. L. (1963). *Stratigraphy and sedimentation*. *A series of books in geology.* Freeman.

Kuerbis, R., & Vaid, Y. P. (1988). Sand Sample Preparation—The Slurry Deposition Method. *Soils and Foundations*, *28*(4), 107–118. https://doi.org/10.3208/sandf1972.28.4_107

Kuhn, M. R., & Mitchell, J. K. (1993). New Perspectives on Soil Creep. *Journal of Geotechnical Engineering*, *119*(3), 507–524. https://doi.org/10.1061/(ASCE)0733-9410(1993)119:3(507)

Kuwano, R., & Jardine, R. J. (2002). On measuring creep behaviour in granular materials through triaxial testing. *Canadian Geotechnical Journal*, *39*(5), 1061–1074. https://doi.org/10.1139/t02-059

Kwok, C. Y., & Bolton, M. D. (2010). DEM simulations of thermally activated creep in soils. *Géotechnique*, *60*(6), 425–433. https://doi.org/10.1680/geot.2010.60.6.425

Ladd, R. S. (1978). Preparing Test Specimens Using Undercompaction. *Geotechnical Testing Journal*, *1*(1), 16–23.

Lade, P. V. (2009). Creep, Stress relaxation, and rate effects in sand. In M. Hamza, M. Shahien, & Y. El-Mossallamy (Eds.), *Proceedings of the 17th International Conference on Soil Mechanics and Geotechnical Engineering: The Academia and Practice of Geotechnical Engineering* (pp. 264–267).

Lade, P. V. (2016). *Triaxial testing of soils*. Wiley Blackwell.

Lade, P. V., & Karimpour, H. (2010). Static fatigue controls particle crushing and time effects in granular materials. *Soils and Foundations*, *50*(5), 573–583. https://doi.org/10.3208/sandf.50.573

Lade, P. V., Liggio, C. D., & Nam, J. (2009). Strain Rate, Creep, and Stress Drop-Creep Experiments on Crushed Coral Sand. *Journal of Geotechnical and Geoenvironmental Engineering*, *135*(7), 941–953. https://doi.org/10.1061/(ASCE)GT.1943-5606.0000067

Lade, P. V., & Liu, C.-T. (1998). Experimental Study of Drained Creep Behavior of Sand. *Journal of Engineering Mechanics*, *124*(8), 912–920. https://doi.org/10.1061/(ASCE)0733-9399(1998)124:8(912)

Laloui, L., Pèron, H., Geiser, F., Rifa, A., & Vulliet, L. (2006). Advances in volume measurement in unsaturated soil triaxial tests. *Soils and Foundations*, *46*(3), 341–349.

Lashin, I. (2021). *Assessment of Shear Modulus for Granular Soils, with Small- to Large-Strain Moduli Correlations* [Dissertation]. Université de Sherbrooke, Québec, Canada.

Lee, J.-S., & Santamarina, J. C. (2005). Bender Elements: Performance and Signal Interpretation. *Journal of Geotechnical and Geoenvironmental Engineering*, *131*(9), 1063–1070. https://doi.org/10.1061/(ASCE)1090-0241(2005)131:9(1063)

Lee, K. L. (1977). Adhesion Bonds in Sands at high pressures. *Journal of the Geotechnical Engineering Division*, *103*(GT8), 908–913.

Lei, X., & Kusunose, K. (1999). Fractal structure and characteristic scale in the distributions of earthquake epicentres, active faults and rivers in Japan. *Geophysical Journal International*, *139*, 754–762.

Leong, E. C., Agus, S. S., & Rahardjo, H. (2004). Volume Change Measurement of Soil Specimen in Triaxial Test. *Geotechnical Testing Journal*, *27*(1), 10704. https://doi.org/10.1520/GTJ10704

Leong, E. C., Yeo, S. H., & Rahardjo, H. (2005). Measuring Shear Wave Velocity Using Bender Elements. *Geotechnical Testing Journal*, *28*(5), 488–498.

Levin, F. (2021). *Time-Dependent Compression Behavior of Sands under Oedometric Conditions* [Dissertation]. Technische Universität München.

Levin, F., Back, M., Vogt, S., & Cudmani, R. (2022). Experiment-based estimation of the settlement potential due to dynamic loads from heavy vehicle traffic on the A 44n motorway built on the dump of the Garzweiler opencast mine. *Transportation Geotechnics*, *32*, 100674. https://doi.org/10.1016/j.trgeo.2021.100674

Levin, F., Cudmani, R., & Vogt, S. (2019). Experimental results and constitutive model for time-dependent behaviour of sands under oedometric compression. In H. Sigursteinsson, S. Erlingsson, & B. Bessason (Eds.), *Proceedings of the XVII European Conference on Soil Mechanics and Geotechnical Engineering.* Icelandic Geotechnical Society.

Levin, F., Vogt, S., & Cudmani, R. (2019). Time-dependent behaviour of sand with different fine contents under oedometric loading. *Canadian Geotechnical Journal*, *56*(1), 102–115. https://doi.org/10.1139/cgj-2017-0565

Li, X., Liu, J., & Li, J. (2022). Fractal dimension, particle shape, and particle breakage analysis for calcareous sand. *Bulletin of Engineering Geology and the Environment*, *81*(3). https://doi.org/10.1007/s10064-022-02585-3

Li, Z., Wang, Y.-H., & Chow, J. K. (2018). Density Effect and Associated Unjamming Events on the Aging-Induced Stiffness Increase in Sand. *International Journal of Geomechanics*, *18*(12), 4018173. https://doi.org/10.1061/(ASCE)GM.1943-5622.0001320

Lin, W., Liu, A., Mao, W., & Koseki, J. (2020). Acoustic emission behavior of granular soils with various ground conditions in drained triaxial compression tests. *Soils and Foundations*, *60*(4), 929–943. https://doi.org/10.1016/j.sandf.2020.06.002

Liu, H., Cascante, G., Maghoul, P., & Shalaby, A. (2022). Experimental investigation and numerical modeling of piezoelectric bender element motion and wave propagation analysis in soils. *Canadian Geotechnical Journal*, *59*(3), 330–341. https://doi.org/10.1139/cgj-2020-0757

Mao, W., Aoyama, S., Goto, S., & Towhata, I. (2015). Acoustic emission characteristics of subsoil subjected to vertical pile loading in sand. *Journal of Applied Geophysics*, *119*, 119–127. https://doi.org/10.1016/j.jappgeo.2015.05.017

Mejia, C. A., Vaid, Y. P., & Negussey, D. (1988). Time dependent behaviour of sand. In M. J. Keedwell (Ed.), *International Conference on Rheology and Soil Mechanics: Proceedings* (pp. 312–326). Spon Press.

Mesri, G., Feng, T. W., & Benak, J. M. (1990). Postdensification Penetration Resistance of Clean Sands. *Journal of Geotechnical Engineering*, *116*(7), 1095–1115. https://doi.org/10.1061/(ASCE)0733-9410(1990)116:7(1095)

Mesri, G., & Vardhanabhuti, B. (2009). Compression of granular materials. *Canadian Geotechnical Journal*, *46*(4), 369–392. https://doi.org/10.1139/T08-123

Michalowski, R. L., Wang, Z., & Nadukuru, S. S. (2018). Maturing of contacts and ageing of silica sand. *Géotechnique*, *68*(2), 133–145. https://doi.org/10.1680/jgeot.18.D.004

Michlmayr, G., Cohen, D., & Or, D. (2012). Sources and characteristics of acoustic emissions from mechanically stressed geologic granular media — A review. *Earth-Science Reviews*, *112*(3-4), 97–114. https://doi.org/10.1016/j.earscirev.2012.02.009

Michlmayr, G., & Or, D. (2014). Mechanisms for acoustic emissions generation during granular shearing. *Granular Matter*, *16*(5), 627–640. https://doi.org/10.1007/s10035-014-0516-2

Mitchell, J. K. (2005). *Fundamentals of soil behavior* (3rd ed.). John Wiley & Sons.

Mitchell, J. K., & Solymar, Z. V. (1984). Time-Dependent Strength Gain in Freshly Deposited or Densified Sand. *Journal of Geotechnical Engineering*, *110*(11), 1589-1576.

Miura, S., & Toki, S. (1982). Sample preparation method and its effect on static and cyclic deformation — strength properties of sand. *Soils and Foundations*, *22*(1), 61–77.

Murayama, S., Michihiro, K., & Sakagami, T. (1984). Creep Characteristics of Sands. *Soils and Foundations*, *24*(2), 1–15. https://doi.org/10.3208/sandf1972.24.2_1

Naderi-Boldaji, M., Bahrami, M., Keller, T., & Or, D. (2017). Characteristics of Acoustic Emissions from Soil Subjected to Confined Uniaxial Compression. *Vadose Zone Journal*, *16*(7). https://doi.org/10.2136/vzj2017.02.0049

Ovalle, C., Dano, C., Hicher, P.-Y., & Cisternas, M. (2015). Effects of Flooding on Crushable Sand. In K.-T. Chau & J. Zhao (Eds.), *Springer Series in Geomechanics and Geoengineering. Bifurcation and Degradation of Geomaterials in the New Millennium: Proceedings of the 10th International Workshop on Bifurcation and Degradation in Geomaterials* (pp. 91–98). Springer Cham. https://doi.org/10.1007/978-3-319-13506-9_14

Peiji, Y., & Richart, F. E. (1983). Stress Ratio Effects on Shear Modulus of Dry Sands. *Journal of Geotechnical Engineering*, *110*(3), 331–346.

Rad, N. S., & Tumay, M. T. (1987). Factors Affecting Sand Specimen Preparation by Raining. *Geotechnical Testing Journal*, *10*(1), 31–37.

Radjai, F., Wolf, D. E., Jean, M., & Moreau, J.-J. (1998). Bimodal Character of Stress Transmission in Granular Packings. *The American Physical Society*, *80*(1), 61–65.

Rundle, J. B., Turcotte, D. L., Shcherbakow. R., Klein, W., & Sammis, C. (2003). Statistical physics approach to understanding the multiscale dynamics of earthquake fault systems. *Reviews of Geophysics*, *41*(4). https://doi.org/10.1029/2003RG000135

Sánchez-Salinero, I., Roesset, J. M., & Stokoe, K. H [I.]. (1986). *Analytical Studies of Body Wave Propagation and Attenuation* (GR86-15) [Report]. University of Texas, Austin.

Santamarina, J. C., & Cascante, G. (1996). Stress anisotropy and wave propagation: a micromechanical view. *Canadian Geotechnical Journal*, *33*(5), 770–782. https://doi.org/10.1139/t96-102-323

Santamarina, J. C., & Fam, M. A. (1997). Discussion: Interpretation of bender element tests. *Géotechnique*, *47*(4), 873–877. https://doi.org/10.1680/geot.1997.47.4.873

Santamarina, J. C., & Fratta, D. (Eds.). (2005). *Discrete signals and inverse problems: An introduction for engineers and scientists*. Wiley. https://doi.org/10.1002/0470021896

Sasche, W., & Pao, Y.-H. (1978). On the determination of phase and group velocities of dispersive waves in solids. *Journal of Applied Physics*(49), 4320–4327.

Sawangsuriya, A. (2012). Wave Propagation Methods for Determining Stiffness of Geomaterials. In P. Giovine (Ed.), *Wave Processes in Classical and New Solids.* InTech. https://doi.org/10.5772/48562

Schmertmann, J. H. (1991). The Mechanical Aging of Soils. *Journal of Geotechnical Engineering*, *117*(9), 1288–1330. https://doi.org/10.1061/(ASCE)0733-9410(1991)117:9(1288)

Serway, R. A., & Jewett, J. W. (2014). *Physics: For scientists and engineers with modern physics* (9. ed.). Brooks/Cole.

Shiotani, T. (2008). Parametric AE Analysis. In C. Grosse & M. Ohtsu (Eds.), *Acoustic emission testing: Basics for research - applications in civil engineering* (pp. 41–52). Springer.

Shiotani, T., & Ohtsu, M. (1999). Prediction of Slope Failure Based on AE Activity. In S. J. Vahaviolos (Ed.), *Acoustic Emission: Standards and Technology Update.* ASTM. https://doi.org/10.1520/STP15787S

Singh, A., & Mitchell, J. K. (1968). General Stress-Strain-Time Function for Soils. *Journal of the Soil Mechanics and Foundations Division*, *94*(1), 21–46. https://doi.org/10.1061/JSFEAQ.0001084

Skov, R., & Denver, H. (1988). Time-dependence of bearing capacity of piles. *Proceedings of 3rd International Conference on the Application of Stress-Wave Theory to Piles*, 879–888.

Smith, A., & Dixon, N. (2019). Acoustic emission behaviour of dense sands. *Géotechnique*, *69*(12), 1107–1122. https://doi.org/10.1680/jgeot.18.P.209

Smith, A., Dixon, N., Meldrum, P., Haslam, E., & Chambers, J. (2014). Acoustic emission monitoring of a soil slope: Comparisons with continuous deformation measurements. *Géotechnique Letters*, *4*(4), 255–261. https://doi.org/10.1680/geolett.14.00053

Suarez, N. R. (2012). *Micromechnical Aspects of Ageing in Granular Soils* [Dissertation]. Virginia Polytechnic Institute and State University, Blacksburg, VA.

Suklje, L. (1957). The analysis of the consolidation process by the isotaches method. *Proceedings of the 4th International Conference on Soil Mechanics and Foundation Engineering*, 200–206.

Tanaka, Y., & Tanimoto, K. (1988). Time Dependent Deformation of Sand as Measured by Acoustic Emission. In M. J. Keedwell (Ed.), *International Conference on Rheology and Soil Mechanics: Proceedings* (pp. 182–193). Spon Press.

Tatsuoka, F., Di Benedetto, H., Kongkitkul, W., Kongsukprasert, L., Nishi, T., & Sano, Y. (2008). Modelling of Ageing Effects on the Elasto-Viscoplastic Behaviour of Geomaterial. *Soils and Foundations*, *48*(2), 155–174. https://doi.org/10.3208/sandf.48.155

Tatsuoka, F., Iwasaki, T., Yoshida, S., Fukushima, S., & Sudo, H. (1979). Shear Modulus and Damping by Drained tests on Clean Sand Specimens Reconstituted by Various Methods. *Soils and Foundations*, *19*(1), 39–54. https://doi.org/10.3208/sandf1972.19.39

Taylor, D. W., & Merchant, W. (1940). A Theory of Clay Consolidation Accounting for Secondary Compression. *Journal of Mathematics and Physics*, *19*(1-4), 167–185.

Terzaghi, K. (1925). *Erdbaumechanik auf bodenphysikalischer Grundlage*. Deuticke.

Thornton, C., & Barnes, D. J. (1986). Computer simulated deformation of compact granular assemblies. *Acta Mechanica*, *64*(1-2), 45–61. https://doi.org/10.1007/BF01180097

TiePie engineering. *Multi Channel oscilloscope software* [Computer software]. https://www.tiepie.com/en/oscilloscope-software

Turcotte, D. L. (1997). *Fractals and chaos in geology and geophysics* (2. ed.). Cambridge Univ. Press.

Vaid, Y. P., & Negussey, D. (1984). Relative Density of Pluviated Sand Samples. *Soils and Foundations*, *24*(2), 101–105. https://doi.org/10.3208/sandf1972.24.2_101

Vallen, H. (2003). *Die Schallemissionsprüfung*. Castell-Verlag GmbH.

Vallen Systeme GmbH (2017). AMSY-6 Operation Manual [*Unpublished Manual]*.

Varotsos, P. A., Sarlis, N. V., Skordas, E. S., & Tanaka, H. (2004). A plausible explanation of the b-value in the Gutenberg-Richter law from first principles. *Proceedings of the Japan Academy*, *80*(9), 429-434.

Viggiani, G., & Atkinson J.H. (1995). Interpretation of bender element tests. *Géotechnique*, *45*(1), 149–154 (Technical Note).

Vogt, N., Heyer, D., Birle, E., Vogt, S., Dahmen, D., Karcher, C., Vinzelberg, G., & Eidam, F. (2013). Aspects for Bulding a Motorway on a 185m Deep Dump. In International Society for Soil Mechanics and Geotechnical Engineering (Ed.), *Proceedings of the 18th Conference on Soil Mechanics and Geotechnical Engineering* (pp. 1377–1380).

Wang, J., & Xia, Z. (2021). DEM study of creep and stress relaxation behaviors of dense sand. *Computers and Geotechnics*, *134*, 104142. https://doi.org/10.1016/j.compgeo.2021.104142

Wang, Y.-H., Lau, Y. M., & Gao, Y. (2014). Examining the mechanisms of sand creep using DEM simulations. *Granular Matter*, *16*(5), 733–750. https://doi.org/10.1007/s10035-014-0514-4

Wang, Y.-H., & Tsui, K.-Y. (2008). Density Effects on the Aging Behavior of Sands and the Anisotropy of Aging-Induced Stiffness Increases. In D. Zeng (Ed.), *Geotechnical special publication: No. 181, Geotechnical Earthquake Engineering and Soil Dynamics IV* (pp. 1–10). American Society of Civil Engineers. https://doi.org/10.1061/40975(318)40

Wang, Y.-H., & Tsui, K.-Y. (2009). Experimental Characterization of Dynamic Property Changes in Aged Sands. *Journal of Geotechnical and Geoenvironmental Engineering*, *135*(2), 259–270. https://doi.org/10.1061/(ASCE)1090-0241(2009)135:2(259)

Wang, Y.-H., Xu, D., & Tsui, K. Y. (2008). Discrete Element Modeling of Contact Creep and Aging in Sand. *Journal of Geotechnical and Geoenvironmental Engineering*, *134*(9), 1407–1411. https://doi.org/10.1061/(ASCE)1090-0241(2008)134:9(1407)

Wiebicke, M., Herle, I., Andò, E., & Viggiani, G. (2020). Measuring the fabric evolution of sand – application and challenges. *Geotechnik*, *44*(2), 114–122. https://doi.org/10.1002/gete.202000019

Yamashita, S., Fujiwara, T., Kawaguchi, T., Mikami, T., Nakata, Y., & Shibuya, S. (2009). International Parallel Test on the Measurement of Gmax Using Bender Elements Organized by TC-29. *Japanese Domestic Committee for TC-29*.

Yamashita, S., Kawaguchi, T., Nakata, Y., Mikami, T., Fujiwara, T., & Shibuya, S. (2009). Interpretation of International Parallel Test on the Measurement of Gmax Using Bender Elements. *Soils and Foundations*, *49*(4), 631–650. https://doi.org/10.3208/sandf.49.631

Ye, J., Haiyilati, Y., Cao, M., Zuo, D., & Chai, X. (2022). Creep characteristics of calcareous coral sand in the South China Sea. *Acta Geotechnica*, *17*(11), 5133–5155. https://doi.org/10.1007/s11440-022-01634-1

Yusa, M. (2015). *Aging and creep of non-plastic silty sand* [Dissertation]. University of Canterbury, Christchurch, New Zealand. https://doi.org/10.26021/1554

Zhang, Z., & Wang, Y.-H. (2016). DEM modeling of aging or creep in sand based on the effects of microfracturing of asperities and evolution of microstructural anisotropy during triaxial creep. *Acta Geotechnica*, *11*(6), 1303–1320. https://doi.org/10.1007/s11440-016-0483-3

A.1 Appendix: Data sheets of measurement techniques

A.1.1 Data sheet of Bender Elements[16]

Type: Classic Parallel v1.0k

Technical Description:

The Bender Elements are designed for generating and receiving shear waves in sand or similar materials. The system consists of two separate transducers with protruding piezo-ceramic crystal elements (a sender and receiving transducer). The crystals are designed to vibrate in response to electrical excitation, and similarly in response to external vibrations the crystals produce an electrical signal. In this way, an electrical signal can be used to send a signal with one transducer into a material sample. The receiving transducer reacts to the wave travelling through the sample. The shear waves travel in a polarised plane with vibrations normal to the plane of the crystal. Due to this polarisation, the sending and receiving elements should be aligned to maximise strength and clarity of the received signal.

Technical Specifications:

Mechanical Resonance	6 kHz
Electrical Resonance	29 kHz
Runtime Delay	1.05 µs
Excitation, waveform	Sine or rectangular burst
Nominal Operating Voltage	10 Vpp
Maximum Operating Voltage	50 Vpp
Temperature Range	-10°C … +60°C (continuous)
Pressure Resistance	2 MPa
Diameter (ultrasonic head)	18 mm
Connection	1 x BNC-plug
Cable	Liycy 4x0.14mm² – 3m
Transverse wave orientation	Dot on top side of piezo-ceramic crystal

[16] APS Antriebs-, Prüf- und Steuertechnik GmbH, Wille Geotechnik ® (2020)

A.1.2 Data sheet of ultrasonic device[17]

Type: USWKE18005

Technical Description:

With this ultrasonic sensor compression as well as shear waves can be generated and received. The sensor is adapted to sand or similar materials. It works with two completely separated electrical transducers. Due to the flat material contact surface, high mechanical loads are possible. For transverse wave transmission, the two sensors must be aligned with the marking.

Technical Specifications:

Mechanical Resonance (longitudinal)	26 kHz
Mechanical resonance (transversal)	47 kHz
Resonance of the ceramic (longitudinal)	179 kHz
Resonance of the ceramic (transversal)	141 kHz
Runtime Delay (longitudinal)	2.20 µs
Runtime Delay (transversal)	1.05 µs
Excitation, waveform	Sine or rectangular burst
Nominal Operating Voltage	10 Vpp
Maximum Operating Voltage	50 Vpp
Temperature Range	-10°C … +60°C
Pressure Resistance	2 MPa
Diameter (ultrasonic head)	18 mm
Connection	2 x BNC-plug to Lemo
Cable	Liycy 4x0.14mm² – 3m
Transverse wave orientation	Colored dot on the contact surface/marker on the side

[17] APS Antriebs-, Prüf- und Steuertechnik GmbH, Wille Geotechnik ® (2020)

A.1.3 Data sheet of acoustic emission[18]

Type: VS45-H

The VS45-H is a passive piezo-electric AE-sensor with a wide frequency response. Its frequency response is characterized by a peak at 280 kHz and can be used in the frequency range from 40 kHz to 450 kHz. It is a broad band response AE-sensor covering the low frequency and standard frequency range.

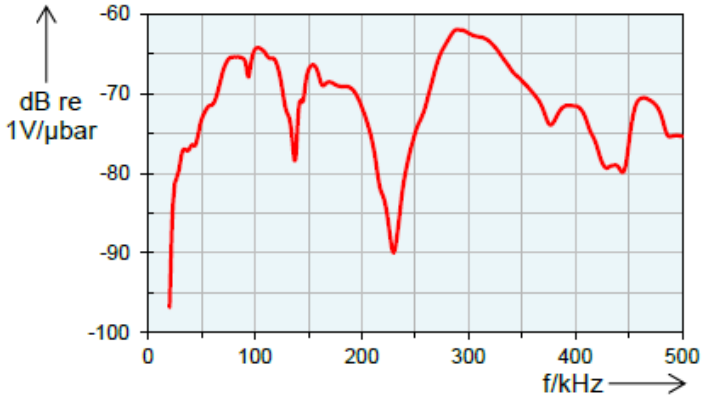

Technical Specifications:

Frequency Range (f_{Peak}) [kHz]	20 to 450 (280)
Capacity [pF]	270
Integrated Preamplifier	No
Operating Temperature [°C]	-20 to +100
Vibration – Sinus sweep	2 Oct/Min, 5 to 180 Hz. 40 g
Ingress Protection Rating	IP40
Size (D x H) [mm]	20.3 x 22.0
Weight [g]	36
Case Material	Stainless Steel (1.4571 / 1.4404)
Wear Plate	Ceramics
Connector	Microdot
Shield Cross-Talk [dB]	< -80

Standards and Directives:

EMC Directive	2014/30/EU
EMC Standards	EN61326-1:2013, EN61326-2-3:2013, EN61000-6-2:2006, EN61000-6-4:2011
Shock and Vibration Stand.	EN60068-2-6:2008
AE Standard	EN13477-1:2013, EN13477-2:2013

Accessoires:

Preamplifier	AEP5, AEP3N
Mounting Holder	MAG4H
Sensor Cable	CBL-1-1M2-V5

[18] Vallen Systeme GmbH (2017)

A.2 Appendix: Sample preparation

A.2.1 Sample preparation mold

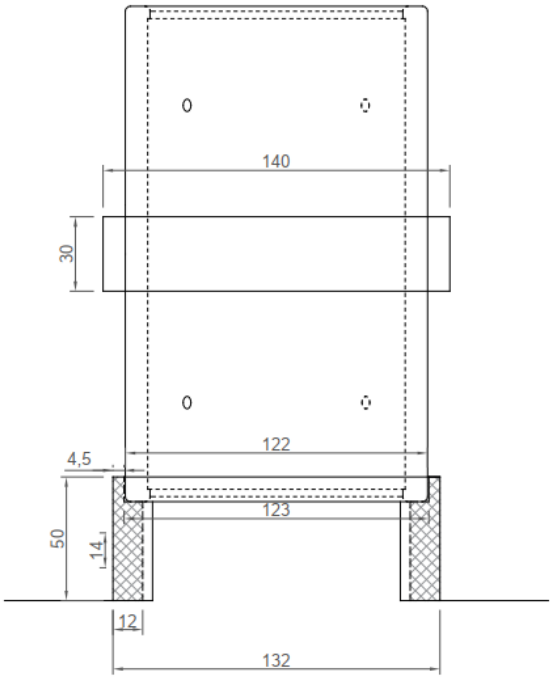

(a)

(b)

Figure 6.1: (a) Dimensioned drawing and (b) photos of the sample preparation mold

A.2.2 Device for the application of the air pluviation method

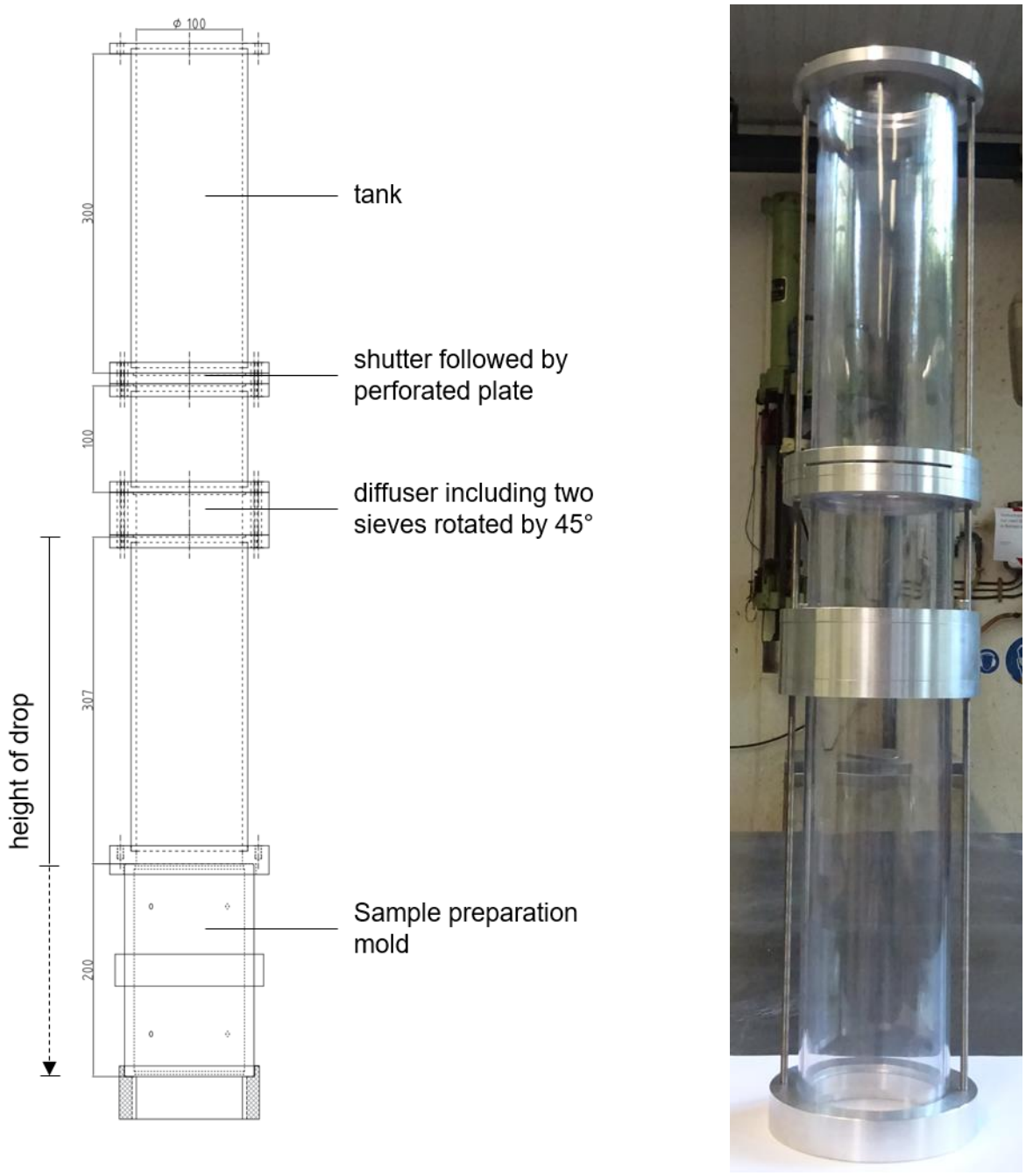

(a) **(b)**

Figure 6.2: (a) Schematic sketch and (b) photograph of the sand pluivator

(a) **(b)**

Figure 6.3: (a) Photo of the diffusor and (b) photo of the perforated plate and shutter

A.2.3 Documentation of sample preparation method by air pluviation

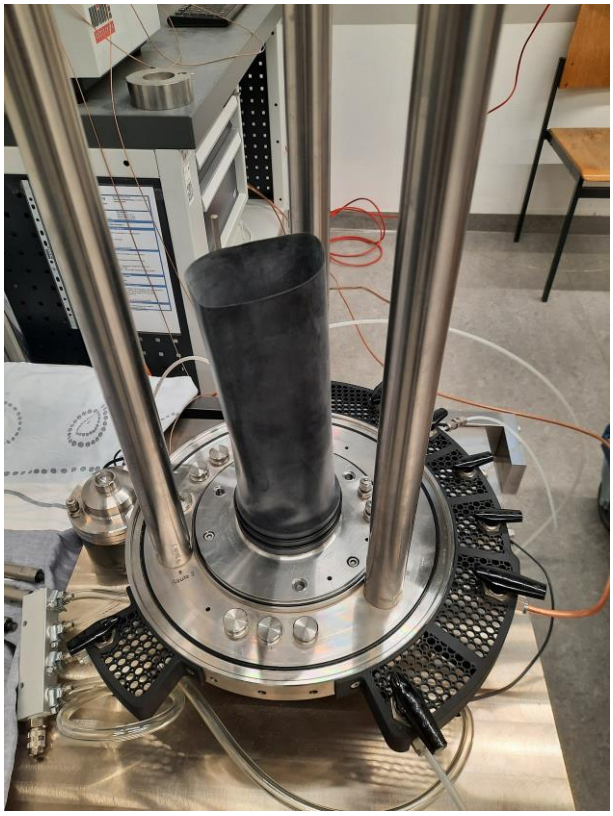

(1)

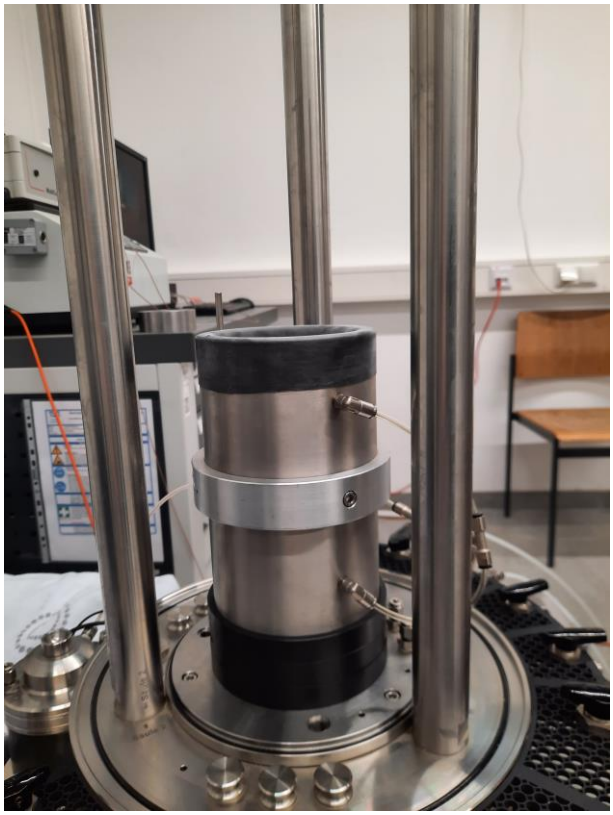

(2)

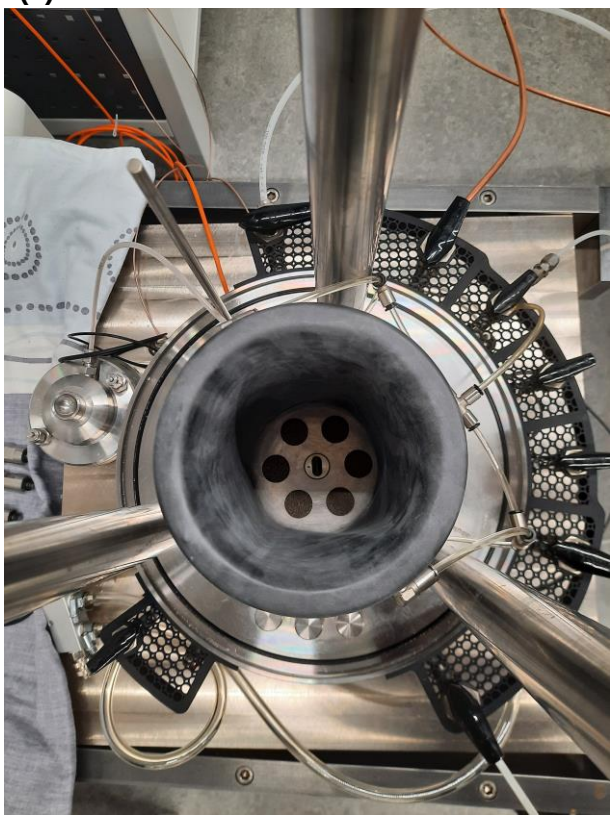

(3)

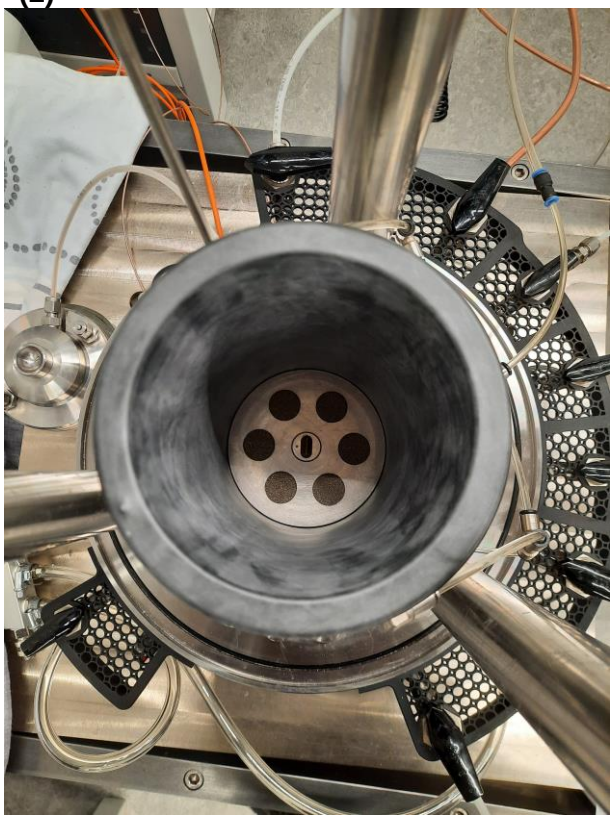

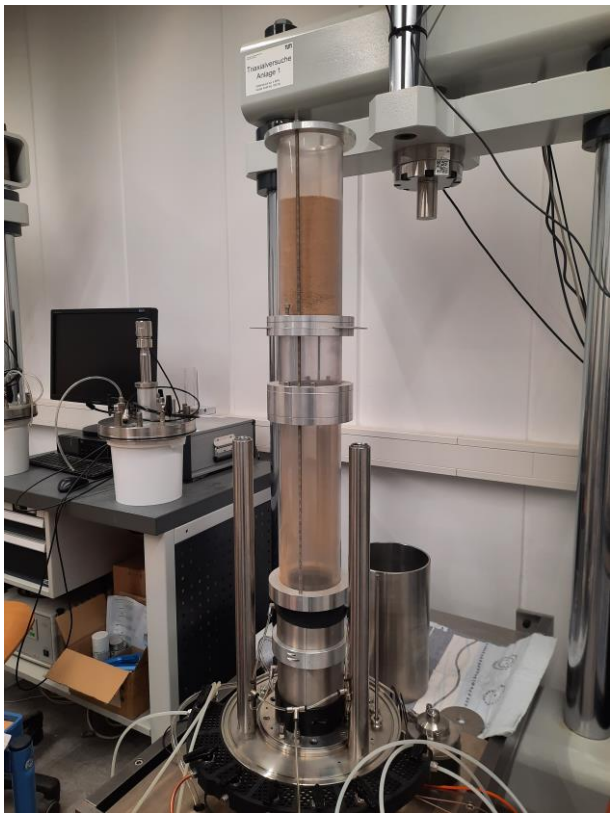

(4)

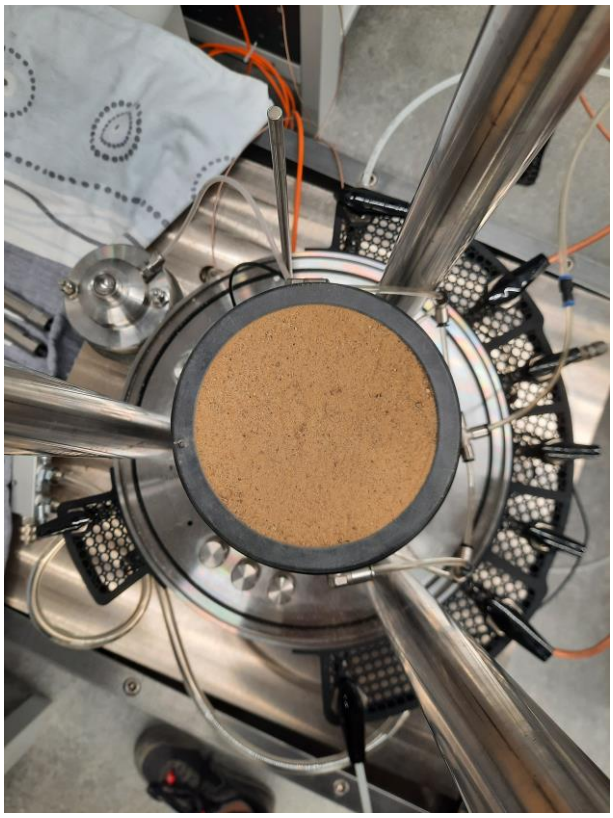

(5)

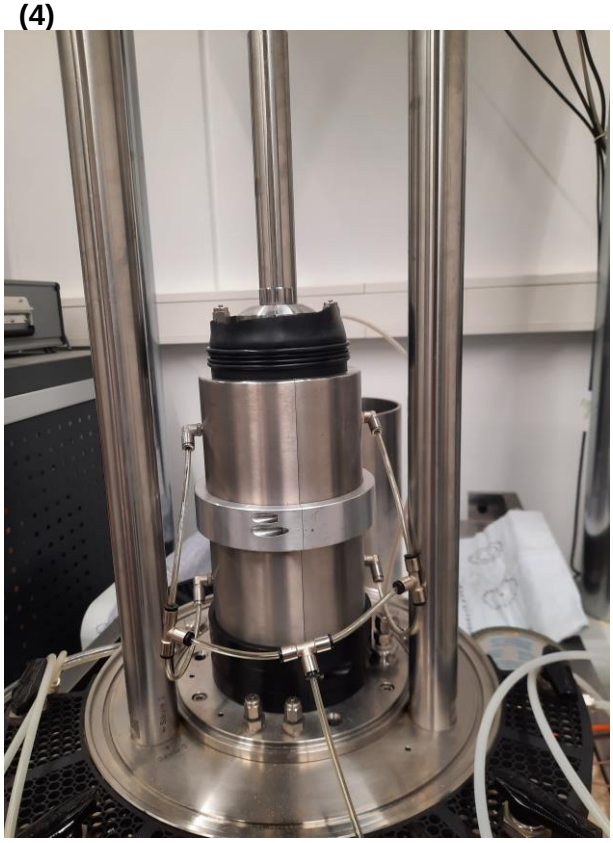

(6)

(7)

(8)

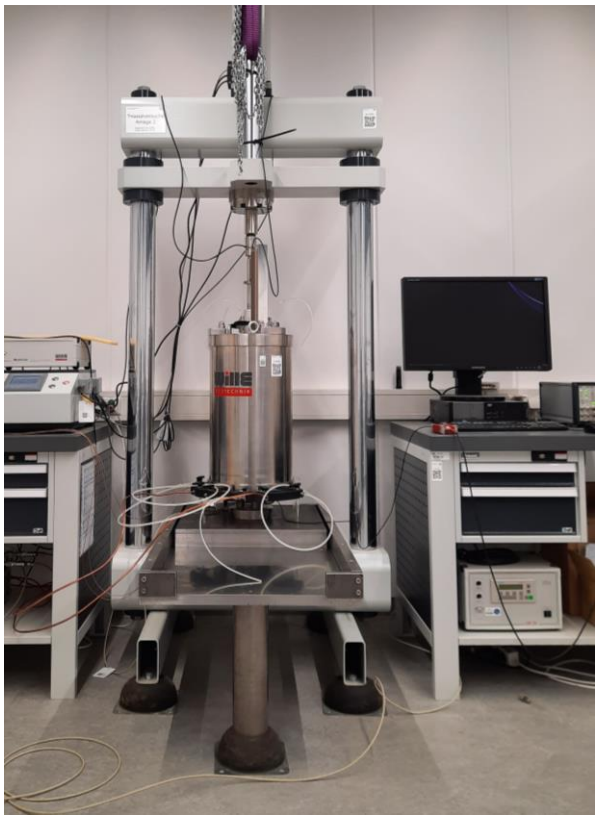

(9)

Figure 6.4: Photo documentation of sample preparation of triaxial samples

(1) Attachment of the membrane to the base of the triaxial cell with O-rings.
(2) Placement of the sample preparation mold on the base plate and attachment of the membrane to it.
(3) Fitting the membrane to the shape of the sample using a vacuum.
(4) Air pluvation of the sand (or alternatively funnel deposition).
(5) Flatten of the surface with a metal ruler.
(6) Placing the loading piston on the sample and wrapping the membrane to it, sealing of membrane with four additional O-rings.
(7) After applying a vacuum to the sample, removing the sample mold; Measurement of the initial sample dimensions.
(8) Building up and filling the inner cell with deaerated water.
(9) Closing and filling the outer cell with water; Installation of the triaxial cell in the loading frame